Calcul des coefficients de fléxoélectricité d'hétérostructures de matériaux 2D avec un modèle (QP) de charges et dipôles effectifs

Yida Yang

THESE DE DOCTORAT DE L'ETABLISSEMENT UNIVERSITE BOURGOGNE FRANCHE-COMTE

PREPAREE A L'UNIVERSITE DE FRANCHE-COMTE

Ecole doctorale n° 37

Sciences Physiques pour l'Ingénieur et Microtechniques

Doctorat en Sciences des Matériaux

Par

M. YANG Yida

Computation of flexoelectric coefficients for heterostructures of 2D materials using an effective charge-dipole (QP) model

Calcul des coefficients de fléxoélectricité d'hétérostructures de matériaux 2D avec un modèle (QP) de charges et dipôles effectifs

Thèse présentée et soutenue à Besançon, le 14/12/2022

Composition du Jury :

Mme	BARTASYTE Ausrine	Professeur, Université de Franche-Comté	Présidente
M.	PARK Harold	Professeur, Boston State University (USA)	Rapporteur
M.	GANGHOFFER Jean-François	Professeur, Université de Lorraine	Rapporteur
M.	MAYER Alexandre	Chercheur qualifié au FNRS, Université de Namur	Examinateur
M.	DEVEL Michel	Professeur, Supmicrotech-ENSMM	Directeur de thèse
M.	HIRSINGER Laurent	Chargé de recherche, CNRS, FEMTO-ST	Codirecteur de thèse
M.	DAHER Naoum	Chargé de recherche CNRS en retraite, FEMTO-ST	Invité

Abstract

Flexoelectricity is a type of electromechanical coupling, pertaining to the electrical polarization response to mechanical strain gradients. Unlike piezoelectricity, this effect is not restricted to non-centrosymmetric materials, but it tends to be rather weak for most macroscale materials, i.e. bulk ceramics. However, it can be comparable and even more important than the piezoelectric effect at the nanoscale. Hence, it becomes increasingly significant to seek for a nanomaterial with a comparably large flexoelectric coefficient for applications in energy harvesters or electromechanical conversion device. The main objective of this thesis is to develop a systematic method for calculating flexoelectric coefficients for two-dimensional (2D) materials and heterostructures of these materials, using continuum mechanics and/or an atomistic model with effective charges and dipoles corresponding to Gaussian radial distributions of charges. We first checked analytically the equivalence of two formulas used to calculate the electrostatic interaction forces between atoms due to an external electric field. Next, we sought to extend a previous work by incorporating terms involving effective charges into an analytical expression for calculating the flexoelectric coefficients of ionic crystals, such as MoS_2. In a second, more numerical part, we were able to find simulation set-ups allowing us to calculate the in-plane μ_{1111} and μ_{2222}, transverse μ_{3311} and out-of-plane μ_{3333} flexoelectric coefficients for a monolayer of MoS_2. For this purpose, we have used a definition of polarization including the effects of both charge and effective dipole, as well as charge conservation enforcement. The results obtained being in good agreement with the data available in the literature, we were able to apply our method to the case of a graphene / h-BN bilayer structure and to study the influence of the relative positions of the two layers.

Résumé

La flexoélectricité est un type de couplage électromécanique relatif à un changement de polarisation électrique d'un matériau en réponse à un gradient de contrainte mécanique. Contrairement à la piézoélectricité, cet effet n'est pas restreint aux matériaux non-centrosymmétriques, mais il a tendance à être plutôt faible à l'échelle macroscopique. Par contre, il peut être comparable et même supérieur à l'effet piézoélectrique à l'échelle nanométrique. Par conséquent, il devient de plus en plus important de rechercher des nanomatériaux avec des coefficients flexoélectriques relativement élevés pour des applications dans des récupérateurs d'énergie ou des dispositifs de conversion électromécaniques. L'objectif principal de cette thèse est de mettre au point une méthode systématique pour calculer des coefficients flexoélectriques pour des matériaux bidimensionnels (2D) et des hétérostructures de ces matériaux, en utilisant la mécanique des milieux continus et/ou un modèle atomistique avec des charges et des dipôles effectifs correspondant à des distributions radiales gaussiennes de charge. Nous avons tout d'abord vérifié analytiquement l'équivalence de deux formules utilisées pour calculer les forces d'interaction électrostatique entre atomes dues à un champ électrique exterieur. Ensuite, nous avons cherché à étendre un travail précédent en incorporant des termes impliquant les charges effectives dans une expression analytique, pour calculer les coefficients flexoélectriques de cristaux ioniques, tels que MoS_2. Dans une deuxième partie plus numérique, nous avons pu trouver des configurations de simulation nous permettant de calculer les coefficients flexoélectriques dans le plan μ_{1111} et μ_{2222}, transversal μ_{3311} et hors-plan μ_{3333} pour une monocouche de MoS_2. Pour cela, nous avons utilisé une définition de la polarisation incluant à la fois les effets des charges et des dipôles effectifs, ainsi que le forçage de la conservation de la charge. Les résultats obtenus étant en bon accord avec les données disponibles dans la littérature, nous avons pu appliquer notre méthode au cas d'une structure bicouche graphène / h-BN et étudier l'influence des positions relatives des deux couches.

Acknowledgment

Undertaking this PhD has been a truly life-changing experience for me and it would not have been possible to do without the support and encouragement that I received from many people. I would like to first say a very big thank you to my supervisors professor Michel Devel and researcher Laurent Hirsinger for all the support and guidance they gave me during the three years I spent at FEMTO-ST. But for the help from my supervisors, this PhD would not have been achievable.

Many thanks also to Muamer Kadic, Vincent Laude, Sébastien Euphrasie, and Patrice Salzenstein from Phomi group for their many suggestions for my papers and oral presentation for an international conference.

I am also very grateful to Pr. Harold Park and Pr. Jean-François Ganghoffer for accepting to report on this document and be part of my oral defense jury, and to Dr. Alexandre Mayer, Pr. Ausrine Bartasyte and Dr. Naoum Daher for accepting to be part of the jury.

My sincere gratitude also goes to administration staffs including Ayoko Afanou, Jocelyne Renaut, Axelle Rabbe, Marilyne Draps, Mireille Schwaar, Lisa Osorio and Alika Rossetti for their help.

I am indebted to all my friends that include Fangnao Xiao, Lianchao Wang, Kouassi Dakmak N'dri, Johnny Moughames, Achraf el Mohajir, Céline Codjiovà balasubramaniam Namasivayam and Fernando Eleazar García Ramírez for their help in my life.

I would also like to say a heartfelt thank you to my Mum, Dad for always believing in me and encouraging me to follow my dreams.

Finally, I gratefully acknowledge the funding received towards my PhD from French government. Without the financial support, this research would not have been fulfilled.

Contents

Acknowledgment v

Contents vii

Introduction xi

I Introduction to Flexoelectricity 1

I.1 Piezoelectricity Versus Flexoelectricity 2

I.2 On the different definitions for flexoelectric coefficients 3

I.3 Historical Review 4

I.3.1 Theoretical Literature Review 4

I.3.2 Experimental Literature Review 5

I.3.3 Experimental setups 6

I.4 Computational methods for flexoelectricity 9

I.4.1 Ab-initio calculations 9

I.4.2 Other calculation methods 10

I.5 Application of flexoelectricity 11

I.5.1 Sensors 11

I.5.2 Nanogenerators 11

I.5.3 Actuators 13

II Effective piezoelectricity coefficient in patterned graphene computed using electrostatic forces calculated within charge dipole model 15

II.1 Introduction 16

II.2 Description of the charge dipole model 17

II.3 Description of the Gaussian regularized charge dipole model 18

II.4 Computation of electrostatic forces for two carbon atoms 20

II.5 Analytical expressions for the force 26
II.5.1 Direct method by direct derivation of the full energy, valid even if charges and dipoles are not equilibrated . 26
II.5.2 Second method with explicit determination of the gradients 28
II.5.3 Third method using the derivative of the block-matrix of interaction tensors 31
II.6 Computation of in-plane piezoelectric coefficient caused by flexoelectricity for patterned graphene 34
II.6.1 A little literature review on computation of piezoelectricity for graphene 34
II.6.2 Introduction to Javvaji's 2018 paper 35
II.6.3 Modifications with respect to the work of Javvaji et al 37
II.6.4 Computation of piezoelectric coefficient 39
II.7 Conclusions 42

III Study of the flexoelectricity of MoS_2 through the development of multi-scale algorithms mixing atomistic approach and continuum physics 45
III.1 Introduction 46
III.2 Representative volume elements 46
III.3 Use of an extended Cauchy-Born rule 47
III.4 Derivation of analytical formula for computation of flexocoupling coefficients 49
III.5 Results and Discussion 56
III.6 Conclusion 60

IV Computation of Flexoelectric Coefficients of a MoS_2 monolayer 61
IV.1 Motivation 62
IV.2 Introduction 62
IV.3 Principle of the method used to compute flexoelectricity coefficients 64
IV.4 Method for the computation of strain gradient G 65
IV.5 Calculation of flexoelectricity coefficients 67

IV.5.1 potential energy functional used for the 'structure' part . . . 67
IV.5.2 Initial conditions for the calculation of μ_{3311} . . . 68
IV.5.3 Detailed description for Stillinger-Weber potential . . . 69
IV.5.4 Calculation of μ_{3311} . . . 71
IV.6 Results and discussion . . . 72
IV.6.1 Out-of-plane flexoelectric coefficient μ_{3333} . . . 73
IV.6.2 Transverse flexoelectric coefficient μ_{3311} . . . 75
IV.6.3 In-plane flexoelectric coefficient μ_{1111} and μ_{2222} . . . 80
IV.7 Conclusions . . . 82

V Computation of Flexoelectric coefficient of bilayered materials . . . 85
V.1 Introduction . . . 86
V.2 Methods . . . 86
V.2.1 First principle calculations . . . 86
V.2.2 Molecular dynamics simulations for computation of μ_{3311} . . . 87
V.2.3 Computation of polarization . . . 88
V.3 Structural properties of graphene/h-BN heterostructures . . . 90
V.4 Parameterization of the charge dipole model for Graphene/Boron Nitride heterostructure system . . . 92
V.5 Validation of the charge dipole model . . . 94
V.6 Computation of bending flexoelectric coefficient for graphene, h-BN and their vertically stacked heterostructure . . . 98
V.7 Conclusion . . . 103

Conclusions and perspectives . . . 105

Bibliography . . . 109

List of Figures . . . 129

List of Tables . . . 135

Introduction

If we consider bone repair and remodelling, barium strontium titanate-fabricated microphone, ultra-high density memories, microcurvature sensor, nanogenerator without piezoelectric materials, we can wonder what all theses recent study subjects have in common? The answer is flexoelectricity.

Flexoelectricity, distinguished from piezoelectricity, is a type of electromechanical coupling between dielectric polarization and strain gradient, whereas piezoelectricity is now restricted to be the coupling between dielectric polarization and uniform strain. This effect does not rely on the breaking of centrosymmetry in the material and therefore universally exists in all condensed phase materials. However, at the macro scale, the flexoelectric effect can be considered too much weaker than piezoelectricity for most materials as regards the ability to convert a strain (uniform or not) into an electric polarization (voltage). A breakthrough, however, came with the realization that flexoelectricity can be enhanced to a level comparable to piezoelectricity at nano scale, for strain gradient at that scale can be much larger than that at the macroscale. Accordingly, the significance of studying flexoelectricity of nanomaterials, i.e., two-dimensional materials (2D materials), is growing due to the urgent needs for miniaturized materials from the technology industry in the current era. Early experimental studies on flexoelectricity mostly focused on liquid crystals. However, this situation changed in the early 2000s, with a series of publications from Cross et al. at Pennsylvania State University, showing that the flexoelectric coefficient in materials with high dielectric constants is measured experimentally to be much larger than previously expected. Since then, the interest of researchers in flexoelectricity increased at an accelerating rate, both computationally and experimentally.

This PhD thesis is thus principally aimed at finding a multilayer nanomaterial with a comparably large bending flexoelectric coefficient for energy conversion use, taking advantage of computational means, for applications such as energy harvesters. In order to do this, we designed and tested a novel simulation setup to compute the bending flexoelectric coefficient for some two-dimensional materials and heterostructures constituted by them. It is organized as follows:

- Chapter 1 is a general introduction to flexoelectricity that include (1): A comparison between piezoelectricity and flexoelectricity (2) Discussion of some different definitions for flexoelectric coefficients (3) Historical investigation to flexoelectricity (theory and experiment development) (4) Computational method on flexoelectricity (5) Application of flexoelectricity. Chapter 1 can make reader get to know flexoelectricity.

- In chapter 2, we give account of our efforts to compare the results we obtained by improving a fortran code developed in our group for years and in particular during a previous PhD [Lecoutre 18], with results published just before the beginning of this thesis in an article by a group working in Hannover [Javvaji 18] in which they used the same model we also use, i.e. the charge dipole model. In this atomistic model, self-consistently computed effective charges and dipoles are used in combination with a 'structure' force field to simulate the effect of an external electric field on a nanosystem. Javvaji *et al.* used that model to compute the in-plane flexoelectric coefficient μ_{1111} for patterned graphene. Unfortunately, we found several typesetting errors in that paper (especially in the appendix) and questioned ourselves about some of the formula. We clarified some problems through exchange of mails with the first author, but some problems remained concerning the analytical expressions used to compute forces as function of the effective charges and dipoles, or the definition of polarization, or the absence of any enforcement of charge conservation. The various steps we took to study the first of these three points is discussed in detail at the beginning of chapter 2, while the other two points are discussed in the second part of chapter 2 based on the computation of in-plane piezoelectric coefficient e_{111} of several patterned graphenes with a circular or triangular defect or a trapezium-shaped graphene.

- In chapter 3, trying to establish a connexion between continuum physics used e.g. in finite element simulations and our atomistic charge dipole model, we tentatively incorporated charge terms into the analytical formula derived by Gautier Lecoutre during his PhD thesis[Lecoutre 18], using virtual power principle and an extended Cauchy-Born homogenization hypothesis, for calculating the flexoelectric coefficients of various carbon nanotubes. We then explain how we tested our new formula for the computation of the full flexoelectric coefficients of 2D MoS_2. The results were however unsatisfactory. We try to propose reasons for that.

- For the work detailed in chapter 4, we took inspiration from another paper of the Hannover group[Zhuang 19] reporting transverse (bending) flexoelectric coefficients for many 2D materials, using the charge dipole model coupled with molecular dynamics, to study the effect of taking into account (or not) a charge term in the polarization and enforcing explicitly charge conservation for an ionic material e.g. 2D MoS_2. Hence, we explain how we computed not only the transverse (bending) flexoelectric coefficient μ_{3311}, but also the out-of-plane flexoelectric coefficient μ_{3333} and the in-plane flexoelectric coefficients μ_{1111} and μ_{2222}. Since we found negative signs for some of these coefficients whereas they are always positive in the literature, we discuss the common use of definitions that favor obtaining a positive material coefficient and we point out the interplay between two opposite effects that can indeed give rise to net negative coefficients.

- In chapter 5, we first describe how we parameterized the charge dipole model for the graphene/hexagonal Boron Nitride (GBN) heterostructure by using an iterative algorithm plus an optimization algorithm named BOBYQA[Powell 09] and how the obtained parameters were then validated by calculating the piezoelectric coefficient e_{222} of GBN system by comparison with ab-initio calculations. At the end of this chapter, we describe how we computed the bending flexoelectric coefficient μ_{3311} for graphene/h-boron nitride heterostructure, using the same simulation setup used in chapter 4. We then compare the values found for various stackings of this heterostructure to the μ_{3311} values we obtained for hexagonal boron nitride alone and graphene alone.
- Finally, we recall the conclusions of our work and propose some perspectives.

Chapter I
Introduction to Flexoelectricity

I.1 Piezoelectricity Versus Flexoelectricity 2
I.2 On the different definitions for flexoelectric coefficients . . . 3
I.3 Historical Review 4
I.3.1 Theoretical Literature Review 4
I.3.2 Experimental Literature Review 5
I.3.3 Experimental setups 6
I.4 Computational methods for flexoelectricity 9
I.4.1 Ab-initio calculations 9
I.4.2 Other calculation methods 10
I.5 Application of flexoelectricity 11
I.5.1 Sensors 11
I.5.2 Nanogenerators 11
I.5.3 Actuators 13

I.1 Piezoelectricity Versus Flexoelectricity

Flexoelectricity is different from piezoelectricity, although both generate polarization as a response to a mechanical stimulus. Piezoelectric materials, which generate polarization induced by uniform strain, must be non centrosymmetric (see Figure I.1a) because an uniform strain is not able to separate the centroids of positive and negative charges (see Figure I.1). In contrast, flexoelectricity generates polarization from strain gradients. Because the deformation gradient yielded eg. by bending, breaks spatial inversion symmetry, a change of polarization can be produced by flexoelectricity even if the crystal is symmetric, since the inhomogeneous deformation separates the centroids of positive and negative charges (see Figure I.1d).

Flexoelectricity describes the generation of electric polarization by a strain gradient, both in the static and dynamic regimes. The dynamic regime occurs in the case of a propagating acoustic wave, which distorts non-uniformly the lattice. However, in this thesis, we only discuss the static regime, as in the bending of a plate. Following the theory of Kogan[Kogan 64], one of the possible constitutive electromechanical equations, for a non-ferroelectric material, can be written:

$$P_k = \epsilon_0 \chi_{kj} E_j + e_{ijk} S_{ij} + \mu_{ijkl} \frac{\partial S_{ij}}{\partial x_l} \tag{I.1}$$

where the first term on the right hand side describes the dielectric polarization with χ_{kj} and E_j being the dielectric susceptibility and the macroscopic electric field respectively; the second term describes the piezoelectric response to symmetrized strain S_{ij} characterized by the piezoelectric tensor e_{ijk}. The last term describes the flexoelectric polarization, where μ_{ijkl} is a flexoelectric coefficient from a fourth rank tensor and $\frac{\partial S_{ij}}{\partial x_k}$ is the gradient of the elastic strain. The Einstein summation convention is assumed with repeating indices i, j, k, and l in a term indicating summation from 1 to 3. In the absence of macroscopic electric fields, piezoelectricity and flexoelectricity are characterized by tensor relationship, as follows:

$$(P_k)_{E=0} = e_{ijk} S_{ij} + \mu_{ijkl} \frac{\partial S_{ij}}{\partial x_l}. \tag{I.2}$$

Let us note that another effect by which a stress is generated as a response to an electric field gradient can be written:

$$T_{ij} = c_{ijkl} S_{kl} - e_{ijk} E_k + \mu_{ijkl} \frac{\partial E_k}{\partial x_l} \tag{I.3}$$

where c_{ijkl} is the tensor of elastic modulus, T_{ij} is the stress tensor and E_k is the electric field inside the material.

More complete descriptions for flexoelectricity from the phenomenology, lattice dynamics and first-principle points of view, can be found in several reviews[Wang 19, Yudin 13, Zubko 13, Tagantsev 16].

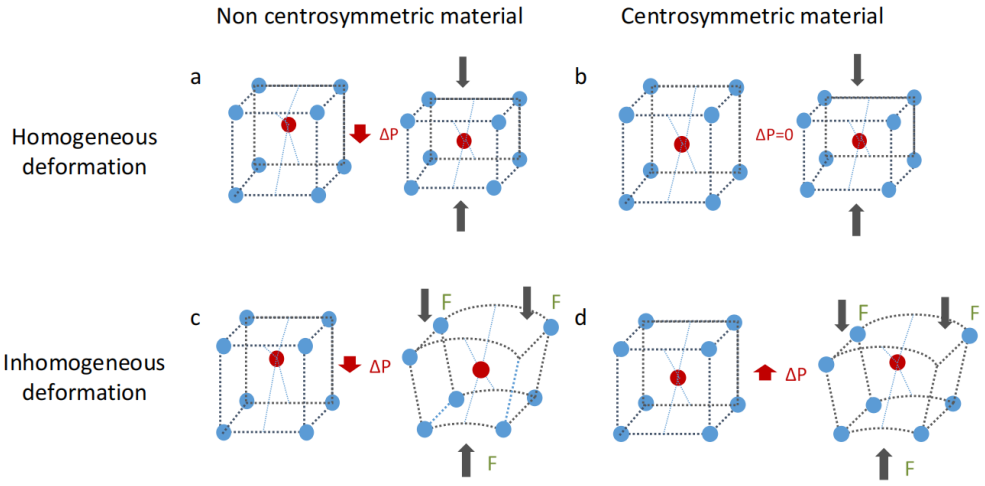

Figure I.1: Effects of mechanical stimulus on centrosymmetric and non-centrosymmetric crystals. (a) and (b) homogeneous deformation polarizes only non-centrosymmetric materials. (c) and (d) inhomogeneous deformation breaks the symmetry of the material to generate non-zero polarization, in both cases.

I.2 On the different definitions for flexoelectric coefficients

There are many different conventions in the literature corresponding to different choices of conjugated thermodynamic variables for the free energy and order of indices of the tensors. Hence the reported flexoelectric coefficients in one paper may not have the same signification or even physical dimension as those reported in other papers and much care should be taken to relate them. Here, we concentrate on two such conventions that seem the most used to us. In order to describe the flexoelectric effect, the traditional equation of piezoelectricity giving the dielectric polarization P_i as a function of the symmetrized strain tensor $S_{ij} = (u_{i,j} + u_{j,i})/2$, with $u_{i,j} = \frac{\partial u_i}{\partial x_j}$ and the product of the dielectric susceptibility at constant strain and entropy density (σ) with the electric field E_j is complemented with a term proportional to the strain gradient (either the symmetrized strain gradient $S_{ij,k}$[Zhu 06, Fu 06, Yudin 13, Tagantsev 16]

$$\Delta P_m = \mu_{ijmk} S_{ij,k} \tag{I.4}$$

or the unsymmetrized strain gradient $u_{j,kl}$[Kogan 64, Tagantsev 86, Maranganti 09, Hong 13])

$$\Delta P_i = \mu_{ijkl} u_{j,kl} \tag{I.5}$$

In equations I.4 and I.5, μ is the fourth order flexoelectric tensor and ΔP_m or ΔP_i is the corresponding induced electric polarization. It can be seen in Eqs. I.4 and I.5 that the indices m or i corresponding to the polarization are respectively put to

the third and the first place in flexoelectric tensor by different researchers. There are also other notations. As an example, in the paper of Zubko et al[Zubko 13], the flexoelectric tensor is defined by $P_l = f_{ijkl}S_{ij,k}$, and in Eq. (1) of Zhuang et al's paper[Zhuang 19] as $P^{\alpha} = d^{\alpha\beta\gamma}\epsilon^{\beta\gamma} + \mu^{\alpha\beta\gamma\delta}\left(\partial\epsilon^{\gamma\delta}/\partial x_{\beta}\right)$. In this thesis, we chose to use

$$\Delta P_i = \mu_{ijkl}u_{j,kl} \tag{I.6}$$

I.3 Historical Review

I.3.1 Theoretical Literature Review

The concept of flexoelectricity was first identified theoretically in solids by Mashkevich and Tolpygo [Mashkevich 57, Tolpygo 63] in the studies of lattice dynamics in crystals and later phenomenologically described by Kogan in 1963 and 1964, based on electron-phonon coupling[Kogan 64] in centrosymmetric crystals. According to his calculations, the characteristic coefficient of the deformation potential, which is now known as flexocoupling coefficient f_{ijkl} (such that $\mu_{ijmk} = \epsilon_0\chi_{mn}f_{ijnk}$), should have a value between $1 - 10$ V. Alternatively, in 1965, Harris[Harris 65] added a term proportional to the gradient of stress to the usual expression for the polarization of a piezoelectric material to account for the existence of the electrical signals observed in the nonpiezoelectric materials subjected to a mechanical disturbances (shock wave) and addressed a microscopic description of dynamic flexoelectricity. In 1968, a macroscopic treatment of the flexoelectric effect, now regarded as the continuum theory of flexoelectricity in the field of mechanics, originated from Mindlin's seminal work on the electromechanical coupling between polarization gradient and strain in elastic dielectrics, which is now referred to as converse flexoelectric effect[Mindlin 68]. In 1970, Askar *et al.* used lattice dynamics and a core-shell model to obtain the macroscopic materials parameters. However, this effect in solid crystals was not "officially" named flexoelectricity until 1981 by Indenbom et al, who directly used the name of a similar phenomenon discovered in liquid crystals by Meyer in 1969[Meyer 69]. Starting in 1985, Tagantsev[Tagantsev 85, Tagantsev 86, Tagantsev 91] systematically formulated the phenomenological and microscopic descriptions of flexoelectricity in crystalline dielectrics, distinguishing the flexoelectric effect from the piezoelectric effect. This author also identified four different contributions to flexoelectric responses, and suggested the significance of flexoelectricity at the nanoscale especially in materials with a large susceptibility χ_{ij}, such as ferroelectrics, since he proposed that the flexoelectric coefficient should be of the order of $\chi e/a$ and not e/a as estimated by Kogan in 1963. In 2008, M. S. Majdoub et al [Majdoub 08] obtained an enhancement of energy harvesting in a bent piezoelectric cantilever nanobeams due to direct flexoelectric effect, employing an atomically informed dynamical continuum model. Based on the surface energy density, Shen and Hu[Shen 10] introduced in 2010 the surface flexoelectric effect for the first time.

Through ab-initio calculation, Resta[Resta 10] made the first effort toward understanding the electronic contribution to flexoelectricity in bulk crystals and proved that the flexoelectric responses induced by a long-wavelength phonon and a uniform strain gradient are identical. In 2011 and 2013, a unified first-principles theory of flexoelectricity in insulating crystals with both ionic and electronic contributions has been formulated in the context of density-functional theory by Hong and Vanderbilt[Hong 11, Hong 13] and within the framework of density-functional perturbation theory (DFPT) by Stengel[Stengel 13]. Very recently, a practical scheme to calculate the full flexoelectric tensor using a unit cell-based method built on density functional perturbation theory has been demonstrated by Dreyer, Stengel, and Vanderbilt[Dreyer 18].

I.3.2 Experimental Literature Review

To understand and further utilize flexoelectricity, it is critical to quantitatively measure the flexoelectric coefficients of a material. First measurements of the flexoelectric effect are said to have been done by J. F. Scott[Scott 68] and E. Bursian and O. Zaikovskii.[Bursian 68]. The first measurements of polarization induced by bending in crystal plates are reported to have been done by Bursian and Trunov in 1974[Bursian 74]. Also the direct and converse flexoelectric effects had been measured in lipidic membranes during the 80's-90's[Petrov 86, Petrov 89, Petrov 93, Derzhanski 90, Todorov 94]. However, the subject really began to get hot in the solid state community only when effects much higher than theoretically estimated (measured μC/m, about 3 orders of magnitude than nC/m estimated from Kogan's estimate) were observed for materials with high dielectric permittivity by Eric Cross's group at Pennsylvania State University[Ma 01a, Ma 06, Ma 05, Ma 03, Ma 01b, Ma 02]. It is precisely due to these pioneering works of Cross and collaborators that a large number of people have shown interest in the measurement of the flexoelectric coefficient of ceramics. For example, Zubko et al.[Zubko 07] measured the full tensor for $SrTiO_3$ and found results of the order estimated by theory. Shu et al also measured the shear flexoelectricity of (Ba,Sr)TiO_3 (BST) ceramics. A comprehensive literature survey on flexoelectric coefficient measurements on ceramics as well as single crystals is listed in Table I.1. Note that as already stated in a previous paragraph, flexoelectric coefficients are defined with different meanings for the four indices i, j, k, l. We therefore indicate the convention used by a digit in the last column of Table I.1, with 1 for $P_l = \mu_{ijkl}\partial\varepsilon_{ij}/\partial x_k$, 2 for $P_i = \mu_{ijkl}\partial\varepsilon_{kl}/\partial x_j$ and 3 for $P_i = \mu_{ijkl}\partial\varepsilon_{jk}/\partial x_l$ in Table I.1. Very recently, Christopher A. Mizzi et al[Mizzi 22] measured the flexoelectric coefficients of $SrTiO_3$, $KTaO_3$, TiO_2, and $YAlO_3$ single crystals, finding values of the order of $\sim$ |1-10| nC/m. They also found that low dielectric constant oxides possess flexocoupling constants (in V) $\sim$ 5-10 times larger than the flexocoupling constants of high dielectric constant oxides. It was also found that the flexoelectric coefficient of $SrTiO_3$ can be significantly improved through doping by graphite[Dai 21]. Measurements on thin films were performed by Catalan et al[Catalan 04] as soon as 2004. More recently, some measurements have been

performed on polymer materials[Baskaran 11a, Baskaran 12, Chu 12, Zhang 17a, Zhang 16, Zhang 15b, Zhang 15a, Baskaran 11b]. Reviews on this subject were published by Cross[Cross 06] in 2006, Maranganti and Sharma[Maranganti 09], Yudin and Tagantsev[Yudin 13], Zubko, Catalan and Tagantsev[Zubko 13], perspectives by Krichen and Sharma[Krichen 16], and Wang[Wang 19]. Furthermore, flexoelectricity can be used at temperature where ferroelectric materials are in fact paraelectric (above the material Curie temperature) and more generally at higher temperatures than for conventional piezoelectric materials[Mbarki 14a]. Indeed, ferroelectrics lose their piezoelectricity above the so-called Curie temperature, whereas the fact that centrosymmetry is lost due to a non-uniform mechanical deformation is not temperature dependent. Furthermore, similarly to extension gauges, flexoelectricity could be used as a mean to electrically measure strain gradients in order to check the health status of some mechanical structure[Huang 16]. Flexoelectricity has also been used to switch the polarization orientation in piezoelectric thin films by applying a mechanical force upon the thin film using an AFM, in order to induce a strain gradient that itself creates a polarization whose effect can exceed the coercive electric field of the thin film.[Cao 15] The strain gradient can also be produced by a lattice mismatch between the substrate and the film, with the magnitude of the strain gradient induced at the interface between different materials ranging from 10^{-4} to 10^{-7} m^{-1}[Wu 21].

I.3.3 Experimental setups

I.3.3.a Measurements of flexoelectric coefficients using the direct effect

A systematical measurement of flexoelectric coefficients was not performed until early 2000s by Ma and Cross at Penn State. In their seminal works[Ma 01a, Ma 01b, Ma 02, Ma 03, Ma 05, Ma 06], three experimental schemes were used to measure the flexoelectric constants of ceramics, as can be seen in Figure I.2. The dynamic cantilever bending (Figure I.2 (a)) and quasi-static four-point bending (Figure I.2 (c)) methods are designed to measure the effective transverse flexoelectric coefficient μ_{1122}, while the pyramid compression (Figure I.2 (e)) method is used for the effective longitudinal flexoelectric coefficient μ_{1111}. A three-point bending (Figure I.2 (d)) scheme was developed by Zubko et al. based on the earlier work of Kityk et al.[Kityk 00] to measure the full flexoelectric tensor. The cantilever twisting (Figure I.2 (e)) approach was devised to measure the shear flexoelectric component.

I.3.3.b Measurements of flexoelectric coefficients using the converse effect

Figure I.3(a) shows a schematic of Piezoresponse Force Microscopy (PFM), as used by Catalan's group[Abdollahi 19] to measure the out of plane polarization response of $SrTiO_3$ crystal induced by the electric field gradient applied through an electrically conducting tip. It operates by delivering a voltage V to the surface of the material via the tip. The tip voltage induces an inhomogeneous electric field

Materials	Materials type	μ_{1111}	μ_{1122}	μ_{1212}	Definition
$Ba_{0.7}Sr_{0.3}TiO_3$[Kwon 14]	Polycrystal thin film		24.5		1
$Ba_{0.67}Sr_{0.33}TiO_3$[Ma 02]	Ceramics		100		1
$Ba_{0.67}Sr_{0.33}TiO_3$[Fu 06]	Ceramics	120			1
$Ba_{0.67}Sr_{0.33}TiO_3$[Cross 06]	Ceramics	150			1
$Ba_{0.67}Sr_{0.33}TiO_3$[Shu 14]	Ceramics			124	1
$Ba_{0.67}Sr_{0.33}TiO_3$[Huang 11]	Ceramics		8.5		1
$Ba_{0.67}Sr_{0.33}TiO_3$[Hu 18]	Ceramics	47.6			2
$BaTiO_3$[Ma 06]	Ceramics		50		1
$BaTi_{0.87}Sn_{0.13}O_3$[Shu 13]	Ceramics		53		3
Magnesium niobate (PMN)[Ma 01a, Ma 01b]	Ceramics		4		1
Magnesium niobate titanate(PMNT)[Hana 06]	Ceramics	∼1000			3
Magnesium niobate titanate(PMNT)[Ma 01a, Ma 01b]	Ceramics	6.2-12.3			1
unpoled lead zirconate titanate [Ma 06]	Ceramics		1.5		1
unpoled lead zirconate titanate [Ma 05]	Ceramics		1.4		1
$Pb_{0.3}Sr_{0.7}TiO_3$[Cross 06]	Ceramics	20			1
$Ba_{0.6}Sr_{0.4}TiO_3$/ $Ni_{0.8}Zn_{0.2}Fe_2O_4$[Li 14]	Ceramics composite		128.6		1
$(Bi_{1.5}Zn_{0.5})$ $(Zn_{0.5}Nb_{1.5})O_7$/Ag[Li 13]	Ceramics composite		0.17		1
$BaTiO_3$[Narvaez 15]	(0 0 1)Single crystal		0.2		2
$BaTiO_3$[Narvaez 15]	(1 1 0)Single crystal		-0.05		2
$BaTiO_3$[Narvaez 15]	(1 1 1)Single crystal		-0.01		2
$Bi_{12}TiO_{20}$[Shandarov 12]	Single crystal	5.3			1
$SrTiO_3$[Zubko 07]	Single crystal	0.0002	0.007	0.0058	2
$Pb(Mg_{1/3}\ Nb_{2/3}\ O_3)$ $-PbTiO_3$[Narvaez 14]	Single crystal		38		2
$BaTiO_3$[Gharbi 11]	Single crystal		4		3
BaTiO3-0.08 Bi (Zn1/2Ti1/2) O3[Huang 17]	Ceramics		25		3
Ba0.6Sr0.4TiO3/epoxy[Li 20]	Composite		25		1
0.3 Pb (In1/2Nb1/2) O3-0.35 Pb (Mg1/3Nb2/3) O3-0.35 PbTiO3 (PIN-PMN-PT)[Shu 17]	single crystal		57		3

Table I.1: Flexoelectric constants of various materials measured experimentally. The unit of measured flexoelectric coefficients shown is this table is in $\mu C/m$. 1, 2 and 3 represent different definitions of flexoelectric coefficients (1 for $P_l = \mu_{ijkl}\partial\varepsilon_{ij}/\partial x_k$, 2 for $P_i = \mu_{ijkl}\partial\varepsilon_{kl}/\partial x_j$ and 3 for $P_i = \mu_{ijkl}\partial\varepsilon_{jk}/\partial x_l$).

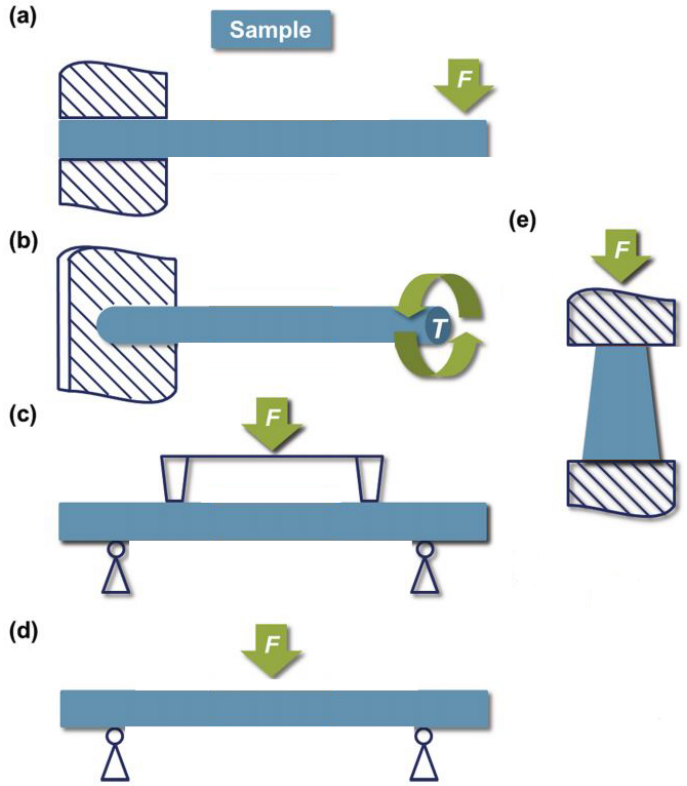

Figure I.2: Schematics of flexoelectric experimental setups for direct measurements of flexoelectric constants (a) Cantilever bending, (b) cylinder twisting, (c) four-point bending, (d) three-point bending, and (e) pyramid compression. Adapted from Figure 3.1 of Wang et al 2019

below the PFM tip, which decays as the tip is moved away from the substrate. The gradient of this electric field effectively induce a strain gradient via the converse flexoelectric effect in all dielectrics, including non-piezoelectric ones, which results in a measured deformation h, and consequently an effective piezoelectric coefficient. A similar experiment was recently performed by Brennan *et al.* to obtain converse flexoelectric coefficients for an MoS_2 monolayer[Brennan 17, Brennan 20]. Figure I.3(b) presents how the electric field gradient induces the generation of deformation thanks to converse flexoelectric effect. Such an experimental setup is normally utilized to measure either the effective converse piezoelectric coefficient or the converse flexoelectric coefficient[Zhang 19]. The configuration shown in Figure I.3(c) can produce a directional electric field gradient. Slightly differently from the experimental setup described above, the deformation of the sample was measured using a high resolution (< 10 pm) laser vibrometer and a lock-in amplifier[Shu 14]. Figure I.3(d) presents an optical experimental setups, designed by Cross' group, for the measurements of converse flexoelectric coefficients[Fu 06].

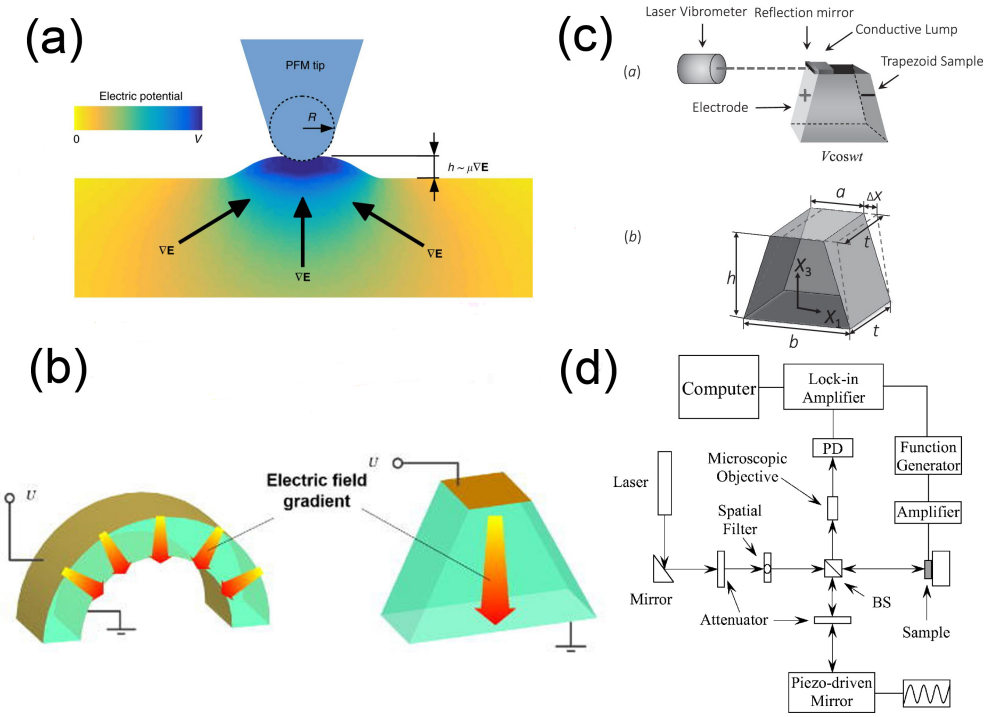

Figure I.3: (a) Schematic of piezoresponse force microscopy measurement, adapted from Figure 1 of Abdollahi et al 2019. (b) electric field gradient generation method with a part-cylindrical bar and a trapezoid-section shaped structure, adapted from Figure 1 of Zhang et al 2019. (c) Diagram of sample assembly for converse flexoelectric measurement of the shear strain along x_1 direction generated by the electric field gradient along x_3 direction. Schematic deformation of the trapezoid sample in the lateral mode, adapted from Figure 1 of Shu et al 2014. (d) An optical measurement system based on the scanning Michelson laser beam interferometer. PD: photodiode; BS: beam splitter, adapted from Figure 3 of Fu et al 2006.

I.4 Computational methods for flexoelectricity

I.4.1 Ab-initio calculations

There are mainly two approaches to estimate the flexoelectric coefficient, computed via first-principles density functional theory calculations.

The direct approach follows the definition of the flexoelectric coefficient ($\Delta P_i = \mu_{ijkl}\partial u_{j,k}/\partial x_l$, if no external electric field exists and piezoelectricity can be canceled out thanks to symmetric strain contribution) since it directly evaluates the polarization induced by an applied strain gradient. In order for side effects to be eliminated, the strain gradient itself must satisfy periodical boundary conditions. Hence, it is usually done by applying a sinusoidal atomic displacement to the su-

percell. Finally, the flexoelectric component can be obtained by dividing the local polarization by the applied strain gradient. Based on the above-mentioned setting of the deformation configuration, a DFT-based first principle calculations was firstly performed by Hong et al.[Hong 10] to obtain the longitudinal component of a flexoelectric tensor for $SrTiO_3$ (STO) and $BaTiO_3$ (BTO). Later, it has been extended by Xu et al.[Xu 13] to evaluate the transverse and shear flexoelectric coefficients. It is worth mentioning that in Refs [Hong 10] and [Xu 13], modern theory of polarization based on Berry phase method was used to compute change in polarization yielded by strain gradient.[Zhong 94, King-Smith 93] Even though this direct method is easy to be understood and implemented, with commercial or open source softwares based on density functional theory, i.e. VASP or Quantum Espresso, the computed results are very sensitive to the selection of sublattice and the size of supercell. Furthermore, the computed flexoelectric coefficients intrinsically include the sum of two contributions, that is lattice and electronic contributions, which are difficult to compute at the same time.

In this paragraph, we focus on the indirect approach based on the first-principles theory of flexoelectricity. Using rigid-ion theory and core-shell model respectively proposed by Tagantsev[Tagantsev 86] and Askar[Askar 70], Maranganti and Sharma [Maranganti 09] computed the flexoelectric coefficients for three semiconductors (GaAs, GaP, and ZnS), cubic perovskite materials $SrTiO_3$ (STO) and $BaTiO_3$ (BTO) and cubic alkali halides NaCl and KCl. A first-principles-based effective Hamiltonian technique is developed to study flexoelectricity in $Ba_{0.5}Sr_{0.5}TiO_3$ thin films of different thicknesses in their paraelectric phase, showing that flexoelectric coefficients depend strongly on the film's thickness and temperature [Ponomareva 12]. Later on, Hong and Vanderbilt[Hong 13] developed a general and unified first-principles theory for the computation of piezoelectric and flexoelectric tensors. They used it to compute the coefficients for a variety of cubic insulating materials including C, Si, MgO, NaCl, CsCl, $BaZrO_3$, $BaTiO_3$, $PbTiO_3$, and $SrTiO_3$, to find that the estimated values are two orders of magnitude smaller than common experimental results, which is attributed by the authors to the absence of surface contribution in ab-initio based first principles theory. Stengel[Stengel 13] derived the complete flexoelectric tensor, including electronic and lattice-mediated effects, of an arbitrary insulator within the framework of the density-functional perturbation theory (DFPT), with the microscopic linear response of the crystal to atomic displacements induced by long-wavelength acoustic phonon. In this theoretical context, a series of paper has been published by Stengel's group[Stengel 14, Schiaffino 19, Royo 19, Royo 22, Stengel 15, Springolo 21] to demonstrate the validity of this theory by computing the flexoelectric coefficient of $SrTiO_3$ and 2D materials, with a good agreement with the available literature data.

I.4.2 Other calculation methods

Molecular dynamics simulations have been utilized to compute the flexoelectric tensors through the direct method (change of polarization divided by change of strain gradient). Chatzopoulos et al[Chatzopoulos 16] obtained the flexoelectric coefficient of MgO using an effective interaction force field. Mbarki et al[Mbarki 14b] developed a molecular dynamics approach based on a specially tailored interatomic force field to extract the temperature dependence of flexoelectricity in $BaTiO_3$ and $SrTiO_3$ perovskite nanostructures. Very recently, Zhuang et al.[Zhuang 19] performed molecular dynamics simulations coupled with an atomic model (regularized charge dipole model) to evaluate the flexoelectric constants of several representative 2D materials.

In addition to the molecular dynamics methods mentioned above, the finite element theory based on continuum mechanics is also commonly used in the study of flexoelectricity. For instance, Abdollahi et al.[Abdollahi 14] firstly applied a meshfree technique to interpret the flexoelectric responses in the cantilever bending and pyramid compression schemes extensively used for flexoelectricity measurement, with higher accuracy. Abdollahi et al. then explored the effect of flexoelectricity on mechanical and electromechanical properties in several complex structures[Abdollahi 15a, Abdollahi 15b, Abdollahi 15c]. Meanwhile, the first phase-field model to treat flexoelectricity was used by Chen *et al.* to study the impact of flexoelectric coupling on domain structure properties in ferroelectric thin films [Chen 14] and ordinary dielectrics[Chen 15]. Compared with atomistic simulation techniques, phase-field simulations are computationally less costly and thus allow to study larger spatial and/or temporal scales.

I.5 Application of flexoelectricity

I.5.1 Sensors

Flexoelectric sensors are becoming increasingly popular because of their small size, absence of depoling, and lead-free composition. Recently, Yan et al.[Yan 13a, Yan 13b] designed a Barium Strontium Titanate (BST) based flexoelectric curvature sensor (see Figure I.4a), which can transfer the bending deflections directly to the charge output (see Figure I.4b). Figure I.4c and d present an experimental setup, commonly used for measurements of flexoelectricity. The use of 6.6 μm-thick soft polyurethane films as large curvature sensors was investigated by Merupo et al. by subjecting a flexible aluminum foil/PET bi-layered substrate to large deflections [Merupo 17]. Other direct curvature sensing measurements based on the flexoelectricity of some materials, i.e., ceramics, through electromechanical coupling can be found in ref [Hu 15]. Recently, Kwon et al. reported that a new type of microphone with both high sensitivity and strong resonance was

fabricated using the flexoelectricity of $Ba_{0.67}Sr_{0.33}TiO_3$[Kwon 16]. This device has the potential to exhibit even higher sensitivity (0.77 – 0.85 pC/Pa) when further miniaturized, which is promising for acoustic sensing applications.

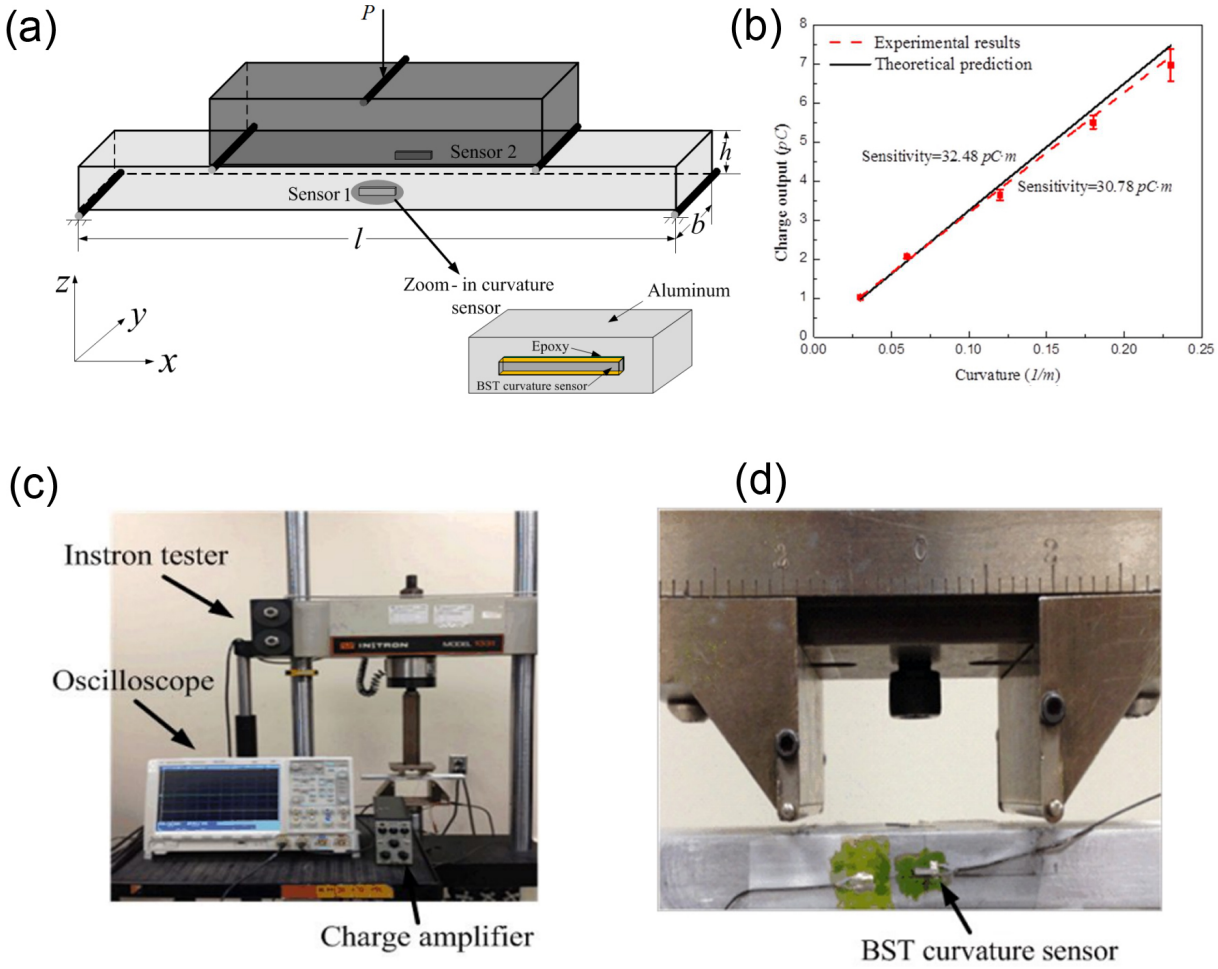

Figure I.4: Beam curvature sensing: BST curvature sensor attached to beam, adapted from Figure 4 of Yan *et al.* 2013. (b) Relationship between charge output and beam curvature-experimental results of BST curvature sensor, adapted from Figure 7 of Yan *et al.* 2013. (c) Experimental set-up and (d) close-up of the actual curvature sensor attached on a beam, adapted from Figure 6 of *et al.* 2013

I.5.2 Nanogenerators

It is known that in practical applications of materials, flexoelectric effect can be difficult to separate from piezoelectric effect. There is therefore not much work on pure flexoelectric nanogenerators. However, the performance of some piezoelectric nanogenerators and systems can be enhanced due to flexoelectric effect[Qi 10]. Han et al.[Han 16] prepared a flexoelectric nanogenerator consisting

of piezoelectric lead zirconate titanate (PZT) particles directly grown on multi-walled carbon nanotubes, which can repeatedly generate a voltage output of 8.6 V and a current output of 47 nA at a mechanical force of 20 N. PZT ribbons can be transferred onto polydimethylsiloxane (PDMS) by attaching the pre-stretched PDMS onto a magnesium oxide host substrate with 500 nm thick PZT ribbons resting on it, as shown in Figure I.5[Qi 10]. With the release of the pre-strain in PDMS, PZT ribbons buckled into sinusoidal waveforms with wavelengths of 80 μm and heights of 11 μm. Uniaxial strain in the midplane was calculated to be 8.5 MPa and maximum strain gradient can be as high as 3×10^4 m^{-1}, which is several orders of magnitude larger than those achieved by pyramid compressing or flexure bending tests using bulk materials. Such high strain gradient would induce a considerable amount of charge separation in addition to piezoelectric charge generation, leading to an enhancement up to 70% comparing with flat regions of PZT ribbons without flexoelectric contribution. Wang et al.[Wang 13] reported that macroscopic strain gradient can induce substantial flexoelectric polarization in a bent PZT diaphragm, with the measured flexoelectric coefficient equal to 2.0×10^{-4} C/m.

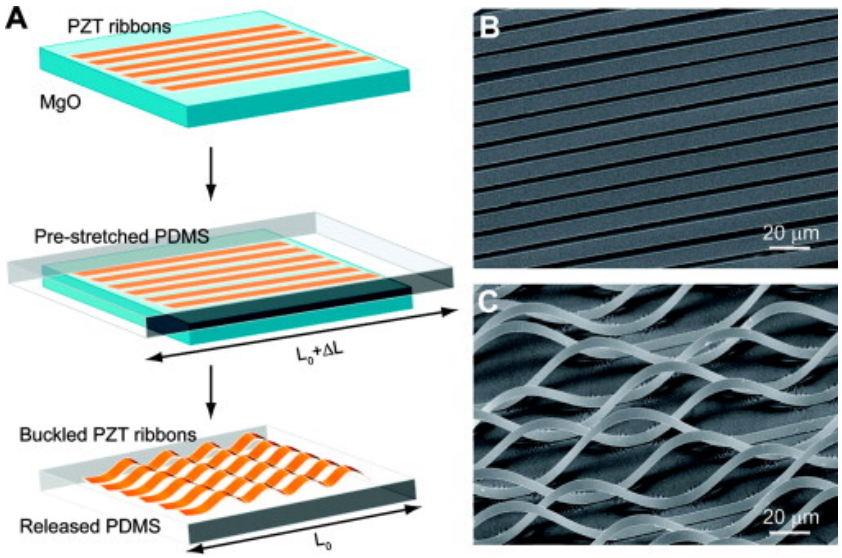

Figure I.5: Fabrication process of buckled PZT ribbons. (A) PZT ribbons were patterned on an MgO substrate. Released PZT ribbons were transferred to a pre-stretched PDMS slab. Relaxation of PDMS caused the peel-off of certain areas of ribbons and formed the buckled structures. (B) SEM image of PZT ribbons transferred to PDMS with no prestrain. (C) Buckled PZT ribbons after transfer to PDMS with prestrain. Adapted from Figure 1 of Qi *et al.* 2011

I.5.3 Actuators

The mechanism for applications of flexoelectric materials as actuators is primarily converse flexoelectricity. The material deforms in response to the electric field gradient (see Figure I.6 a and c). As shown in Fig. I.6(a), Zhang et al.[Zhang 17b] designed and fabricated a polymer-based actuator with which a converse flexoelectric coefficient was measured. This actuator exhibited good actuation properties with a resolution of the displacement reaching up to 1.0 nm and a largest displacement as high as 63.6 nm (as shown in Fig. I.6(b)). It is also worth highlighting that Bhaskar et al.[Bhaskar 16] implemented a flexoelectric actuator made of micron-sized barium titanate (as shown in Fig. I.6(c)) which is fully compatible with the silicon semiconductor technology. Particularly, the flexoelectric layer is compatible with silicon or any of its gate dielectrics in a completely complementary metal oxide semiconductor-compatible environment. The performance result (Fig. I.6(d)) suggests that this flexoelectric actuator displays comparable performance to the actuators using lead-containing piezoelectric material.

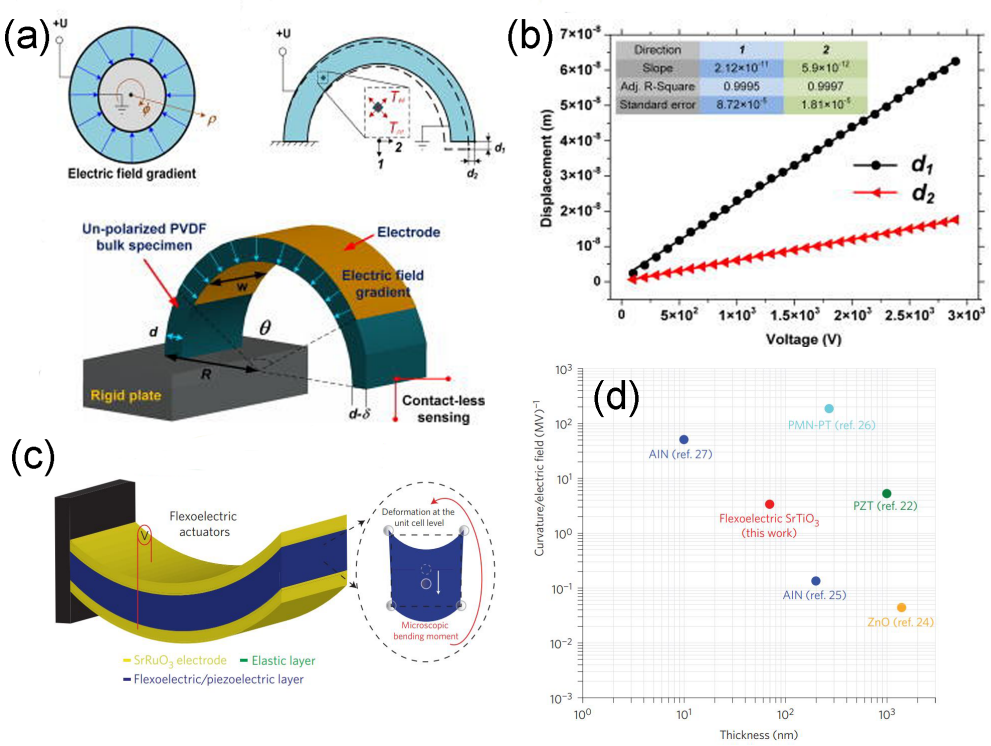

Figure I.6: (a) Schematic diagram of a PVDF-based actuator. The symbol θ represents the angle of electrode attachment. To achieve a uniform electric field gradient and application safety, θ in this actuator is set as 120°, adapted from Figure 1 of Zhang *et al.* 2017. (b) Induced displacement as a function of voltage in that PVDF-based actuator, adapted from Figure 4 of Zhang *et al.* 2017. (c) Schematic view of the $SrTiO_3$-based actuator of Bhaskar *et al.*, adapted from Figure 1 of Bhaskar *et al.* 2016. (d) Comparison of the performance of flexoelectric $SrTiO_3$ with those of state-of-the-art piezoelectric bimorphs, adapted from Figure 4 of Bhaskar *et al.* 2016.

Chapter II

Effective piezoelectricity coefficient in patterned graphene computed using electrostatic forces calculated within charge dipole model

II.1 Introduction 16

II.2 Description of the charge dipole model 17

II.3 Description of the Gaussian regularized charge dipole model 18

II.4 Computation of electrostatic forces for two carbon atoms 20

II.5 Analytical expressions for the force 26

II.5.1 Direct method by direct derivation of the full energy, valid even if charges and dipoles are not equilibrated 26

II.5.2 Second method with explicit determination of the gradients 28

II.5.3 Third method using the derivative of the block-matrix of interaction tensors 31

II.6 Computation of in-plane piezoelectric coefficient caused by flexoelectricity for patterned graphene 34

II.6.1 A little literature review on computation of piezoelectricity for graphene 34

II.6.2 Introduction to Javvaji's 2018 paper 35

II.6.3 Modifications with respect to the work of Javvaji et al. . . 37

II.6.4 Computation of piezoelectric coefficient 39

II.7 Conclusions 42

II.1 Introduction

At the beginning of my PhD thesis, a necessary work was to prove the analytical formulas for calculating flexoelectric coefficient proposed by G. Lecoutre, derived by means of virtual power principle and an extended Cauchy-Born homogenization hypothesis, to be effective and robust by making a comparison between the results for flexoelectric coefficient of patterned graphene computed with G. Lecoutre's method[Lecoutre 18] and those obtained from a paper by B. Javvaji et al[Javvaji 18], published in 2018. In the paper of B. Javvaji et al, the authors computed piezoelectric and flexoelectric coefficients for some structured graphene flakes through implementing a stretching simulation using Large-scale Atomic/Molecular Massively Parallel Simulator (LAMMPS) combined with charge dipole model by using the command "addforce" and "shell". Since we have the relevant code for the charge dipole model and have been using the charge dipole model in our group for more than 10 years, we tried to reproduce the results of Javvaji et al. In the process of doing that, however, we found several typos/errors in formulas for computing forces on atoms in the Appendix of [Javvaji 18] and an inappropriate definition of polarization. Specifically, a term involving effective charges is neglected/omitted in the definition of polarization though it is necessary in the context of charge dipole model. Also, it seemed strange for us that gradient of effective charges and dipoles were not considered in [Javvaji 18], whereas we have been using them in the group since 2007[Wang 07b]. Indeed, in our method, the forces are computed with the gradient of a simplified expression of the total energy at electrostatic equilibrium using values of effective charges and dipoles at equilibrium computed as functions of the positions of the atoms at each time step of the optimization of the geometry of the system. More information on this point will be given in this chapter. After finding this problem, we thought necessary to check whether results shown in [Javvaji 18] would be correct or not. Hence, we computed piezoelectric and flexoelectric coefficients of trapezium shaped graphene under the proper definition of polarization (charge term included in the definition of polarization) and our expression for the forces. Since we found results different from those published in [Javvaji 18], we contacted the first author (B. Javvaji) and agreed, among other things, to choose a very simple system with only two carbon atoms to compute the interaction forces between them, with and without taking into account the gradient of charges and dipoles. However, to our surprise, the values of total forces that we obtained were the same for the two different cases, though the breaking of the total force in force between charges, between charges and dipoles and between dipoles, was different. We then turned all of our attention to the derivation of expression for force to figure out why this equivalence occurred. Once this was done, we computed the in-plane piezoelectric coefficient e_{111} of a patterned graphene (with a hole defect and triangle defect and trapezium-shaped graphene) with the proper definition of polarization. This chapter is devoted to the description of these verifications.

II.2 Description of the charge dipole model

Historically, the development of the charge-dipole model was initially centered on computation for the polarizability of molecules which had been in fact a tricky problem due to the limitation of computer technology, until in 1972, Applequist et al [Applequist 72, Applequist 77] computed the polarizability tensors of some small molecules principally including C, H, O, N elements using a method called atomic dipole interaction model, also pointing out the shortcomings of calculating molecular polarizability by the sum of atomic polarizabilities. Since then, a series of studies on computation of molecular polarizability has been done using the above-mentioned point dipole interaction model, which we here call PDI model or dipole only model. For instance, F. Torrens[Torrens 02b] computed molecular polarizability of semiconductor clusters, such as, Si_n, Ge_n and Ga_nAs_m small clusters and some nanostructures using dipole only model, the results for the polarizability being in agreement with reference calculations reported. This suggests to some extent the success in predicting molecular polarizabilities via PDI model. In a general case, however, failure of the PDI model tends to occur especially when two atoms are too close to each other, which is usually called "polarization catastrophe". This led the researchers to improve the model by introducing a damping function in the calculation of the interaction tensor in order to prevent the polarizability from going to infinity [Thole 81, Birge 80, Miller 90, Jensen 02, Torrens 99, Torrens 00, Torrens 01, Torrens 02a, Torrens 03, Torrens 04]. Of these modifications of PDI model, the gaussian dipole interaction model consisting of convolution of the interaction tensor with two radial gaussian functions is found to be the most robust for it allows continuity of the charge interaction tensor and its gradients, which is good for molecular dynamics simulations. We note that adopting Gaussian-regularized point dipole interaction model (convolution with only one gaussian), R. Langlet et al studied the influence of molecular adsorption on the dielectric properties of a single wall nanotube[Langlet 04, Picaud 05] and successfully reproduced experimental static polarizabilities of multi-wall carbon nanotubes and fullerenes[Langlet 06].

However, it is inadequate to apply the Gaussian-regularized point dipole interaction model to compute electrostatic properties of some materials, for example, metallic nanotubes or ionic crystals, since partial charge transfer in those materials is allowed to happen, either because of the existence of π delocalized electrons or because of the intrinsic large difference in electronegativity between atoms. For this reason, in 1978, Olson and Sundberg[Olson 78] used a non-regularized charge dipole model for the treatment of the computation of polarizability of molecules with conjugated π bond, with a better agreement with experimental polarizabilities. Starting in 2005, A. Mayer modified the original charge dipole model by adding convolution with two Gaussian functions into the interaction tensor and linked to the polarizability the radius of the Gaussian function in the convoluted interaction tensors between dipoles, and to the atomic capacitance (or chemical hardness) the radius of the Gaussian function in the convoluted interaction ten-

sors between charges [Mayer 05a, Mayer 05b]. A Mayer then published many papers on calculation of electrostatic properties for nanotubes or fullerenes[Mayer 06, Mayer 07a, Langlet 07, Mayer 07b], carbon-containing small molecules[Mayer 08], silver clusters[Mayer 09b] and some other relevant studies[Langlet 08, Mayer 09a, Mayer 05c]. Meanwhile, Z. Wang and M. Devel published a series of papers on the computation of electrostatic and electromechanical properties for nanotubes with various chirality[Wang 07a, Wang 08b, Wang 09b, Wang 09c] and graphene[Wang 09a, Wang 10a, Wang 10b] by using Gaussian-regularized charge dipole model. Recently, the charge dipole model, was parameterized using DFT-computed Bader-type charges as reference data, for the prediction of charge density distribution of 2D molybdenum disulfide[Yang 18] and h-boron nitride[Song 21]. This participates to studies on electromechanical couplings such as piezoelectricity and flexoelectricity, using the charge dipole model to calculate polarization of carbon-doped boron nitride nanosheets[Kundalwal 20], structured graphene[Javvaji 21, Javvaji 18], many varieties of 2D materials[Zhuang 19] and Janus transition-metal dichalcogenides[Javvaji 19].

II.3 Description of the Gaussian regularized charge dipole model

In the regularized charge-dipole (QP) model, each atom is described by the combination of an effective charge and a dipole both delocalized with a spherical symmetry and a Gaussian radial distribution, plus an effective electronegativity. The total electrostatic energy U_{elec} associated with those effective charges $\{q_\alpha\}$ and dipoles $\{\vec{p}_\alpha\}$ located at the atomic positions $\{\vec{r}_\alpha\}$ (with $\alpha = 1, \cdots, N$), in the presence of an external electric field $\vec{E}_{ext}$ (derived from an external electric potential V_{ext}) is given by:

$$\begin{aligned} U_{elec} = & \sum_{\alpha=1}^{N} q_\alpha(\chi_\alpha + V_{ext,\alpha}) - \sum_{\alpha=1}^{N} \vec{p}_\alpha \cdot \vec{E}_{ext} + \frac{1}{2}\sum_{\alpha=1}^{N}\sum_{\beta=1}^{N} q_\alpha T_{q-q}^{(0,0)}(\vec{r}_\alpha, \vec{r}_\beta) q_\beta \\ & - \frac{1}{2}\sum_{\alpha=1}^{N}\sum_{\beta=1}^{N} \vec{p}_\alpha \cdot T_{p-q}^{(1,0)}(\vec{r}_\alpha, \vec{r}_\beta) q_\beta + \frac{1}{2}\sum_{\alpha=1}^{N}\sum_{\beta=1}^{N} q_\alpha T_{q-p}^{(0,1)}(\vec{r}_\alpha, \vec{r}_\beta) \cdot \vec{p}_\beta \\ & - \frac{1}{2}\sum_{\alpha=1}^{N}\sum_{\beta=1}^{N} \vec{p}_\alpha \cdot T_{p-p}^{(1,1)}(\vec{r}_\alpha, \vec{r}_\beta) \cdot \vec{p}_\beta \end{aligned} \tag{II.1}$$

where N stands for the number of atoms in the structure considered and χ_α is the electronegativity of atom α, once inserted in the molecule. $V_{ext,\alpha}$ is the electrostatic potential at $\vec{r}_\alpha$ corresponding to the external electric field. $V_{ext,\alpha}$ can be expressed as $-\vec{E}_{ext} \cdot \vec{r}_\alpha$ in the case of a uniform external field. $T_{q-q}^{(0,0)}$, $T_{p-q}^{(1,0)}$, $T_{p-q}^{(0,1)}$ and $T_{p-p}^{(1,1)}$ are interaction tensors between effective charges or dipoles in vacuum (see equation II.1), which have been convoluted with one Gaussian radial distribution per atom, of the form $\pi^{3/2} R_\alpha^3 \exp(-|\vec{r} - \vec{r}_\alpha|^2 / R_\alpha^2)$. This allows to take into

account approximately the extension of the electronic clouds, and prevents the occurrence of divergence problems, i.e. polarization catastrophes, that can occur in simulations when two atoms are so close to each other that the approximation of an interaction between point charges or dipoles is not a good approximation any more. The expression of those interaction tensors are:

$$T^{(m,n)}\left(\vec{r}_\alpha,\vec{r}_\beta\right)=\underbrace{\left(-\vec{\nabla}_\alpha\right)\otimes\ldots\otimes\left(-\vec{\nabla}_\alpha\right)}_{m\text{ times}}\otimes\underbrace{\vec{\nabla}_\beta\otimes\vec{\nabla}_\beta\otimes\ldots\otimes\vec{\nabla}_\beta}_{n\text{ times}}T^{(0,0)}_{q-q}(\vec{r}_\alpha,\vec{r}_\beta) \tag{II.2}$$

$$\forall\alpha\neq\beta\begin{cases}
T^{(0,0)}_{q-q}(\vec{r}_\alpha,\vec{r}_\beta) &= \frac{1}{4\pi\epsilon_0 r_{\alpha\beta}}\mathrm{erf}\left(\frac{r_{\alpha\beta}}{\sqrt{R_\alpha^2+R_\beta^2}}\right)\\
T^{(1,0)}_{p-q}(\vec{r}_\alpha,\vec{r}_\beta) &= -\vec{\nabla}_\alpha T^{(0,0)}_{q-q}(\vec{r}_\alpha,\vec{r}_\beta)\\
&= -\frac{1}{4\pi\epsilon_0}\frac{\vec{r}_{\alpha\beta}}{r^3_{\alpha\beta}}\left[\mathrm{erf}\left(\frac{r_{\alpha\beta}}{\sqrt{R_\alpha^2+R_\beta^2}}\right)-\frac{2}{\sqrt{\pi}}\frac{r_{\alpha,\beta}}{\sqrt{R_\alpha^2+R_\beta^2}}\exp\left(-\frac{r^2_{\alpha\beta}}{R_\alpha^2+R_\beta^2}\right)\right]\\
T^{(0,1)}_{q-p}(\vec{r}_\alpha,\vec{r}_\beta) &= \vec{\nabla}_\beta T^{(0,0)}_{q-q}(\vec{r}_\alpha,\vec{r}_\beta)\\
&= -\frac{1}{4\pi\epsilon_0}\frac{\vec{r}_{\alpha\beta}}{r^3_{\alpha\beta}}\left[\mathrm{erf}\left(\frac{r_{\alpha\beta}}{\sqrt{R_\alpha^2+R_\beta^2}}\right)-\frac{2}{\sqrt{\pi}}\frac{r_{\alpha,\beta}}{\sqrt{R_\alpha^2+R_\beta^2}}\exp\left(-\frac{r^2_{\alpha\beta}}{R_\alpha^2+R_\beta^2}\right)\right]\\
T^{(1,1)}_{p-p}(\vec{r}_\alpha,\vec{r}_\beta) &= \left(-\vec{\nabla}_\alpha\right)\otimes\vec{\nabla}_\beta T^{(0,0)}_{q-q}(\vec{r}_\alpha,\vec{r}_\beta)\\
&= \frac{1}{4\pi\epsilon_0}\left\{\frac{3\vec{r}_{\alpha\beta}\otimes\vec{r}_{\alpha\beta}-r^2_{\alpha\beta}\bar{\bar{I}}}{r^5_{\alpha\beta}}\left[\mathrm{erf}\left(\frac{r_{\alpha\beta}}{\sqrt{R_\alpha^2+R_\beta^2}}\right)-\frac{2}{\sqrt{\pi}}\frac{r_{\alpha,\beta}}{\sqrt{R_\alpha^2+R_\beta^2}}\exp\left(-\frac{r^2_{\alpha,\beta}}{R_\alpha^2+R_\beta^2}\right)\right]\right.\\
&\quad\left.-\frac{4}{\sqrt{\pi}}\frac{\vec{r}_{\alpha\beta}\otimes\vec{r}_{\alpha\beta}}{r^2_{\alpha\beta}}\frac{1}{(\sqrt{R_\alpha^2+R_\beta^2})^3}\exp\left(-\frac{r^2_{\alpha\beta}}{R_\alpha^2+R_\beta^2}\right)\right\}\\
T^{(2,1)}_{p-p}(\vec{r}_\alpha,\vec{r}_\beta) &= \left(-\vec{\nabla}_\alpha\right)\otimes\left(-\vec{\nabla}_\alpha\right)\otimes\vec{\nabla}_\beta T^{(0,0)}_{q-q}(\vec{r}_\alpha,\vec{r}_\beta)\\
&= -\frac{1}{4\pi\epsilon_0}\left[\frac{15\vec{r}_{\alpha\beta}\otimes\vec{r}_{\alpha\beta}\otimes\vec{r}_{\alpha\beta}-3r^2_{\alpha\beta}\left(\bar{\bar{I}}\otimes\vec{r}_{\alpha\beta}+\bar{I}\otimes\vec{r}_{\alpha\beta}\otimes\bar{I}+\vec{r}_{\alpha\beta}\otimes\bar{\bar{I}}\right)}{r^7_{\alpha\beta}}\right]\\
&\quad\left\{\mathrm{erf}\left(\frac{r_{\alpha\beta}}{\sqrt{R_\alpha^2+R_\beta^2}}\right)-\frac{2}{\sqrt{\pi}}\left[\frac{r_{\alpha\beta}}{\sqrt{R_\alpha^2+R_\beta^2}}+\frac{2}{3}\left(\frac{r_{\alpha\beta}}{\sqrt{R_\alpha^2+R_\beta^2}}\right)^3\right]\exp\left(-\frac{r^2_{\alpha\beta}}{R_\alpha^2+R_\beta^2}\right)\right\}\\
&\quad-\frac{\vec{r}_{\alpha\beta}\otimes\vec{r}_{\alpha\beta}\otimes\vec{r}_{\alpha\beta}}{4\pi\epsilon_0 r^7_{\alpha\beta}}\frac{8}{\sqrt{\pi}}\left(\frac{r_{\alpha\beta}}{\sqrt{R_\alpha^2+R_\beta^2}}\right)^5\exp\left(-\frac{r^2_{\alpha\beta}}{R_\alpha^2+R_\beta^2}\right)\\
T^{(1,2)}_{p-p}(\vec{r}_\alpha,\vec{r}_\beta) &= \left(-\vec{\nabla}_\alpha\right)\otimes\vec{\nabla}_\beta\otimes\vec{\nabla}_\beta T^{(0,0)}_{q-q}(\vec{r}_\alpha,\vec{r}_\beta)=T^{(2,1)}_{p-p}(\vec{r}_\alpha,\vec{r}_\beta)
\end{cases} \tag{II.3}$$

where $\vec{\nabla}_\alpha=\partial/\partial\vec{r}_\alpha$, $\vec{r}_{\alpha\beta}=\vec{r}_\beta-\vec{r}_\alpha$ is the vector pointing from α^{th} atom to β^{th} atom. R_α and R_β are the characteristic widths of Gaussian charge distributions for atom type α and β respectively, $\otimes$ is the tensor product and $(\bar{I}\otimes\vec{\mathrm{r}}_{\alpha\beta}\otimes\bar{I})_{ijk}=(\vec{r}_\beta-\vec{r}_\alpha)_j\delta_{ik}$. In the limit $\vec{r}_\alpha=\vec{r}_\beta$, the expressions of the various $T(\vec{r}_\alpha,\vec{r}_\beta)$ interaction tensors in equation II.3 converge to finite values (Eq. II.4) related to the self-energy for each atom (atomic 'capacitance' c_α or chemical hardness and isotropic polarizability α_α).

$$\begin{cases}
q_\alpha T^{(0,0)}_{q-q}(\vec{r}_\alpha,\vec{r}_\alpha)q_\alpha=\frac{q_\alpha^2}{4\pi\epsilon_0}\frac{\sqrt{2/\pi}}{R_\alpha}=\frac{q_\alpha^2}{c_\alpha}\\
\vec{p}_\alpha\cdot T^{(1,0)}_{p-q}(\vec{r}_\alpha,\vec{r}_\alpha)q_\alpha=0\\
q_\alpha T^{(0,1)}_{q-p}(\vec{r}_\alpha,\vec{r}_\alpha)\cdot\vec{p}_\alpha=0\\
\vec{p}_\alpha\cdot T^{(1,1)}_{p-p}(\vec{r}_\alpha,\vec{r}_\alpha)\cdot\vec{p}_\alpha=-\frac{p_\alpha^2}{4\pi\epsilon_0}\frac{\sqrt{2/\pi}}{3R_\alpha^3}=-\frac{p_\alpha^2}{\alpha_\alpha}.
\end{cases} \tag{II.4}$$

The charges and dipoles at electrostatic equilibrium are then determined by minimizing the electrostatic energy (Eq. II.1) using a Lagrange multiplier λ to enforce charge conservation in the nanoribbon:

$$U'_{elec} = U_{elec} + \lambda(\sum_{\alpha=1}^{N} q_\alpha - Q_{tot}) \tag{II.5}$$

This Lagrange multiplier can be physically interpreted as minus the electronegativity of the molecule at equilibrium common to all the atoms [Mayer 07a].

Requiring the derivatives of function $U'_{elec}(q, \boldsymbol{p}, \lambda)$ with respect to q_α, $p_{x,\alpha}$, $p_{y,\alpha}$, $p_{z,\alpha}$ and λ to be zero for electrostatic equilibrium values q^*, $\vec{p}^*$, and λ^*, it can be demonstrated (in a following section) that the equilibrium values of the the $4N+1$ scalar unknowns ($\{q_\alpha, p_{x,\alpha}, p_{y,\alpha}, p_{z,\alpha}\}_{\alpha=1,\cdots,N}$ and λ) are solutions of a system of $4N+1$ linear equations. These linear equations may be written in a matrix form:

$$\begin{bmatrix} T^{(0,0)}_{q-q} & \left(T^{(0,1)}_{q-p}\right)^T & 1 \\ T^{(1,0)}_{p-q} & T^{(1,1)}_{p-p} & 0 \\ 1 & 0 & 0 \end{bmatrix} \begin{bmatrix} q^* \\ \vec{p}^* \\ \lambda^* \end{bmatrix} = \begin{bmatrix} -(\chi + V_{ext}) \\ -\vec{E}_{ext} \\ Q_{tot} \end{bmatrix} \tag{II.6}$$

where $T^{(0,0)}_{q-q}$ is a block matrix with N rows and N columns. $T^{(1,1)}_{p-p}$ is a block matrix with $3N$ rows and $3N$ columns. $T^{(1,0)}_{p-q}$ is a block matrix with $3N$ rows and N columns. $\left(T^{(1,0)}_{p-q}\right)^T$ is the transpose of $T^{(1,0)}_{p-q}$. Similarly, blocks q^* and $-(\chi+V_{ext})$ have N rows and 1 column, while blocks $\vec{p}^*$ and $-\vec{E}_{ext}$ have $3N$ rows and 1 column. More information on that can be found in the PhD thesis of Z. Wang[Wang 08a] and G. Lecoutre[Lecoutre 18]. Note that q^* and $\vec{p}^*$ are the solution of equation II.6. In other word, q^* and $\vec{p}^*$ are the charge and dipole moment distributions at the electrostatic equilibrium and they are determined as functions of the positions of the atoms using radii of Gaussian radial distributions and electronegativities as parameters.

II.4 Computation of electrostatic forces for two carbon atoms

Here we selected a simple system containing only two carbon atoms to compute their electrostatic force, with the consideration of gradient of electrostatic equilibrium charges and dipoles and without taking into account those gradients, respectively. The energy of the whole system U_{tot} can be decomposed into three terms including the interaction between charges, charges and dipoles, dipoles, termed U_{q-q}, $U_{p-q}(U_{q-p})$, U_{p-p}, respectively.

$$U_{tot} = U_{q-q} + U_{p-q} + U_{q-p} + U_{p-p} \tag{II.7}$$

with

$$
\begin{aligned}
U_{q-q} &= \frac{1}{2}\sum_{\alpha=1}^{2}\sum_{\beta=1}^{2} q_\alpha^* T_{q-q}^{(0,0)}\left(\vec{r}_\alpha,\vec{r}_\beta\right) q_\beta^* + \sum_{\alpha=1}^{2} q_\alpha^*\chi_\alpha \\
&= \frac{1}{2}q_1^* T_{q-q}^{(0,0)}\left(\vec{r}_1,\vec{r}_1\right) q_1^* + \frac{1}{2}q_2^* T_{q-q}^{(0,0)}\left(\vec{r}_2,\vec{r}_2\right) q_2^* + \frac{1}{2}q_1^* T_{q-q}^{(0,0)}\left(\vec{r}_1,\vec{r}_2\right) q_2^* + \frac{1}{2}q_2^* T_{q-q}^{(0,0)}\left(\vec{r}_2,\vec{r}_1\right) q_1^* \\
&+ q_1^*\chi_1 + q_2^*\chi_2
\end{aligned}
\tag{II.8}
$$

$$
\begin{aligned}
U_{p-q} &= -\frac{1}{2}\sum_{\alpha=1}^{2}\sum_{\beta=1}^{2} \vec{p}_\alpha^* \cdot T_{p-q}^{(1,0)}\left(\vec{r}_\alpha,\vec{r}_\beta\right) q_\beta^* \\
&= -\frac{1}{2}\left(\vec{p}_1^* \cdot T_{p-q}^{(1,0)}\left(\vec{r}_1,\vec{r}_1\right) q_1^* + \vec{p}_1^* \cdot T_{p-q}^{(1,0)}\left(\vec{r}_1,\vec{r}_2\right) q_2^* + \vec{p}_2^* \cdot T_{p-q}^{(1,0)}\left(\vec{r}_2,\vec{r}_1\right) q_1^* + \vec{p}_2^* \cdot T_{p-q}^{(1,0)}\left(\vec{r}_2,\vec{r}_2\right) q_2^*\right)
\end{aligned}
\tag{II.9}
$$

$$
\begin{aligned}
U_{q-p} &= \frac{1}{2}\sum_{\alpha=1}^{2}\sum_{\beta=1}^{2} T_{q-p}^{(0,1)} q_\alpha^*\left(\vec{r}_\alpha,\vec{r}_\beta\right)\cdot \vec{p}_\beta^* \\
&= \frac{1}{2}\left(q_1^* T_{q-p}^{(0,1)}\left(\vec{r}_1,\vec{r}_1\right)\cdot\vec{p}_1^* + q_2^* T_{q-p}^{(0,1)}\left(\vec{r}_1,\vec{r}_2\right)\cdot\vec{p}_1^* + q_1^* T_{q-p}^{(0,1)}\left(\vec{r}_2,\vec{r}_1\right)\cdot\vec{p}_2^* + q_2^* T_{q-p}^{(0,1)}\left(\vec{r}_2,\vec{r}_2\right)\cdot\vec{p}_2^*\right)
\end{aligned}
\tag{II.10}
$$

$$
\begin{aligned}
U_{p-p} &= -\frac{1}{2}\sum_{\alpha=1}^{2}\sum_{\beta=1}^{2} \vec{p}_\alpha^* \cdot T_{p-p}^{(1,1)}\left(\vec{r}_\alpha,\vec{r}_\beta\right)\cdot \vec{p}_\beta^* \\
&= -\frac{1}{2}\left(\vec{p}_1^* \cdot T_{p-p}^{(1,1)}\left(\vec{r}_1,\vec{r}_1\right)\cdot\vec{p}_1^* + \vec{p}_1^* \cdot T_{p-p}^{(1,1)}\left(\vec{r}_1,\vec{r}_2\right)\cdot\vec{p}_2^* + \vec{p}_2^* \cdot T_{p-p}^{(1,1)}\left(\vec{r}_2^*,\vec{r}_1\right)\cdot\vec{p}_1^*\right. \\
&\left. + \vec{p}_2^* \cdot T_{p-p}^{(1,1)}\left(\vec{r}_2,\vec{r}_2\right)\cdot\vec{p}_2^*\right)
\end{aligned}
\tag{II.11}
$$

The force acting on each atom can be defined as the negative gradient of U_{tot} with respect to the coordinates of that atom, by which the force on the two atoms may be expressed as: $\vec{F}_1 = -\vec{\nabla}_{\vec{r}_1} U_{tot}$ and $\vec{F}_2 = -\vec{\nabla}_{\vec{r}_2} U_{tot}$, with $\vec{F}_2 = -\vec{F}_1$, as required by Newton's third law of motion. Hence, we here compute analytically only $\vec{F}_1$, but we used $\vec{F}_2 = -\vec{F}_1$ as a consistency check in our symbolic and numeric computations. Considering that q_1^*, q_2^*, $\vec{p}_1^*$ and $\vec{p}_2^*$ are functions of position coordinates $\vec{r}_1, \vec{r}_2$, respectively, *e.g.* $q_1^*\left(\vec{r}_1,\vec{r}_2\right)$, $\vec{F}_{q-q}$, $\vec{F}_{p-q}$ and $\vec{F}_{p-p}$ may be written as:

$$
\begin{aligned}
\vec{F}_{1,q-q} &= -\vec{\nabla}_{\vec{r}_1} U_{q-q} \\
&= -\left(\frac{1}{2}\vec{\nabla}_{\vec{r}_1} q_1^* T_{q-q}^{(0,0)}\left(\vec{r}_1,\vec{r}_1\right) q_1^* + \frac{1}{2}q_1^* T_{q-q}^{(0,0)}\left(\vec{r}_1,\vec{r}_1\right)\vec{\nabla}_{\vec{r}_1} q_1^* + \frac{1}{2}\vec{\nabla}_{\vec{r}_1} q_2^* T_{q-q}^{(0,0)}\left(\vec{r}_2,\vec{r}_2\right) q_2^*\right. \\
&+ \frac{1}{2}q_2^* T_{q-q}^{(0,0)}\left(\vec{r}_2,\vec{r}_2\right)\vec{\nabla}_{\vec{r}_1} q_2^* + \frac{1}{2}\vec{\nabla}_{\vec{r}_1} q_1^* T_{q-q}^{(0,0)}\left(\vec{r}_1,\vec{r}_2\right) q_2^* + \frac{1}{2}q_1^*\vec{\nabla}_{\vec{r}_1} T_{q-q}^{(0,0)}\left(\vec{r}_1,\vec{r}_2\right) q_2^* \\
&+ \frac{1}{2}q_1^* T_{q-q}^{(0,0)}\left(\vec{r}_1,\vec{r}_2\right)\vec{\nabla}_{\vec{r}_1} q_2^* + \frac{1}{2}\vec{\nabla}_{\vec{r}_1} q_2^* \widetilde{T}_{q-q}^{(0,0)}\left(\vec{r}_2,\vec{r}_1\right) q_1^* + \frac{1}{2}q_2^*\vec{\nabla}_{\vec{r}_1} T_{q-q}^{(0,0)}\left(\vec{r}_2,\vec{r}_1\right) q_1^* \\
&\left. + \frac{1}{2}q_2^* T_{q-q}^{(0,0)}\left(\vec{r}_2,\vec{r}_1\right)\vec{\nabla}_{\vec{r}_1} q_1^* + \vec{\nabla}_{\vec{r}_1} q_1^*\chi_1 + \vec{\nabla}_{\vec{r}_1} q_2^*\chi_2\right)
\end{aligned}
\tag{II.12}
$$

$$\begin{aligned}
\vec{F}_{1,p-q} &= -\vec{\nabla}_{\vec{r}_1} U_{p-q} \\
&= \frac{1}{2}\left(\vec{\nabla}_{\vec{r}_1} \otimes \vec{p}_1^{\,*}\right) \cdot T_{p-q}^{(1,0)}\left(\vec{r}_1, \vec{r}_2\right) q_2^* + \frac{1}{2}\left(\vec{\nabla}_{\vec{r}_1} \otimes T_{p-q}^{(1,0)}\left(\vec{r}_1, \vec{r}_2\right)\right) \cdot \vec{p}_1^{\,*} q_2^* \\
&+ \frac{1}{2}\left(\vec{p}_1^{\,*} \cdot T_{p-q}^{(1,0)}\left(\vec{r}_1, \vec{r}_2\right)\right)\left(\vec{\nabla}_{\vec{r}_1} q_2^*\right) \\
&+ \frac{1}{2}\left(\vec{\nabla}_{\vec{r}_1} \otimes \vec{p}_2^{\,*}\right) \cdot T_{p-q}^{(1,0)}\left(\vec{r}_2, \vec{r}_1\right) q_1^* + \frac{1}{2}\left(\vec{\nabla}_{\vec{r}_1} \otimes T_{p-q}^{(1,0)}\left(\vec{r}_2, \vec{r}_1\right)\right) \cdot \vec{p}_2^{\,*} q_1^* \\
&+ \frac{1}{2}\left(\vec{p}_2^{\,*} \cdot T_{p-q}^{(1,0)}\left(\vec{r}_2, \vec{r}_1\right)\right)\left(\vec{\nabla}_{\vec{r}_1} q_1^*\right)
\end{aligned} \tag{II.13}$$

$$\begin{aligned}
\vec{F}_{1,q-p} &= -\vec{\nabla}_{\vec{r}_1} U_{q-p} \\
&= -\frac{1}{2}\left(\vec{\nabla}_{\vec{r}_1} q_1^*\right)\left(T_{q-p}^{(0,1)}\left(\vec{r}_1, \vec{r}_2\right) \cdot \vec{p}_2^{\,*}\right) - \frac{1}{2} q_1^*\left(\vec{\nabla}_{\vec{r}_1} \otimes T_{q-p}^{(0,1)}\left(\vec{r}_1, \vec{r}_2\right)\right) \cdot \vec{p}_2^{\,*} \\
&- \frac{1}{2} q_1^*\left(\vec{\nabla}_{\vec{r}_1} \otimes \vec{p}_2^{\,*}\right) \cdot T_{q-p}^{(0,1)}\left(\vec{r}_1, \vec{r}_2\right) \\
&- \frac{1}{2}\left(\vec{\nabla}_{\vec{r}_1} q_2^*\right)\left(T_{q-p}^{(0,1)}\left(\vec{r}_2, \vec{r}_1\right) \cdot \vec{p}_1^{\,*}\right) - \frac{1}{2} q_2^*\left(\vec{\nabla}_{\vec{r}_1} \otimes T_{q-p}^{(0,1)}\left(\vec{r}_2, \vec{r}_1\right)\right) \cdot \vec{p}_1^{\,*} \\
&- \frac{1}{2} q_2^*\left(\vec{\nabla}_{\vec{r}_1} \otimes \vec{p}_1^{\,*}\right) \cdot T_{q-p}^{(0,1)}\left(\vec{r}_2, \vec{r}_1\right)
\end{aligned} \tag{II.14}$$

$$\begin{aligned}
\vec{F}_{1,p-p} &= -\vec{\nabla}_{\vec{r}_1} U_{p-p} \\
&= \frac{1}{2}\left(\vec{\nabla}_{\vec{r}_1} \otimes \vec{p}_1^{\,*}\right) \cdot T_{p-p}^{(1,1)}\left(\vec{r}_1, \vec{r}_1\right) \cdot \vec{p}_1^{\,*} + \frac{1}{2}\left[\left(\vec{\nabla}_{\vec{r}_1} \otimes T_{p-p}^{(1,1)}\left(\vec{r}_1, \vec{r}_1\right)\right) \cdot \vec{p}_1^{\,*}\right] \cdot \vec{p}_1^{\,*} \\
&+ \frac{1}{2}\left(\vec{\nabla}_{\vec{r}_1} \otimes \vec{p}_1^{\,*}\right) \cdot \left[\vec{p}_1^{\,*} \cdot T_{p-p}^{(1,1)}\left(\vec{r}_1, \vec{r}_1\right)\right] \\
&+ \frac{1}{2}\left(\vec{\nabla}_{\vec{r}_1} \otimes \vec{p}_1^{\,*}\right) \cdot T_{p-p}^{(1,1)}\left(\vec{r}_1, \vec{r}_2\right) \cdot \vec{p}_2^{\,*} + \frac{1}{2}\left[\left(\vec{\nabla}_{\vec{r}_1} \otimes T_{p-p}^{(1,1)}\left(\vec{r}_1, \vec{r}_2\right)\right) \cdot \vec{p}_2^{\,*}\right] \cdot \vec{p}_1^{\,*} \\
&+ \frac{1}{2}\left(\vec{\nabla}_{\vec{r}_1} \otimes \vec{p}_2^{\,*}\right) \cdot \left[\vec{p}_1^{\,*} \cdot T_{p-p}^{(1,1)}\left(\vec{r}_1, \vec{r}_2\right)\right] \\
&+ \frac{1}{2}\left(\vec{\nabla}_{\vec{r}_1} \otimes \vec{p}_2^{\,*}\right) \cdot T_{p-p}^{(1,1)}\left(\vec{r}_2, \vec{r}_1\right) \cdot \vec{p}_1^{\,*} + \frac{1}{2}\left[\left(\vec{\nabla}_{\vec{r}_1} \otimes T_{p-p}^{(1,1)}\left(\vec{r}_2, \vec{r}_1\right)\right) \cdot \vec{p}_1^{\,*}\right] \cdot \vec{p}_2^{\,*} \\
&+ \frac{1}{2}\left(\vec{\nabla}_{\vec{r}_1} \otimes \vec{p}_1^{\,*}\right) \cdot \left[\vec{p}_2^{\,*} \cdot T_{p-p}^{(1,1)}\left(\vec{r}_2, \vec{r}_1\right)\right] \\
&+ \frac{1}{2}\left(\vec{\nabla}_{\vec{r}_1} \otimes \vec{p}_2^{\,*}\right) \cdot T_{p-p}^{(1,1)}\left(\vec{r}_2, \vec{r}_2\right) \cdot \vec{p}_2^{\,*} + \frac{1}{2}\left[\left(\vec{\nabla}_{\vec{r}_1} \otimes T_{p-p}^{(1,1)}\left(\vec{r}_2, \vec{r}_2\right)\right) \cdot \vec{p}_2^{\,*}\right] \cdot \vec{p}_2^{\,*} \\
&+ \frac{1}{2}\left(\vec{\nabla}_{\vec{r}_1} \otimes \vec{p}_2^{\,*}\right) \cdot \left[\vec{p}_2^{\,*} \cdot T_{p-p}^{(1,1)}\left(\vec{r}_2, \vec{r}_2\right)\right]
\end{aligned} \tag{II.15}$$

where we used $T_{p-q}^{(1,0)}\left(\vec{r}_1, \vec{r}_1\right) = T_{p-q}^{(1,0)}\left(\vec{r}_2, \vec{r}_2\right) = T_{q-p}^{(0,1)}\left(\vec{r}_1, \vec{r}_1\right) = T_{q-p}^{(0,1)}\left(\vec{r}_2, \vec{r}_2\right) = \vec{0}$. Now, using $T_{q-q}^{(0,0)}\left(\vec{r}_1, \vec{r}_2\right) = T_{q-q}^{(0,0)}\left(\vec{r}_2, \vec{r}_1\right)$, $T_{q-p}^{(0,1)}\left(\vec{r}_1, \vec{r}_2\right) = -T_{q-p}^{(0,1)}\left(\vec{r}_2, \vec{r}_1\right)$, $T_{p-q}^{(1,0)}\left(\vec{r}_1, \vec{r}_2\right) = -T_{p-q}^{(1,0)}\left(\vec{r}_2, \vec{r}_1\right)$, $T_{p-p}^{(1,1)}\left(\vec{r}_1, \vec{r}_2\right) = T_{p-p}^{(1,1)}\left(\vec{r}_2, \vec{r}_1\right)$, $\vec{\nabla}_{\vec{r}_1} T_{q-q}^{(0,0)}\left(\vec{r}_1, \vec{r}_2\right) = -T_{q-q}^{(1,0)}\left(\vec{r}_1, \vec{r}_2\right)$, $\vec{\nabla}_{\vec{r}_1} T_{p-q}^{(1,0)}\left(\vec{r}_1, \vec{r}_2\right) = -T_{p-q}^{(2,0)}\left(\vec{r}_1, \vec{r}_2\right)$, $\vec{\nabla}_{\vec{r}_1} T_{p-p}^{(1,1)}\left(\vec{r}_1, \vec{r}_2\right) = -T_{p-p}^{(2,1)}\left(\vec{r}_1, \vec{r}_2\right)$, $T_{p-p}^{(2,1)}\left(\vec{r}_1, \vec{r}_1\right) =$

$T^{(2,1)}_{p-p}\left(\vec{r}_2,\vec{r}_2\right)=\bar{\bar{0}}$, we have:

$$\begin{aligned}\vec{F}_{1,q-q}&=-\vec{\nabla}_{\vec{r}_1}U_{q-q}\\&=-\left(\vec{\nabla}_{\vec{r}_1}q_1^*\right)T^{(0,0)}_{q-q}\left(\vec{r}_1,\vec{r}_1\right)q_1^*-\left(\vec{\nabla}_{\vec{r}_1}q_2^*\right)T^{(0,0)}_{q-q}\left(\vec{r}_2,\vec{r}_2\right)q_2^*\\&-\left(\vec{\nabla}_{\vec{r}_1}q_1^*\right)T^{(0,0)}_{q-q}\left(\vec{r}_1,\vec{r}_2\right)q_2^*-q_1^*T^{(0,0)}_{q-q}\left(\vec{r}_1,\vec{r}_2\right)\left(\vec{\nabla}_{\vec{r}_1}q_2^*\right)\\&+q_1^*q_2^*T^{(1,0)}_{q-q}\left(\vec{r}_1,\vec{r}_2\right)-\left(\vec{\nabla}_{\vec{r}_1}q_1^*\right)\chi_1-\left(\vec{\nabla}_{\vec{r}_1}q_2^*\right)\chi_2\end{aligned}\tag{II.16}$$

$$\begin{aligned}\vec{F}_{1,p-q}&=-\vec{\nabla}_{\vec{r}_1}U_{p-q}\\&=\frac{1}{2}\left(\vec{\nabla}_{\vec{r}_1}\otimes\vec{p}_1^*\right)\cdot T^{(1,0)}_{p-q}\left(\vec{r}_1,\vec{r}_2\right)q_2^*-\frac{1}{2}T^{(2,0)}_{p-q}\left(\vec{r}_1,\vec{r}_2\right)\cdot\vec{p}_1^*q_2^*+\frac{1}{2}\left(\vec{p}_1^*\cdot T^{(1,0)}_{p-q}\left(\vec{r}_1,\vec{r}_2\right)\right)\left(\vec{\nabla}_{\vec{r}_1}q_2^*\right)\\&+\frac{1}{2}\left(\vec{\nabla}_{\vec{r}_1}\otimes\vec{p}_2^*\right)\cdot T^{(1,0)}_{p-q}\left(\vec{r}_2,\vec{r}_1\right)q_1^*+\frac{1}{2}T^{(1,1)}_{p-q}\left(\vec{r}_2,\vec{r}_1\right)\cdot\vec{p}_2^*q_1^*+\frac{1}{2}\left(\vec{p}_2^*\cdot T^{(1,0)}_{p-q}\left(\vec{r}_2,\vec{r}_1\right)\right)\left(\vec{\nabla}_{\vec{r}_1}q_1^*\right)\end{aligned}\tag{II.17}$$

$$\begin{aligned}\vec{F}_{1,q-p}&=-\vec{\nabla}_{\vec{r}_1}U_{q-p}\\&=-\frac{1}{2}\left(\vec{\nabla}_{\vec{r}_1}q_1^*\right)\left(T^{(0,1)}_{q-p}\left(\vec{r}_1,\vec{r}_2\right)\cdot\vec{p}_2^*\right)+\frac{1}{2}q_1^*T^{(1,1)}_{q-p}\left(\vec{r}_1,\vec{r}_2\right)\cdot\vec{p}_2^*-\frac{1}{2}q_1^*\left(\vec{\nabla}_{\vec{r}_1}\otimes\vec{p}_2^*\right)\cdot T^{(0,1)}_{q-p}\left(\vec{r}_1,\vec{r}_2\right)\\&-\frac{1}{2}\left(\vec{\nabla}_{\vec{r}_1}q_2^*\right)\left(T^{(0,1)}_{q-p}\left(\vec{r}_2,\vec{r}_1\right)\cdot\vec{p}_1^*\right)-\frac{1}{2}q_2^*T^{(0,2)}_{q-p}\left(\vec{r}_2,\vec{r}_1\right)\cdot\vec{p}_1^*-\frac{1}{2}q_2^*\left(\vec{\nabla}_{\vec{r}_1}\otimes\vec{p}_1^*\right)\cdot T^{(0,1)}_{q-p}\left(\vec{r}_2,\vec{r}_1\right)\end{aligned}\tag{II.18}$$

$$\begin{aligned}\vec{F}_{1,p-p}&=-\vec{\nabla}_{\vec{r}_1}U_{p-p}\\&=\left(\vec{\nabla}_{\vec{r}_1}\otimes\vec{p}_1^*\right)\cdot T^{(1,1)}_{p-p}\left(\vec{r}_1,\vec{r}_1\right)\cdot\vec{p}_1^*+\left(\vec{\nabla}_{\vec{r}_1}\otimes\vec{p}_2^*\right)\cdot T^{(1,1)}_{p-p}\left(\vec{r}_2,\vec{r}_2\right)\cdot\vec{p}_2^*\\&+\left(\vec{\nabla}_{\vec{r}_1}\otimes\vec{p}_1^*\right)\cdot T^{(1,1)}_{p-p}\left(\vec{r}_1,\vec{r}_2\right)\cdot\vec{p}_2^*+\left(\vec{\nabla}_{\vec{r}_1}\otimes\vec{p}_2^*\right)\cdot T^{(1,1)}_{p-p}\left(\vec{r}_2,\vec{r}_1\right)\cdot\vec{p}_1^*\\&-\left[T^{(2,1)}_{p-p}\left(\vec{r}_1,\vec{r}_2\right)\cdot\vec{p}_2^*\right]\cdot\vec{p}_1^*\end{aligned}\tag{II.19}$$

For the sake of convenience, we first adopt the method of finite difference to estimate the value of $\vec{\nabla}_{\vec{r}_1}q_1^*$ and $\vec{\nabla}_{\vec{r}_1}q_2^*$, which can be computed as $\frac{\left[q_1^*(\vec{r}_1+h\vec{u},\vec{r}_2)-q_1^*(\vec{r}_1-h\vec{u},\vec{r}_2)\right]}{2h}$ and $\frac{\left[q_2^*(\vec{r}_1+h\vec{u},\vec{r}_2)-q_2^*(\vec{r}_1-h\vec{u},\vec{r}_2)\right]}{2h}$, respectively, with h being a very small number, i.e., 0.00001. Similarly, $\vec{\nabla}_{\vec{r}_1}\otimes\vec{p}_1^*$ and $\vec{\nabla}_{\vec{r}_1}\otimes\vec{p}_2^*$ are computed as $\frac{\left[\vec{p}_1^*(\vec{r}_1+h\vec{u},\vec{r}_2)-\vec{p}_1^*(\vec{r}_1-h\vec{u},\vec{r}_2)\right]}{2h}$ and $\frac{\left[\vec{p}_2^*(\vec{r}_1+h\vec{u},\vec{r}_2)-\vec{p}_2^*(\vec{r}_1-h\vec{u},\vec{r}_2)\right]}{2h}$, with $\vec{u}$ a unit vector respectively along the three coordinate axis.

With these formulas, we compute numerically the electrostatic force for one of the two carbon atoms. To our big surprise, we found that the total force computed with the gradient of charges and dipoles considered is totally the same as that computed when they are not included, while F_{q-q}, F_{p-q}, F_{q-p} and F_{p-p} are different in the two cases, as shown in Table II.2, in which F^{gra}_{qq}, F^{gra}_{pq}, F^{gra}_{qp}, F^{gra}_{pp} denotes the interaction forces, respectively computed considering the gradient of

effective charges and dipoles using equation II.16, II.17, II.18 and II.19, whereas F_{q-q}, F_{p-q}, F_{q-p} and F_{p-p} is computed without taking into account the gradient of charges and dipoles (The third methods in the next section). In order for readers to reproduce the computation of forces described above, we gave, in Table II.1, some necessary values that we used for the two atoms, including characteristic widths R_q and R_p, electronegativities χ, coordinates x, y, z, electric equilibrium effective charges q^* and dipole moment p_x^*, p_y^* ,p_z^*, numerical derivative of q^* and $\vec{p}^*$ with respect to their positions $\vec{\nabla}_{\vec{r}_1} q^*$, $\vec{\nabla}_{\vec{r}_1} \otimes \vec{p}^*$. Taking into account some accidental cancellations that may occur in the process of calculation of the forces, we assigned four completely different values to characteristic widths R, as can be seen in Table II.3. The calculated results of forces displayed in Table II.4 suggest that the arguments that we stated above still hold true, which further confirms the correctness of the conclusions that we made in this chapter. We also checked analytically these results using Mathematica, with the same result. Finally, the fact that the computed total force is the same made us figure out why the gradients of charges and dipoles cancel each other in the derivation of force in the context of charge dipole model. We will see in the next section how this result can in fact be proven analytically in the general case.

	atom 1	atom 2
R_q (Å)	0.6862	0.6862
R_p (Å)	0.6862	0.6862
χ(V)	1.26212	3.3000
x (Å)	1.21222	2.37479
y (Å)	0.19103	0.37429
z (Å)	-3.9745	-3.22534
q^*(e)	0.230474360788924	-0.415859060071387
p_x^*(eÅ)	0.207141805257659	0.151045856651196
p_y^*(eÅ)	3.265249166202350E-002	2.380988989041366E-002
p_z^*(eÅ)	0.133482160065052	9.733393599422840E-002
$\nabla_x q^*$(e/Å)	0.780207211479353	-0.763296521992390
$\nabla_y q^*$(e/Å)	0.122986802608226	-0.120321111120645
$\nabla_z q^*$(e/Å)	0.502765440961283	-0.491868194231213
$\nabla_x p_x^*$(e)	0.435777113543773	0.418413380078719
$\nabla_x p_y^*$(e)	9.677955349577556E-002	8.643636593079529E-002
$\nabla_x p_z^*$(e)	0.395631181362689	0.353348618906962
$\nabla_y p_x^*$(e)	9.677955346246887E-002	8.643636589592735E-002
$\nabla_y p_y^*$(e)	-0.162920068699334	-0.116298827783905
$\nabla_y p_z^*$(e)	6.236473525828387E-002	5.569958615227900E-002
$\nabla_z p_x^*$(e)	0.395631181235013	0.353348618782756
$\nabla_z p_y^*$(e)	6.236473526175332E-002	5.569958615696275E-002
$\nabla_z p_z^*$(e)	7.676892612502347E-002	9.777372077774175E-002

Table II.1: Data necessary to computing the forces in our two atoms case.

	x	y	z
F_{q-q}^{gra}	-1.3991655031301486	-0.22055535594621295	-0.90162206420616364
F_{q-q}	0.444694330764454	7.009872981105415E-002	0.286561005149064
F_{p-q}^{gra}	2.1662472838748457	0.34147316769617464	1.3959294647347280
F_{p-q}	0.21049326950213698	3.3180793648775561E-002	0.13564185264505890
F_{q-p}^{gra}	2.1662472838748457	0.34147316769617464	1.3959294647347280
F_{q-p}	0.21049326950213698	3.3180793648775561E-002	0.13564185264505890
F_{p-p}^{gra}	-2.1662471844500915	-0.34147316472099265	-1.3959294555160222
F_{p-p}	-9.859923287488231E-002	-1.554254351071221E-002	-6.353734087633076E-002
F_{tot}^{gra}	0.76708188016945122	0.12091781472514362	0.49430740974726994
F_{tot}	0.767081656168877	0.120917780711355	0.494307348017673

Table II.2: Computed forces (in eV/Å) considering the gradients of effective charges and dipoles, using equations II.16, II.17, II.18 and II.19 and without taking them into account (by removing the gradient terms in the previous equations)

	atom 1	atom 2
R_q(Å)	0.6862	0.9704
R_p(Å)	1.44102	1.18853
χ(V)	1.26212	3.3000
x(Å)	1.21222	2.37479
y(Å)	0.19103	0.37429
z(Å)	-3.9745	-3.22534
q^*(e)	0.51507613411954423	-0.88505378132072787
p_x^*(eÅ)	0.99756646503020385	0.41765481506183688
p_y^*(eÅ)	0.15724990687538171	6.5836395946349352E-002
p_z^*(eÅ)	0.64283178162095822	0.26913674254340836
$\nabla_x q^*$(e/Å)	0.62307904865939978	-0.65327001236428317
$\nabla_y q^*$(e/Å)	9.8218139655211492E-002	-0.10297724734126144
$\nabla_z q^*$(e/Å)	0.40151210869772669	-0.42096716424299935
$\nabla_x p_x^*$(e)	-4.2689248543164471E-002	0.18394256166338507
$\nabla_x p_y^*$(e)	0.12853133617039747	8.5625561197106154E-002
$\nabla_x p_z^*$(e)	0.52543133071625481	0.35003411544307439
$\nabla_y p_x^*$(e)	0.12853133617039739	8.5625561197106015E-002
$\nabla_y p_y^*$(e)	-0.83780917572040559	-0.34575386888872933
$\nabla_y p_z^*$(e)	8.2825586786377497E-002	5.5177107477208144E-002
$\nabla_z p_x^*$(e)	0.52543133071625459	0.35003411544307350
$\nabla_z p_y^*$(e)	8.2825586786377553E-002	5.5177107477208068E-002
$\nabla_z p_z^*$(e)	-0.51948209784412258	-0.13368935995639944

Table II.3: Data necessary to computing the forces in our two atoms case, with different values for all parameters.

	x	y	z
F_{q-q}^{gra}	-2.5726892588569177	-0.40554204712795427	-1.6578408334707038
F_{q-q}	1.5995650997157405	0.25214506680895221	1.0307596725776487
F_{p-q}^{gra}	1.8142747388684368	0.28599050162014189	1.1691185536207718
F_{p-q}	-0.15645534198667646	-2.4662605269931467E-002	-0.10081981477832261
F_{q-p}^{gra}	1.8142747388684368	0.28599050162014189	1.1691185536207718
F_{q-p}	-0.15645534198667646	-2.4662605269931467E-002	-0.10081981477832261
F_{p-p}^{gra}	-1.0558602188799542	-0.16643895611232959	-0.68039627377084033
F_{p-p}	-0.60195917800180532	-9.4888940237880928E-002	-0.38790246507160969
F_{tot}^{gra}	0.68469523774058416	0.10793091603120825	0.44121757794939320
F_{tot}	0.68469523774058205	0.10793091603120834	0.44121757794939381

Table II.4: Computed forces (in eV/Å) considering the gradients of effective charges and dipoles, using equations II.16, II.17, II.18 and II.19 and without taking them into account (by removing the gradient terms in the previous equations), with different values for all parameters.

II.5 Analytical expressions for the force

II.5.1 Direct method by direct derivation of the full energy, valid even if charges and dipoles are not equilibrated

Using the expression of U'_{elec} constructed in the previous section (Eqs. II.1 and II.5), we have:

$$\begin{aligned}\vec{F}_\gamma \equiv -\vec{\nabla}_\gamma U'_{elec} \\ &= -\vec{\nabla}_\gamma \left[\frac{1}{2} \sum_{\alpha=1}^{N} \sum_{\beta=1}^{N} q_\alpha T_{q-q}^{(0,0)} \left(\vec{r}_\alpha, \vec{r}_\beta\right) q_\beta + \sum_{\alpha=1}^{N} q_\alpha \left(\chi_\alpha + V_{ext}\left(\vec{r}_\alpha\right)\right) \right. \\ &+ \lambda \left(\sum_{\alpha=1}^{N} q_\alpha - Q_{tot} \right) - \frac{1}{2} \sum_{\alpha=1}^{N} \sum_{\beta=1}^{N} \vec{p}_\alpha \cdot T_{p-p}^{(1,1)} \left(\vec{r}_\alpha, \vec{r}_\beta\right) \cdot \vec{p}_\beta \\ &- \sum_{\alpha=1}^{N} \vec{p}_\alpha \cdot \vec{E}_{ext}\left(\vec{r}_\alpha\right) - \frac{1}{2} \sum_{\alpha=1}^{N} \sum_{\beta=1}^{N} \vec{p}_\alpha \cdot T_{p-q}^{(1,0)} \left(\vec{r}_\alpha, \vec{r}_\beta\right) q_\beta \\ &\left. + \frac{1}{2} \sum_{\alpha=1}^{N} \sum_{\beta=1}^{N} q_\alpha T_{q-p}^{(0,1)} \left(\vec{r}_\alpha, \vec{r}_\beta\right) \cdot \vec{p}_\beta \right], \forall \gamma = 1, \cdots, N \end{aligned} \tag{II.20}$$

In this expression, the charges can have non electric equilibrium values, so that they can be considered independent of the positions. The only parts to differentiate are the external potential and field and the interaction tensors. Thus, we find:

$$\begin{aligned}\vec{F}_\gamma = &\left\{ \frac{1}{2} \sum_{\beta=1}^{N} T_{q-q}^{(1,0)} \left(\vec{r}_\gamma, \vec{r}_\beta\right) q_\beta - \frac{1}{2} \sum_{\alpha=1}^{N} T_{q-q}^{(0,1)} \left(\vec{r}_\alpha, \vec{r}_\gamma\right) q_\alpha + \vec{E}_{\text{ext}}\left(\vec{r}_\gamma\right) \right. \\ &\left. + \frac{1}{2} \sum_{\alpha=1, \alpha\neq\gamma}^{N} T_{p-q}^{(1,1)} \left(\vec{r}_\alpha, \vec{r}_\gamma\right) \cdot \vec{p}_\alpha + \frac{1}{2} \sum_{\beta=1, \beta\neq\gamma}^{N} T_{q-p}^{(1,1)} \left(\vec{r}_\gamma, \vec{r}_\beta\right) \cdot \vec{p}_\beta \right\} q_\gamma \\ &+ \left\{ -\frac{1}{2} \sum_{\beta=1}^{N} T_{p-p}^{(2,1)} \left(\vec{r}_\gamma, \vec{r}_\beta\right) \cdot \vec{p}_\beta + \frac{1}{2} \sum_{\alpha=1}^{N} T_{p-p}^{(1,2)} \left(\vec{r}_\alpha, \vec{r}_\gamma\right) \cdot \vec{p}_\alpha + \vec{\nabla}_\gamma \otimes E_{ext}\left(\vec{r}_\gamma\right) \right. \\ &\left. - \frac{1}{2} \sum_{\beta=1, \beta\neq\gamma}^{N} T_{p-q}^{(2,0)} \left(\vec{r}_\gamma, \vec{r}_\beta\right) q_\beta - \frac{1}{2} \sum_{\alpha=1, \alpha\neq\gamma}^{N} T_{q-p}^{(0,2)} \left(\vec{r}_\alpha, \vec{r}_\gamma\right) q_\alpha \right\} \vec{p}_\gamma \end{aligned} \tag{II.21}$$

Using $T^{(1,0)}_{q-q}\left(\vec{r}_\alpha,\vec{r}_\beta\right) = -T^{(0,1)}_{q-q}\left(\vec{r}_\beta,\vec{r}_\alpha\right)$ (in vacuum), $T^{(1,1)}_{p-q}\left(\vec{r}_\alpha,\vec{r}_\beta\right) = \left(T^{(1,1)}_{q-\mathrm{p}}\left(\vec{r}_\beta,\vec{r}_\alpha\right)\right)^T$, $T^{(2,0)}_{p-q}\left(\vec{r}_\alpha,\vec{r}_\beta\right) = \left(T^{(0,2)}_{q-p}\left(\vec{r}_\beta,\vec{r}_\alpha\right)\right)^T$, $T^{(2,1)}_{p-p}\left(\vec{r}_\alpha,\vec{r}_\beta\right) = -T^{(1,2)}_{p-p}\left(\vec{r}_\beta,\vec{r}_\alpha\right)$, the expression of the forces simplifies as: $\forall\gamma = 1,\cdots,N$

$$\begin{aligned}\vec{F}_\gamma = &\left\{\vec{E}_{ext}\left(\vec{r}_\gamma\right) + \sum_{\beta=1}^{N} T^{(1,0)}_{q-q}\left(\vec{r}_\gamma,\vec{r}_\beta\right) q_\beta + \sum_{\beta=1,\beta\neq\gamma}^{N} T^{(1,1)}_{q-p}\left(\vec{r}_\gamma,\vec{r}_\beta\right)\cdot\vec{p}_\beta\right\} q_\gamma \\ &+ \left\{\vec{\nabla}_\gamma \otimes \vec{E}_{\text{ext}}\ \left(\vec{r}_\gamma\right) - \sum_{\beta=1,\beta\neq\gamma}^{N} T^{(2,0)}_{p-q}\left(\vec{r}_\gamma,\vec{r}_\beta\right) q_\beta - \sum_{\beta=1}^{N} T^{(2,1)}_{p-p}\left(\vec{r}_\gamma,\vec{r}_\beta\right)\cdot\vec{p}_\beta\right\}\cdot\vec{p}_\gamma\end{aligned} \tag{II.22}$$

Note that if the characteristic radius of the radial Gaussian charge density distribution is the same for the charge and the dipole of a given atom, which seems physically reasonable, then $T^{(1,0)}_{q-q} = T^{(1,0)}_{p-q}$ and $T^{(1,1)}_{q-p} = T^{(1,1)}_{p-p}$, so that the first term between braces (right multiplied by q_γ) is zero at electrostatic equilibrium, since it is then equal to $\partial U'_{elec}/\partial\vec{p}_\alpha$

II.5.2 Second method with explicit determination of the gradients

In this method, we use the electrostatic equilibrium equation to simplify the expression of U'_{elec} before taking its gradient. We first reorder the terms in U'_{elec} to get:

$$\begin{aligned}U'_{\text{elec}} = &\frac{1}{2}\sum_{\alpha=1}^{N} q_\alpha\left[\sum_{\beta=1}^{N} T^{(0,0)}_{q-q}\left(\vec{r}_\alpha,\vec{r}_\beta\right) q_\beta + \sum_{\beta=1}^{N} T^{(0,1)}_{q-p}\left(\vec{r}_\alpha,\vec{r}_\beta\right)\cdot\vec{p}_\beta + \left(\chi_\alpha + V_{ext}\left(\vec{r}_\alpha\right)\right)\right] \\ &+ \frac{1}{2}\sum_{\alpha=1}^{N} q_\alpha\left(\chi_\alpha + V_{ext}\left(\vec{r}_\alpha\right)\right) \\ &- \frac{1}{2}\sum_{\alpha=1}^{N}\vec{p}_\alpha\cdot\left[\sum_{\beta=1}^{N} T^{(1,0)}_{q-q}\left(\vec{r}_\alpha,\vec{r}_\beta\right) q_\beta + \sum_{\beta=1}^{N} T^{(1,1)}_{p-p}\left(\vec{r}_\alpha,\vec{r}_\beta\right)\cdot\vec{p}_\beta + \vec{E}_{ext}\left(\vec{r}_\alpha\right)\right] \\ &- \frac{1}{2}\sum_{\alpha=1}^{N}\vec{p}_\alpha\cdot\vec{E}_{\text{ext}}\ \left(\vec{r}_\alpha\right) + \lambda\left(\sum_{\alpha=1}^{N} q_\alpha - Q_{\text{tot}}\right)\end{aligned} \tag{II.23}$$

Then by expressing explicitly the linear system of II.6, we have: $\forall\alpha = 1,\cdots,N$

$$\left\{\begin{array}{c}\sum_{\beta=1}^{N} T^{(0,0)}_{q-q}\left(\vec{r}_\alpha,\vec{r}_\beta\right) q^*_\beta + \sum_{\beta=1}^{N} T^{(0,1)}_{q-p}\left(\vec{r}_\alpha,\vec{r}_\beta\right)\cdot\vec{p}^*_\beta + \lambda^* = -\left(\chi_\alpha + V_{ext}\left(\vec{r}_\alpha\right)\right) \\ \sum_{\beta=1}^{N} T^{(1,0)}_{p-q}\left(\vec{r}_\alpha,\vec{r}_\beta\right) q^*_\beta + \sum_{\beta=1}^{N} T^{(1,1)}_{p-p}\left(\vec{r}_\alpha,\vec{r}_\beta\right)\cdot\vec{p}^*_\beta = -\vec{E}_{ext}\left(\vec{r}_\alpha\right) \\ \sum_{\beta=1}^{N} q^*_\beta = Q_{tot}\end{array}\right. \tag{II.24}$$

Inserting those generalized equilibrium equations into the definition of U'_{elec} (Eq.II.23) to compute its value at electrostatic equilibrium, we get a simplified U^*_{elec}:

$$\begin{aligned} U^*_{elec} &= \frac{1}{2}\sum_{\alpha=1}^{N} q^*_\alpha \left(\chi_\alpha + V_{ext}\left(\vec{r}_\alpha\right) - \lambda^*\right) - \frac{1}{2}\sum_{\alpha=1}^{N} \vec{p}^*_\alpha \cdot \vec{E}_{\text{ext}}\ \left(\vec{r}_\alpha\right) \\ &= \frac{1}{2}\sum_{\alpha=1}^{N} q^*_\alpha \left(\chi_\alpha + V_{\text{ext}}\ \left(\vec{r}_\alpha\right)\right) - \frac{1}{2}\sum_{\alpha=1}^{N} \vec{p}^*_\alpha \cdot \vec{E}_{\text{ext}}\ \left(\vec{r}_\alpha\right) - \frac{1}{2}\lambda^* Q_{\text{tot}} \end{aligned} \tag{II.25}$$

Let us now derive the force acting on the atom γ, by the other atoms of the system, starting from the above simplified expression of the total energy of the system at generalized equilibrium. We get:

$$\vec{F}_\gamma \equiv -\vec{\nabla}_\gamma U^*_{elec} = -\vec{\nabla}_\gamma \left[\frac{1}{2}\sum_{\alpha=1}^{N} q^*_\alpha \left(\chi_\alpha + V_{ext}\left(\vec{r}_\alpha\right)\right) - \frac{1}{2}\sum_{\alpha=1}^{N} \vec{p}^*_\alpha \cdot \vec{E}_{ext}\left(\vec{r}_\alpha\right) - \frac{1}{2}\lambda^* Q_{tot}\right] \tag{II.26}$$

$$\begin{aligned} \vec{F}_\gamma &= \frac{1}{2} q^*_\gamma \vec{E}_{ext}\left(\vec{r}_\gamma\right) + \frac{1}{2}\left[\vec{\nabla}_\gamma \otimes \vec{E}_{\text{ext}}\ \left(\vec{r}_\gamma\right)\right] \cdot \vec{p}^*_\gamma \\ &- \frac{1}{2}\sum_{\alpha=1}^{N} \left(\vec{\nabla}_\gamma q^*_\alpha\right)\left(\chi_\alpha + V_{ext}\left(\vec{r}_\alpha\right)\right) + \frac{1}{2}\sum_{\alpha=1}^{N}\left[\vec{\nabla}_\gamma \otimes \vec{p}^*_\alpha\right] \cdot \vec{E}_{\text{ext}}\ \left(\vec{r}_\alpha\right) + \frac{1}{2}\sum_{m=1}^{n}\left(\vec{\nabla}_\gamma \lambda^*\right) Q_{tot} \end{aligned} \tag{II.27}$$

Thus, we need to compute gradient terms such as $\vec{\nabla}_\gamma q^*_\alpha, \vec{\nabla}_\gamma \otimes \vec{p}^*_\alpha$ and $\vec{\nabla}_\gamma \lambda^*$. In the following, we prove that this can be done thanks to systems of equations coming from the derivation with respect to the N vectors $\vec{r}_\gamma$, of the equations obtained during the minimization of the (total energy + Lagrangian term) with respect to the charges, dipoles and Lagrange multipliers, which we recall once more:

$$\begin{cases} \sum_{\beta=1}^{N} T^{(0,0)}_{q-q}\left(\vec{r}_\alpha, \vec{r}_\beta\right) q^*_\beta + \sum_{\beta=1}^{N} T^{(0,1)}_{q-p}\left(\vec{r}_\alpha, \vec{r}_\beta\right) \cdot \vec{p}^*_\beta + \lambda^* = -\left(\chi_\alpha + V_{ext}\left(\vec{r}_\alpha\right)\right) \\ \sum_{\beta=1}^{N} T^{(1,0)}_{p-q}\left(\vec{r}_\alpha, \vec{r}_\beta\right) q^*_\beta + \sum_{\beta=1}^{N} T^{(1,1)}_{p-p}\left(\vec{r}_\alpha, \vec{r}_\beta\right) \cdot \vec{p}^*_\beta = -\vec{E}_{ext}\left(\vec{r}_\alpha\right) \\ \sum_{\beta=1}^{N} q^*_\beta = Q_{tot} \end{cases}$$
$$\forall \alpha = 1, \cdots, N \tag{II.28}$$

Applying $-\vec{\nabla}_\gamma$ to these equations gives: $\forall \alpha = 1, \cdots, N; \forall \gamma = 1, \cdots, N$

$$\begin{aligned} &\left[\sum_{\beta=1}^{N} T^{(1,0)}_{q-q}\left(\vec{r}_\alpha, \vec{r}_\beta\right) q^*_\beta\right]\delta_{\gamma\alpha} - T^{(0,1)}_{q-q}\left(\vec{r}_\alpha, \vec{r}_\beta\right) q^*_\beta \delta_{\gamma\beta} - \sum_{\beta=1}^{N} T^{(0,0)}_{q-q}\left(\vec{r}_\alpha, \vec{r}_\beta\right) \vec{\nabla}_\gamma q^*_\beta \\ &\qquad + \left[\sum_{\beta=1, \beta\neq\alpha}^{N} T^{(1,1)}_{q-p}\left(\vec{r}_\alpha, \vec{r}_\beta\right) \cdot \vec{p}^*_\beta\right]\delta_{\gamma\alpha} - T^{(0,2)}_{q-p}\left(\vec{r}_\alpha, \vec{r}_\beta\right) \cdot \vec{p}^*_\beta \delta_{\gamma\beta} \\ &\qquad - \sum_{\beta=1}^{N}\left(\vec{\nabla}_\gamma \otimes \vec{p}^*_\beta\right) \cdot T^{(0,1)}_{q-p}\left(\vec{r}_\alpha, \vec{r}_\beta\right) - \vec{\nabla}_\gamma \lambda^* = -\vec{E}_{ext}\left(\vec{r}_\alpha\right)\delta_{\gamma\alpha} \end{aligned} \tag{II.29}$$

$$\left[\sum_{\beta=1,\beta\neq\alpha}^{N} T_{p-q}^{(2,0)}\left(\vec{r}_\alpha,\vec{r}_\beta\right) q_\beta^*\right]\delta_{\gamma\alpha} - T_{p-q}^{(1,1)}\left(\vec{r}_\alpha,\vec{r}_\beta\right) q_\beta^*\delta_{\beta\gamma} - \sum_{\beta=1}^{N}\left(\vec{\nabla}_\gamma q_\beta^*\right)\otimes T_{p-q}^{(1,0)}\left(\vec{r}_\alpha,\vec{r}_\beta\right)$$
$$+\left[\sum_{\beta=1}^{N} T_{p-p}^{(2,1)}\left(\vec{r}_\alpha,\vec{r}_\beta\right)\cdot\vec{p}_\beta^*\right]\delta_{\gamma\alpha} - T_{p-p}^{(1,2)}\left(\vec{r}_\alpha,\vec{r}_\beta\right)\cdot\vec{p}_\beta^*\delta_{\beta\gamma} - \sum_{\beta=1}^{N}\left(\vec{\nabla}_\gamma\otimes\vec{p}_\beta^*\right)\cdot\left(T_{p-p}^{(1,1)}\left(\vec{r}_\alpha,\vec{r}_\beta\right)\right)^T$$
$$= \left[\vec{\nabla}_\gamma\otimes\vec{E}_{ext}\left(\vec{r}_\alpha\right)\right]\delta_{\gamma\alpha} \tag{II.30}$$

$$\sum_{\beta=1}^{N}\vec{\nabla}_\gamma q_\beta^* = \vec{0} \tag{II.31}$$

In order to cast these equations into a block-matrix form, we reorder them and transpose both hand sides: $\forall\alpha = 1,\cdots,N; \forall\gamma = 1,\cdots,N$

$$\sum_{\beta=1}^{N} T_{q-q}^{(0,0)}\left(\vec{r}_\alpha,\vec{r}_\beta\right)\left(\vec{\nabla}_\gamma q_\beta^*\right)^T + \sum_{\beta=1}^{N}\left(T_{q-p}^{(0,1)}\left(\vec{r}_\alpha,\vec{r}_\beta\right)\right)\cdot\left(\vec{\nabla}_\gamma\otimes\vec{p}_\beta^*\right)^T + \left(\vec{\nabla}_\gamma\lambda^*\right)^T$$
$$= \left[\sum_{\beta=1}^{N} T_{q-q}^{(1,0)}\left(\vec{r}_\alpha,\vec{r}_\beta\right) q_\beta^* + \sum_{\beta=1,\beta\neq\gamma}^{N} T_{q-p}^{(1,1)}\left(\vec{r}_\alpha,\vec{r}_\beta\right)\cdot\vec{p}_\beta^* + \vec{E}_{ext}\left(\vec{r}_\alpha\right)\right]^T\delta_{\gamma\alpha}$$
$$-\left[T_{q-q}^{(0,1)}\left(\vec{r}_\alpha,\vec{r}_\gamma\right) q_\gamma^* + T_{q-p}^{(0,2)}\left(\vec{r}_\alpha,\vec{r}_\gamma\right)\cdot\vec{p}_\gamma^*\right]^T\left(1-\delta_{\gamma\alpha}\right) \tag{II.32}$$

$$\sum_{\beta=1}^{N} T_{p-q}^{(1,0)}\left(\vec{r}_\alpha,\vec{r}_\beta\right)\otimes\left(\vec{\nabla}_\gamma q_\beta^*\right) + \sum_{\beta=1}^{N} T_{p-p}^{(1,1)}\left(\vec{r}_\alpha,\vec{r}_\beta\right)\left(\vec{\nabla}_\gamma\otimes\vec{p}_\beta^*\right)^T$$
$$= \left[\sum_{\beta=1,\beta\neq\alpha}^{N} T_{p-q}^{(2,0)}\left(\vec{r}_\alpha,\vec{r}_\beta\right) q_\beta^* + \sum_{\beta=1}^{N} T_{p-p}^{(2,1)}\left(\vec{r}_\alpha,\vec{r}_\beta\right)\cdot\vec{p}_\beta^* - \vec{\nabla}_\gamma\otimes\vec{E}_{ext}\left(\vec{r}_\alpha\right)\right]^T\delta_{\gamma\alpha} \tag{II.33}$$
$$-\left[T_{p-q}^{(1,1)}\left(\vec{r}_\alpha,\vec{r}_\gamma\right) q_\gamma^* + T_{p-p}^{(1,2)}\left(\vec{r}_\alpha,\vec{r}_\gamma\right)\cdot\vec{p}_\gamma^*\right]^T\left(1-\delta_{\gamma\alpha}\right)$$

$$\sum_{\beta=1}^{N}\left(\vec{\nabla}_\gamma q_\beta^*\right)^T = \vec{0}^T \tag{II.34}$$

The resulting block matrix linear system can then be written for a given value of index γ as:

$$\begin{bmatrix} \left(\widehat{T_{q-q}^{(0,0)}}\right)_{N\times N} & \left(\left(\widehat{T_{q-p}^{(0,1)}}\right)^T\right)_{N\times 3N} & \hat{1}_{N\times 1} \\ \left(\widehat{T_{p-q}^{(1,0)}}\right)_{3N\times N} & \left(\widehat{T_{p-p}^{(1,1)}}\right)_{3N\times 3N} & \hat{0}_{3N\times 1} \\ \hat{1}_{1\times N} & \hat{0}_{1\times 3N} & \hat{0}_{1\times 1} \end{bmatrix}\begin{bmatrix} \left(\widehat{\vec{\nabla}_\gamma q_\beta^*}\right)_{N\times 3}^T \\ \left(\widehat{\vec{\nabla}_\gamma\otimes\vec{p}_\beta^*}\right)_{3N\times 3}^T \\ \left(\widehat{\vec{\nabla}_\gamma\lambda^*}\right)_{1\times 3}^T \end{bmatrix} = \begin{bmatrix} \left(\widehat{\vec{V}_{\alpha\gamma}}\right)_{N\times 3} \\ \left(\widehat{\bar{\bar{M}}_{\alpha\gamma}}\right)_{3N\times 3} \\ \left(\widehat{\vec{0}}\right)_{1\times 3} \end{bmatrix} \tag{II.35}$$

with

$$\forall \alpha, \gamma = 1, \cdots, N$$
$$\bar{V}_{\alpha\gamma} \equiv \left[\sum_{\beta=1}^{N} T_{q-q}^{(1,0)}\left(\vec{r}_\alpha, \vec{r}_\beta\right) q_\beta^* + \sum_{\beta=1, \beta\neq\alpha}^{N} T_{q-p}^{(1,1)}\left(\vec{r}_\alpha, \vec{r}_\beta\right) \cdot \vec{p}_\beta^* + \vec{E}_{ext}\left(\vec{r}_\gamma\right) \right]^T \delta_{\gamma\alpha} \quad \text{(II.36)}$$
$$- \left[T_{q-q}^{(0,1)}\left(\vec{r}_\alpha, \vec{r}_\gamma\right) q_\gamma^* + T_{q-p}^{(0,2)}\left(\vec{r}_\alpha, \vec{r}_\gamma\right) \cdot \vec{p}_\gamma^* \right]^T \left(1 - \delta_{\gamma\alpha}\right)$$

and

$$\forall \alpha, \gamma = 1, \cdots, N$$
$$\bar{\bar{M}}_{\alpha\gamma} \equiv \left[\sum_{\beta=1, \beta\neq\alpha}^{N} T_{p-q}^{(2,0)}\left(\vec{r}_\alpha, \vec{r}_\beta\right) q_\beta^* + \sum_{\beta=1}^{N} T_{p-p}^{(2,1)}\left(\vec{r}_\alpha, \vec{r}_\beta\right) \cdot \vec{p}_\beta^* - \vec{\nabla}_\gamma \otimes \vec{E}_{ext}\left(\vec{r}_\gamma\right) \right]^T \delta_{\gamma\alpha}$$
$$- \left[T_{p-q}^{(1,1)}\left(\vec{r}_\alpha, \vec{r}_\gamma\right) q_\gamma^* + T_{p-p}^{(1,2)}\left(\vec{r}_\alpha, \vec{r}_\gamma\right) \cdot \vec{p}_\gamma^* \right]^T \left(1 - \delta_{\gamma\alpha}\right) \quad \text{(II.37)}$$

Hence, we obtain N systems (γ index) of $4N+1$ equations (α index + equation due to Lagrange multiplier) with $4N+1$ row-vector unknowns (β index) each with a right hand-side with 3 columns constituted by the superposition of a $N\times 3$ matrix (itself constituted by the superposition of the N row vectors with 3 components $\bar{V}_{\alpha\gamma}$ with $\alpha = 1, \cdots, N$) above a $4N \times 3$ matrix (itself constituted by the superposition of the N (3×3) matrices $\bar{\bar{M}}_{\alpha\gamma}$ with $\gamma = 1, \cdots, N$) above a 1×3 matrix of zeros). It is then numerically advantageous to invert the matrix of the system, since it will be enough to multiply that inverse with the row-vector right hand sides to obtain all the gradients in a single operation! The forces are then finally obtained by putting the values of all these gradients in Eq. II.26.

These were the formula used in previous works of Devel and collaborators who checked numerically that they gave the same values as the first method.

II.5.3 Third method using the derivative of the block-matrix of interaction tensors

In order to prove that the two previous methods would be analytically equivalent in all cases, let us try once more to start from the simplified electric equilibrium expression of the system energy (Eq. II.25), but this time put into block matrix form right from the start:

$$U_{elec}^* = \frac{1}{2} \sum_{\alpha=1}^{N} q_\alpha^* \left(\chi_\alpha + V_{ext}\left(\vec{r}_\alpha\right)\right) - \frac{1}{2} \sum_{\alpha=1}^{N} \vec{p}_\alpha^* \cdot \vec{E}_{ext}\left(\vec{r}_\alpha\right) - \frac{1}{2} \lambda^* Q_{tot}$$
$$= -\frac{1}{2} \left(\widehat{\bar{B}'}\right)^T \cdot \hat{\bar{X}} = -\frac{1}{2} \left(\widehat{\bar{B}'}\right)^T \cdot \left[\left(\widehat{\bar{\bar{M}}}\right) \cdot \left(\hat{\bar{B}}\right)\right] \quad \text{(II.38)}$$

with $\hat{\bar{M}} \equiv (\hat{\bar{A}})^{-1}$, $\left(\hat{\bar{B}}'\right)^T = \begin{pmatrix} -(\widehat{V_{ext}+\chi}) & \hat{\vec{E}}_{ext} & \hat{Q}_{tot} \end{pmatrix}$ and

$$\hat{\bar{A}}\hat{X} = \begin{bmatrix} \left(\widehat{T^{(0,0)}_{q-q}}\right)_{N\times N} & \left(\left(\widehat{T^{(0,1)}_{q-p}}\right)^T\right)_{N\times 3N} & \hat{1}_{N\times 1} \\ \left(\widehat{T^{(1,0)}_{p-q}}\right)_{3N\times N} & \left(\widehat{T^{(1,1)}_{p-p}}\right)_{3N\times 3N} & \hat{0}_{3N\times 1} \\ \left(\hat{1}^T\right)_{1\times N} & \hat{0}_{1\times 3N} & \hat{0}_{1\times 1} \end{bmatrix} \begin{bmatrix} \hat{q}^* \\ \hat{\vec{p}}^* \\ \hat{\lambda}^* \end{bmatrix} = \begin{bmatrix} -(\widehat{V_{ext}+\chi}) \\ -\hat{\vec{E}}_{ext} \\ \hat{Q}_{tot} \end{bmatrix} = \hat{\bar{B}} \tag{II.39}$$

Note that this could easily be generalized by using several Lagrange multipliers to provide the possibility to enforce charge conservation on several different molecules or parts of the system (done by M. Devel). Also note that the block $\left(\widehat{T^{(0,1)}_{q-p}}\right)^T$ is not the transpose of block $\left(\widehat{T^{(1,0)}_{p-q}}\right)$, but its opposite (recall that $T^{(0,1)}_{q-p}(\vec{r}_\alpha, \vec{r}_\beta) = -T^{(1,0)}_{p-q}(\vec{r}_\beta, \vec{r}_\alpha)$), so that the block matrix $\hat{\bar{A}}$ is not symmetric!

Using Eq. II.38, the i^{th} Cartesian coordinate of the force on atom γ can be calculated as:

$$\begin{aligned} \left(\vec{F}_\gamma\right)_i &= -\nabla_{\gamma,i} U^*_{elec} = \frac{1}{2}\nabla_{\gamma,i}\left[\left(\hat{\bar{B}}'\right)^T \cdot \hat{\bar{M}} \cdot \hat{\bar{B}}\right] \\ &= \frac{1}{2}\left[\nabla_{\gamma,i}\left(\left(\hat{\bar{B}}'\right)^T\right) \cdot \hat{\bar{M}} \cdot \hat{\bar{B}} + \left(\hat{\bar{B}}'\right)^T \cdot \nabla_{\gamma,i}(\hat{\bar{M}}) \cdot \hat{\bar{B}} + \left(\hat{\bar{B}}'\right)^T \cdot \hat{\bar{M}} \cdot \nabla_{\gamma,i}(\hat{\bar{B}})\right] \end{aligned} \tag{II.40}$$

We thus have three different terms to compute. Concerning the first term, since

$$\begin{aligned} &\nabla_{\gamma,i}\left(\left(\hat{\bar{B}}'\right)^T\right) = \nabla_{\gamma,i}\left(-(\widehat{V_{ext}+\chi}) \quad \widehat{\vec{E}_{ext}} \quad \hat{Q}_{tot}\right) \\ &= \left((0\ldots E_{ext,i}(\vec{r}_\gamma)\ldots 0)_{1\times N} \quad \left(\vec{0}^T \ldots \nabla_{\gamma,i}\vec{E}_{ext}(\vec{r}_\gamma)\ldots \vec{0}^T\right)_{1\times 3N} \quad 0_{1\times 1}\right) \end{aligned} \tag{II.41}$$

we have

$$\vec{\nabla}_\gamma\left(\left(\hat{\bar{B}}^*\right)^T\right) \cdot \hat{\bar{X}} = q^*_\gamma \vec{E}_{ext}(\vec{r}_\gamma) + \left[\vec{\nabla}_\gamma \otimes \vec{E}_{ext}(\vec{r}_\gamma)\right] \cdot \vec{p}^*_\gamma \tag{II.42}$$

As for the second term, since $[\hat{\bar{A}}]^{-1} \cdot [\hat{\bar{A}}] = \bar{\bar{1}}_{(4N+1)\times(4N+1)}$ and $\hat{\bar{M}} \equiv (\hat{\bar{A}})^{-1}$, one has: $\forall \gamma = 1, \ldots, N; \forall i = x, y, z$

$$\nabla_{\gamma,i}\hat{\bar{M}} \cdot \hat{\bar{A}} + \hat{\bar{M}} \cdot \nabla_{\gamma,i}\hat{\bar{A}} = \bar{\bar{0}}_{(4N+1)\times(4N+1)} \Leftrightarrow \nabla_{\gamma,i}\hat{\bar{M}} = -\hat{\bar{M}} \cdot \nabla_{\gamma,i}\hat{\bar{A}} \cdot \hat{\bar{M}} \tag{II.43}$$

$$\text{with: } \nabla_{\gamma,i}\hat{\bar{A}} = \begin{bmatrix} \nabla_{\gamma,i}\left(\widehat{T^{(0,0)}_{q-q}}\right) & \nabla_{\gamma,i}\left(\widehat{T^{(0,1)}_{q-p}}\right)^T & \nabla_{\gamma,i}\hat{1} \\ \nabla_{\gamma,i}\left(\widehat{T^{(1,0)}_{p-q}}\right) & \nabla_{\gamma,i}\left(\widehat{T^{(1,1)}_{p-p}}\right) & \nabla_{\gamma,i}\hat{0} \\ \nabla_{\gamma,i}\left(\hat{1}^T\right) & \nabla_{\gamma,i}\hat{0} & \nabla_{\gamma,i}\hat{0} \end{bmatrix}$$

Hence, $\left(\hat{\bar{B}}'\right)^T \cdot \vec{\nabla}_{\gamma,i}(\hat{\bar{\bar{M}}}) \cdot \hat{\bar{B}} = -\left(\hat{\bar{B}}'\right)^T \cdot \hat{\bar{\bar{M}}} \cdot \nabla_{\gamma,i} \hat{\bar{\bar{A}}} \cdot \hat{\bar{\bar{M}}} \cdot \hat{\bar{B}} = -\left(\hat{\bar{X}}'\right)^T \cdot \nabla_{\gamma,i} \hat{\bar{\bar{A}}} \cdot \hat{\bar{X}}$, where we have defined $\left(\hat{\bar{X}}'\right)^T \equiv \left(\hat{\bar{B}}'\right)^T \cdot \hat{\bar{\bar{M}}}$.

Furthermore, we can also use $\left(\hat{\bar{X}}'\right)^T$ in the third term, so that $\left(\hat{\bar{B}}'\right)^T \cdot \hat{\bar{\bar{M}}} \cdot \nabla_{\gamma,i}(\hat{\bar{B}}) = \left(\hat{\bar{X}}'\right)^T \cdot \nabla_{\gamma,i}(\hat{\bar{B}})$. We therefore have:

$$
\begin{aligned}
&\left(\hat{\bar{B}}'\right)^T \cdot \vec{\nabla}_{\gamma,i}(\hat{\bar{\bar{M}}}) \cdot \hat{\bar{B}} + \left(\hat{\bar{B}}'\right)^T \cdot \hat{\bar{\bar{M}}} \cdot \nabla_{\gamma,i} \hat{\bar{B}} \\
&= \left(\hat{\bar{X}}'\right)^T \cdot \left[\nabla_{\gamma,i}(\hat{\bar{B}}) - \nabla_{\gamma,i} \hat{\bar{\bar{A}}} \cdot \hat{\bar{X}}\right] \\
&= \left(\hat{\bar{X}}'\right)^T \cdot \hat{\bar{\bar{A}}} \cdot \nabla_{\gamma,i}(\hat{\bar{X}}) = \left(\hat{\bar{B}}'\right)^T \cdot \hat{\bar{\bar{M}}} \cdot \hat{\bar{\bar{A}}} \cdot \nabla_{\gamma,i}(\hat{\bar{X}}) \\
&= \left(\hat{\bar{B}}'\right)^T \cdot \nabla_{\gamma,i}(\hat{\bar{X}})
\end{aligned}
\tag{II.44}
$$

Putting Eqs. II.42 and II.44 into Eq. II.40, we recover the result of the second method (Eq. II.27):

$$
\begin{aligned}
&\vec{F}_\gamma = \frac{1}{2} q_\gamma^* \vec{E}_{ext}\left(\vec{r}_\gamma\right) + \frac{1}{2}\left[\vec{\nabla}_\gamma \otimes \vec{E}_{\text{ext}}\ \left(\vec{r}_\gamma\right)\right] \cdot \vec{p}_\gamma^* \\
&- \frac{1}{2} \sum_{\alpha=1}^{N} \left(\vec{\nabla}_\gamma q_\alpha^*\right)\left(\chi_\alpha + V_{ext}\left(\vec{r}_\alpha\right)\right) + \frac{1}{2} \sum_{\alpha=1}^{N}\left[\vec{\nabla}_\gamma \otimes \vec{p}_\alpha^*\right] \cdot \vec{E}_{\text{ext}}\ \left(\vec{r}_\alpha\right) + \frac{1}{2} \sum_{m=1}^{n} \left(\vec{\nabla}_\gamma \lambda^*\right) Q_{tot}
\end{aligned}
\tag{II.45}
$$

Alternatively, we can recover the result of the first method by decomposing $\hat{\bar{\bar{M}}}$ in the same block matrix form as $\hat{\bar{\bar{A}}}$:

$$
\begin{pmatrix}
\widehat{M}_{N\times N} & \left(-\left(\widehat{M}_{3N\times N}\right)^T\right)_{N\times 3N} & \widehat{M}_{N\times 1} \\
\widehat{M}_{3N\times N} & \widehat{M}_{3N\times 3N} & \widehat{M}_{3N\times 1} \\
\widehat{M}_{1\times N} & \widehat{M}_{1\times 3N} & \widehat{M}_{1\times 1}
\end{pmatrix}
\tag{II.46}
$$

Hence, using $\hat{\hat{X}}' = \left[\left(\hat{\hat{B}}'\right)^T \cdot \hat{\hat{M}}\right]^T$ and $\hat{\hat{X}} = \hat{\hat{M}} \cdot \hat{\hat{B}}$, we have:

$$\begin{aligned}
&\left[\begin{pmatrix} -\left(\widehat{V_{ext}}+\chi\right)_{1\times N} & \left(\widehat{E_{ext}}^T\right)_{1\times 3N} & \widehat{Q}_{tot} \end{pmatrix} \begin{pmatrix} \widehat{M}_{N\times N} & \left(-\left(\widehat{M}_{3N\times N}\right)^T\right)_{N\times 3N} & \widehat{M}_{N\times 1} \\ \widehat{M}_{3N\times N} & \widehat{M}_{3N\times 3N} & \widehat{M}_{3N\times 1} \\ \widehat{M}_{1\times N} & \widehat{M}_{1\times 3N} & \widehat{M}_{1\times 1} \end{pmatrix}\right]^T \\
&= \begin{pmatrix} \left[-\left(\widehat{V_{ext}}+\chi\right)_{1\times N}\widehat{M}_{N\times N} + \left(\widehat{\vec{E}_{ext}}\right)^T_{1\times 3N}\widehat{M}_{3N\times N} + \widehat{Q}_{tot}\widehat{M}_{1\times N}\right]^T \\ \left[(V_{\text{ext}}+\chi)_{1\times N}\left(\left(\widehat{M_{3N\times N}}\right)^T\right)_{N\times 3N} + \left(\widehat{\vec{E}_{ext}}\right)^T_{1\times 3N}\widehat{M}_{3N\times 3N} + \widehat{Q}_{tot}\widehat{M}_{1\times 3N}\right]^T \\ \left[-\left(\widehat{V_{ext}}+\chi\right)_{1\times N}\widehat{M}_{N\times 1} + \left(\widehat{E}_{ext}\right)^T_{1\times 3N}\widehat{M}_{3N\times 1} + \widehat{Q}_{tot}\widehat{M}_{1\times 1}\right]^T \end{pmatrix} \\
&= \begin{pmatrix} \widehat{X'}_{N\times 1} \\ \widehat{X'}_{3N\times 1} \\ \widehat{X'}_{1\times 1} \end{pmatrix}
\end{aligned} \tag{II.47}$$

and

$$\begin{aligned}
\begin{pmatrix} \hat{q}^* \\ \hat{\vec{p}}^* \\ \hat{\lambda}^* \end{pmatrix} = \begin{pmatrix} \widehat{X}_{N\times 1} \\ \widehat{X}_{3N\times 1} \\ \widehat{X}_{N\times 1} \end{pmatrix} &= \begin{pmatrix} \widehat{M}_{N\times N} & -\left(\left(\widehat{M}_{3N\times N}\right)^T\right)_{N\times 3N} & \widehat{M}_{N\times 1} \\ \widehat{M}_{3N\times N} & \widehat{M}_{3N\times 3N} & \widehat{M}_{3N\times 1} \\ \widehat{M}_{1\times N} & \widehat{M}_{1\times 3N} & \widehat{M}_{1\times 1} \end{pmatrix} \begin{pmatrix} -\left(\widehat{V_{\text{ext}}+\chi}\right) \\ -\widehat{\vec{E}_{ext}} \\ Q_{tot} \end{pmatrix} \\
&= \begin{pmatrix} -\widehat{M}_{N\times N}\left(V_{ext}+\chi\right)_{N\times 1} + \left(\left(\widehat{M}_{3N\times N}\right)^T\right)_{N\times 3N}\left(\widehat{\vec{E}}_{\text{ext}}\right)_{3N\times 1} + \widehat{M}_{N\times 1}\widehat{Q}_{tot} \\ -\widehat{M}_{3N\times N}\left(V_{ext}+\chi\right)_{N\times 1} - \widehat{M}_{3N\times 3N}\left(\widehat{\vec{E}}_{\text{ext}}\right)_{3N\times 1} + \widehat{M}_{3N\times 1}\widehat{Q}_{tot} \\ -\widehat{M}_{1\times N}\left(V_{ext}+\chi\right)_{N\times 1} - \widehat{M}_{1\times 3N}\left(\widehat{E}_{ext}\right)_{3N\times 1} + \widehat{M}_{1\times 1}\widehat{Q}_{tot} \end{pmatrix}
\end{aligned} \tag{II.48}$$

Using the fact the $\widehat{M}_{N\times N}$ is symmetric since $\widehat{A}_{N\times N} = \widehat{T^{(0,0)}_{q-q}}$ is symmetric, we see that:

$$\widehat{X'}_{N\times 1} = \widehat{X}_{N\times 1} = \widehat{q^*} \tag{II.49}$$

Furthermore

$$\widehat{X'}_{3N\times 1} = -\widehat{X}_{3N\times 1} + 2\widehat{M}_{3N\times 1}\widehat{Q}_{tot} = -\widehat{\vec{p}^*} + 2\widehat{M}_{3N\times 1}\widehat{Q}_{tot} \tag{II.50}$$

If we now suppose that $\widehat{M}_{3N\times 1} = 0$ as in $\hat{\hat{A}}$ or that $Q_{tot} = 0$, we have $\widehat{X'}_{3N\times 1} = -\widehat{\vec{p}^*}$.

Now, noting that only a few elements are non zero in $\nabla_{\gamma,i}\hat{\hat{A}}$ and $\nabla_{\gamma,i}(\hat{\hat{B}})$:
$\forall \alpha, \beta = 1, \ldots, N$

$$\left[\nabla_{\gamma,i}\left(\widehat{T^{(0,0)}_{q-q}}\right)\right]_{\alpha,\beta} = \left[T^{(0,1)}_{q-q}\left(\vec{r}_\alpha, \vec{r}_\gamma\right)\right]_i \delta_{\beta\gamma} - \left[T^{(1,0)}_{q-q}\left(\vec{r}_\gamma, \vec{r}_\beta\right)\right]_i \delta_{\alpha\gamma}$$

$$\left[\nabla_{\gamma,i}\left(\widehat{T^{(0,1)}_{q-p}}\right)\right]_{\alpha,\beta} = \left[T^{(0,2)}_{q-p}\left(\vec{r}_\alpha, \vec{r}_\gamma\right)\right]_{i,\cdot} \delta_{\beta\gamma} - \left[T^{(1,1)}_{q-p}\left(\vec{r}_\gamma, \vec{r}_\beta\right)\right]_{i,\cdot} \delta_{\alpha\gamma}$$

$$\left[\nabla_{\gamma,i}\left(\widehat{T^{(1,0)}_{p-q}}\right)\right]_{\alpha,\beta} = \left[T^{(1,1)}_{p-q}\left(\vec{r}_\alpha,\vec{r}_\gamma\right)\right]_{i,\cdot}\delta_{\beta\gamma} - \left[T^{(2,0)}_{p-q}\left(\vec{r}_\gamma,\vec{r}_\beta\right)\right]_{i,\cdot}\delta_{\alpha\gamma}$$
$$\left[\nabla_{\gamma,i}\left(\widehat{T^{(1,1)}_{p-p}}\right)\right]_{\alpha,\beta} = \left[T^{(1,2)}_{p-p}\left(\vec{r}_\alpha,\vec{r}_\gamma\right)\right]_{i,\cdot,\cdot}\delta_{\beta\gamma} - \left[T^{(2,1)}_{p-p}\left(\vec{r}_\gamma,\vec{r}_\beta\right)\right]_{i,\cdot,\cdot}\delta_{\alpha\gamma}$$

and

$$\begin{aligned}\nabla_{\gamma,i}(\hat{\hat{B}}) &= \nabla_{\gamma,i}\begin{pmatrix}-(\widehat{V_{ext}+\chi}) & -\hat{\vec{E}}_{ext} & \hat{Q}_{tot}\end{pmatrix}^T \\ &= \begin{pmatrix}(0\dots E_{ext,i}\left(\vec{r}_\gamma\right)\dots 0)_{1\times N} & \left(\vec{0}^T\dots -\nabla_{\gamma,i}\vec{E}_{ext}\left(\vec{r}_\gamma\right)\dots\vec{0}^T\right)_{1\times 3N} & 0_{1\times 1}\end{pmatrix}^T\end{aligned} \tag{II.51}$$

We finally recover Eq. II.21:

$$\begin{aligned}\vec{F}_\gamma = &\left\{\vec{E}_{ext}\left(\vec{r}_\gamma\right) + \sum_{\beta=1}^{N}\left[T^{(1,0)}_{q-q}\left(\vec{r}_\gamma,\vec{r}_\beta\right)\right]q^*_\beta + \sum_{\beta=1}^{N}\left[T^{(1,1)}_{q-p}\left(\vec{r}_\gamma,\vec{r}_\beta\right)\right]\cdot\vec{p}^*_\beta\right\}q^*_\gamma + \\ &\left\{\left[\vec{\nabla}_\gamma\otimes\vec{E}_{ext}\left(\vec{r}_\gamma\right)\right] - \sum_{\beta=1}^{N}\left[T^{(2,0)}_{p-q}\left(\vec{r}_\gamma,\vec{r}_\beta\right)\right]q^*_\beta - \sum_{\beta=1}^{N}\left[T^{(2,1)}_{p-p}\left(\vec{r}_\gamma,\vec{r}_\beta\right)\right]\cdot\vec{p}^*_\beta\right\}\cdot\vec{p}^*_\gamma\end{aligned} \tag{II.52}$$

Hence we do recover exactly the same analytical result than with the first method.

II.6 Computation of in-plane piezoelectric coefficient caused by flexoelectricity for patterned graphene

II.6.1 A little literature review on computation of piezoelectricity for graphene

Among the now numerous 2D materials, graphene, an atomically thin hexagonal monolayer structure, has extensive application in various aspects due to its mechanical, electric, optical and thermal properties[Zhu 10]. The centrosymmetry of pristine graphene, however, leads to some challenges to design electromechanical nanodevices with graphene. To overcome this difficulty, considerable efforts have been made within the framework of ab-initio-based calculation. For instance, Kalinin and Meunier reported that polarization can be induced through bending the graphene[Kalinin 08]. Chandrate *et al.* introduced defects with various shapes in a graphene flake to induce a net polarization[Chandratre 12]. The same method for inducing polarization in pristine graphene by breaking the symmetry was also adopted by Kundalwal *et al.*[Kundalwal 17] to yield a non-zero piezoelectric coefficient ($\approx$0.27 C/m^2). Moreover, chemical functionalization[Pandey 21b, Ong 12, El-Kelany 16] and doping[Ong 12, El-Kelany 16] were recently used to generate a localized net polarization due to which piezoelectric coefficient can be improved

by several orders of magnitude, compared to their corresponding pure material. In 2018, Javvaji *et al.* published a paper on the calculation of piezoelectricity and flexoelectricity coefficients for a patterned graphene, using molecular dynamics (MD) simulations coupled with a charge dipole model[Javvaji 18]. This is the article from which we want to compare their results with ours.

II.6.2 Introduction to Javvaji's 2018 paper

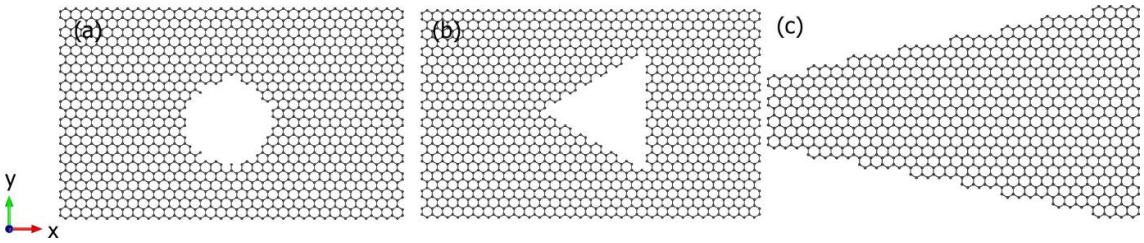

Figure II.1: The three types of patterned graphene used by Javvaji et al. and us for our stretching simulations: (a) with a circular hole defect, (b) with a triangular hole defect, (c) trapezium shaped

Javvaji *et al*[Javvaji 18] performed stretching simulations using molecular mechanics as implemented in LAMMPS (Large-scale Atomic/Molecular Massively Parallel Simulator)[Thompson 22],using the Adaptive Interatomic Reactive Empirical Bond Order (AIREBO) potential[Stuart 00] plus the charge dipole potential described in the previous parts of this chapter, to compute piezoelectric and flexoelectric coefficients for three sorts of structured graphene (with cicular hole defect, with triangular hole defect, and trapezium-shaped graphene, see Fig. II.1). These structures are first stretched a small distance (displacement of the atoms in the boundary regions by $u_x = 0.1$ Å, see Fig. II.2), then they are relaxed in LAMMPS by energy optimization, with atoms in the boundary regions on both sides of the structured graphene held fixed during relaxation. Once the energy optimization is finished, all the obtained configurations are stored for the computation of polarization, using only the atoms in the calculation region (see Fig. II.2), then the structure is stretched once more to begin a new cycle. A total of about 15 stretching cycles were performed to achieve the target strain (0.03).

The Polarization for the stored atom configuration is then computed in two steps by Javvaji *et al.* First, the polarization of a unit cell is computed as (Eq. (12) of [Javvaji 18]):

$$\vec{P}_m = \frac{1}{V_m}\left(\sum_{i=1}^{n} \vec{p}_i\right) \tag{II.53}$$

where n is the number of basis atoms present in the unit cell m. V_m is the volume of the unit cell (see Figure II.2). The polarization of the complete graphene sheet is then supposed to be equal to the sum of the polarization from each individual

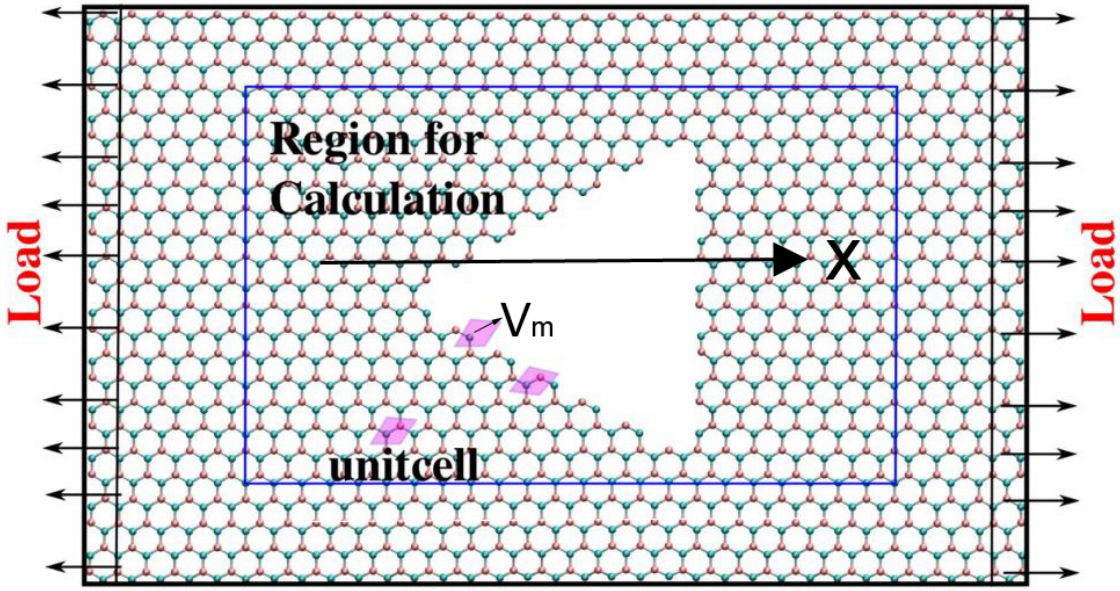

Figure II.2: A schematic representation of graphene under loading. Boundary and calculation regions are shown. Unit cell of the graphene lattice is highlighted.

cell. Total polarization $\vec{P}$ is then (Eq. (13) of [Javvaji 18]):

$$\vec{P} = \sum_{m=1}^{M} \vec{P}_m \tag{II.54}$$

The total polarization induced by the x-direction mechanical deformation is given by Eq. (14) of [Javvaji 18]:

$$P_x = d_{xxx}\varepsilon_{xx} + \mu_{xxxx}\frac{\partial \varepsilon_{xx}}{\partial x} + P_{0,x} \tag{II.55}$$

where d_{xxx} is the piezoelectric coefficient, μ_{xxxx} is the flexoelectric coefficient. $P_{0,x}$ is the polarization contribution from other components of strain and strain gradient. ε_{xx} refers to the engineering strain, which is defined as $(l_x - l_x^0)/l_x^0$, where l_x is the instantaneous length along x direction and l_x^0 is its initial value after the energy minimization. The engineering strain ε_{xx} delivers the information on the global strain in the atomic system. $\frac{\partial \varepsilon_{xx}}{\partial x}$ represents the strain gradient.

To compute piezoelectric coefficient d_{xxx} and flexoelectric coefficient μ_{xxxx}, Javvaji *et al.* split the equation II.55 into two equations II.56 and II.57.

$$P_x = d_{xxx}\varepsilon_{xx} + P_x^f, \tag{II.56}$$

where P_x^f is

$$P_x^f = \mu_{xxxx}\frac{\partial \varepsilon_{xx}}{\partial x} + P_{0,x} \tag{II.57}$$

The least squares fitting between variation of P_x and ε_{xx} will give the coefficient d_{xxx} and constant P_x^f (see Figure II.4b). With P_x^f and $\frac{\partial \varepsilon_{xx}}{\partial x}$, μ_{xxxx} can then be obtained by the slope of the fit of P_x^f as a function of $\frac{\partial \varepsilon_{xx}}{\partial x}$ [Javvaji 18].

II.6.3 Modifications with respect to the work of Javvaji et al

In this subsection, we describe the changes done with repect to the work of Javvaji *et al.* during our attempts to understand their results.

Before starting the stretching simulation, we initially relaxed the structure by the minimization of U_{AIREBO}, with all the atoms kept free to move in the whole space. Then, we shifted the atoms on the rightmost row of the patterned graphene to exert strain, followed by an energy-minimization calculation, which was carried out by minimizing $U_{AIREBO}+U_{elec}$ with x-direction degree of freedom for the leftmost and rightmost row of atoms constrained. This algorithm is depicted in Fig.II.3. This stretching operation is performed fifteen times to reach an engineering strain of 0.03. Conjugate gradient (CG) algorithm is used to minimize the energy function. Similarly to Javvaji et al., we used a simplified version of Eq. II.1 to compute U_{elec}, in order to take into account the fact there is no external electric field or potential in these simulations:

$$\begin{aligned} U_{\text{elec}} &= \sum_{\alpha=1}^{N} q_\alpha \chi_\alpha + \frac{1}{2}\sum_{\alpha=1}^{N}\sum_{\beta=1}^{N} q_\alpha T_{q-q}^{(0,0)}\left(\vec{r}_\alpha,\vec{r}_\beta\right) q_\beta - \sum_{\alpha=1}^{N}\sum_{\beta=1}^{N} \vec{p}_\alpha \cdot T_{p-q}^{(1,0)}\left(\vec{r}_\alpha,\vec{r}_\beta\right) q_\beta \\ &- \frac{1}{2}\sum_{\alpha=1}^{N}\sum_{\beta=1}^{N} \vec{p}_\alpha \cdot T_{p-p}^{(1,1)}\left(\vec{r}_\alpha,\vec{r}_\beta\right) \cdot \vec{p}_\beta \end{aligned} \tag{II.58}$$

where N is the total number of atoms. $T_{q-q}^{(0,0)}$, $T_{p-q}^{(1,0)}$ and $T_{p-p}^{(1,1)}$ are the electrostatic interacting tensors between charges and dipoles in vacuum already used in previous sections of this chapter. We note incidentally that there are several coherence problems in the definitions of these tensors in [Javvaji 18] and in the calculation of the forces in their Appendix (a complete list is available upon request to M. Devel). As in [Javvaji 18], the characteristic width R of the Gaussian radial function is set to be 0.06862 nm[Mayer 07b] and electronegativity 1.26212 V[Bresteau 16], for all atoms, independently of their number of nearest neighbors, which we believe is a debatable approximation. As in the first part of this chapter, in order to compute the effective charges and dipoles at electrostatic equilibrium for each atom, we minimize the total electrostatic energy by respectively making $\frac{\partial U_{elec}}{\partial q_i}$ and $\frac{\partial U_{elec}}{\partial \vec{p}_i}$ equal zero. By doing that, we then have: $\forall \alpha = 1, \ldots, N$

$$\begin{cases} \sum_{\beta=1}^{N} T_{p-p}^{(1,1)}\left(\vec{r}_\alpha,\vec{r}_\beta\right) \cdot \vec{p}_\beta^{\,*} + \sum_{\beta=1}^{N} T_{p-q}^{(1,0)}\left(\vec{r}_\alpha,\vec{r}_\beta\right) q_\beta^* = \vec{0} \\ \sum_{\beta=1}^{N} T_{p-q}^{(1,0)}\left(\vec{r}_\alpha,\vec{r}_\beta\right) \cdot \vec{p}_\beta^{\,*} + \sum_{\beta=1}^{N} T_{q-q}^{(0,0)}\left(\vec{r}_\alpha,\vec{r}_\beta\right) q_\beta^* = -\chi_\alpha \end{cases} \tag{II.59}$$

With the computed charges and dipoles from the above system of linear equation, we then compute the total polarization as:

$$\vec{P}^{tot} = \sum_{\alpha=1}^{N} \frac{\vec{p}_\alpha^{\,*} + q_\alpha^*\left(\vec{r}_\alpha - \vec{r}_c\right)}{V} \tag{II.60}$$

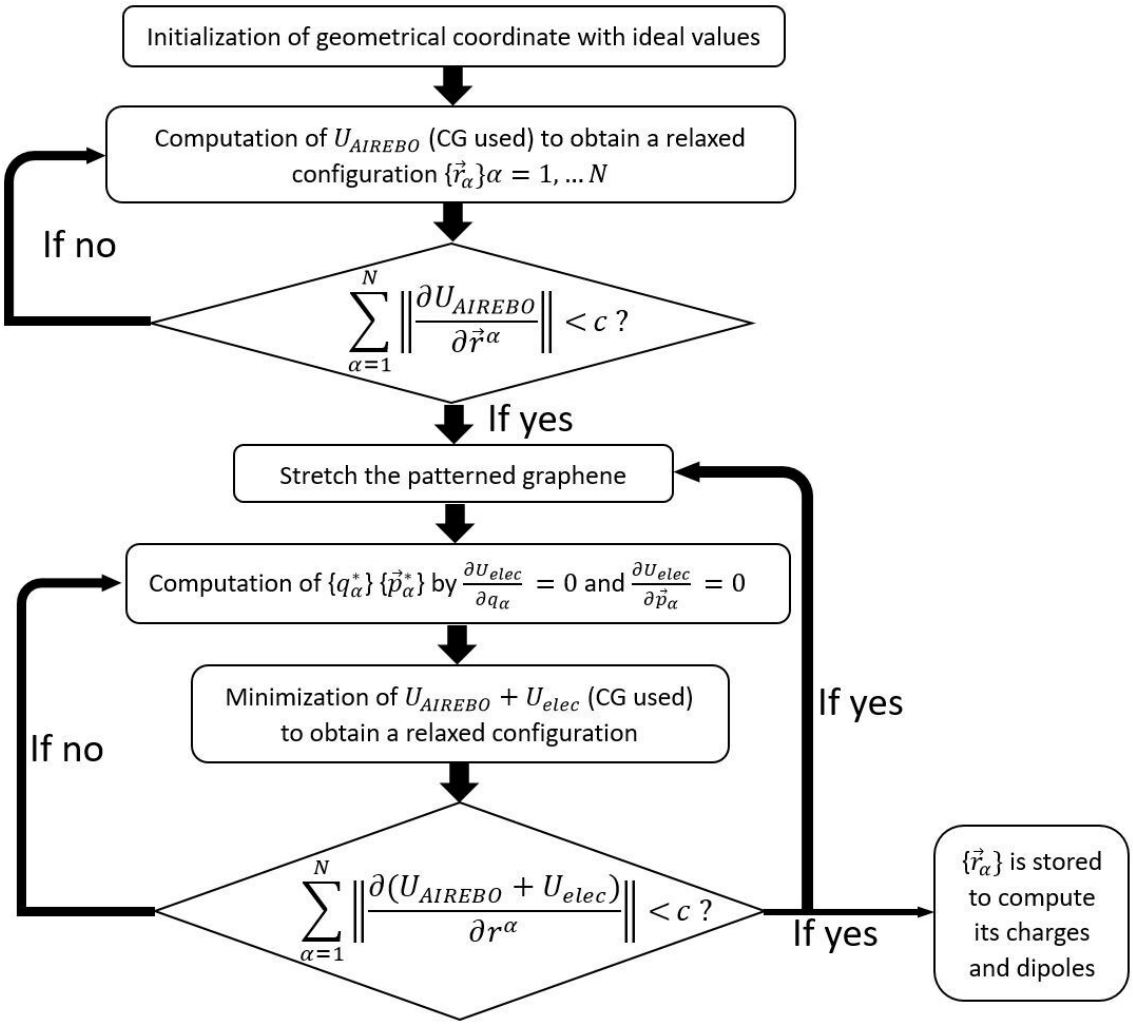

Figure II.3: Search algorithm for the static equilibrium of the system subjected to the action of an external load. The convergence criteria c of forces is set to 0.00004 eV/Å.

where V and $\vec{r}_c$ respectively are the volume and centroid of the configuration considered. It is worth mentioning here that centroid $\vec{r}_c$ must be involved in the definition of dipole moment because the configurations to be computed may not be neutral due to the lack of global charge neutrality conservation enforced through a Lagrange factor (third equation missing in system II.59). Furthermore, even if we would use dipoles only, our definition of polarization would not be equivalent to the definition of Javvaji et al. (Eqs. II.53 and II.54 do not lead to Eq. II.60 even if all effective charges equal zero).

Then, we follow Javvaji *et al.* in considering that the total change of polarization $\vec{P}^{tot}$ with strain can be viewed as coming from an effective piezoelectricity term, formulated as $e_{ijk}\varepsilon_{jk}$, which is in fact caused by flexoelectricity in this case, with e_{ijk} being the piezoelectric coefficient and ε_{jk} being the 3 by 3 strain tensor. Note that we here only consider the polarization caused by principal component ε_{11}

owing to the fact that we found ε_{11} is relatively large, compared to the other components of the strain tensor, so that the x-direction polarization can be expressed as:

$$P_1 = P_1^0 + e_{111}\varepsilon_{11} + h \tag{II.61}$$

where P_1^0 is the preexisting polarization due to the inflow of charges from the external environment due to the absence of charge conservation in system II.59 and to spontaneous strain gradient due to difference in material properties at the interface between atoms and space. h accounts for higher-order terms, which are here neglected with respect to piezoelectricity. Engineering strain ε_{11} is defined as $\frac{l-l_0}{l_0}$, where l_0 is the initial length before applying load and l is length along x axis of graphene after stretching.

II.6.4 Computation of piezoelectric coefficient

We obtain a piezoelectric coefficient of 0.03911 C/m^2 for trapezium-shaped graphene, of -0.0062 C/m^2 for graphene with a triangular defect, and of 0.00056 C/m^2 for graphene with a circular defect (Fig. II.4 and Table IV.1).

	Piezoelectric coefficient for trapezium-shaped graphene (C/m^2)	Piezoelectric coefficient for graphene with triangular defect (C/m^2)	Piezoelectric coefficient for graphene with hole defect (C/m^2)
Present	0.03911	-0.0062 (for 7.9% defect)	0.00056
B. Javvaji et al[Javvaji 18]	0.08013	0.02826	≈ 0
Kundalwal et al[Kundalwal 17]	—	0.027 (for 4.5% defect)	—
Kundalwal et al[Kundalwal 17]	—	0.12 (for 20% defect)	—
Chandratre et al[Chandratre 12]	—	(-)0.124 (defect size is large)	—

Table II.5: piezoelectric coefficients for trapezium-shaped graphene, graphene with triangular defect, and circular hole defect

It can be noticed that the intercept of the linear fit function, which denotes the value of the polarization corresponding to engineering strain equal to zero (unstretched state), is not zero. This preexisting polarization before stretching is in fact due to the absence of the charge conservation in Eq. II.59), which allows charges to freely flow into or out of material as if it were being charged. In fact, the enforcement of charge conservation could readily work out the problem mentioned above. However, in that case, the computed effective charges and dipoles would all be close to zero. This should be due to the value of affinity (electronegativity)

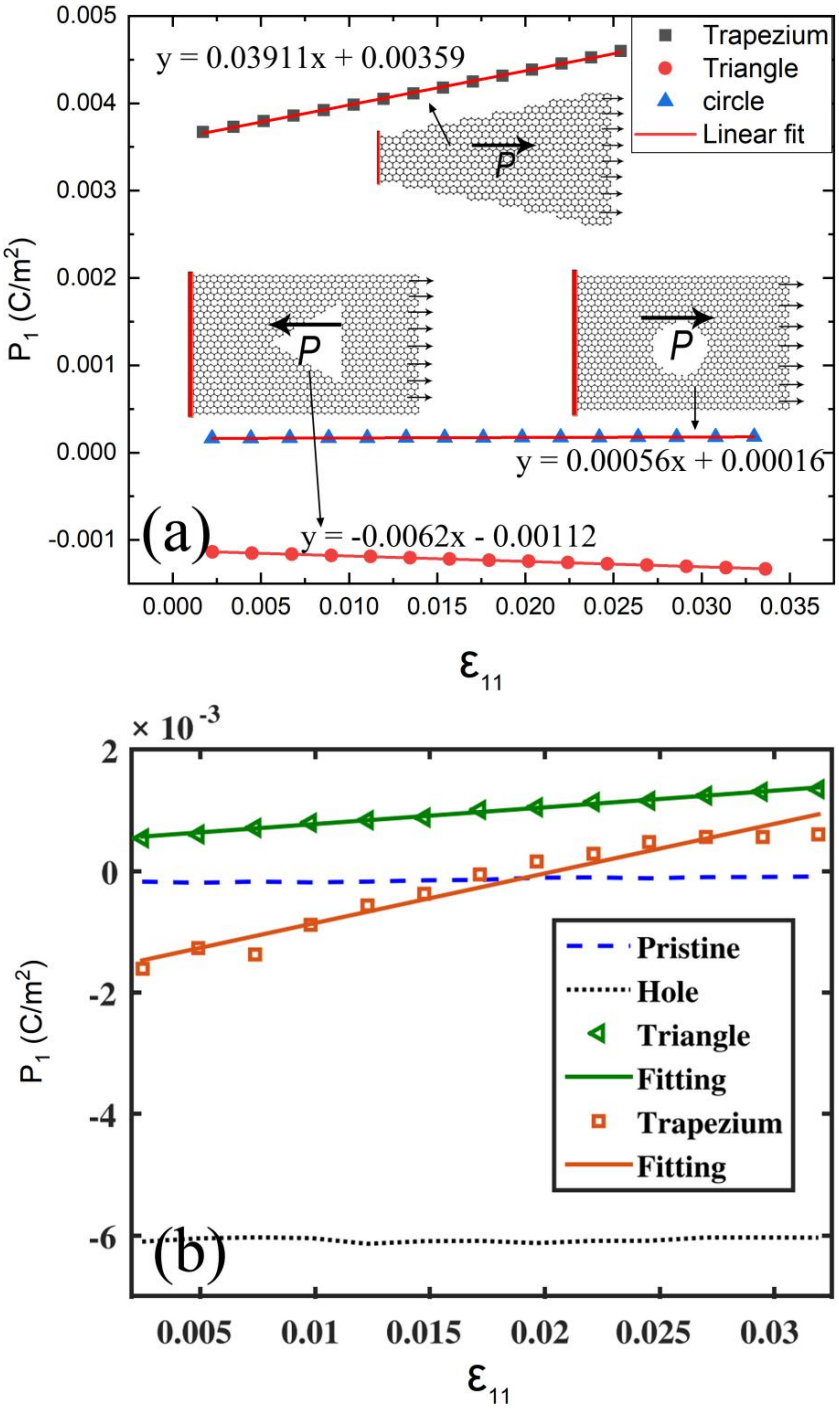

Figure II.4: (a) Variation of polarization along x axis with strain, for trapezium-shaped graphene, graphene with a triangular defect and circular hole defect. The red straight line is the fitting result. The atoms covered with the red regions are fixed during the stretching simulations. (b) Fig. 2b from [Javvaji 18], shown for comparison.

obtained in the experimental measurement, reported in [Bresteau 16], not being suitable for all the atoms (*e.g.* not for edge atoms), even though it is an experimental value. It can also be found that the computed piezoelectric coefficient for the graphene with circular hole is the smallest one (as expected), which can be interpreted by the fact that the oppositely signed charges induced at the interface between the internal circular space and the graphene can cancel each other out due to the high symmetry of the circle, resulting in a very small polarization, whereas, for the other two cases, a larger polarization is induced due to the broken symmetry along the x-direction. Furthermore, sign-wise, it should be noted that differently from the other two cases, sign of the polarization (or of the total dipole moment) for the case of trapezium graphene is computed to be negative. A same computing result can be seen in the paper of Chandratre *et al.*[Chandratre 12], in which the direction of the induced polarization by stretching a graphene flake with a triangle hole computed through ab-initio calculation points to $-x$ axis(left) as well, though they quote a positive number (hence the minus between parenthesis in Table IV.1. This means that charge dipole model is, to a certain degree, effective as concerns the calculation of the polarization. In order to further understand the differences in sign between these two cases, we plot Figure II.5, showing the graphene sheet with a triangle hole divided into four regions marked A, B, C, D. It can be observed that region B and C may coincidentally make up a trapezoid with the same shape as Figure II.1c). Compared to regions B and C, the polarizations in regions A and D are negligible due to their relatively high symmetry. We thus respectively computed the direction of the dipole moment in region B and C, pointing to the $-x$ (left) direction, in agreement with that for trapezium-shaped graphene (Figure II.1c). This thus illustrates the self-consistency of the charge dipole model in the calculation of polarization due to the fact that the calculations for the polarizations in graphene with triangle hole and trapezium-shaped graphene can be mutually confirmed. Finally, for comparison, the relevant results for piezoelectric coefficients of patterned graphene with several defects are shown in Table II.5, from which it can be seen that the piezoelectric coefficient for the graphene with triangle hole obtained by Javvaji *et al.* is different from ours. We attribute this to the a priori inappropriate definition of polarization in [Javvaji 18] and possibly to other problems we found in their paper. Further discussion concerning this point can be found in chapter 4 on the study of flexoelectric coefficient of MoS_2 monolayer.

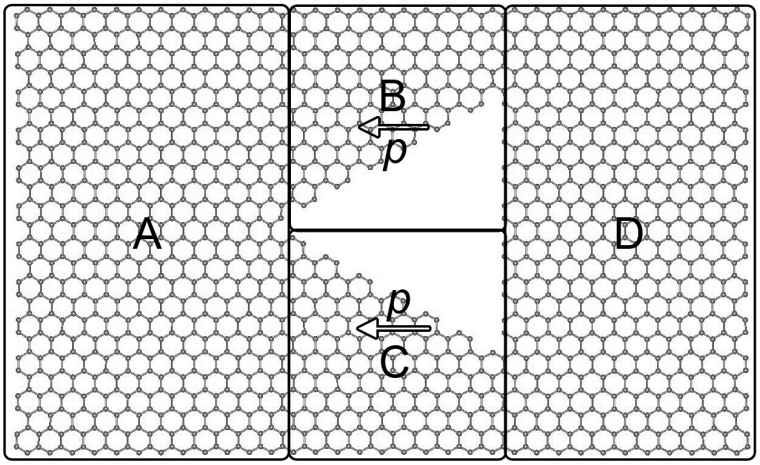

Figure II.5: Graphene divided into four pieces marked with A, B, C, D with p meaning dipole moment.

II.7 Conclusions

Using a numerical differentiation method, we found, in the particular case of the interaction between two carbon atoms, that the forces between these atoms at electrostatic equilibrium could be computed either by taking into account the gradients of $\{q_\alpha^*\}$, $\{\vec{p}_\alpha^*\}$ and λ^* in an expression of energy simplified to take into account the equations valid at electrostatic equilibrium, or by not taking them into account when differenciating the full expression of energy, valid even out of electrostatic equilibrium. We then showed how to compute gradients of $\{q_\alpha^*\}$, $\{\vec{p}_\alpha^*\}$ and λ^* by solving linear systems with the same system matrix as the one used to get $\{q_\alpha^*\}$, $\{\vec{p}_\alpha^*\}$ and λ^*). We then showed analytically, using a supermatrix formulation, that the resulting forces were the same as the ones obtained from the gradient of the non-simplified general expression for the energy, without using any gradient of charge or dipole (thus validating our simplified expression of the total energy of the system and our way to compute the gradients of effective charges and dipoles). We believe that this is the first time that such equivalence is reported.

Finally, using the charge dipole model and a definition of polarization including a charge term (unlike what was done in [Javvaji 18]), we computed the in-plane piezoelectric coefficient for trapezium-shaped graphene and graphene with triangular or circular defects. We found results significantly different from those obtained by Javvaji *et al.* in [Javvaji 18]. We thus believe that our computed results are physically more meaningful, even if we think that using different parameters for carbon atoms with different numbers of nearest neighbors and enforcing charge conservation, would give even more meaningful results.

In chapter 4, we will use again this improved definition of polarization and add charge conservation to compute the flexoelectric coefficients for monolayer MoS_2 and see that our results compare better to reported experimental results than those published in another paper by the same Hannover group. However, before that,

we will describe out attempt to find an analytical formula for the flexoelectric coefficients of an ionic 2D material, using an extended Cauchy-Born rule to bridge continuum electromechanics and atomistic electromechanics.

Chapter III

Study of the flexoelectricity of MoS_2 through the development of multi-scale algorithms mixing atomistic approach and continuum physics

III.1 Introduction 46
III.2 Representative volume elements 46
III.3 Use of an extended Cauchy-Born rule 47
III.4 Derivation of analytical formula for computation of flexocoupling coefficients 49
III.5 Results and Discussion 56
III.6 Conclusion 60

III.1 Introduction

In 2018, G. Lecoutre et al[Lecoutre 18] derived a constitutive equation, with which the expression for flexocoupling coefficients f_{ijKL} (see below) can be obtained, by applying the principle of virtual powers and classical thermodynamics:

$$f_{ijKL} = \frac{1}{V}\frac{\partial^2 U_{elec}}{\partial P_i \partial G_{jKL}} = -\frac{\partial {}^L E_i}{\partial G_{jKL}} \tag{III.1}$$

where $\partial^2 U_{elec}/\partial P_i \partial G_{jKL}$ represents the variation of the electrostatic part of of the interaction energies between constituents, in a given volume V, due to variations of polarization component P_i and second-order deformation gradient component G_{iKL}. ${}^L E_i$ is the i^{th} component of the local electric field.

Based on equation III.1, an analytic expression for the flexocoupling tensor (see equation III.2) has also been obtained by G. Lecoutre thanks to the use of an extended Cauchy-Born homogenization hypothesis[Sunyk 03] and an atomic model with distributed induced and permanent dipoles. This analytic formula was used to compute the flexocoupling tensor for various carbon nanotubes[Lecoutre 18], which at first order was found to be equal to:

$$f_{ijKL} = \frac{1}{2n}\sum_{\lambda=1}^{n}\sum_{k=1}^{3}\left[\sum_{\alpha=1}^{n}\sum_{\beta=1}^{n}\left(\nabla_j^\lambda T^{(2)}\left(\vec{r}^{\alpha},\vec{r}^{\beta}\right)\right)_{ik}\left(\mu_k^\beta\right) + \left(T^{(2)}\left(\vec{r}^{\alpha},\vec{r}^{\beta}\right)\right)_{ik}\left(\nabla_j^\lambda \mu_k^\beta\right)\right] R_K^\lambda R_L^\lambda \tag{III.2}$$

where, n is the total number of atoms in a Representative Volume Element (RVE) to be defined in next paragraph. The four indices i, j, K, L represent components x, y, z of cartesian coordinate with uppercase letters when in the deformed coordinate system, and lowercase letters when in the undeformed coordinate system. $T^{(2)}\left(\vec{r}^{\alpha},\vec{r}^{\beta}\right)$ is a second order interaction tensor between dipoles located at $\vec{r}^{\alpha}$ and $\vec{r}^{\beta}$. μ_k^β is component k of the permanent dipole on atom β. R_K^λ and R_L^λ are coordinates in the undeformed coordinate system of atom λ. In this chapter, we extend that approach to incorporate effective charges for computing the flexoelectric coefficient of a MoS_2 monolayer.

III.2 Representative volume elements

For a macroscopic heterogeneous material, it is impossible to simulate or calculate the properties of the entire material at the atomistic level, due to the limitation of computational resources and time. It becomes particularly important to find a region in the material that can represent the properties of the entire material. Historically, the definition of a representative volume element (RVE) was first given by Hill[Hill 63], according to which, RVE must contain a sufficiently large number of atoms and structurally represent the properties of the entire system.

In continuum physics, the RVE concept plays a critical role in the computation of mechanical properties, electromechanical properties and other averaged quantities that are used to describe physical systems constituted with several materials. Defining RVE can be quite complicated for heterogeneous materials such as composite materials, but it is simpler for homogeneous materials with a periodic structure, such as, for example, a perfect single crystal. Actually, the unit cell is always chosen as RVE in homogeneous crystalline materials such as 2D MoS_2. Fig.III.1 shows a unit cell of MoS_2 as RVE extracted from large MoS_2.

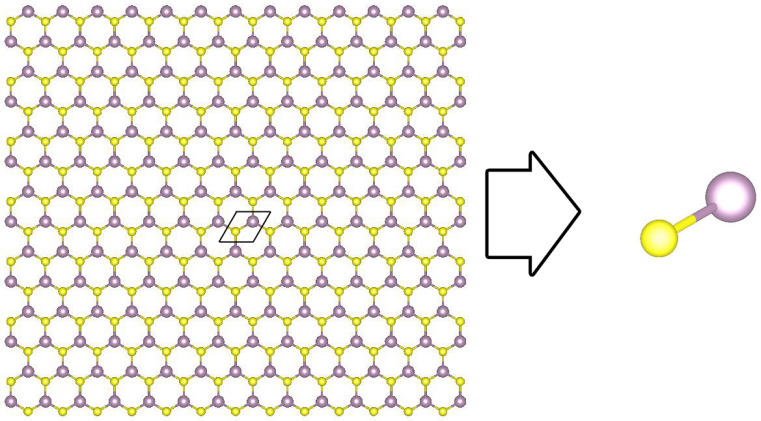

Figure III.1: Representative volume element of MoS_2, with 3 atoms (1 Mo, and 2S on top of one another)

III.3 Use of an extended Cauchy-Born rule

In our calculations, we will make the approximation that the deformation of the whole monolayer is characterized by a single second order transformation gradient which corresponds to an extended Cauchy-Born hypothesis.

Let us name $\boldsymbol{\mathcal{F}}$ the mapping between the coordinates of the atoms in the undeformed ($\vec{R}$) and deformed ($\vec{r}$) configurations:

$$\forall \alpha = 1, ..., N \qquad \vec{r}^{\alpha} = \boldsymbol{\mathcal{F}}(\vec{R}^{\alpha}) \tag{III.3}$$

with r^{α} and R^{α}, the positions of the α^{th} atom in the deformed and undeformed configurations, respectively. Now, if we turn our attention to vectors between atoms (cf. Fig.III.2), we can write:

$$\forall \alpha, \beta = 1, ..., N \qquad \vec{r}^{\alpha\beta} = \boldsymbol{\mathcal{F}}(\vec{R}^{\alpha} + \vec{R}^{\alpha\beta}) - \boldsymbol{\mathcal{F}}(\vec{R}^{\alpha}) \tag{III.4}$$

with $\vec{R}^{\alpha\beta} = \vec{R}^{\beta} - \vec{R}^{\alpha}$ and $\vec{r}^{\alpha\beta} = \vec{r}^{\beta} - \vec{r}^{\alpha}$.

The local Cauchy-Born rule states that this mapping can be approximated to be linear in a representative volume element (RVE), characterized by a local deformation gradient characteristic of that RVE, so that the deformation is assumed to

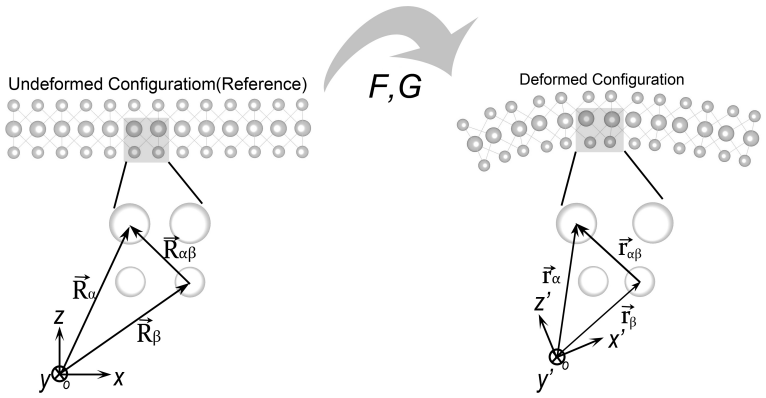

Figure III.2: Illustration of the extended Cauchy-Born rule. F and G are respectively the first-order and second-order transformation gradients, in a mechanical continuum.

be the same for all the atoms in the RVE (see ref[Falk 98] and ref[Javvaji 17] for a numerical scheme to compute the local strain in such a case). In the extended Cauchy-Born rule, the Taylor expansion of the mapping $\boldsymbol{\mathcal{F}}$ is pushed one step further and it is the second order transformation gradient that is assumed to be constant in the RVE. This corresponds to the following approximation:

$$\vec{r}^{\alpha\beta} = \nabla_R \boldsymbol{\mathcal{F}}(\vec{R}^{\alpha}) \cdot \vec{R}^{\alpha\beta} + \frac{1}{2} \nabla_R \nabla_R \boldsymbol{\mathcal{F}}(\vec{R}^{\alpha}) : (\vec{R}^{\alpha\beta} \otimes \vec{R}^{\alpha\beta}) \tag{III.5}$$

where the transformation gradient $F = \nabla_{\vec{R}} \boldsymbol{\mathcal{F}}(\vec{R}^{\alpha})$ is a second order tensor with 9 tensor components and the second order transformation gradient (related to the strain gradient) $G = \nabla_{\vec{R}} \nabla_{\vec{R}} \boldsymbol{\mathcal{F}}(\vec{R}^{\alpha})$ is a third order tensor with 27 tensor components, '$\cdot$' denotes the scalar product, ':' denotes the contraction on two indices, here between a third rank tensor and a second rank tensor, and '$\otimes$' is the standard tensor product. Using cartesian coordinates $(1:x, 2:y, 3:z)$, this can be restated as:

$$\forall i = 1,2,3, \qquad r_i^{\alpha\beta} = F_{iJ} R_J^{\alpha\beta} + \frac{1}{2} G_{iJK} R_J^{\alpha\beta} R_K^{\alpha\beta} \tag{III.6}$$

with summation from 1 to 3, on indices J and K being implied, following Einstein's convention.

Equation III.6 gives an explicit expression for the deformed interatomic displacement vector and bridges the gap between microscopic and macroscopic quantities. Note that higher order terms are omitted in Eq.III.6.

III.4 Derivation of analytical formula for computation of flexocoupling coefficients

The total energy for QP model for MoS_2 in the absence of external electric potential and field is written as:

$$U^{elec} = \frac{1}{2}\sum_{\alpha=1}^{N}\sum_{\beta=1}^{N} q_\alpha T^{(0,0)}_{q-q}\left(\vec{r^\alpha},\vec{r^\beta}\right) q^\beta - \frac{1}{2}\sum_{\alpha=1}^{N}\sum_{\beta=1}^{N} \vec{p^\alpha}\cdot T^{(1,0)}_{p-q}\left(\vec{r^\alpha},\vec{r^\beta}\right) q^\beta + \frac{1}{2}\sum_{\alpha=1}^{N}\sum_{\beta=1}^{N} q^\alpha T^{(0,1)}_{q-p}\left(\vec{r^\alpha},\vec{r^\beta}\right)\cdot\vec{p^\beta} - \frac{1}{2}\sum_{\alpha=1}^{N}\sum_{\beta=1}^{N} \vec{p^\alpha}\cdot T^{(1,1)}_{p-p}\left(\vec{r^\alpha},\vec{r^\beta}\right)\cdot\vec{p^\beta} + \sum_{\alpha=1}^{N} q^\alpha\chi^\alpha \tag{III.7}$$

with $T^{0,0}_{q-q}(\vec{r^\alpha},\vec{r^\alpha}) = \frac{1}{4\pi\epsilon_0}\frac{\sqrt{2/\pi}}{R_\alpha}$, $T^{(1,0)}_{p-q}(\vec{r^\alpha},\vec{r^\alpha}) = T^{(0,1)}_{q-p}(\vec{r^\alpha},\vec{r^\alpha}) = 0$ and $T^{(1,1)}_{p-p}(\vec{r^\alpha},\vec{r^\alpha}) = -\frac{1}{4\pi\epsilon_0}\frac{\sqrt{2/\pi}}{3R^3_\alpha}$, with R_α being the characteristic radius of the radial Gaussian charge distribution of atom α

The total electrostatic internal energy due to the induced effective charges and dipoles in a RVE containing n atoms can then be written as:

$$U^{RVE,int,ind} = \frac{1}{2}\sum_{\alpha=1}^{n}\sum_{\beta=1}^{n} q^\alpha T^{(0,0)}_{q-q}\left(\vec{r^\alpha},\vec{r^\beta}\right) q^\beta - \frac{1}{2}\sum_{\alpha=1}^{n}\sum_{\beta=1}^{n} \vec{p^\alpha}\cdot T^{(1,0)}_{p-q}\left(\vec{r^\alpha},\vec{r^\beta}\right) q^\beta + \frac{1}{2}\sum_{\alpha=1}^{n}\sum_{\beta=1}^{n} q^\alpha T^{(0,1)}_{q-p}\left(\vec{r^\alpha},\vec{r^\beta}\right)\cdot\vec{p^\beta} - \frac{1}{2}\sum_{\alpha=1}^{n}\sum_{\beta=1}^{n} \vec{p^\alpha}\cdot T^{(1,1)}_{p-p}\left(\vec{r^\alpha},\vec{r^\beta}\right)\cdot\vec{p^\beta} + \sum_{\alpha=1}^{n} q^\alpha\chi^\alpha \tag{III.8}$$

which, using $T^{(1,0)}_{p-q}\left(\vec{r^\alpha},\vec{r^\beta}\right) = -T^{(0,1)}_{q-p}\left(\vec{r^\beta},\vec{r^\alpha}\right)$ simplifies into:

$$U^{RVE,int,ind} = \frac{1}{2}\sum_{\alpha=1}^{n}\sum_{\beta=1}^{n} q^\alpha T^{(0,0)}_{q-q}\left(\vec{r^\alpha},\vec{r^\beta}\right) q^\beta - \sum_{\alpha=1}^{n}\sum_{\beta=1}^{n} \vec{p^\alpha}\cdot T^{(1,0)}_{p-q}\left(\vec{r^\alpha},\vec{r^\beta}\right) q^\beta - \frac{1}{2}\sum_{\alpha=1}^{n}\sum_{\beta=1}^{n} \vec{p^\alpha}\cdot T^{(1,1)}_{p-p}\left(\vec{r^\alpha},\vec{r^\beta}\right)\cdot\vec{p^\beta} + \sum_{\alpha=1}^{n} q^\alpha\chi^\alpha \tag{III.9}$$

Additionaly, the total polarization in RVE can be expressed as:

$$\vec{P} = \sum_{\alpha=1}^{n}\frac{1}{V_{RVE}}\left(q^\alpha\cdot(\vec{r^\alpha}-\vec{r_c}) + \vec{p^\alpha}\right) \tag{III.10}$$

with V_{RVE} being the volume of RVE and $\vec{r_c}$ denoting the center of charges in RVE.

In order to further deduce an atomistic expression for the flexoelectric tensor, we first define the effective local electric field in the continuum approximation (Eq. III.11), then use the chain rule of derivation and the atomistic definitions of polarization (Eq. III.10) and internal induced electrostatic energy volume density (Eq. III.9) to express the connections between the atomic quantities and the

continuum ones (Eqs. III.12 and III.13):

$$\begin{aligned} E_k^L &= -\frac{1}{V_{RVE}}\left(\frac{\partial U^{RVE,\text{ int,ind}}(\{\boldsymbol{p}\},\{q\},\{\boldsymbol{r}\})}{\partial P_k}\right) \\ &= -\frac{1}{V_{RVE}}\left[\sum_{i=1}^{3}\sum_{\alpha=1}^{n}\frac{\partial U^{RVE,int,ind}(\{\boldsymbol{p}\},\{q\},\{\boldsymbol{r}\})}{\partial p_i^\alpha}\frac{\partial p_i^\alpha}{\partial P_k}+\sum_{\alpha=1}^{n}\frac{\partial U^{RVE,int,ind}(\{\boldsymbol{p}\},\{q\},\{\boldsymbol{r}\})}{\partial q^\alpha}\frac{\partial q^\alpha}{\partial P_k}\right. \\ &\quad \left.+\sum_{i=1}^{3}\sum_{\alpha=1}^{n}\frac{\partial U^{RVE,\ int,ind}(\{\boldsymbol{p}\},\{q\},\{\boldsymbol{r}\})}{\partial r_i^\alpha}\frac{\partial r_i^\alpha}{\partial P_k}\right] \end{aligned} \tag{III.11}$$

where,

$$\begin{aligned} \left(\frac{\partial p_i^\alpha}{\partial P_k}\right)_{\{q\}\{\boldsymbol{r}\}\left\{\vec{p}^{\beta\neq\alpha}\right\}} &= V_{RVE}\cdot\delta_{ki} \\ \left(\frac{\partial q^\alpha}{\partial P_k}\right)_{\left\{q^{\beta\neq\alpha}\right\}\{\boldsymbol{r}\}\{\boldsymbol{p}\}} &= \frac{V_{RVE}}{r_k^\alpha - r_{c,k}} \\ \left(\frac{\partial r_i^\alpha}{\partial P_k}\right)_{\{q\}\left\{\vec{r}^{\beta\neq\alpha}\right\}\{\boldsymbol{p}\}} &= \frac{V_{RVE}}{q^\alpha}\cdot\delta_{ki} \end{aligned} \tag{III.12}$$

$$\begin{aligned} \frac{\partial U^{RVE,int,ind}(\{\vec{p}\},\{q\},\{\vec{r}\})}{\partial p_i^\alpha} &= \sum_{\beta=1}^{n}\sum_{j=1}^{3}\left[T_{p-p}^{(1,1)}\left(\vec{r}^{\,\alpha},\vec{r}^{\,\beta}\right)\right]_{ij}p_j^\beta+\sum_{\beta=1}^{n}\left[T_{p-q}^{(1,0)}\left(\vec{r}^{\,\alpha},\vec{r}^{\,\beta}\right)\right]_i q^\beta \\ \frac{\partial U^{RVE,int,ind}(\{\vec{p}\},\{q\},\{\vec{r}\})}{\partial q^\alpha} &= \sum_{\beta=1}^{n}\sum_{j=1}^{3}\left[T_{p-q}^{(1,0)}\left(\vec{r}^{\,\alpha},\vec{r}^{\,\beta}\right)\right]_j p_j^\beta+\sum_{\beta=1}^{n}T_{q-q}^{(0,0)}\left(\vec{r}^{\,\alpha},\vec{r}^{\,\beta}\right)q^\beta+\chi^\alpha \\ \frac{\partial U^{RVE,int,ind}(\vec{p},q,\vec{r})}{\partial r_i^\alpha} &= \frac{1}{2}\sum_{\gamma=1}^{n}\sum_{\beta=1}^{n}\left(q^\gamma\nabla_i^\alpha T_{q-q}^{(0,0)}\left(\vec{r}^{\,\gamma},\vec{r}^{\,\beta}\right)q^\beta\right) \\ &\quad -\sum_{\gamma=1}^{n}\sum_{\beta=1,}^{n}\sum_{j=1}^{3}\left(p_j^\gamma\nabla_i^\alpha\left[T_{p-q}^{(1,0)}\left(\vec{r}^{\,\gamma},\vec{r}^{\,\beta}\right)\right]_j q^\beta\right) \\ &\quad -\frac{1}{2}\sum_{\gamma=1}^{n}\sum_{\beta=1}^{n}\sum_{j=1}^{3}\sum_{l=1}^{3}\left(p_j^\gamma\nabla_i^\alpha\left[T_{p-p}^{(1,1)}\left(\vec{r}^{\,\gamma},\vec{r}^{\,\beta}\right)\right]_{jl}p_l^\beta\right) \end{aligned} \tag{III.13}$$

where ∇_i^α is the derivative with respect to the component i of the position of atom α. Substituting formulas III.12 and III.13 into formula III.11, we have:

$$\begin{aligned}
E_k^L = -\sum_{\alpha=1}^{n} \Bigg\{ & \left[\sum_{\beta=1}^{n} \sum_{i=1}^{3} \left[T_{p-p}^{(1,1)} \left(\vec{r}^{\alpha}, \vec{r}^{\beta} \right) \right]_{ki} p_i^\beta + \sum_{\substack{\beta=1 \\ \beta \neq \alpha}}^{n} \left[T_{p-q}^{(1,0)} \left(\vec{r}^{\alpha}, \vec{r}^{\beta} \right) \right]_k q^\beta \right] \\
& + \left[\sum_{\substack{\beta=1 \\ \beta \neq \alpha}}^{n} \sum_{i=1}^{3} \left[T_{p-q}^{(1,0)} \left(\vec{r}^{\alpha}, \vec{r}^{\beta} \right) \right]_i p_i^\beta + \sum_{\beta=1}^{n} T_{q-q}^{(0,0)} \left(\vec{r}^{\alpha}, \vec{r}^{\beta} \right) q^\beta + \chi^\alpha \right] \frac{1}{r_k^\alpha - r_{c,k}} \\
& + \Bigg[\frac{1}{2} \sum_{\gamma=1}^{n} \sum_{\beta=1}^{n} q^\gamma \nabla_k^\alpha T_{q-q}^{(0,0)} \left(\vec{r}^{\gamma}, \vec{r}^{\beta} \right) q^\beta - \sum_{\gamma=1}^{n} \sum_{\substack{\beta=1 \\ \beta \neq \gamma}}^{n} \sum_{j=1}^{3} \left(p_j^\gamma \nabla_k^\alpha \left[T_{p-q}^{(1,0)} \left(\vec{r}^{\gamma}, \vec{r}^{\beta} \right) \right]_j q^\beta \right) \\
& - \frac{1}{2} \sum_{\gamma=1}^{n} \sum_{\beta=1}^{n} \sum_{j=1}^{3} \sum_{l=1}^{3} \left(p_j^\gamma \nabla_k^\alpha \left[T_{p-p}^{(1,1)} \left(\vec{r}^{\gamma}, \vec{r}^{\beta} \right) \right]_{jl} p_l^\beta \right) \Bigg] \frac{1}{q^\alpha} \Bigg\}
\end{aligned} \tag{III.14}$$

The last term (coming from the gradient of the energy, i.e. the opposite of the force) can be simplified, thanks to equation III.15 and similar formula for the other interaction tensors (Recall that we defined $T^{(1,0)} \left(\vec{r}^{\alpha}, \vec{r}^{\beta} \right) = -\vec{\nabla}^\alpha T^{(0,0)} \left(\vec{r}^{\alpha}, \vec{r}^{\beta} \right) = T^{(0,1)} \left(\vec{r}^{\alpha}, \vec{r}^{\beta} \right) = \vec{\nabla}^\beta T^{(0,0)} \left(\vec{r}^{\alpha}, \vec{r}^{\beta} \right)$, which leads to a sign difference with respect to the other common definition $T^{(1)}(\vec{R}) = \vec{\nabla}_R T^{(0)}(\vec{R})$ with $\vec{R} = \vec{r}^{\alpha} - \vec{r}^{\beta}$):

$$\nabla_i^\alpha T_{q-q}^{(0,0)} \left(\vec{r}^{\gamma}, \vec{r}^{\beta} \right) = -\delta_{\alpha\gamma} \left[T_{q-q}^{(1,0)} \left(\vec{r}^{\gamma}, \vec{r}^{\beta} \right) \right]_i + \delta_{\alpha\beta} \left[T_{q-q}^{(0,1)} \left(\vec{r}^{\gamma}, \vec{r}^{\beta} \right) \right]_i \tag{III.15}$$

$$\begin{aligned}
E_k^L = -\sum_{\alpha=1}^{n} \Bigg\{ & \left[\sum_{\beta=1}^{n} \sum_{i=1}^{3} \left[T_{p-p}^{(1,1)} \left(\vec{r}^{\alpha}, \vec{r}^{\beta} \right) \right]_{ki} p_i^\beta + \sum_{\substack{\beta=1 \\ \beta \neq \alpha}}^{n} \left[T_{p-q}^{(1,0)} \left(\vec{r}^{\alpha}, \vec{r}^{\beta} \right) \right]_k q^\beta \right] \\
& + \left[\sum_{\substack{\beta=1 \\ \beta \neq \alpha}}^{n} \sum_{i=1}^{3} \left[T_{p-q}^{(1,0)} \left(\vec{r}^{\alpha}, \vec{r}^{\beta} \right) \right]_i p_i^\beta + \sum_{\beta=1}^{n} T_{q-q}^{(0,0)} \left(\vec{r}^{\alpha}, \vec{r}^{\beta} \right) q^\beta + \chi^\alpha \right] \frac{1}{r_k^\alpha - r_{c,k}} \Bigg\} \\
& - \Bigg\{ \frac{1}{2} \sum_{\alpha=1}^{n} \frac{1}{q^\alpha} \sum_{\substack{\beta=1 \\ \beta \neq \alpha}}^{n} \left[-T_{q-q}^{(1,0)} \left(\vec{r}^{\alpha}, \vec{r}^{\beta} \right) \right]_k q^\alpha q^\beta + \frac{1}{2} \sum_{\alpha=1}^{n} \frac{1}{q^\alpha} \sum_{\substack{\gamma=1 \\ \gamma \neq \alpha}}^{n} \left[T_{q-q}^{(1,0)} \left(\vec{r}^{\gamma}, \vec{r}^{\alpha} \right) \right]_k q^\gamma q^\alpha \\
& - \sum_{\alpha=1}^{n} \frac{1}{q^\alpha} \sum_{\substack{\beta=1, \\ \beta \neq \alpha}}^{n} \sum_{j=1}^{3} \left[-T_{p-q}^{(2,0)} \left(\vec{r}^{\alpha}, \vec{r}^{\beta} \right) \right]_{kj} p_j^\alpha q^\beta - \sum_{\alpha=1}^{n} \frac{1}{q^\alpha} \sum_{\substack{\gamma=1, \\ \gamma \neq \alpha}}^{n} \sum_{j=1}^{3} \left[T_{p-q}^{(2,0)} \left(\vec{r}^{\gamma}, \vec{r}^{\alpha} \right) \right]_{kj} p_j^\gamma q^\alpha \\
& - \frac{1}{2} \sum_{\alpha=1}^{n} \frac{1}{q^\alpha} \sum_{\substack{\beta=1 \\ \beta \neq \alpha}}^{n} \sum_{j=1}^{3} \sum_{l=1}^{3} \left[T_{p-p}^{(2,1)} \left(\vec{r}^{\alpha}, \vec{r}^{\beta} \right) \right]_{kjl} p_j^\alpha p_l^\beta - \frac{1}{2} \sum_{\alpha=1}^{n} \frac{1}{q^\alpha} \sum_{\substack{\gamma=1 \\ \gamma \neq \alpha}}^{n} \sum_{j=1}^{3} \sum_{l=1}^{3} \left[T_{p-p}^{(2,1)} \left(\vec{r}^{\gamma}, \vec{r}^{\alpha} \right) \right]_{kjl} p_j^\gamma p_l^\alpha \Bigg\}
\end{aligned} \tag{III.16}$$

Using $T^{(1,0)}_{q-q}\left(\vec{r}^{\alpha},\vec{r}^{\beta}\right) = -T^{(1,0)}_{q-q}\left(\vec{r}^{\beta},\vec{r}^{\alpha}\right)$, $T^{(2,0)}_{p-q}\left(\vec{r}^{\alpha},\vec{r}^{\beta}\right) = T^{(2,0)}_{p-q}\left(\vec{r}^{\beta},\vec{r}^{\alpha}\right)$ and $T^{(2,1)}_{p-p}\left(\vec{r}^{\alpha},\vec{r}^{\beta}\right) = -T^{(2,1)}_{p-p}\left(\vec{r}^{\beta},\vec{r}^{\alpha}\right)$, this simplifies into:

$$
\begin{aligned}
E^L_k = -\sum_{\alpha=1}^{n}\Bigg\{ & \left[\sum_{\beta=1}^{n}\sum_{i=1}^{3}\left[T^{(1,1)}_{p-p}\left(\vec{r}^{\alpha},\vec{r}^{\beta}\right)\right]_{ki} p_i^{\beta} + \sum_{\substack{\beta=1\\ \beta\neq\alpha}}^{n}\left[T^{(1,0)}_{q-q}\left(\vec{r}^{\alpha},\vec{r}^{\beta}\right)\right]_{k} q^{\beta}\right] \\
& + \left[\sum_{\substack{\beta=1\\ \beta\neq\alpha}}^{n}\sum_{i=1}^{3}\left[T^{(1,0)}_{p-q}\left(\vec{r}^{\alpha},\vec{r}^{\beta}\right)\right]_{i} p_i^{\beta} + \sum_{\beta=1}^{n} T^{(0,0)}_{q-q}\left(\vec{r}^{\alpha},\vec{r}^{\beta}\right) q^{\beta} + \chi^{\alpha}\right]\frac{1}{r^{\alpha}_k - r_{c,k}}\Bigg\} \\
& - \left[-\sum_{\alpha=1}^{n}\sum_{\substack{\beta=1\\ \beta\neq\alpha}}^{n}\left[T^{(1,0)}_{q-q}\left(\vec{r}_{\alpha,},\vec{r}^{\beta}\right)\right]_{k} q^{\beta} + \sum_{\alpha=1}^{n}\frac{1}{q^{\alpha}}\sum_{\substack{\beta=1\\ \beta\neq\alpha}}^{n}\sum_{j=1}^{3}\sum_{l=1}^{3}\left(T^{(2,1)}_{p-p}\left[\vec{r}^{\alpha},\vec{r}^{\beta}\right)\right]_{kjl} p_j^{\alpha} p_l^{\beta}\right]
\end{aligned}
\tag{III.17}
$$

If we take the same Gaussian radii for charges and dipoles, then $\left[T^{(1,0)}_{q-q}\left(\vec{r}^{\alpha},\vec{r}^{\beta}\right)\right]_i = \left[T^{(1,0)}_{p-q}\left(\vec{r}^{\alpha},\vec{r}^{\beta}\right)\right]_i$ and there is a further simplification:

$$
\begin{aligned}
E^L_k = & -\sum_{\alpha=1}^{n}\sum_{\beta=1}^{n}\sum_{i=1}^{3}\left[T^{(1,1)}_{p-p}\left(\vec{r}^{\alpha},\vec{r}^{\beta}\right)\right]_{ki} p_i^{\beta} - \sum_{\alpha=1}^{n}\frac{1}{r^{\alpha}_k - r_{c,k}}\left(\sum_{\substack{\beta=1\\ \beta\neq\alpha}}^{n}\sum_{i=1}^{3}\left[T^{(1,0)}_{p-q}\left(\vec{r}^{\alpha},\vec{r}^{\beta}\right)\right]_{i} p_i^{\beta}\right. \\
& \left. + \sum_{\beta=1}^{n} T^{(0,0)}_{q-q}\left(\vec{r}^{\alpha},\vec{r}^{\beta}\right)\cdot q^{\beta} + \chi^{\alpha}\right) - \sum_{\alpha=1}^{n}\frac{1}{q^{\alpha}}\sum_{\substack{\beta=1\\ \beta\neq\alpha}}^{n}\sum_{j=1}^{3}\sum_{l=1}^{3}\left[T^{(2,1)}_{p-p}(\vec{r}^{\alpha},\vec{r}^{\beta})\right]_{kjl} p_j^{\alpha} p_l^{\beta}.
\end{aligned}
\tag{III.18}
$$

Now we have to compute $\frac{\partial E^L_i}{\partial r^{\alpha}_j}$

$$
\begin{aligned}
\frac{\partial E^L_i}{\partial r^{\alpha}_j} = \nabla^{\alpha}_j\Big\{ & -\sum_{\gamma=1}^{n}\sum_{\beta=1}^{n}\sum_{l=1}^{3}\left[T^{(1,1)}_{p-p}\left(\vec{r}^{\alpha},\vec{r}^{\beta}\right)\right]_{il} p_l^{\beta} \\
& - \sum_{\gamma=1}^{n}\frac{1}{r^{\gamma}_i - r_{c,i}}\left(\sum_{\substack{\beta=1\\ \beta\neq\alpha}}^{n}\sum_{l=1}^{3}\left[T^{(1,0)}_{p-q}\left(\vec{r}^{\gamma},\vec{r}^{\beta}\right)\right]_{l} p_l^{\beta} + \sum_{\beta=1}^{n} T^{(0,0)}_{q-q}\left(\vec{r}^{\gamma},\vec{r}^{\beta}\right) q^{\beta} + \chi^{\gamma}\right) \\
& - \sum_{\gamma=1}^{n}\frac{1}{q^{\gamma}}\sum_{\substack{\beta=1\\ \beta\neq\gamma}}^{n}\sum_{k=1}^{3}\sum_{l=1}^{3}\left[T^{(2,1)}_{p-p}\left(\vec{r}^{\gamma},\vec{r}^{\beta}\right)\right]_{ikl} p_k^{\gamma} p_l^{\beta}\Big\}
\end{aligned}
\tag{III.19}
$$

Using equation III.15, $\frac{\partial E_i^L}{\partial r_j^\alpha}$ can be further simplified as:

$$\begin{aligned}
\frac{\partial E_i^L}{\partial r_j^\alpha} &= \sum_{\substack{\beta=1\\\beta\neq\alpha}}^{n}\sum_{l=1}^{3}\left[T_{p-p}^{(2,1)}\left(\vec{r}^{\alpha},\vec{r}^{\beta}\right)\right]_{jil} p_l^\beta - \sum_{\substack{\gamma=1\\\gamma\neq\alpha}}^{n}\sum_{l=1}^{3}\left[T_{p-p}^{(2,1)}\left(\vec{r}^{\gamma},\vec{r}^{\alpha}\right)\right]_{jil} p_l^\alpha \\
&+ \left(\frac{1}{r_i^\alpha - r_{c,i}}\right)^2 \delta_{ij}\left(\sum_{\substack{\beta=1\\\beta\neq\alpha}}^{n}\sum_{l=1}^{3}\left[T_{p-q}^{(1,0)}\left(\vec{r}^{\alpha},\vec{r}^{\beta}\right)\right]_{l} p_l^\beta + \sum_{\beta=1}^{n} T_{q-q}^{(0,0)}\left(\vec{r}^{\alpha},\vec{r}^{\beta}\right) q^\beta + \chi^\alpha\right) \\
&+ \frac{1}{r_i^\alpha - r_{c,i}}\sum_{\substack{\beta=1\\\beta\neq\alpha}}^{n}\left(\sum_{l=1}^{3}\left[T_{p-q}^{(2,0)}\left(\vec{r}^{\alpha},\vec{r}^{\beta}\right)\right]_{jl} p_l^\beta + \left[T_{q-q}^{(1,0)}\left(\vec{r}^{\alpha},\vec{r}^{\beta}\right)\right]_{j} q^\beta\right) \\
&- \sum_{\substack{\gamma=1\\\gamma\neq\alpha}}^{n}\frac{1}{r_i^\gamma - r_{c,i}}\left(\sum_{l=1}^{3}\left[T_{p-q}^{(2,0)}\left(\vec{r}^{\gamma},\vec{r}^{\alpha}\right)\right]_{jl} p_l^\alpha + \left[T_{q-q}^{(1,0)}\left(\vec{r}^{\gamma},\vec{r}^{\alpha}\right)\right]_{j} q^\alpha\right) \\
&+ \frac{1}{q^\alpha}\sum_{\substack{\beta=1\\\beta\neq\alpha}}^{n}\sum_{k=1}^{3}\sum_{l=1}^{3}\left[T_{p-p}^{(3,1)}\left(\vec{r}^{\alpha},\vec{r}^{\beta}\right)\right]_{jikl} p_k^\alpha p_l^\beta - \sum_{\substack{\gamma=1\\\gamma\neq\alpha}}^{n}\frac{1}{q^\gamma}\sum_{k=1}^{\beta}\sum_{l=1}^{3}\left[T_{p-p}^{(3,1)}\left(\vec{r}^{\gamma},\vec{r}^{\alpha}\right)\right]_{jikl} p_k^\gamma p_l^\alpha
\end{aligned} \tag{III.20}$$

Now, recalling Eq. III.1, we have:

$$f_{ijKL} = -\frac{\partial E_i^L}{\partial G_{jKL}} = -\sum_{\alpha=1}^{n}\sum_{k=1}^{3}\frac{\partial E_i^L}{\partial r_k^\alpha}\frac{\partial r_k^\alpha}{\partial G_{jKL}} = -\sum_{\alpha=1}^{n}\frac{\partial E_i^L}{\partial r_j^\alpha}\times\frac{(R_K^\alpha - R_{c,K})(R_L^\alpha - R_{c,L})}{2} \tag{III.21}$$

since $\forall\alpha \in RVE, r_k^\alpha - r_{c,k} = \sum_{J=1}^{3} F_{kJ}(R_J^\alpha - R_{c,J}) + \frac{1}{2}\sum_{J=1}^{3}\sum_{K=1}^{3} G_{kKL}(R_K^\alpha - R_{c,K})(R_L^\alpha - R_{c,L})$ so that $\frac{\partial r_k^\alpha}{\partial G_{jKL}} = \frac{(R_K^\alpha - R_{c,K})(R_L^\alpha - R_{c,L})}{2}\delta_{kj}$

Finally,

$$
\begin{aligned}
f_{ijKL} = &- \sum_{\alpha=1}^{n} \sum_{\substack{\beta=1 \\ \beta\neq\alpha}}^{n} \sum_{l=1}^{3} \left[T_{p-p}^{(2,1)} \left(\vec{r}^{\alpha}, \vec{r}^{\beta} \right) \right]_{jil} p_l^{\beta} \frac{(R_K^{\alpha} - R_{c,K})(R_L^{\alpha} - R_{c,L})}{2} \\
&- \sum_{\alpha=1}^{n} \sum_{\substack{\gamma=1 \\ \beta\neq\alpha}}^{n} \sum_{l=1}^{3} \left[T_{p-p}^{(2,1)} \left(\vec{r}^{\alpha}, \vec{r}^{\beta} \right) \right]_{jil} p_l^{\alpha} \frac{(R_K^{\alpha} - R_{c,K})(R_L^{\alpha} - R_{c,L})}{2} \\
&- \sum_{\alpha=1}^{n} \left(\frac{1}{r_i^{\alpha} - r_{c,i}} \right)^2 \delta_{ij} \begin{pmatrix} \sum_{\substack{\beta=1 \\ \beta\neq\alpha}}^{n} \sum_{l=1}^{3} \left[T_{p-q}^{(1,0)} \left(\vec{r}^{\alpha}, \vec{r}^{\beta} \right) \right]_l p_l^{\beta} \\ + \sum_{\beta=1}^{n} T_{q-q}^{(0,0)} \left(\vec{r}^{\alpha}, \vec{r}^{\beta} \right) q^{\beta} + \chi^{\alpha} \end{pmatrix} \frac{(R_K^{\alpha} - R_{c,K})(R_L^{\alpha} - R_{c,L})}{2} \\
&- \sum_{\alpha=1}^{n} \frac{1}{r_i^{\alpha} - r_{c,i}} \sum_{\beta=1}^{n} \left(\sum_{l=1}^{3} \left[T_{p-q}^{(2,0)} \left(\vec{r}^{\alpha}, \vec{r}^{\beta} \right) \right]_{jl} p_l^{\beta} + \left[T_{p-q}^{(1,0)} \left(\vec{r}^{\alpha}, \vec{r}^{\beta} \right) \right]_j q^{\beta} \right) \frac{(R_K^{\alpha} - R_{c,K})(R_L^{\alpha} - R_{c,L})}{2} \\
&+ \sum_{\alpha=1}^{n} \sum_{\substack{\beta=1 \\ \beta\neq\alpha}}^{n} \frac{1}{r_i^{\beta} - r_{c,i}} \left(\sum_{l=1}^{\beta} \left[T_{p-q}^{(2,0)} \left(\vec{r}^{\alpha}, \vec{r}^{\beta} \right) \right]_{jl} p_l^{\alpha} - \left[T_{p-q}^{(1,0)} \left(\vec{r}^{\alpha}, \vec{r}^{\beta} \right) \right]_j q^{\alpha} \right) \frac{(R_K^{\alpha} - R_{c,K})(R_L^{\alpha} - R_{c,L})}{2} \\
&- \sum_{\alpha=1}^{n} \frac{1}{q^{\alpha}} \sum_{\substack{\beta=1 \\ \beta\neq\alpha}}^{n} \sum_{k=1}^{3} \sum_{l=1}^{3} \left[T_{p-p}^{(3,1)} \left(\vec{r}^{\alpha}, \vec{r}^{\beta} \right) \right]_{jikl} p_k^{\alpha} p_l^{\beta} \frac{(R_K^{\alpha} - R_{c,K})(R_L^{\alpha} - R_{c,L})}{2} \\
&+ \sum_{\alpha=1}^{n} \sum_{\substack{\beta=1 \\ \beta\neq\alpha}}^{n} \frac{1}{q^{\beta}} \sum_{k=1}^{3} \sum_{l=1}^{3} \left[T_{p-p}^{(3,1)} \left(\vec{r}^{\alpha}, \vec{r}^{\beta} \right) \right]_{jikl} p_k^{\beta} p_l^{\alpha} \frac{(R_K^{\alpha} - R_{c,K})(R_L^{\alpha} - R_{c,L})}{2}
\end{aligned}
\tag{III.22}
$$

Equation III.22 is the final derived expression for computing the flexocoupling tensor f_{ijKL} for an ionic material such as MoS_2. However, in order to compute the flexoelectric coefficients which are usually used in experiments and theory, we have to compute the susceptibility tensor $\chi_{im} = \epsilon_0^{-1} \partial P_i / \partial E_m$ of MoS_2 that can link the flexocoupling coefficients with the flexoelectric coefficients, since $\mu_{ijkl} = \varepsilon_0 \chi_{im} f_{mjkl}$, since we defined $\Delta P_i = \mu_{ijkl} u_{j,kl}$.

In our case, the easiest to write is not $\partial P_i / \partial E_m$, but $\frac{\partial E_i^L}{\partial P_j}$. We therefore proceed to write its explicit expression:

$$
\begin{aligned}
\frac{\partial E_i^L}{\partial P_j} = &\sum_{k=1}^{3} \sum_{\alpha=1}^{n} \frac{\partial E_i^L(\{\vec{p}\},\{q\},\{\vec{r}\})}{\partial p_k^{\alpha}} \frac{\partial p_k^{\alpha}}{\partial P_j} + \sum_{\alpha=1}^{n} \frac{\partial E_i^L(\{\vec{p}\},\{q\},\{\vec{r}\})}{\partial q^{\alpha}} \frac{\partial q^{\alpha}}{\partial P_j} \\
&+ \sum_{k=1}^{3} \sum_{\alpha=1}^{n} \frac{\partial E_i^L(\{\vec{p}\},\{q\},\{\vec{r}\})}{\partial r_k^{\alpha}} \frac{\partial r_k^{\alpha}}{\partial P_j}
\end{aligned}
\tag{III.23}
$$

in which, $\frac{\partial E_i^L(\{\boldsymbol{p}\},\{q\},\{\boldsymbol{r}\})}{\partial p_j^\alpha}$ and $\frac{\partial E_i^L(\{\boldsymbol{p}\},\{q\},\{\boldsymbol{r}\})}{\partial q^\alpha}$ can be derived as follow:

$$\begin{aligned}
&\frac{\partial E_i^L(\{\boldsymbol{p}\},\{q\},\{\boldsymbol{r}\})}{\partial p_j^\alpha} \\
&= -\sum_{\beta=1}^{n}\left[T_{p-p}^{(1,1)}\left(\vec{r}^{\,\beta},\vec{r}^{\,\alpha}\right)\right]_{ij} - \sum_{\beta=1}^{n}\frac{1}{r_i^\beta - r_{c,i}}\left[T_{p-q}^{(1,0)}\left(\vec{r}^{\,\beta},\vec{r}^{\,\alpha}\right)\right]_j \\
&- \frac{1}{q^\alpha}\sum_{\substack{\beta=1\\\beta\neq\alpha}}^{n}\sum_{l=1}^{3}\left[T_{p-p}^{(2,1)}\left(\vec{r}^{\,\alpha},\vec{r}^{\,\beta}\right)\right]_{ijl} p_l^\beta - \sum_{\substack{\beta=1\\\beta\neq\alpha}}^{n}\frac{1}{q^\beta}\sum_{l=1}^{3}\left[T_{p-p}^{(2,1)}\left(\vec{r}^{\,\beta},\vec{r}^{\,\alpha}\right)\right]_{ilj} p_l^\alpha \\
&= -\sum_{\beta=1}^{n}\left[T_{p-p}^{(1,1)}\left(\vec{r}^{\,\alpha},\vec{r}^{\,\beta}\right)\right]_{ij} + \sum_{\beta=1}^{n}\frac{1}{r_i^\beta - r_{c,i}}\left[T_{p-q}^{(1,0)}\left(\vec{r}^{\,\alpha},\vec{r}^{\,\beta}\right)\right]_j \\
&- \frac{1}{q^\alpha}\sum_{\substack{\beta=1\\\beta\neq\alpha}}^{n}\sum_{l=1}^{3}\left[T_{p-p}^{(2,1)}\left(\vec{r}^{\,\alpha},\vec{r}^{\,\beta}\right)\right]_{ijl} p_l^\beta + \sum_{\substack{\beta=1\\\beta\neq\alpha}}^{n}\frac{1}{q^\beta}\sum_{l=1}^{3}\left[T_{p-p}^{(2,1)}\left(\vec{r}^{\,\alpha},\vec{r}^{\,\beta}\right)\right]_{ilj} p_l^\alpha
\end{aligned} \tag{III.24}$$

$$\begin{aligned}
\frac{\partial E_i^L(\{\boldsymbol{p}\},\{q\},\{\boldsymbol{r}\})}{\partial q^\alpha} &= -\sum_{\beta=1}^{n}\frac{1}{r_i^\beta - r_{c,i}} T_{q-q}^{(0,0)}\left(\vec{r}^{\,\beta},\vec{r}^{\,\alpha}\right) + \left(\frac{1}{q^\alpha}\right)^2 \sum_{\substack{\beta=1\\\beta\neq\alpha}}^{n}\sum_{j=1}^{3}\sum_{l=1}^{3}\left[T_{p-p}^{(2,1)}\left(\vec{r}^{\,\beta},\vec{r}^{\,\alpha}\right)\right]_{ijl} p_j^\alpha p_l^\beta \\
&= -\sum_{\beta=1}^{n}\frac{1}{r_i^\beta - r_{c,i}} T_{q-q}^{(0,0)}\left(\vec{r}^{\,\alpha},\vec{r}^{\,\beta}\right) - \left(\frac{1}{q^\alpha}\right)^2 \sum_{\substack{\beta=1\\\beta\neq\alpha}}^{n}\sum_{j=1}^{3}\sum_{l=1}^{3}\left[T_{p-p}^{(2,1)}\left(\vec{r}^{\,\alpha},\vec{r}^{\,\beta}\right)\right]_{ijl} p_j^\alpha p_l^\beta
\end{aligned} \tag{III.25}$$

Substituting the formula III.25, III.24 and III.20 into formula III.23, we get:

$$\begin{aligned}
\frac{\partial E_i^L}{\partial P_j} =& V_{RVE}\left\{ -\sum_{\alpha=1}^{n}\sum_{\beta=1}^{n}\left[T_{p-p}^{(1,1)}\left(\vec{r}^{\alpha},\vec{r}^{\beta}\right)\right]_{ij} + \sum_{\alpha=1}^{n}\sum_{\substack{\beta=1\\\beta\neq\alpha}}^{n}\frac{1}{r_i^{\beta}-r_{c,i}}\left[T_{p-q}^{(1,0)}\left(\vec{r}^{\alpha},\vec{r}^{\beta}\right)\right]_{j}\right.\\
&-\sum_{\alpha=1}^{n}\frac{1}{q^{\alpha}}\sum_{\substack{\beta=1\\\beta\neq\alpha}}^{n}\sum_{l=1}^{3}\left[T_{p-p}^{(2,1)}\left(\vec{r}^{\alpha},\vec{r}^{\beta}\right)\right]_{ijl}p_l^{\beta} + \sum_{\alpha=1}^{n}\sum_{\substack{\beta=1\\\beta\neq\alpha}}^{n}\frac{1}{q^{\beta}}\sum_{l=1}^{n}\left[T_{p-p}^{(2,1)}\left(\vec{r}^{\alpha},\vec{r}^{\beta}\right)\right]_{ilj}p_l^{\alpha}\\
&-\sum_{\alpha=1}^{n}\sum_{\beta=1}^{n}\frac{1}{r_i^{\beta}-r_{c,i}}\frac{1}{r_j^{\alpha}-r_{c,j}}T_{q-q}^{(0,0)}\left(\vec{r}^{\alpha},\vec{r}^{\beta}\right) - \sum_{\alpha=1}^{n}\left(\frac{1}{q^{\alpha}}\right)^2\frac{1}{r_j^{\alpha}-r_{c,j}}\sum_{\substack{\beta=1\\\beta\neq\alpha}}^{n}\sum_{k=1}^{3}\sum_{\beta=\alpha}^{3}\left[T_{p-p}^{(2,1)}\left(\vec{r}^{\alpha},\vec{r}^{\beta}\right)\right.\\
&+\sum_{\alpha=1}^{n}\frac{1}{q^{\alpha}}\sum_{\substack{\beta=1\\\beta\neq\alpha}}^{n}\sum_{l=1}^{3}\left[T_{p-p}^{(2,1)}\left(\vec{r}^{\alpha},\vec{r}^{\beta}\right)\right]_{jil}p_l^{\beta} + \sum_{\alpha=1}^{n}\frac{1}{q^{\alpha}}\sum_{\substack{\beta=1\\\beta\neq\alpha}}^{n}\sum_{l=1}^{3}\left[T_{p-p}^{(2,1)}\left(\vec{r}^{\alpha},\vec{r}^{\beta}\right)\right]_{jil}p_l^{\alpha}\\
&+\sum_{\alpha=1}^{n}\left(\frac{1}{r_i^{\alpha}-r_{c,i}}\right)^2\frac{1}{q^{\alpha}}\delta_{ij}\left[\sum_{\substack{\beta=1\\\beta\neq\alpha}}^{n}\sum_{l=1}^{3}\left[T_{p-q}^{(1,0)}\left(\vec{r}^{\alpha},\vec{r}^{\beta}\right)\right]_{l}p_l^{\beta} + \sum_{\beta=1}^{n}T_{q-q}^{(0,0)}\left(\vec{r}^{\alpha},\vec{r}^{\beta}\right)q^{\beta} + \chi^{\alpha}\right]\\
&+\sum_{\alpha=1}^{n}\frac{1}{r_i^{\alpha}-r_{c,i}}\frac{1}{q^{\alpha}}\sum_{\substack{\beta=1\\\beta\neq\alpha}}^{n}\left[\sum_{l=1}^{3}\left[T_{p-q}^{(2,0)}\left(\vec{r}^{\alpha},\vec{r}^{\beta}\right)\right]_{jl}p_l^{\beta} + \left[T_{q-q}^{(1,0)}\left(\vec{r}^{\alpha},\vec{r}^{\beta}\right)\right]_{j}q^{\beta}\right]\\
&-\sum_{\alpha=1}^{n}\sum_{\beta=1}^{n}\frac{1}{r_i^{\beta}-r_{c,i}}\frac{1}{q^{\alpha}}\left[\sum_{l=1}^{3}\left[T_{p-q}^{(2,0)}\left(\vec{r}^{\alpha},\vec{r}^{\beta}\right)\right]_{jl}p_l^{\alpha} - \left[T_{q-q}^{(1,0)}\left(\vec{r}^{\alpha},\vec{r}^{\beta}\right)\right]_{j}q^{\alpha}\right]\\
&+\sum_{\alpha=1}^{n}\frac{1}{q^{\alpha}}\frac{1}{q^{\alpha}}\sum_{\substack{\beta=1\\\beta\neq\alpha}}^{n}\sum_{k=1}^{3}\sum_{l=1}^{3}\left[T_{p-p}^{(3,1)}\left(\vec{r}^{\alpha},\vec{r}^{\beta}\right)\right]_{jikl}p_k^{\alpha}p_l^{\beta}\\
&\left.-\sum_{\alpha=1}^{n}\frac{1}{q^{\alpha}}\sum_{\substack{\beta=1\\\beta\neq\alpha}}^{n}\frac{1}{q^{\beta}}\sum_{k=1}^{3}\sum_{l=1}^{3}\left[T_{p-p}^{(3,1)}\left(\vec{r}^{\alpha},\vec{r}^{\beta}\right)\right]_{jikl}p_k^{\beta}p_l^{\alpha}\right\}
\end{aligned} \tag{III.26}$$

Finally, the susceptibility tensor χ_{ij} can be written as[Lecoutre 18]:

$$\chi_{ij} = \left[\left\{\varepsilon_0\left(\frac{\partial^L E_{\cdot}^T}{\partial P_{\cdot}}\right)_{F,G}\right\}^{-1}\right]_{ij} \tag{III.27}$$

III.5 Results and Discussion

Using the derived expression for flexocoupling tensor III.22, we computed the flexocoupling coefficient f_{2222} of MoS_2 for two different shapes of the RVE. As can be seen by comparing the values of two color scale bars in Figure III.3, the value for flexoelectric coupling f_{2222} computed in rectangle-shaped RVE III.3 (b) is much

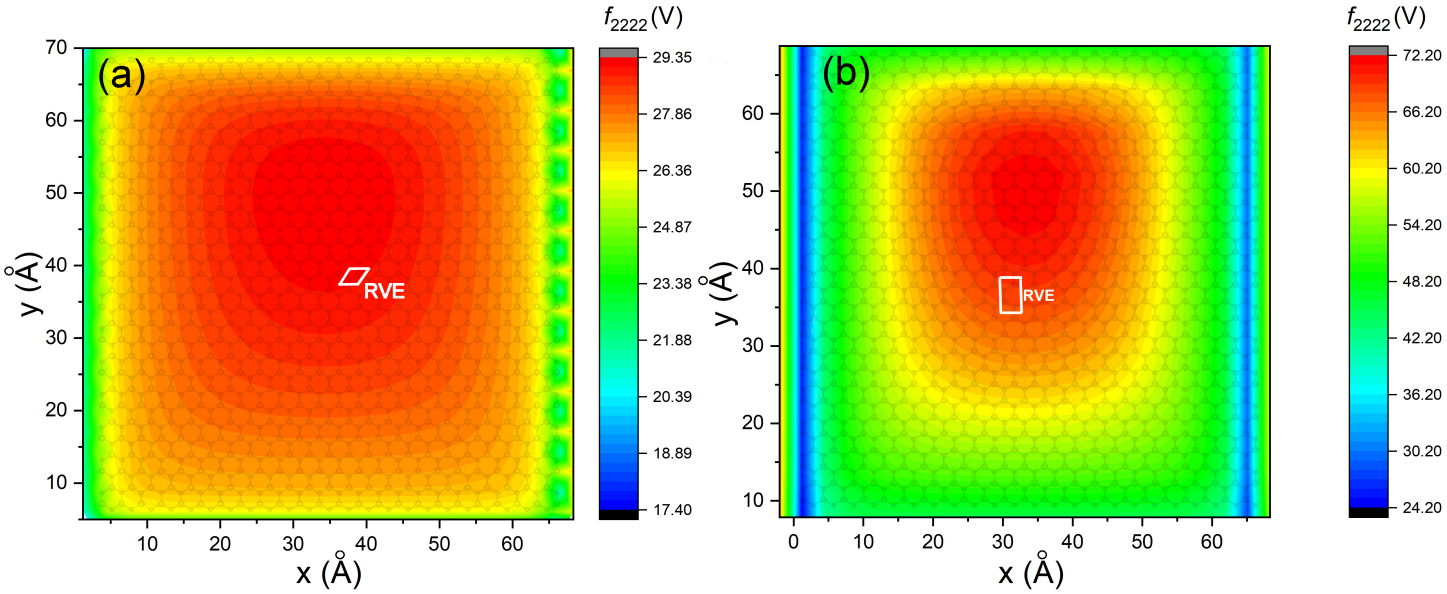

Figure III.3: Computed distribution profiles for flexocoupling coefficient f_{2222} for (a) parallelogram-shaped and (b) rectangular RVE for MoS_2 monolayer, with three and six atoms included in (a) parallelogram-shaped and (b) rectangular RVE, respectively

larger than that computed for a parallelogram shape III.3 (a). This means that the calculated flexoelectric coefficients will vary accordingly with different choices of RVE, which obviously violates the invariance of the flexoelectric coefficients under different RVE choices. Furthermore, it can also be seen on Figure III.3, that the calculated flexocoupling coefficient distribution correlates strongly with the location of RVE. We attribute this to the fact that, due to side effects, the values of charges and dipoles on atoms are different for different RVEs located in different position. The flexocoupling coefficient in the inner RVE (red region in Figure III.3a) will be insusceptible to the side of MoS_2 flake and therefore approach to bulk value. Hence, we chose the inner flexocoupling coefficients in the parallelogram-shaped RVE case, for the final calculated results tabulated in Table III.1. It can be seen that some of the computed flexocoupling tensor components are infinite, which can be ascribed to the fact that the term $1/(r_i^\alpha - r_{c,i})$ is infinite when $r_i^\alpha = r_{c,i}$, which is the case for the z component of the positions of the Mo atoms, in the undeformed configuration. We also find that the first two terms in the expression III.22 represent the major (99%) contribution to the computed flexocoupling tensor. In order to obtain the flexoelectric coefficient μ_{ijkl} in units of nC/m, as commonly reported in the literatures, we use $\mu_{ijkl} = \varepsilon_0 \chi_{im} f_{mjkl}$ to associate μ_{ijkl} with f_{ijkl}, with χ_{im} being susceptibility tensor. We now turn to the computation of susceptibility tensor χ_{ij} by using equation III.27 derived above. Unfortunately, the computed χ_{ij} is infinitely great, which is again attributable to the term including $1/(r_i^\alpha - r_{c,i})$ in equation III.26. To get a finite value, we

f_{1111}	-4.7	f_{1321}	0	f_{2231}	0	f_{3211}	I
f_{1112}	2.7	f_{1322}	0	f_{2232}	0	f_{3212}	I
f_{1113}	0	f_{1323}	7.5	f_{2233}	0	f_{3213}	807.5
f_{1121}	2.7	f_{1331}	-12.9	f_{2311}	0	f_{3221}	I
f_{1122}	-1.6	f_{1332}	7.5	f_{2312}	0	f_{3222}	I
f_{1123}	0	f_{1333}	0	f_{2313}	5.7	f_{3223}	-465.0
f_{1131}	0	f_{2111}	38.2	f_{2321}	0	f_{3231}	807.5
f_{1132}	0	f_{2112}	-22.1	f_{2322}	0	f_{3232}	-465.0
f_{1133}	0	f_{2113}	0	f_{2323}	-3.3	f_{3233}	I
f_{1211}	33.8	f_{2121}	-22.1	f_{2331}	5.7	f_{3311}	I
f_{1212}	-19.5	f_{2122}	12.8	f_{2332}	-3.3	f_{3312}	I
f_{1213}	0	f_{2123}	0	f_{2333}	0	f_{3313}	I
f_{1221}	-19.5	f_{2131}	0	f_{3111}	I	f_{3321}	I
f_{1222}	11.3	f_{2132}	0	f_{3112}	I	f_{3322}	I
f_{1223}	0	f_{2133}	0	f_{3113}	-1140.0	f_{3323}	I
f_{1231}	0	f_{2211}	88.1	f_{3121}	I	f_{3331}	I
f_{1232}	0	f_{2212}	-50.9	f_{3122}	I	f_{3332}	I
f_{1233}	0	f_{2213}	0	f_{3123}	657.5	f_{3333}	28.0
f_{1311}	0	f_{2221}	-50.9	f_{3131}	-1140.0		
f_{1312}	0	f_{2222}	29.4	f_{3132}	657.5		
f_{1313}	-12.9	f_{2223}	0	f_{3133}	I		

Table III.1: Flexocoupling coefficients in volt for MoS_2 monolayer. I means infinity.

removed the terms with $1/(r_i^\alpha - r_{c,i})$ in equation III.26, so that:

$$\begin{aligned}\frac{\partial E_i^L}{\partial P_j} =& V_{RVE}\left\{-\sum_{\alpha=1}^{n}\sum_{\beta=1}^{n}\left[T_{p-p}^{(1,1)}\left(\vec{r}^{\alpha},\vec{r}^{\beta}\right)\right]_{ij} - \sum_{\alpha=1}^{n}\frac{1}{q^\alpha}\sum_{\substack{\beta=1\\\beta\neq\alpha}}^{n}\sum_{l=1}^{3}\left[T_{p-p}^{(2,1)}\left(\vec{r}^{\alpha},\vec{r}^{\beta}\right)\right]_{ijl}p_l^\beta\right.\\
&+\sum_{\alpha=1}^{n}\sum_{\substack{\beta=1\\\beta\neq\alpha}}^{n}\frac{1}{q^\beta}\sum_{l=1}^{n}\left[T_{p-p}^{(2,1)}\left(\vec{r}^{\alpha},\vec{r}^{\beta}\right)\right]_{ilj}p_l^\alpha + \sum_{\alpha=1}^{n}\frac{1}{q^\alpha}\sum_{\substack{\beta=1\\\beta\neq\alpha}}^{n}\sum_{l=1}^{3}\left[T_{p-p}^{(2,1)}\left(\vec{r}^{\alpha},\vec{r}^{\beta}\right)\right]_{jil}p_l^\beta\\
&+\sum_{\alpha=1}^{n}\frac{1}{q^\alpha}\sum_{\substack{\beta=1\\\beta\neq\alpha}}^{n}\sum_{l=1}^{3}\left[T_{p-p}^{(2,1)}\left(\vec{r}^{\alpha},\vec{r}^{\beta}\right)\right]_{jil}p_l^\alpha + \sum_{\alpha=1}^{n}\frac{1}{q^\alpha}\frac{1}{q^\alpha}\sum_{\substack{\beta=1\\\beta\neq\alpha}}^{n}\sum_{k=1}^{3}\sum_{l=1}^{3}\left[T_{p-p}^{(3,1)}\left(\vec{r}^{\alpha},\vec{r}^{\beta}\right)\right]_{jikl}p_k^\alpha p_l^\beta\\
&\left.-\sum_{\alpha=1}^{n}\frac{1}{q^\alpha}\sum_{\substack{\beta=1\\\beta\neq\alpha}}^{n}\frac{1}{q^\beta}\sum_{k=1}^{3}\sum_{l=1}^{3}\left[T_{p-p}^{(3,1)}\left(\vec{r}^{\alpha},\vec{r}^{\beta}\right)\right]_{jikl}p_k^\beta p_l^\alpha\right\}.\end{aligned} \tag{III.28}$$

Susceptibility tensor for MoS_2 is computed with the equation III.28 to be $\begin{bmatrix} -12.73 & 0 & 0 \\ 0 & -12.67 & 0 \\ 0 & 0 & -12.77 \end{bmatrix}$, which are of the same order of magnitude as the result reported in the literature[Laturia 18]. However, the sign of it is not reasonable since it is negative. With the calculated susceptibility tensor and flexocoupling coefficients, the values of flexoelectric coefficients can be computed using $\mu_{ijkl} = \varepsilon_0 \chi_{im} f_{mjkl}$, as shown in Table III.3. We compare these computed results with those obtained from the experimental measurements conducted by Brennan et al.[Brennan 17, Brennan 20] and atomic-level calculations by Gaussian-regularized charge dipole model in combination with the interatomic interaction (Chapter IV), as shown in Table III.2. It can be seen that μ_{1111} and μ_{2222} are of the same order of magnitude as those calculated using the atomistic model introduced in the previous chapters. However, the obtained results show that the magnitude of μ_{1111} and μ_{2222} are much different, which is inconsistent with the quantitative relationship ($\mu_{1111} \approx \mu_{2222}$) obtained in the next chapter. This could result from the discrepancy in lattice symmetry between RVE and the MoS_2 flake with four sides perpendicular to each other. In order to illustrate this problem, we computed and then compared the numerical relationship of $f(\mu)_{1111}$ and $f(\mu)_{2222}$ with the shape of the RVE changed from a parallelogram to a rectangle (see Fig. III.3b). The computed results are 55.25 V and 72.2 V for f_{1111} and f_{2222}, respectively. f_{2222} is bigger than f_{1111} by a factor of around one (as expected), suggesting that different choices for RVEs do affect the calculation results. We can also see from Table III.2 that the computed μ_{3333} is two orders of magnitude larger than that reported. Furthermore, some of the calculated flexoelectric coefficients, i.e. μ_{3123} and μ_{3131} etc, are two orders of magnitude larger than the previously generally measured and calculated values (0.1-1 nC/m) for most 2D materials.

Table III.2: Comparison between transverse flexoelectric coefficient μ_{3311} obtained by charge dipole model and theoretical computation.

Ref.	μ_{3333} (nC/m)	μ_{1111}(nC/m)	μ_{2222}(nC/m)
present work	-2.9	0.5	-3.3
Yang et al	-0.0416	0.68	0.71
Brennan et al	0.08 or 0.12	–	–
Brennan et al	0.065	–	–

μ_{1111}	0.5	μ_{1321}	0	μ_{2231}	0	μ_{3211}	I
μ_{1112}	-0.3	μ_{1322}	0	μ_{2232}	0	μ_{3212}	I
μ_{1113}	0	μ_{1323}	-0.8	μ_{2233}	0	μ_{3213}	-91.0
μ_{1121}	-0.3	μ_{1331}	1.5	μ_{2311}	0	μ_{3221}	I
μ_{1122}	0.2	μ_{1332}	-0.8	μ_{2312}	0	μ_{3222}	I
μ_{1123}	0	μ_{1333}	0	μ_{2313}	-0.6	μ_{3223}	52.5
μ_{1131}	0	μ_{2111}	-4.3	μ_{2321}	0	μ_{3231}	-91.0
μ_{1132}	0	μ_{2112}	2.5	μ_{2322}	0	μ_{3232}	52.5
μ_{1133}	0	μ_{2113}	0	μ_{2323}	0.4	μ_{3233}	I
μ_{1211}	-3.8	μ_{2121}	2.5	μ_{2331}	-0.6	μ_{3311}	I
μ_{1212}	2.2	μ_{2122}	-1.4	μ_{2332}	0.4	μ_{3312}	I
μ_{1213}	0	μ_{2123}	0	μ_{2333}	0	μ_{3313}	I
μ_{1221}	2.2	μ_{2131}	0	μ_{3111}	I	μ_{3321}	I
μ_{1222}	-1.3	μ_{2132}	0	μ_{3112}	I	μ_{3322}	I
μ_{1223}	0	μ_{2133}	0	μ_{3113}	53.0	μ_{3323}	I
μ_{1231}	0	μ_{2211}	-9.9	μ_{3121}	I	μ_{3331}	I
μ_{1232}	0	μ_{2212}	5.7	μ_{3122}	I	μ_{3332}	I
μ_{1233}	0	μ_{2213}	0	μ_{3123}	-45.4	μ_{3333}	-2.9
μ_{1311}	0	μ_{2221}	5.7	μ_{3131}	53.0		
μ_{1312}	0	μ_{2222}	-3.3	μ_{3132}	-45.4		
μ_{1313}	1.5	μ_{2223}	0	μ_{3133}	I		

Table III.3: Flexoelectric coefficients in nC/m for MoS2 monolayer. I means infinity.

III.6 Conclusion

In this chapter, we describe how we tried to incorporate charge terms in the analytical formula involving only dipoles, derived by G. Lecoutre to compute the flexocoupling coefficients of carbon nanotubes, in order to be able to deal with ionic materials such as 2D MoS_2 for which the charge-dipole model is supposed to be more adequate than the pure dipole model. With the derived analytic formula, we calculated many components of the flexoelectric tensor of 2D MoS_2. Results indicate that those flexoelectric coefficients cannot be well predicted with the method proposed in the current chapter. However, due to the complexity of those calculations, we chose to keep that chapter in the thesis, in hope that at least part of it may be useful for someone having a new try to this problem. However, as a result of the problems with our results, we changed our method and finally used numerical computations to calculate the flexoelectric tensor of MoS_2. This will be described in the next chapter.

Chapter IV

Computation of Flexoelectric Coefficients of a MoS_2 monolayer

IV.1 Motivation 62

IV.2 Introduction 62

IV.3 Principle of the method used to compute flexoelectricity coefficients 64

IV.4 Method for the computation of strain gradient G 65

IV.5 Calculation of flexoelectricity coefficients 67

IV.5.1 potential energy functional used for the 'structure' part . . 67

IV.5.2 Initial conditions for the calculation of μ_{3311} 68

IV.5.3 Detailed description for Stillinger-Weber potential 69

IV.5.4 Calculation of μ_{3311} 71

IV.6 Results and discussion 72

IV.6.1 Out-of-plane flexoelectric coefficient μ_{3333} 73

IV.6.2 Transverse flexoelectric coefficient μ_{3311} 75

IV.6.3 In-plane flexoelectric coefficient μ_{1111} and μ_{2222} 80

IV.7 Conclusions 82

IV.1 Motivation

Since we did not manage to obtain the same order of magnitude as the experimental measurement of the flexoelectric coefficients of MoS_2 using the analytical formula derived in Chapter 3, we tentatively tried to adopt a relatively safe way. The regularized charge dipole model (already used in the previous chapters) was employed to numerically compute polarization of material so that we could use the direct flexoelectric effect to calculate the flexoelectric coefficient of molybdenum disulfide[Zhuang 19]. Furthermore, the charge dipole model was recently used to compute flexoelectric coefficients of some representative 2D materials in an article by Zhuang and co-workers[Zhuang 19]. Studying this paper in details, we found that, as in the paper by Javvaji et al discussed in chapter 2[Javvaji 18], the polarization seems inappropriately defined and charge conservation is also not included (which seems normal since both papers have almost the same authors). These reasons lead us to begin our research detailed in this chapter.

IV.2 Introduction

Two-dimensional transition metal dichalcogenides (TMDs) are semiconducting and have excellent optoelectronic properties, making them good candidates for photodetection and light-emitting devices[Tian 16, Choi 17, Singh 21]. In several experiments, 2D MoS_2 materials are found to possess strong in-plane piezoelectricity and piezotronic effects, which could be used in piezoelectric and triboelectric nanogenerators[Fan 19, Han 19, Kim 19]. Recently, another experiment reports that monolayer MoS_2 exhibits remarkable out-of-plane polarization when a compressive loading exerted by the tip of atomic force microscopy acts on it, and the enhancement of vertical piezoelectricity in the MoS_2 is explained by the possible flexoelectric effect induced by structural deformation[Brennan 20, Brennan 17]. Hence, 2D materials can easily undergo out-of-plane deformation due to deformation, eg. bending. The bending of 2D materials leads to nonuniform deformation, which could cause a significant strain gradient. Further understanding the influence of structural bending on the charge polarization in monolayer TMDs will be of importance in unveiling their flexoelectricity, for which, some of studies on calculation of flexoelectric coefficient for 2D materials have been conducted in the context of density functional theory. For example, the dependency of the global dipole moment (polarization) on curvature of carbon nanotube and graphene was investigated by Dumitrică[Dumitrică 02] and Kalinin [Kalinin 08], respectively. Kvashnin et al[Kvashnin 15] studied and then established the universality of the linear dependence of flexoelectric atomic dipole moments on local curvature in various carbon networks (carbon nanotubes, fullerenes and nanocones). Chandratre et al[Chandratre 12] and Kundalwal et al[Kundalwal 17] created hole with different shapes (triangle, circle, trapezoid) on graphene to generate an in-plane net polarization due to symmetry breaking. Such a treatment makes it possible for non-

piezoelectric materials to behave as effective piezoelectric materials. Furthermore, the bending-mode flexoelectric coefficient of Phosphorene[Pandey 21a], hexagonal boron nitride[Kundalwal 21, Guo 22], monolayer GaSe[Zhang 22] and transition-metal dichalcogenides[Shi 18, Shi 19] have been also calculated by means of first-principle calculations. Remarkably, Kumar et al very recently calculated the flexoelectric coefficient for fifty-four representative atomic monolayers selected from distinct groups in the periodic table of elements using ab-initio Density Functional Theory (DFT)[Kumar 21].

Recently, Zhuang and co-workers used molecular dynamics simulations coupled with a charge dipole (QP) model to compute flexoelectric coefficients for transition-metal dichalcogenides[Zhuang 19] and related materials[Javvaji 19]. This kind of method uses calculations much faster than DFT calculations, and provides an easier way to predict the properties of bigger and less symmetric heterostructures. Since we have some experience in using the QP model[Wang 07a, Wang 08b, Yang 18] we studied those papers in details and noticed that a term involving effective charges was neglected/omitted in the definition of polarization that only used the effective dipoles, as in the case of covalent materials such as e.g. graphene. Furthermore, the enforcement of charge conservation was also not implemented, meaning that charges could flow in or out of the materials without any constraint, which can conflict with the fact that an insulating substrate (Polydimethylsiloxane (PDMS), Au, Al_2O_3)[Brennan 17, Brennan 20] was used to obtain the out-of-plane effective flexoelectricity coefficient of monolayer MoS_2, by using an equation for converse flexoelectricity to compute a flexoelectric coefficient using the measured out-of-plane effective piezoelectric coefficient[Brennan 17, Brennan 20]. We also note that in-plane flexoelectric coefficients μ_{1111} or μ_{2222} for such 2D materials have not yet been experimentally obtained, since it has been difficult to isolate the relative contributions of piezoelectricity and flexoelectricity to the resulting polarization.

In this chapter, we computed the in-plane flexoelectric coefficients μ_{1111}, μ_{2222}, transverse flexoelectric coefficient μ_{3311} and out-of-plane flexoelectric coefficient μ_{3333} for monolayer MoS_2 using the charge-dipole model[Olson 78] with radial Gaussian regularization[Mayer 06, Mayer 07a, Wang 07a, Mayer 08, Mayer 09b, Yang 18] enforcing charge conservation with a Lagrange multiplier and adding an ionic charge term in the definition of polarization. The significance of the missing charge term is estimated in the computation of μ_{3333}, by comparison with the simulation paper of Javvaji et al.[Javvaji 19] and the experimental papers of Brennan et al.[Brennan 17, Brennan 20]. Our calculations illustrate that the results for this flexoelectric coefficient computed with the improved definition of polarization agree in magnitude with experimental measurements, with the possible reason causing the discrepancy in sign discussed. Moreover, two critical factors capable of affecting the sign of flexoelectric coefficient are fully elucidated while μ_{3311} is computed. Additionally, μ_{1111} and μ_{2222} are calculated by using an in-plane displacement field that effectively eliminates the piezoelectric contribution to the polarization.

IV.3 Principle of the method used to compute flexoelectricity coefficients

As written in chapter 1, the direct flexoelectric effect describes the fact that a strain gradient in a material will cause an (additional) electric polarization of the material, because of the inhomogeneous distribution of positive and negative charge centers caused by the inhomogeneous deformation. Polarization being a vector described by a vector (first order tensor) and strain gradient a third order tensor, the supposedly linear relation between these two quantities is represented by a fourth order flexoelectricity tensor. Various conventions for the signification of the indices, leading to different matrix compressed representations, are used in the literature. We chose the one that puts the index corresponding to the polarization in first place, since we do not make use of the equivalence of the two strain indices:

$$\Delta P_i = \mu_{ijkl} G_{jkl} \tag{IV.1}$$

where G is the second order displacement gradient and i, j, k, l are indices labeling the coordinates x, y, z or $1, 2, 3$. The Einstein implied summation convention for repeated indices is used.

Our goal is to compute values for these μ_{ijkl} coefficients. For that purpose we will use an inverse effect: when submitted to an external electric field, a dielectric material tends to deform so as to align its global dielectric polarization vector with the external field. Hence, we use various symmetric field configurations designed to deform inhomogeneously a MoS_2 monolayer, while not changing the global polarization contributions due to the dielectric susceptibility of the material or its piezoelectric properties. Then, we compute both the global polarization and the global strain gradient of the deformed structure and fit the (hopefully linear) relation between these two quantities to find the μ coefficients.

We shall therefore describe now, how we compute the global polarization and strain gradient in the monolayer. Since the description on regularized charge dipole model has been discussed in the previous chapter, we omit this part in this chapter. Our version of the QP model for MoS_2 possesses 8 parameters: 2 (χ and R) per kind of atoms by 4 kinds: Mo and S 'bulk' + Mo and S 'edge'. Details on this parameterization, by comparison with DFT data, are given in our previous work[Yang 18]. Recalling equation II.6, the solution can be written in two parts as:

$$\begin{bmatrix} q \\ \vec{p} \\ \lambda \end{bmatrix} = \begin{bmatrix} T^{(0,0)}_{q-q} & \left(T^{(1,0)}_{p-q}\right)^T & 1 \\ T^{(1,0)}_{p-q} & T^{(1,1)}_{p-p} & 0 \\ 1 & 0 & 0 \end{bmatrix}^{-1} \begin{bmatrix} -\chi \\ 0 \\ Q_{tot} \end{bmatrix} + \begin{bmatrix} T^{(0,0)}_{q-q} & \left(T^{(1,0)}_{p-q}\right)^T & 1 \\ T^{(1,0)}_{p-q} & T^{(1,1)}_{p-p} & 0 \\ 1 & 0 & 0 \end{bmatrix}^{-1} \begin{bmatrix} -V_{ext} \\ -\vec{E}_{ext} \\ 0 \end{bmatrix} \tag{IV.2}$$

where the first term on the right side corresponds to intrinsic charges q^0_α and dipoles $\vec{p}^0_\alpha$, i.e. charges and dipoles in the absence of any external electric field, that can however vary due to a mechanical deformation. The electronegativities

χ_α uniquely determine these intrinsic charges and dipoles (given the atomic positions), independently from any external electric field $\vec{E}_{ext}$ or potential V_{ext}. For our calculations, the total charge of the nanoribbon (Q_{tot}) is set to be zero because of the fact that flexoelectricity is supposed to be an intrinsic property, therefore requiring no extra charge to appear. The second term on the right side corresponds to effective additional charges (q_α^{ind}) and dipoles (p_α^{ind} generated by the external electric field and potential). This can be summarized under the form:

$$\begin{cases} p_x = \sum_{\alpha=1}^{N} (p_{x,\alpha}^0 + p_{x,\alpha}^{ind}) \\ p_y = \sum_{\alpha=1}^{N} (p_{y,\alpha}^0 + p_{y,\alpha}^{ind}) \\ p_z = \sum_{\alpha=1}^{N} (p_{z,\alpha}^0 + p_{z,\alpha}^{ind}) \\ q = \sum_{\alpha=1}^{N} (q_\alpha^0 + q_\alpha^{ind}) \end{cases} \tag{IV.3}$$

In terms of the calculated dipoles $\vec{p}$ and charges q, the global polarization $\vec{P}$ for MoS_2 nanoribbon is defined as[Olson 78]:

$$\vec{P} = \frac{\sum_{\alpha=1}^{N} (q_\alpha \vec{r}_\alpha + \vec{p}_\alpha)}{V} \tag{IV.4}$$

in which V is the volume of MoS_2 nanoribbon. A thickness of 6.5 Å is used in computing V.[Li 15] More information on the charge dipole model for MoS_2 can be found in our previous work[Yang 18]. Note that since MoS_2 is not ferroelectric, the total contribution to polarization of the q_α^0 and $\vec{p}_\alpha^0$ is zero (verified numerically), so that Eq. IV.4 could be rewritten by taking into account the induced charges and dipoles only.

In order to compare with some DFT results or remove edge effects, periodic boundary conditions can be applied in the QP model by adding the contributions of periodic images in the interaction tensors, i.e. adding contributions obtained by replacing $r_{\alpha\beta}$ in Eq.II.3 with $r_{\alpha\beta} + L * p$ $(p \in [-k, k])$, with L denoting the periodic length in a given direction and k being a very large integer. We verified that setting $k = 100$ in our calculation is already sufficiently large to reach convergence in the computation of in-plane flexoelectric coefficients μ_{1111}, μ_{2222} and out-of-plane flexoelectric coefficient μ_{3333}, thus eliminating edge effects.

IV.4 Method for the computation of strain gradient G

To compute the second order strain gradient G, we considered that the RVE was the whole system if non periodized and the supercell if periodized. Then, we tried several methods implemented using various functions of the LAPACK library.[Anderson 99]

As a first common step, we choose the centroid (C) of the undeformed configuration as the origin of this undeformed configuration and make the continuum approximation that Eq.III.6 also apply to that point taken as atom α. Then, by inserting $\vec{R}_{\alpha\beta} = \vec{R}_\beta - \vec{R}_\alpha$ and $\vec{r}_{\alpha\beta} = \vec{r}_\beta - \vec{r}_\alpha$ into Eq.III.6 and simplifying the result using $\forall J = 1,2,3,\ R_{J,\alpha} = R_{J,C} = 0$, we have:

$$\begin{array}{l} \forall i = 1,2,3,\ \forall \beta = 1,...,N \\ r_{i,\beta} - r_{i,\alpha} = \sum_{J=1}^{3} F_{iJ} R_{J,\beta} + \sum_{J=1}^{3}\sum_{K=1}^{3} \frac{G_{iJK}}{2} R_{J,\beta} R_{K,\beta} \end{array} \tag{IV.5}$$

Let us insist that, in this equation, all the components of $r_{i,\beta}, r_{i,\alpha}$ and $R_{J,\beta}$ are now taken in the frame with its origin in C and the three axes x, y and z and that the three values of $r_{i,\alpha} = r_{i,C}$ are a priori unknown. Eq.IV.5 can be cast into matrix form, component-wise, by defining a N by 13 (or 10 if we take into account the symmetry between J and K indices) matrix A, a 13 (or 10) by 3 matrix X and a N by 3 matrix B, such that $AX = B$, with:

$$A = \begin{bmatrix} 1 & \{R_{J,1}\}_{J=1,2,3} & (1/2)\{R_{J,1}R_{K,1}\}_{J,K=1,2,3} \\ \vdots & \vdots & \\ 1 & \{R_{J,\alpha}\}_{J=1,2,3} & (1/2)\{R_{J,\alpha}R_{K,\alpha}\}_{J,K=1,2,3} \\ \vdots & \vdots & \\ 1 & \{R_{J,N}\}_{J=1,2,3} & (1/2)\{R_{J,N}R_{K,N}\}_{J,K=1,2,3} \end{bmatrix}, \tag{IV.6}$$

$$X = \begin{bmatrix} r_{1,C} & r_{2,C} & r_{3,C} \\ \{F_{1J}\}^T_{J=1,2,3} & \{F_{2J}\}^T_{J=1,2,3} & \{F_{3J}\}^T_{J=1,2,3} \\ \{G_{1JK}\}^T_{J,K=1,2,3} & \{G_{2JK}\}^T_{J,K=1,2,3} & \{G_{3JK}\}^T_{J,K=1,2,3} \end{bmatrix}, \tag{IV.7}$$

$$B = \begin{bmatrix} r_{1,1} & r_{2,1} & r_{3,1} \\ \vdots & \vdots & \vdots \\ r_{1,\beta} & r_{2,\beta} & r_{3,\beta} \\ \vdots & \vdots & \vdots \\ r_{1,N} & r_{2,N} & r_{3,N} \end{bmatrix} \tag{IV.8}$$

This problem could then be solved directly using routine DGELS of LAPACK, which computes the least squares solution vector, by QR or LQ factorization, for this *a priori* overdetermined problem (provided that there are more than 13 (or 10) atoms in the RVE). However, DGELS requires that matrix A be full rank which is not the case for a 2D material with a flat undeformed configuration, since in that case there is a degeneracy due to the fact that all the atoms in a given layer (e.g. all Mo atoms in our case) have very similar coordinates along the axis perpendicular to the plane (z axis in our case, also called axis 3). We therefore used routine DGELSD that solves overdetermined linear systems as linear least squares problems using Singular Value Decomposition (with an algorithm that is said to be much faster than DGELSS in LAPACK user's guide[Anderson 99]).

We also tested another method that minimize more explicitly the sum of the squares of the residuals of Eq.IV.5:

$\forall i = 1, 2, 3$

$$\chi_i^2(r_{i,\alpha}, \{F_{iJ}\}, \{G_{iJK}\}) = \sum_{\beta=1}^{N} \left(r_{i,\beta} - r_{i,\alpha} - \sum_{J=1}^{3} F_{iJ} R_{J,\beta} - \sum_{J=1}^{3}\sum_{K=1}^{3} \frac{G_{iJK}}{2} R_{J,\beta} R_{K,\beta} \right)^2, \tag{IV.9}$$

Indeed this can be cast into matrix form by defining a 14 (or 11) by N matrix A_i and a 1 by N vector Y_i for the three values of i, such that:

$$A_i = \begin{bmatrix} -r_{i,1} & 1 & \{X_J^1\}_{J=1,2,3} & \{X_J^1 X_K^1\}_{J,K=1,2,3} \\ \vdots & \vdots & \vdots & \vdots \\ -r_{i,\alpha} & 1 & \{X_J^\alpha\}_{J=1,2,3} & \{X_J^\alpha X_K^\alpha\}_{J,K=1,2,3} \\ \vdots & \vdots & \vdots & \vdots \\ -r_{i,N} & 1 & \{X_J^N\}_{J=1,2,3} & \{X_J^N X_K^N\}_{J,K=1,2,3} \end{bmatrix}, Y_i = \begin{bmatrix} 1 \\ r_{i,C} \\ \{F_{iJ}\}_{J=1,2,3}^T \\ \{2G_{iJK}\}_{J,K=1,2,3}^T \end{bmatrix} \tag{IV.10}$$

since using these definitions (Eq. IV.5) into Eq.IV.9, we have:

$$\chi_i^2 = (A_i Y_i)^T A_i Y_i = Y_i^T A_i^T A_i Y_i = Y_i^T N_i Y_i \tag{IV.11}$$

with $N_i = A_i^T A_i$. The minimum of $\chi_i^2(Y)$ can then be obtained when Y_i is the ratio of the eigenvector (given by DSYEV) corresponding to the smallest non-zero eigenvalue of matrix N_i (selected with a threshold set to 10^{-6}), divided by the value of the first component of this eigenvector.

We tested these methods and variants using explicitly the symmetry between indices J and K of G_{iJK} using various imposed deformation, and checked whether we could recover what we put. We found that the method using DGELSD was the most stable and allowed a check of consistency by assessing the respect of the symmetry between J and K indices.

IV.5 Calculation of flexoelectricity coefficients

We illustrate the method we use to compute the flexoelectric coefficients on the special case of the determination of μ_{3311}.

IV.5.1 potential energy functional used for the 'structure' part

The key of the molecular simulations is actually the interatomic potential, which is applied to describe the interaction among atoms. For single-layer MoS_2, the Stillinger-Weber many-body potential (E_{SW}) as parameterized by Wen et al[Wen 17] was very recently proven to be robust through a quantitative systematic comparison of structural and mechanical properties, as well as phonon dispersion

for single-layer MoS_2 using density functional theory (DFT) and molecular statics calculations.[Madziarz 21] We therefore used this parameterization of the SW potential (E_{SW}) in our simulations, and found it very stable. The various MoS_2 nanoribbons we use in our simulations are thus initially relaxed by minimizing E_{SW}. This gives the undeformed configuration mentioned in the previous subsection.

To compute the deformed configurations, we removed the interactions between intrinsic charges and dipoles in E_{elec}, since they are already included in E_{SW}. We also neglected the total contribution of the interactions between intrinsic and induced charges and dipoles to keep only the total contributions of the interactions between charges and dipoles induced by the external field and potential (which we name E'_{elec}).

IV.5.2 Initial conditions for the calculation of μ_{3311}

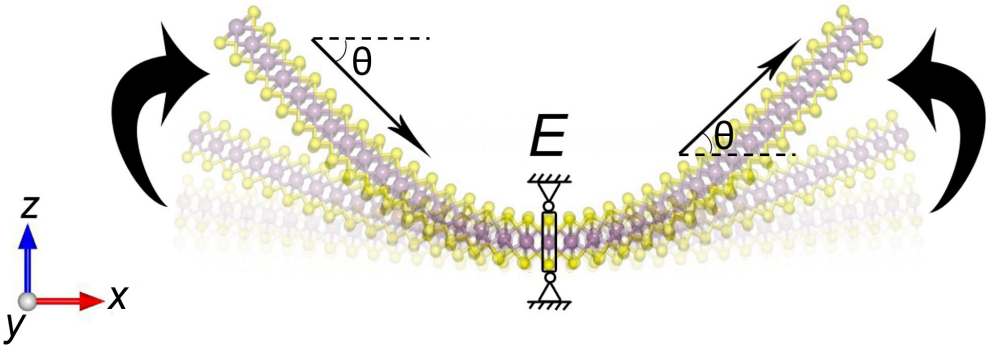

Figure IV.1: Schematic of bending simulation for MoS_2 nanoribbon subjected to an external electric field. The left and right parts of the MoS_2 sheet are submitted to an electric field in the bottom-right and top-right direction, respectively. The external electric field $\vec{E}$ is represented by the arrows. θ is the angle with the $+x$ direction.

In order to compute μ_{3311}, a $\searrow\nearrow$-like external electric field $\vec{E}_{ext}$, with both directions of $\vec{E}_{ext}$ in the x-z plane, is applied to the MoS_2 nanoribbon, keeping the middle row of atoms fixed (as if it were attached to a virtual fixed object). This field generates a bending deformation of the nanoribbon because of the inverse flexoelectric effect, as seen in Fig IV.1. The conjugate gradient algorithm is then used to minimize the energy function $E_{tot} = E_{SW} + E'_{elec}$ which now includes the interactions with the external field and potential and the contributions of the effective induced charges and dipoles. The energy optimization simulation then makes the MoS_2 flake bend towards the direction of the applied electric field by adjusting the positions of the atoms until the computed average force is less than 0.00004 eV/Å. Note that all these simulations are done with a FORTRAN code that has been continuously developed in the group for years.

The mechanism of electrostatic bending of MoS_2 flake is depicted in Figure IV.2. We can see that negative and positive charges are shifted to opposite directions due to the non-zero transversal electric field (positive charges move to top right and negative ones move to upper left of the MoS_2 flake). The interaction between the total dipoles induced on each side by the changes of the effective charges and the external electric field produces two torques with opposite direction, termed τ_1 and τ_2, making the two sides of the MoS_2 flake respectively bend towards the direction of the external electric field with the fixed atoms as the rotation axis, while giving a zero total polarization along the vertical axis.

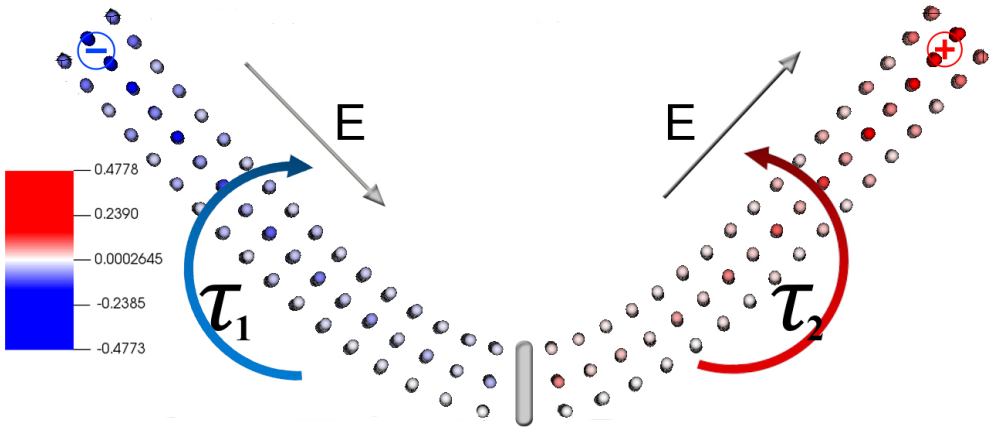

Figure IV.2: Induced charge on a MoS_2 nanoribbon subjected to external electric field. The positive charges move to the right side and the negative ones move to the left side. E represents external electric field, whose direction is denoted by the arrows. The atoms colored red and blue are positively and negatively charged, respectively. The atoms in the central gray zone are fixed. $\vec{\tau}_1$ and $\vec{\tau}_2$ stand for the induced bending moments acting on the MoS_2.

IV.5.3 Detailed description for Stillinger-Weber potential

The SW potential is obtained as a combination of two- and three-body interactions.

$$U_{SW}\left(\{\vec{r}_\alpha\}_{\alpha=1,\cdots,N}\right) = \frac{1}{2}\sum_{\substack{\alpha,\beta=1\\ \alpha\neq\beta}}^{N} U_2\left(r_{\alpha\beta}\right) + \frac{1}{6}\sum_{\substack{\alpha,\beta,\gamma=1\\ \alpha\neq\beta\neq\gamma}}^{N} U_3\left(\vec{r}_\alpha,\vec{r}_\beta,\vec{r}_\gamma\right) \tag{IV.12}$$

with:

$$U_2\left(r_{\alpha\beta}\right) = \begin{cases} \varepsilon A\left[B\left(\frac{\sigma}{r_{\alpha\beta}}\right)^p - \left(\frac{\sigma}{r_{\alpha\beta}}\right)^q\right]\exp\left(\frac{\sigma}{r_{\alpha\beta}-r_c^{U_2}}\right) & r_{\alpha\beta} < r_c^{U_2} \\ 0 & r_{\alpha\beta} \geq r_c^{U_2} \end{cases} \tag{IV.13}$$

$$U_3\left(\vec{r}_\alpha,\vec{r}_\beta,\vec{r}_\gamma\right) = h\left(r_{\alpha\beta},r_{\alpha\gamma},\theta_{\beta\alpha\gamma}\right) + h\left(r_{\beta\alpha},r_{\beta\gamma},\theta_{\alpha\beta\gamma}\right) + h\left(r_{\gamma\alpha},r_{\gamma\beta},\theta_{\alpha\gamma\beta}\right) \tag{IV.14}$$

$$h\left(r_{\alpha\beta}, r_{\alpha\gamma}, \theta_{\beta\alpha\gamma}\right) = \begin{cases} \varepsilon\lambda \exp\left[\left(\frac{\zeta\sigma}{r_{\alpha\beta}-r_c^{U_3}}\right) + \left(\frac{\zeta\sigma}{r_{\alpha\gamma}-r_c^{U_3}}\right)\right]\left(\cos\theta_{\beta\alpha\gamma} - \cos\theta_0\right)^2 & r_{\alpha\beta}, r_{\alpha\gamma} < r_c^{U_3} \\ 0 & r_{\alpha\beta} \text{ or } r_{\alpha\gamma} \geq r_c^{U_3} \end{cases} \tag{IV.15}$$

In these definitions, $r_{\alpha\beta}$ is the distance between α^{th} and β^{th} atoms which are within the range of cutoff radius r_c. $\theta_{\beta\alpha\gamma}$ is the bond angle subtended by the bonds $r_{\alpha\beta}$ and $r_{\alpha\gamma}$ at vertex α, θ_0 is the angle between nearest neighbor atoms at equilibrium state of MoS_2, with $\cos\theta_0 = -1/3$ for the symmetric tetravalent equilibrium configuration. The values of the parameters (θ_0, ϵ, A, B, p, q, σ, $r_c^{U_2}$, $r_c^{U_3}$, λ and ζ) depend on the chemical nature of atoms α, β and γ. The values we used[Wen 17] are given in Table IV.1 and IV.2.

Table IV.1: SW potential parameters (part 1)

Interaction \ Parameters	A (eV)	B	p	q	σ (Å)	$r_c^{U_2}$ (Å)
Mo-Mo	3.9781804791	0.4446021306	5	0	2.85295	5.54660
Mo-S	11.3797414404	0.5266688197	5	0	2.17517	4.02692
S-S	1.1907355764	0.9015152673	5	0	2.84133	4.51956

Table IV.2: SW potential parameters (part 2)

ϵ (eV)	λ_{S-Mo-S} (eV)	$\lambda_{Mo-S-Mo}$ (eV)	ζ (Å)	θ_0	$r_{c(U_3)}^{Mo-S}$ (Å)	$r_{c(U_3)}^{S-S}$ (Å)
1.	7.4767529158	8.1595181220	1.3566322033	81.7868°	4.02692	3.86095

To compute the forces, we will need several intermediate point (using $\vec{r}_{\alpha\beta} \equiv \vec{r}_{\alpha\to\beta} \equiv \vec{r}_\beta - \vec{r}_\alpha$), we have

$$\forall n, \alpha \neq \beta, \vec{\nabla}_n f\left(r_{\alpha\beta}\right) \equiv \frac{\partial f\left(r_{\alpha\beta}\right)}{\partial \vec{r}_n} = \frac{\vec{r}_\alpha - \vec{r}_\beta}{\left\|\vec{r}_\alpha - \vec{r}_\beta\right\|} f'\left(r_{\alpha\beta}\right)\left(\delta_{n\alpha} - \delta_{n\beta}\right) \tag{IV.16}$$

Then:

$$\begin{aligned} \vec{\nabla}_n \cos\theta_{\beta\alpha\gamma} \equiv \frac{\partial}{\partial \vec{r}_n}\left(\frac{\vec{r}_{\alpha\beta}\cdot\vec{r}_{\alpha\gamma}}{r_{\alpha\beta}r_{\alpha\gamma}}\right) &= \frac{1}{r_{\alpha\beta}r_{\alpha\gamma}}\left[\left(\vec{r}_\alpha - \vec{r}_\gamma\right)\left(\delta_{n\alpha} - \delta_{n\beta}\right) + \left(\vec{r}_\alpha - \vec{r}_\beta\right)\left(\delta_{n\alpha} - \delta_{n\gamma}\right)\right] \\ &+ \left(\frac{\vec{r}_{\alpha\beta}\cdot\vec{r}_{\alpha\gamma}}{r_{\alpha\gamma}}\right)\left[-\frac{\vec{r}_n - \vec{r}_\beta}{\left\|\vec{r}_n - \vec{r}_\beta\right\|^3}\delta_{n\alpha} + \frac{\vec{r}_\alpha - \vec{r}_n}{\left\|\vec{r}_\alpha - \vec{r}_n\right\|^3}\delta_{n\beta}\right] \\ &+ \left(\frac{\vec{r}_{\alpha\beta}\cdot\vec{r}_{\alpha\gamma}}{r_{\alpha\beta}}\right)\left[-\frac{\vec{r}_n - \vec{r}_\gamma}{\left\|\vec{r}_n - \vec{r}_\gamma\right\|^3}\delta_{n\alpha} + \frac{\vec{r}_\alpha - \vec{r}_n}{\left\|\vec{r}_\alpha - \vec{r}_n\right\|^3}\delta_{n\gamma}\right] \\ \forall n, \alpha \neq \beta \neq \gamma \end{aligned} \tag{IV.17}$$

So that:

$$\begin{aligned}
\vec{\nabla}_\alpha \cos\theta_{\beta\alpha\gamma} &= \frac{1}{r_{\alpha\beta}r_{\alpha\gamma}}\left[(\vec{r}_\alpha-\vec{r}_\gamma)+(\vec{r}_\alpha-\vec{r}_\beta)\right]-\cos\theta_{\beta\alpha\gamma}\left[\frac{\vec{r}_\alpha-\vec{r}_\beta}{\|\vec{r}_\alpha-\vec{r}_\beta\|^2}+\frac{\vec{r}_\alpha-\vec{r}_\gamma}{\|\vec{r}_\alpha-\vec{r}_\gamma\|^2}\right]\\
\vec{\nabla}_\beta \cos\theta_{\beta\alpha\gamma} &= -\frac{(\vec{r}_\alpha-\vec{r}_\gamma)}{r_{\alpha\beta}r_{\alpha\gamma}}+\cos\theta_{\beta\alpha\gamma}\left[\frac{\vec{r}_\alpha-\vec{r}_\beta}{\|\vec{r}_\alpha-\vec{r}_\beta\|^2}\right] \qquad \forall\alpha\neq\beta\neq\gamma\\
\vec{\nabla}_\gamma \cos\theta_{\beta\alpha\gamma} &= -\frac{(\vec{r}_\alpha-\vec{r}_\beta)}{r_{\alpha\beta}r_{\alpha\gamma}}+\cos\theta_{\beta\alpha\gamma}\left[\frac{\vec{r}_\alpha-\vec{r}_\gamma}{\|\vec{r}_\alpha-\vec{r}_\gamma\|^2}\right]
\end{aligned} \tag{IV.18}$$

Then, in the case $f=U_2$, we have: $f'(r_{\alpha\beta})=0$ if $r_{\alpha\beta}\geq r_c^{U_2}$, and otherwise:

$$\begin{aligned}
U_2'(r_{\alpha\beta}) = \frac{\varepsilon A}{\sigma}\{[&-pB\left(\frac{\sigma}{r_{\alpha\beta}}\right)^{p+1}+q\left(\frac{\sigma}{r_{\alpha\beta}}\right)^{q+1}]\exp\left(\frac{\sigma}{r_{\alpha\beta}-r_c^{U_2}}\right)\\
&-\left[B\left(\frac{\sigma}{r_{\alpha\beta}}\right)^{p}-\left(\frac{\sigma}{r_{\alpha\beta}}\right)^{q}\right]\left(\frac{\sigma}{r_{\alpha\beta}-r_c^{U_2}}\right)^2\exp\left(\frac{\sigma}{r_{\alpha\beta}-r_c^{U_2}}\right)\Bigg\}
\end{aligned} \tag{IV.19}$$

Finally, in the case $f=h$, we have, e.g.: $h(r_{\alpha\beta},r_{\alpha\gamma},\theta_{\beta\alpha\gamma})=0$ if $r_{\alpha\beta}$ or $r_{\alpha\gamma}\geq r_c$, and otherwise:

$$\begin{aligned}
&\vec{\nabla}_n h(r_{\alpha\beta},r_{\alpha\gamma},\theta_{\beta\alpha\gamma})\\
&\quad=-\frac{\varepsilon\lambda}{\zeta\sigma}\left[\left(\frac{\zeta\sigma}{r_{\alpha\beta}-r_c^{U_3}}\right)^2\frac{\vec{r}_\alpha-\vec{r}_\beta}{\|\vec{r}_\alpha-\vec{r}_\beta\|}(\delta_{n\alpha}-\delta_{n\beta})\right.\\
&\quad+\left.\left(\frac{\zeta\sigma}{r_{\alpha\gamma}-r_c^{U_3}}\right)^2\frac{\vec{r}_\alpha-\vec{r}_\gamma}{\|\vec{r}_\alpha-\vec{r}_\gamma\|}(\delta_{n\alpha}-\delta_{n\gamma})\right]\exp\left[\left(\frac{\zeta\sigma}{r_{\alpha\beta}-r_c^{U_3}}\right)\right.\\
&\quad+\left.\left(\frac{\zeta\sigma}{r_{\alpha\gamma}-r_c^{U_3}}\right)\right](\cos\theta_{\beta\alpha\gamma}-\cos\theta_0)^2\\
&\quad+2\varepsilon\lambda\exp\left[\left(\frac{\zeta\sigma}{r_{\alpha\beta}-r_c^{U_3}}\right)+\left(\frac{\zeta\sigma}{r_{\alpha\gamma}-r_c^{U_3}}\right)\right](\cos\theta_{\beta\alpha\gamma}-\cos\theta_0)\,\vec{\nabla}_n\cos\theta_{\beta\alpha\gamma}
\end{aligned} \tag{IV.20}$$

IV.5.4 Calculation of μ_{3311}

Contributions to the polarization of a given dielectric material submitted to an external electric field may come from piezoelectricity, flexoelectricity and electric susceptibility. In the simulations defined in the previous subsection, piezoelectricity need not be taken into account due to the symmetric bending deformation[Zhuang 19]. This makes the total induced polarization due to the first order deformation gradient become zero. Additionally, one can find the total external electric field along the out-of-plane is also zero. Hence, the out-of-plane polarization equal to the product of the susceptibility and the electric field should be removed as well. The

remaining flexoelectric part of the out-of-plane polarization P_3 can be written as:

$$P_3 = \sum_{j=1}^{3}\sum_{k=1}^{3}\sum_{l=1}^{3} \mu_{3jkl} G_{jkl} \tag{IV.21}$$

with μ_{3jkl} standing for flexoelectric tensor components. With the setup defined in the previous section, this can be approximated by:

$$P_3 = \mu_{3311} G_{311} \tag{IV.22}$$

Hence μ_{3311} can be determined as the slope of the supposedly linear relation between P_3 and G_{311}.

IV.6 Results and discussion

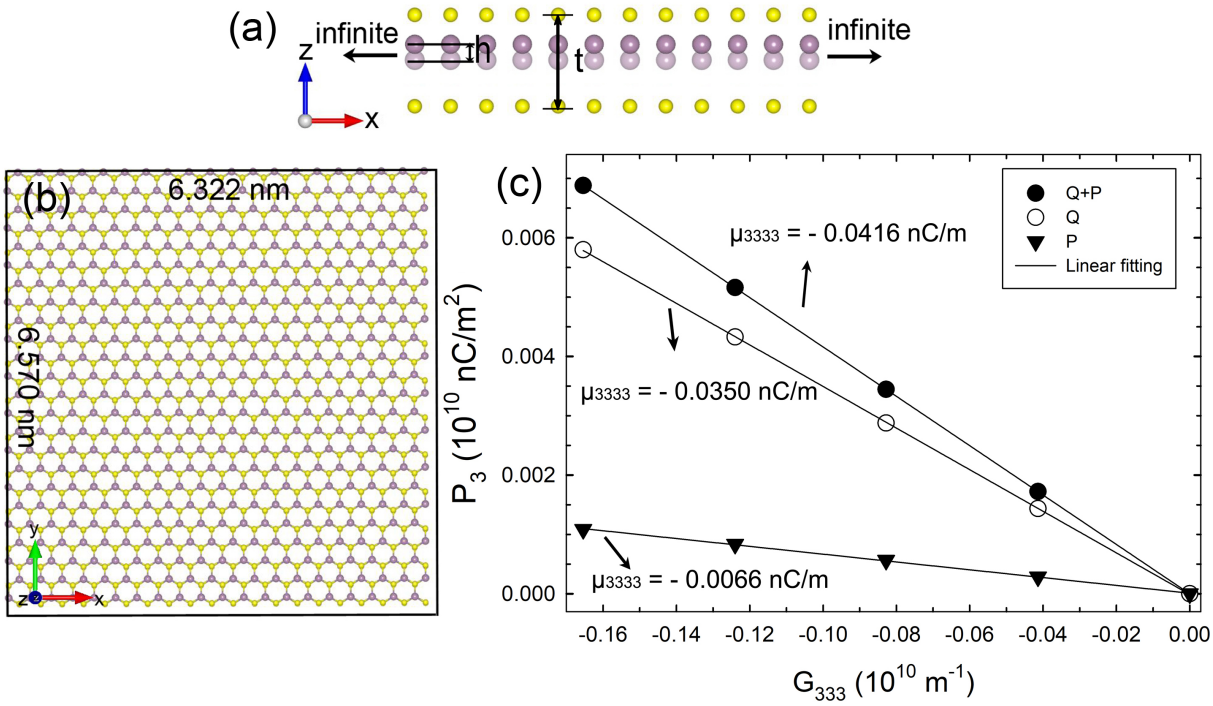

Figure IV.3: (a) Schematic diagram of creation of strain gradient G_{333} inside monolayer MoS_2. h and t stand for the small upward shift for a layer of molybdenum atom and the geometric thickness of monolayer MoS_2, respectively. (b) Basic unit for periodic monolayer MoS_2, with length and width of basic unit being 6.570 nm and 6.322 nm, respectively. (c) Variation of polarization P_3 with strain gradient G_{333} for monolayer MoS_2.

In this section, we discuss the results we got for the computation of the in-plane flexoelectric coefficients μ_{1111}, μ_{2222}, the transverse flexoelectric coefficient μ_{3311} and the out-of-plane coefficient μ_{3333}. In order to check the accuracy of

our parameterized charge dipole model, we computed in-plane piezoelectric coefficient e_{222} for MoS_2 monolayer, defined as $e_{222} = (\frac{\partial P_2}{\partial \varepsilon_{22}})_{E,T}$. As can be seen on Fig.IV.4, the value of in-plane piezoelectric coefficient e_{222} (0.76×10^{-10}C/m) is of the same order of magnitude as the experimental result (2.9×10^{-10}C/m) reported in ref[Zhu 15].

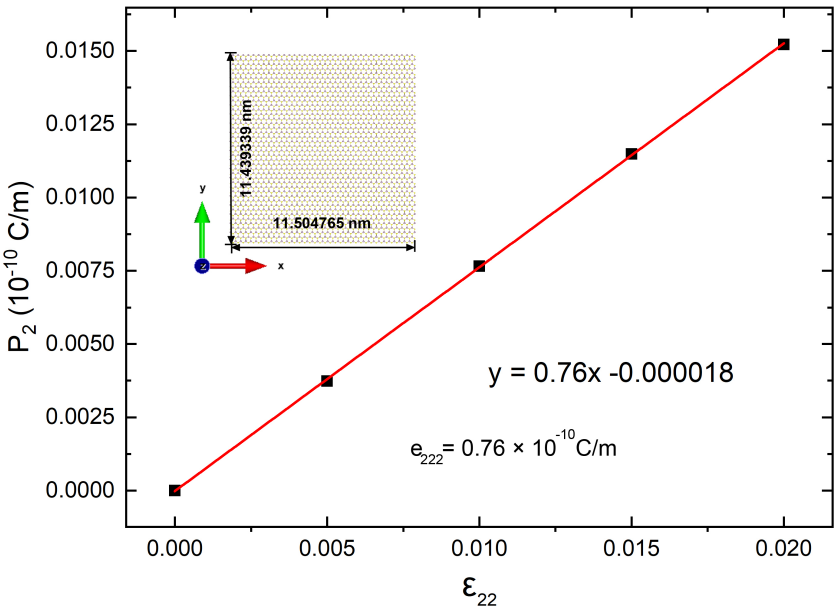

Figure IV.4: y-axis polarization P_2 vs uniaxial strain ε_{22} for an MoS_2 monolayer. The x axis corresponds to a zigzag edge while the y axis corresponds to an armchair edge.

IV.6.1 Out-of-plane flexoelectric coefficient μ_{3333}

As can be seen on Fig.IV.3a, for this calculation, the layer of molybdenum atoms is shifted a small distance h to the positive direction of z axis to generate a strain gradient only along the out-of-plane (z) direction. In this case, the unique strain gradient that does exist is G_{333} and the expression for computing μ_{3333} can be written as $\mu_{3333} = \frac{\partial P_3}{\partial G_{333}}$. The geometric thickness of monolayer MoS_2 is t. With both h and t, the strain gradient G_{333} can be computed as $-\frac{8h}{t^2}$, which may be derived by: $G_{333} = \frac{d^2u_z(0)}{dz^2} \approx \frac{u_z(-\frac{t}{2})+u_z(\frac{t}{2})-2u_z(0)}{(t/2)^2} = \frac{0+0-2h}{(t/2)^2} = -\frac{8h}{t^2}$, with $u_z(\frac{t}{2})$, $u_z(-\frac{t}{2})$ and $u_z(0)$ representing the displacement of atoms for top sulfur layer, bottom sulfur layer and molybdenum layer, respectively. In this calculation, we enforce periodic boundary conditions to eliminate edge effects that can be quite important in such a setup. As can be seen on Fig.IV.3b, we use a MoS_2 flake with a width of 6.164 nm and a length of 6.388 nm as supercell, which gives periods along x and y direction of 6.322 nm and 6.570 nm, respectively. Bond length between Mo and S is set as 2.39763 Å in the presence of periodic boundary conditions. On Fig.IV.3c, we plot the polarization P_3 as a function of G_{333}, in

order to obtain the flexoelectric coefficient μ_{3333} of 2D MoS_2. Three different ways to compute the polarization are used (using $q_\alpha \vec{r}_\alpha$ only, using $\vec{p}_\alpha$ only or using both terms in Eq.IV.4, with charges and dipoles computed using the QP scheme in the three cases). The units of polarization P_3 and strain gradient G_{333} are converted from e/Å^2 and Å^{-1} to 10^{10} nC/m^2 and 10^{10} m^{-1} respectively, so as to readily obtain μ_{3333} in nC/m from the slope of the fitted straight line. We compare μ_{3333} computed under the various definitions of polarization with that obtained from the experimental measurements conducted by Brennan et al in 2017 and 2020[Brennan 17, Brennan 20], respectively, as shown in Table IV.3.

Table IV.3: Comparison between out-of-plane flexoelectric coefficients μ_{3333} obtained by charge-dipole model and experimental measurements. The two different contributions to the polarization coming from charges alone or dipoles alone are considered separately then together for the computation of μ_{3333} by the charge-dipole model.

Ref.	μ_{3333} (nC/m)	Definition of polarization
present work	-0.0416	$P_3 = \frac{\sum_{\alpha=1}^{N}(q_\alpha r_{3,\alpha}+p_{3,\alpha})}{V}$
present work	-0.0350	$P_3 = \frac{\sum_{\alpha=1}^{N} q_\alpha r_{3,\alpha}}{V}$
present work	-0.0066	$P_3 = \frac{\sum_{\alpha=1}^{N} p_{3,\alpha}}{V}$
Brennan et al (2017)[Brennan 17]	0.08 or 0.12	———
Brennan et al (2020)[Brennan 20]	0.065	———

It can be seen that the result for μ_{3333} computed when the charge term is included in the definition of polarization will be comparatively closer to the experimental result in absolute value whereas μ_{3333} computed with the dipole term only considered is of the same order of magnitude but much smaller than the experimental value. This manifests that the charge term, omitted/neglected in Ref.[Zhuang 19], cannot be neglected for the calculation of polarization for MoS_2. We do not take into account the discrepancy in sign between our computed results and the results of the Piezoresponse Force Microscopy (PFM) measurements of Brennan et al., since we believe that it is due to a problem of different definition for the algebraic (or not) radius of curvature. This is reflected in another experimental measurement of out-of-plane flexoelectric coefficient μ_{3333} for few-layers MoS_2 with PFM, very recently conducted by Hirakata et al[Hirakata 21]. In their work, the sign of the out-of-plane flexoelectric coefficient is measured to be negative, though they quote a positive number. Indeed, using their Eq. 9, one can get $\mu_{3333} = -c_{33}\epsilon_3/\frac{\partial E_3}{\partial x_3}$, with c_{33} meaning elastic constant of MoS_2. Since c_{33}, ϵ_3 and $\frac{\partial E_3}{\partial x_3}$ (see their Figure 11) are all positive, their μ_{3333} is in fact negative.[Hirakata 21]

Other problems could arise because the MoS_2 samples used in the PFM experiments might not be as perfect as that used in our calculation. Indeed, intrinsic atomic defects have been observed in the CVD-grown monolayer MoS_2 using near-field photoluminescence imaging[Lee 15]. These defects could give rise to very localized strain gradients and therefore to noticeable additional polarization due to flexoelectricity, since monolayer MoS_2 is sensitive to any tiny deformation along vertical direction (z) due to its atomically thin thickness. Furthermore, the possibly existing interfacial contamination between substrate and MoS_2 sample and the other uncertainties relevant to the measurements could be another cause of discrepancy between our theoretical results and the experimental ones. It would be useful if these (difficult) experiments could be repeated many times, so as to reduce the large uncertainties on the experimental results, but we feel that our present results for μ_{3333} of a MoS_2 monolayer, agree well enough with experiment, to encourage us to compute other flexoelectric coefficients for MoS_2 monolayer, for which we do not have experimental data to compare with.

IV.6.2 Transverse flexoelectric coefficient μ_{3311}

The bending simulation described in the 'Methods' section is employed to compute the transverse flexoelectric coefficient μ_{3311} of MoS_2. Since the visible displacements are mostly along z direction, the strain gradient enabling polarization to be nonzero is principally G_{311}. Hence, μ_{3311} may be approximately expressed as $\mu_{3311} = \frac{\partial P_3}{\partial G_{311}}$. Fig.IV.5a presents the variations of the out-of-plane polarization P_3 for a MoS_2 flake bent along (x) zigzag direction with respect to the strain gradient G_{311}. One can notice that the intercept of the linear-fitting straight line is almost zero, meaning that the nonzero polarization is mainly caused by G_{311}.

Contrarily to what we did for the computation of μ_{3333}, periodic boundary conditions cannot be exerted in the bending simulation because bending of material submitted to the external electric field will break the periodicity of the lattice itself. We therefore studied the effect of the size of the MoS_2 flake, on the computed flexoelectric coefficient. Fig.IV.5b is plotted to present the variation of transverse flexoelectric coefficient μ_{3311} with the increasing number of atoms. It can be seen that the value of μ_{3311} scales non-linearly down with the number of atoms. The larger the number of atoms, the more obvious the trend of curve convergence. To obtain a converged value, data is fitted with an exponential function. With the number of atoms increasing, the transverse flexoelectric coefficient μ_{3311} converges to -0.1075 nC/m, comparable to that for phosphorene[Pandey 21a] and boron nitride sheet[Kundalwal 21]. A comparison is made between μ_{3311} computed with QP model and that obtained by DFT-based first principle calculation by Shashikant et al[Kumar 21], as listed in Table IV.4. It can be seen that our computed result for μ_{3311} agrees much better in absolute value with that obtained from DFT calculations than the one computed by Zhuang et al.[Zhuang 19], signifying that the computation of transverse flexoelectric coefficient of MoS_2 can be well captured by the QP model, if the proper definition for the polarization is used. Note that the radial polarization $\vec{p}_r$ defined in reference [Kumar 21] and [Springolo 21] to

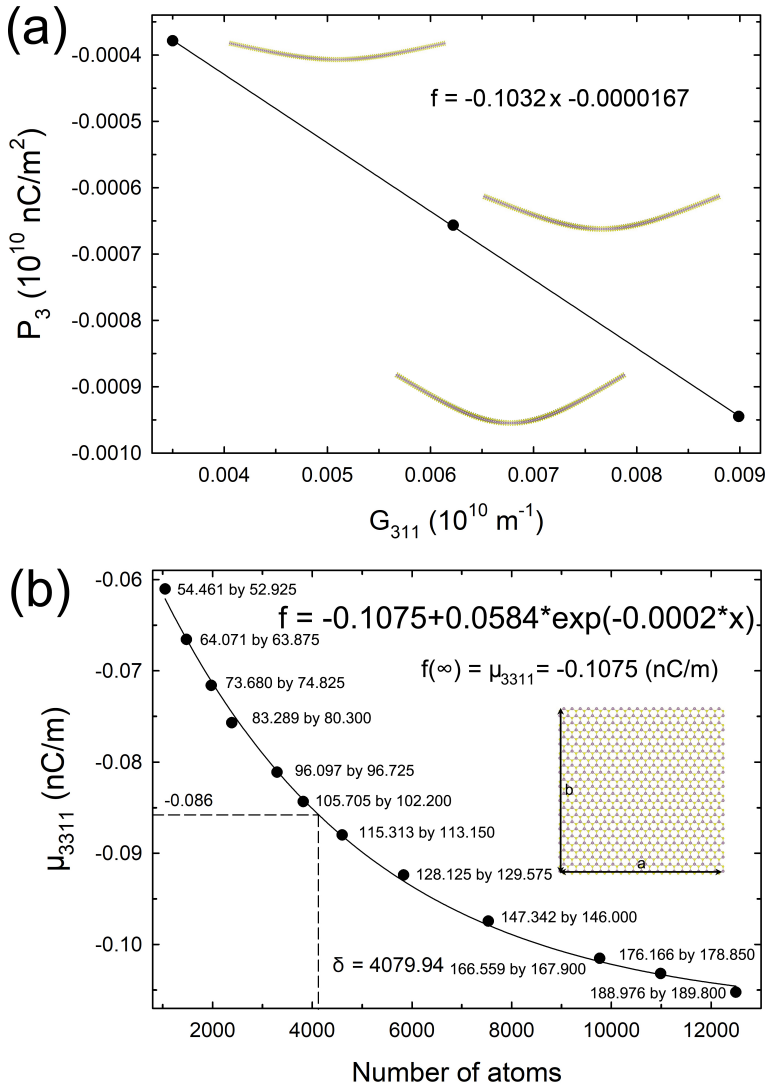

Figure IV.5: (a)Variation of P_3 with strain gradient G_{311}. The magnitude of the electric fields imposed to the MoS_2 monolayer for bending simulation are 0.0424 V/Å, 0.0566 V/Å, 0.0707 V/Å, respectively. (b)Transverse flexoelectric coefficient μ_{3311} vs number of atoms. An exponential function is used to describe the tendency to convergence. The lengths a and b of the sides of the MoS_2 flakes are marked next to each computed μ_{3311}. The first and second number for the size of MoS_2 flake corresponds to a and b, respectively. The unit of a and b is Å. δ denotes characteristic length of exponential function. The angle between the electric field and the positive direction of the x-axis is set to 45 degrees.

compute μ_{3311} can be considered equivalent to the p_z used in our work, since it is always locally perpendicular to the 2D material. We will now turn again to the question of the sign of the flexoelectric coefficients.

Table IV.4: Comparison between transverse flexoelectric coefficient μ_{3311} obtained by charge dipole model and theoretical computation.

Ref.	μ_{3311} (nC/m)
present work	-0.1075
Shashikant et al [Kumar 21]	0.14
Zhuang et al [Zhuang 19]	0.016

Understanding the reason causing the discrepancy in the sign of flexoelectric coefficients is essential because the direction of the electric polarization induced by flexoelectricity is of significance for sensors and energy harvesters. We will study successively the sign of the polarization and the strain gradient.

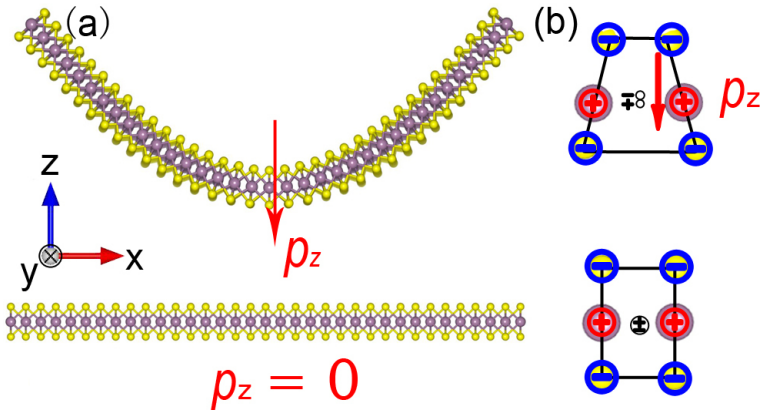

Figure IV.6: Origin of flexoelectric effect in bending deformation. (a) Under bending deformation, the direction of induced dipole moment points to -z direction. For an undeformed MoS_2 flake, the total dipole moment along the direction normal to the surface of MoS_2 is zero. (b) Separation of the centers (in black) of positive (in red) and negative charges (in blue) due to bending deformation.

Concerning polarization, we separate two distinct contributions: one due to the deformation of the lattice and the other one due to charge transfer between the inner and outer layers during bending. For that purpose we first compute the relaxed positions of a MoS_2 flake deformed under the action of an electric field, using the QP model (Fig.IV.6a). Then we compute the polarization for that bent MoS_2 flake, for an hypothetical case where the charges of the sulfur atoms would be the same in the upper and lower layers. In that hypothetical case, the computation gives a polarization in the negative direction of z axis, whereas in the undeformed MoS_2 flake, the total dipole moment along the out-of-plane direction is always zero due to the fact that the molybdenum atomic layer is equidistantly sandwiched between two layers of sulfur atoms. Fig.IV.6b illustrates this phenomenon with the case of the two rows of atoms nearest to the symmetry plane of the deformed

flake: the molybdenum cations are repelled away from the inner part of the bend (which is its denser part). The consequence is that, while the charge center of the sulfur anions stays half way between the two layers, the charge center of the molybdenum is lower which results in a polarization pointing downwards (hence a negative contribution to μ_{3311} since G_{311} is positive in that case).

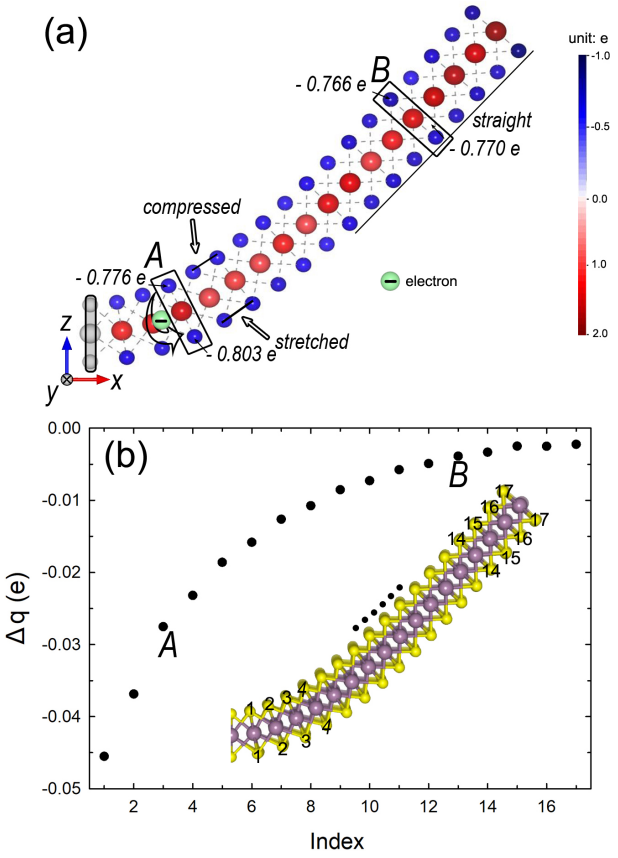

Figure IV.7: (a) Charge distribution of a bent MoS_2 subjected to $E_x = E_z = 0.4$ V/Å. A and B are two representative regions for explanation of charges transfer from the upper layer to the lower layer, respectively. (b) Δq vs index. Δq is calculated as the charge of sulfur atoms in the lower layer minus the corresponding quantity for the upper layer. The upper and lower sulfur atoms are numbered by increasing value of z. Only the right portion of the bent MoS_2 is shown here.

However, the above effect is not enough to fully account for the polarization since we artificially used identical charges for the sulfur atoms. In reality, since the overlapping of the electronic clouds of two nearby ions change during bending, partial charges can be transferred from one sulfur layer to the other. In order to understand that second contribution to the polarization, two representative areas of the same deformed MoS_2 flake, named A and B, are considered in Fig.IV.7a. The average charge for the sulfur atoms in the upper and lower layers, calculated by averaging net charges obtained by the QP model along y direction perpendicular

to the figure, are $-0.776\ e$ and $-0.803\ e$, respectively. Therefore the atoms of the lower sulfur layer appear to be more negative than those of the upper layer. This creates a net dipole moment pointing from the outside to the inside of the curvature (in the positive direction of z axis in our case). At the B site, the curvature is much smaller than at the A site and consequently the difference in charges between sulfur atoms in the upper and lower layer is smaller. In Fig.IV.7b, we plotted the average charge difference $\Delta q = q_{lower} - q_{upper}$ between sulfur atoms in the lower and upper layer, as a function of their index along the x coordinate (see numbers on the molecular picture inside the graph). It can be seen that the absolute value of Δq decreases with the increasing index of sulfur, which agrees with what we expected before implementing the computation, since it corresponds to the flexoelectric effect: if the strain gradient is smaller, then the polarization is smaller (in absolute value). Hence, we have two contributions in opposite directions: a downward electric dipole moment due to bending of the lattice and an upward electric dipole moment due to charge transfer. In the case of MoS_2, our computations show that polarization caused by bending deformation of lattice (which tends to give a negative flexoelectric coefficient) surpasses that resulting from charge transfer (which tends to give a positive flexoelectric coefficient). It is worth mentioning here that a negative μ_{3311} for MoS_2 monolayer has very recently been obtained using first-principles linear-response theory[Springolo 21]. Very interestingly, it can be found in their calculations that two contributions coming from the dipolar and the lattice-mediated response, respectively, to the total polarization response also play a competing role, the signs of the former and the latter tending to be opposite, as in our study.

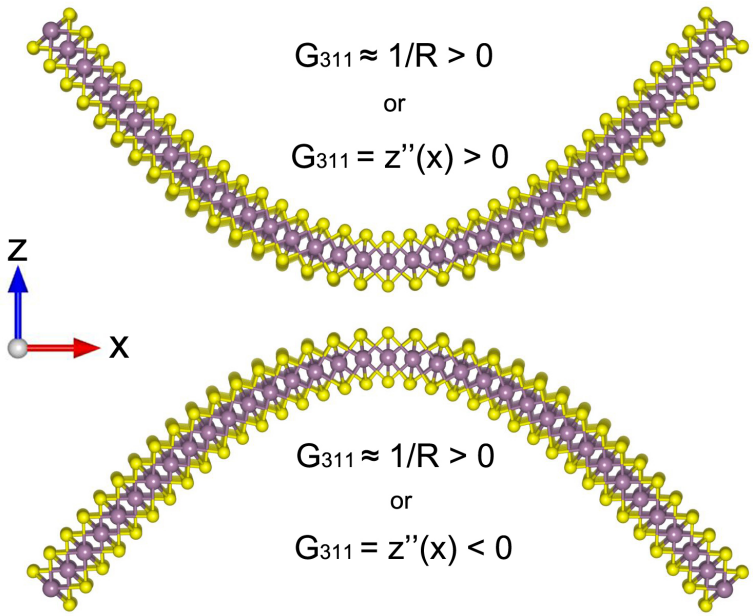

Figure IV.8: Illustration of the different definitions for strain gradient G_{311}.

We now turn to the sign of the strain gradient. In a review paper, Wang et al[Wang 19] pointed the discrepancies between definitions and symbols of physical quantities to be one of the reasons for the inconsistency of the reported signs of flexoelectric coefficients. It is often the case for the strain gradient G_{311}. Indeed, on Fig.IV.8 we illustrate that the strain gradient, defined as $G_{311} = u_z''(x)$ which can be either positive or negative, is often approximated as the inverse of the radius of curvature. Since, for some authors, the radius of curvature is always positive, G_{311} is always positive for them, regardless of the bending direction of the material. Slightly differently, Kundalwal et al[Kundalwal 21] considered a boron nitride sheet shaped as an upward convex curved arch and defined G_{311} as the absolute value of the inverse of radius of curvature. We note, however, that we used a downward pointing bend (top part of Fig.IV.8 and Fig.IV.6) which gives a positive strain gradient for all these definitions.

The previous considerations tentatively explain why flexoelectric coefficients can be either positive or negative, due to a competition between lattice and charge transfer effect, and not always positive as some authors define it by using absolute values inside their definition.

IV.6.3 In-plane flexoelectric coefficient μ_{1111} and μ_{2222}

Inspired by the work of Hong et al[Hong 10], the in-plane flexoelectric coefficients μ_{1111} and μ_{2222} are computed in the present work. Strain gradient G_{111} is created by displacing every atoms along x axis, according to a parabolic displacement function $u_x(x)$. Fig.IV.9a is a schematic diagram showing the transverse displacement of atoms for a MoS_2 flake with a bigger (so that it be visible thanks to the two vertical lines) strain gradient imposed along x axis. Fig.IV.9b shows the variation of displacement of atoms along x direction in the case $\Delta d = u_x(x) = 0.01 - 10^{-5}x^2$, strain ϵ_{xx} and strain gradient $\epsilon_{xx,x}$ (G_{111}) as functions of the position along x axis for MoS_2. We can see that the total strain is zero due to the symmetric distribution of displacement with respect to $x = 0$. Hence, the polarization due to piezoelectricity can be fully removed from the total polarization, leaving only flexoelectricity. Furthermore, μ_{1111} can be expressed as $\mu_{1111} = \frac{\partial P_1}{\partial G_{111}}$ and for a similar simulation with parabolic displacement along y, $\mu_{2222} = \frac{\partial P_2}{\partial G_{222}}$. The magnitude of strain gradient for our calculations of μ_{1111} and μ_{2222} ranges from 0 to 0.00004 $Å^{-1}$, which is small enough to neglect any non-linear effect.

The dependence of in-plane flexoelectric coefficients μ_{1111} and μ_{2222} on the width of nanoribbon with infinite lengths is shown in Figure IV.10. Clearly, the in-plane flexoelectric coefficients increase as the width of nanoribbons increases (polynomial fits are guides to the eye). The non-convergence behavior of those flexoelectric coefficients with the increase of the width of the nanoribbons has been elaborately discussed[Hao 21]. Hao et al. reveals through DFT calculations that the flexoelectric coefficients of the 2D Janus TMDs nanoribbons depend strongly upon their widths. The (slightly) different results for the two orientations are probably due to edge effects different for armchair and zigzag edges. To completely

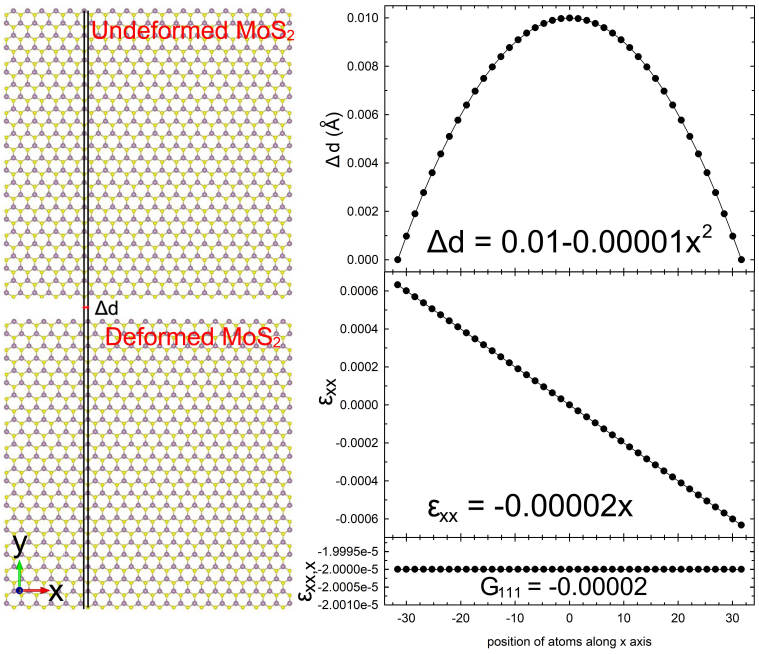

Figure IV.9: (a) Applied displacement field along x axis for each atom with Δd denoting the difference between the x coordinate of atoms in deformed MoS_2 and that in undeformed MoS_2. The two vertical lines are guides to the eye to see the displacements along x between the top and bottom sub-figures. (b) Displacement field $\Delta d = u_x(x)$, strain (ϵ_{xx}) and strain gradient ($\epsilon_{xx,x} = G_{111}$) vs the position along x axis for MoS_2.

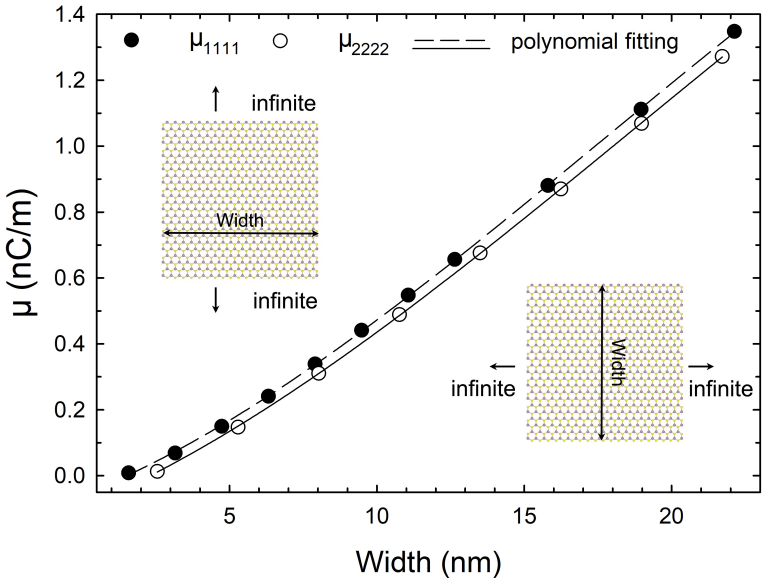

Figure IV.10: μ_{1111} and μ_{2222} as a function of width for MoS_2 nanoribbons with an infinite length and a finite width

eliminate edge effect we use periodic boundary conditions in both directions for the displacements. In their article,[Hong 10] Hong et al. computed the in-plane flexoelectric coefficients of $SrTiO_3$ using a strain gradient with a cosine form, to be compatible with the periodic boundary conditions.

In our work, strain gradient is a constant function (see Fig.IV.9b), which is an even simpler case. Fig.IV.11 shows the variations of polarization P_1 and P_2 with strain gradient G_{111} and G_{222} for those doubly-periodic setups. The computed flexoelectric coefficients μ_{1111} and μ_{2222} are 0.6872 nC/m and 0.7119 nC/m, respectively. Hence, the in-plane flexoelectric properties of doubly-infinite MoS_2 are nearly isotropic, i.e. independent of the zigzag or armchair direction.

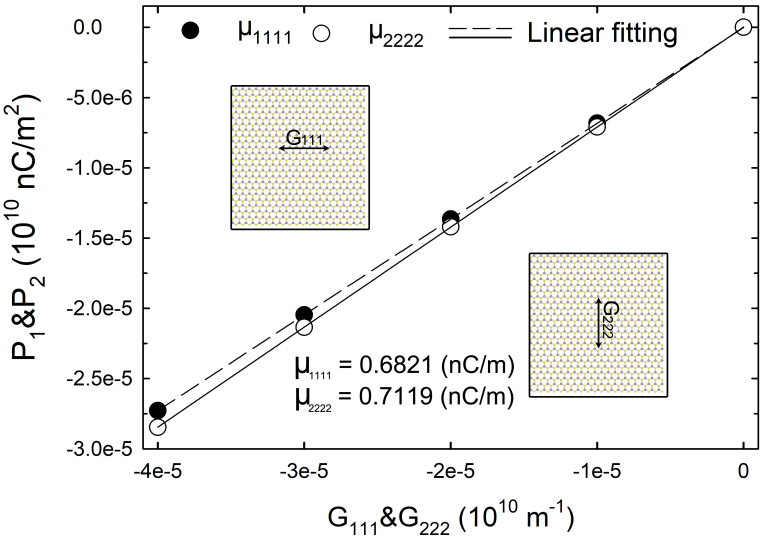

Figure IV.11: Variations of polarization P_1 and P_2 with strain gradient G_{111} and G_{222}, respectively. The rectangular frame surrounding the edge of molybdenum disulfide represents the enforcement of periodic boundary conditions in both directions.

IV.7 Conclusions

Employing three different simulation setups, we calculated in-plane flexoelectric coefficients μ_{1111}, μ_{2222}, transverse flexoelectric coefficient μ_{3311} and out of plane flexoelectric coefficient μ_{3333} for monolayer MoS_2 using the charge dipole model and charge conservation. The out-of-plane flexoelectric coefficient μ_{3333} and transverse flexoelectric coefficient μ_{3311} computed by the charge-dipole model are compared with those obtained by experimental measurements and DFT-based first principle calculations, by which good agreement in absolute value can be seen when the charge term is included in the computation of the polarization. We discuss in details possible origins of discrepancy in sign between our calculated flexoelectric coefficient μ_{3311} and other reported results, by showing two opposite effects for the

sign of the polarization. Furthermore, we emphasize that comparison of flexoelectric coefficients between different computational works requires a careful check for the sign of strain gradient and the way of defining the polarization. Concerning the computed in-plane flexoelectric coefficient μ_{1111} and μ_{2222} are found to be quasi identical, which is consistent with the analysis of symmetry for the flexoelectric coefficient tensor of a 2D continuum.

Finally, it is worth pointing out that the computed in-plane flexoelectric coefficient is about twenty times greater than out-of-plane flexoelectric coefficient for MoS_2, which can be ascribed to the fact that the net charges induced by in-plane strain gradient between every primitive cells lead to the generation of larger electric dipole moments, whereas the movement of the charge in the out-of-plane direction is restricted due to the finite thickness. Hence, a relatively small polarization is then induced in the out-of-plane direction. For 2D materials, bending seems to be the easiest way to externally generate a big strain gradient at nanoscale, on a large area. Therefore, even if in-plane flexoelectric coefficients may play a role in some systems, the differences between in-plane, out-of-plane and transverse coefficients in MoS_2 flakes is not big enough to compensate for the bigger and more homogeneous strain gradient that can be realized by bending. It is thus important to find 2D materials that optimize the transverse flexoelectric coefficients μ_{3311} for applications in energy harvesting.

Chapter V

Computation of Flexoelectric coefficient of bilayered materials

V.1 Introduction 86

V.2 Methods 86

V.2.1 First principle calculations 86

V.2.2 Molecular dynamics simulations for computation of μ_{3311} 87

V.2.3 Computation of polarization. 88

V.3 Structural properties of graphene/h-BN heterostructures 90

V.4 Parameterization of the charge dipole model for Graphene/Boron Nitride heterostructure system 92

V.5 Validation of the charge dipole model 94

V.6 Computation of bending flexoelectric coefficient for graphene, h-BN and their vertically stacked heterostructure 98

V.7 Conclusion 103

V.1 Introduction

As we saw in chapter 1 and in the introduction of chapter 4, recently, there has been an upsurge in studies on flexoelectricity in two-dimensional materials, leading to computations for bilayer or multilayer homogeneous or heterogeneous materials constituted by previously studied 2D materials. For instance, Zhuang's group very recently reported flexoelectric coefficient μ_{3311} for bilayer MoS_2[Sun 22], computed using charge dipole model in combination with a machine-learning potential. With the same computation method, they also computed flexoelectric coefficient μ_{3311} of some bilayer materials composed of those from several materials groups, e.g. TMDs, Diamanes and BN diamanes[Javvaji 22]. Furthermore, V.K. Choyal computed μ_{3311} of BN with odd-numbered layers(1 layer-11 layer) and studied the relationship between the flexoelectric coefficients of multilayer BN and the number of layers[Choyal 22]. The flexoelectricity in a 100 nm-thick $BaTiO_3$ (BTO) thin film based metal/ferroelectric insulator/semiconductor heterostructure was studied[Huang 18].

Due to relevance of our implementation of the charge dipole model in the calculation of the flexoelectric coefficients of an MoS_2 monolayer, we also wanted to go one step further and focus in this chapter on the calculation of the flexoelectric coefficient of a bilayered heterostructure of graphene and 2D Boron Nitride, with mostly the same research methodology as in the previous chapter.

V.2 Methods

V.2.1 First principle calculations

We perform density-functional theory (DFT) calculations using the projector-augmented wave method with a plane wave basis set, as implemented in the Vienna *ab initio* Simulation Package (VASP) [Kresse 96]. Perdew-Burke-Ernzerhof (PBE) exchange-correlation functionals are used within the generalized gradient approximation (GGA)[Perdew 96]. The plane-wave cutoff energy is taken to be 450 eV for structure relaxation and 600 eV for the computation of properties of polarization. In order to minimize the periodic interaction along the z-direction, the vacuum space between the layers is taken to be at least 15 Å. Brillouin zone integration is applied with a $6 \times 6 \times 1$ grid for geometry optimization and a $26 \times 26 \times 1$ grid for polarization calculations, using the Γ-center scheme. Conjugate gradient algorithm is applied for energy minimization calculation, with convergence criteria for electronic and ionic relaxations set as 10^{-6} eV and 10^{-3} eV/Å, for the total energy and force, respectively.

Table V.1: Parameters of LJ potential for the interactions between carbon and boron and between carbon and nitrogen

	σ (Å)	ε (eV)
carbon-boron	3.411	0.003293
carbon-nitrogen	3.367	0.004068

V.2.2 Molecular dynamics simulations for computation of μ_{3311}

The Large scale Atomic Molecular Massively Parallel Simulation (LAMMPS) software[Plimpton 95] is employed to simulate the bending deformation of graphene alone, hexagonal boron nitride (h-BN) alone and several Graphene/hexagonal Boron Nitride (GBN) heterostructures. Regarding force field, Adaptive Intermolecular Reactive Empirical Bond Order (AIREBO) potential[Stuart 00] is adopted to describe the interaction between carbon atoms in graphene. Tersoff potential[Tersoff 88] is utilized to describe the interaction between boron and nitrogen atoms in h-BN. Finally, interactions between carbon and boron or carbon and nitrogen are described by a Lennard-Jones (LJ) potential[Jones 24a, Jones 24b]:

$$V(r) = 4\varepsilon \left[\left(\frac{\sigma}{r}\right)^{12} - \left(\frac{\sigma}{r}\right)^{6} \right] \tag{V.1}$$

where the parameters σ and ε represent the characteristic distance and energy for a given pair of atoms, and r represents the actual distance between those atoms. The cutoff radius is taken to be 2.5σ, as is common in comparable simulations. The LJ parameters we used, are listed in Table V.1[Iwata 18, Neek-Amal 14].

For simulation setup, we consider a rectangular supercell with a width of 12.5621 nm and a length of 2.0308 nm. A period of 2.2356 nm is applied in the width direction of the flake to avoid edge ripples caused by concentrations of stress field occurring at the edge of the flake. Periodic boundary conditions are considered in both charge dipole model and potential function used in LAMMPS. The bending simulation for GBN heterostructure is performed by minimizing the total energy function which includes the interaction between carbons (AIREBO potential), between boron and nitrogen (Tersoff) and intermolecular pair potential for carbon-boron and carbon-nitrogen interactions (LJ potential). The additional energy (E_{QP}) and force (F_{QP}) due to the action of an external electric field are added to the total energy and force via the command "addforce" in LAMMPS. Furthermore, we kept fixed the coordinates of some atoms (the middle rows of atoms) by applying "fix setforce 0.0 0.0 0.0" to those atoms. A built-in "shell" command is used to call a compiled binary executable for computing E_{QP} and F_{QP} in the input file of LAMMPS. The FIRE algorithm, as proposed in 2006[Bitzek 06], is used for energy minimization calculation. The time step is set to 0.002 picoseconds. Velocity Verlet integration is used. Energy minimization is performed until

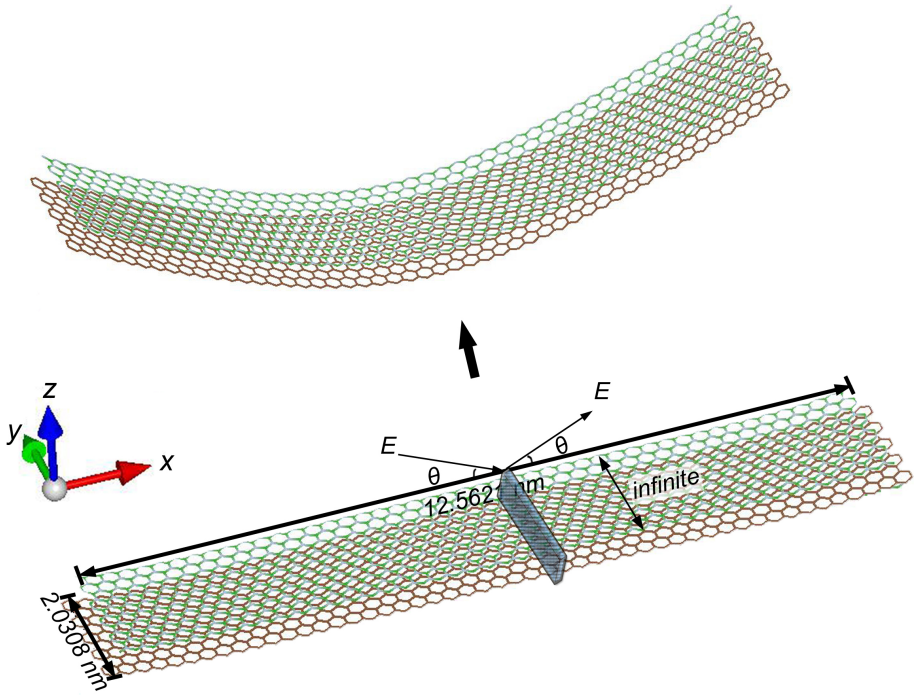

Figure V.1: Schematic of bending simulation for a 12.5621 nm by 2.0308 nm graphene/h-BN nanoribbon in which the upper layer is graphene and the lower layer is h-boron nitride. A ↘↗-like external electric field $\vec{E}$ is applied to the graphene/h-BN nanoribbon, keeping the middle row of atoms fixed. Periodic boundary conditions are imposed along the y axis. θ is the angle with the $+x$ direction.

force falls below 0.0001 eV/Å. The application of some constraints is entirely the same as in chapter 4. More information on the bending simulation can thus be found in chapter 4.

V.2.3 Computation of polarization

In curved graphene, the curvature of the graphene sheet causes a change in the hybridization of the orbitals of the valence electrons of the carbon atoms. In 2002, Dumitrică et al.[Dumitrică 02] showed by ab-initio calculations that this change of hybridization creates a permanent dipole on each carbon atom, which is function of the angle $\theta_{\sigma\pi}$ between the σ and π bonds (cf. Fig. V.2). This was then utilized again in the context of the flexoelectricity of sp^2-hybrided carbon nanomaterial, such as, nanotubes, fullerenes, and nanocones by Kvashnin et al[Kvashnin 15] in 2015. According to these authors, the permanent dipole created by the local curvature of the graphene sheet can be calculated by:

$$\forall \alpha = 1, \ldots, N, \quad \vec{\mu}^{\alpha} = \vec{\mu}\left(\theta_p^{\alpha}, \vec{n}^{\alpha}\right) = f_{\theta}\theta_p^{\alpha}\vec{n}^{\alpha} \tag{V.2}$$

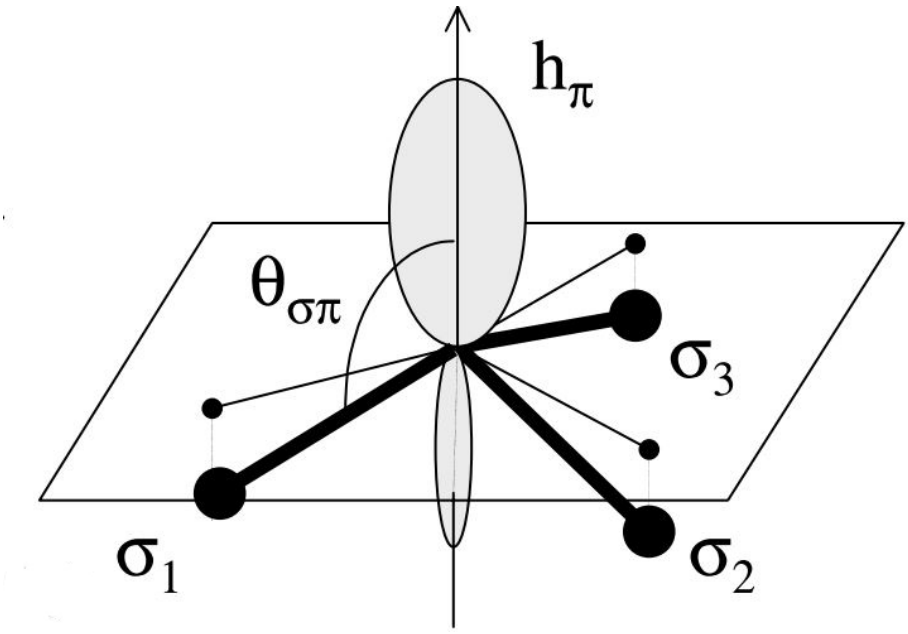

Figure V.2: Before bending, the π-orbitals of graphene are symmetric and oriented perpendicularly to the plane formed by the three C-C bonds. After bending, charges in π-orbitals are redistributed due to hybridization with σ orbitals.

where $\theta_p^\alpha = \theta_{\sigma\pi} - \pi/2$ is the pyramidal angle between the atom α and the plane formed by its three nearest neighbors. $\vec{n}^\alpha$ corresponds to unit normal vector perpendicular to the π plane. The effective flexoelectric constant f_θ was calculated, by Kvashnin et al, to be 2.34 D/rad by linear regression of the calculated values of $\vec{\mu}^\alpha$ as a function of θ_p^α for nanotubes with various indices. For graphene, we therefore used Eq.V.2 to compute the 'permanent' dipoles $\vec{\mu}^\alpha$ that allowed us to calculate the z component of polarization as:

$$P_3^{tot} = \frac{\sum_{\alpha=1}^{N} \mu_3^\alpha}{V} \tag{V.3}$$

with N being the total number of atoms, 3 meaning the z direction and V denoting volume of the graphene sheet, computed using a thickness equal to 3.50 Å [Ishigami 07]. Finally, for the computation of polarization for h-BN alone or in the GBN heterostructure, we followed exactly the same procedure as that described in the previous chapter, with a thickness for h-BN equal to 0.906 Å[Yan 19] and a thickness for AB-stacked, AB′-stacked and AA-stacked GBN equal to 5.593 Å, 5.753 Å and 5.753 Å respectively, which were obtained as the sum of the interlayer spacing (obtained in next section), half the thickness of h-BN and half the thickness of graphene.

Table V.2: Nearest neighbor distance in Å of graphene and h-BN monolayer

	graphene	h-BN
Nearest neighbour distance (Our work)	1.42	1.45
Nearest neighbour distance ([Pakdel 12])	1.42	1.44

V.3 Structural properties of graphene/h-BN heterostructures

We first discuss the physical structures of a pristine graphene monolayer and an h-BN monolayer considered independently, at their mechanical equilibrium state, by calculating their nearest-neighbor and next nearest-neighbor distance, using VASP with parameters given in subsection V.2.1. It can be seen from Figure V.3 (a) and (b) that the nearest-neighbor distance is computed to be 1.45 Å and 1.42 Å for h-BN monolayer and graphene, well consistent with that reported experimentally in [Pakdel 12] (see Table V.2). The next nearest-neighbor distance computed for h-BN and graphene monolayer are 2.51 Å and 2.47 Å, respectively, as marked in Figure V.3 (a) and (b).

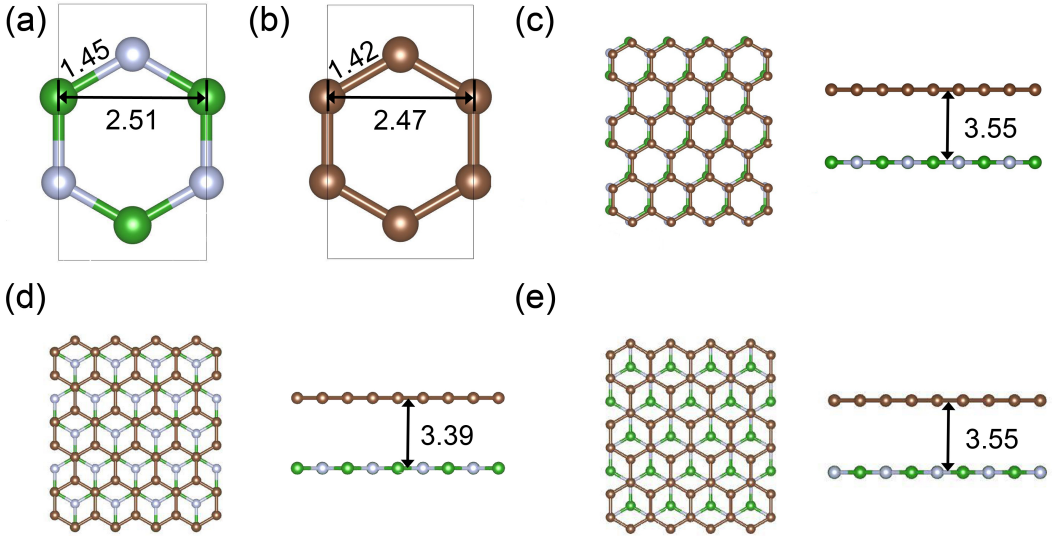

Figure V.3: Computationally obtained configurations for h-BN (a), graphene (b), AA-stacked (c), AB-stacked (d) and AB′ (e) graphene/h-BN heterostructure. Nearest and next-nearest neighbour distances for graphene and h-BN are respectively marked in (a) and (b). Boron atoms are in green and nitrogen atoms in white. The equilibrium inter-layer distances, computed within DFT-D3 plus PBE, for AA-stacked (c), AB-stacked (d) and AB′ (e) graphene/h-BN heterostructure are indicated in the corresponding subfigures

Regarding the graphene/h-BN heterostructure, we consider three inequivalent stackings of graphene on h-BN, see Figure V.3 (c), (d) and (e):

1. AA-stacking configuration where all carbon atoms directly sit on either boron or nitrogen atom in h-BN.

2. AB-stacking configuration with one carbon over boron and the other carbon centered above an h-BN hexagon.

3. AB′-stacking configuration with one carbon over nitrogen and the other carbon centered above an h-BN hexagon.

The knowledge of equilibrium layer spacing of vertically stacked GBN heterostructure is of importance for the calculation of the flexoelectric coefficient to be reported in section V.6 and we therefore computed inter-layer distance of three stackings of graphene on h-BN with Grimme et al's DFT-D3 correction[Grimme 11] that is considered to be computationally efficient and robust across the periodic table, which makes this correction particularly valuable for the treatment of large systems[Goerigk 17].

The computed equilibrium interlayer distances are 3.55 Å for AA stacking, 3.39 Å for AB stacking and 3.55 Å for AB′ stacking, in agreement with previous computational results[Fan 11], as tabulated in Table V.3. Experimentally, a value of 3.32 Å was reported[Haigh 12], well consistent with our computed result for AB-stacked GBN heterostructure. The differences in the calculated inter-layer distances between these three different stacking cases are mainly related to the attractive interaction between π electrons and cations (boron) and repulsive interaction between π electrons and anions (nitrogen). Nitrogen atoms tend to stay below the center of carbon hexagons since the density of π electrons is very low there, whereas boron prefers to be right on top of the carbon around which the density of electron is relatively high. Therefore, among the three cases, the GBN heterostructure stacked in AB form has the lowest inter-layer distance, and is also the most energetically favorable structure. These computationally obtained results completely accord with those previously reported[Fan 11]. For further illustration of the results, we also performed molecular static energy minimization calculation using LAMMPS with LJ potential describing the interlayer vdW interaction of GBN heterostructure. It can be found that no matter how the GBN heterostructure is stacked in the initial configuration, its energy-converged structure always tends to the AB-stacked GBN heterostructure. The layer spacing of GBN heterostructure was also calculated without vdW correction (see Table V.3). It can be found that the calculated results differ significantly with and without vdW correction, demonstrating that within density functional theory, the enforcement of vdW correction plays an indispensable role in the calculation of the interlayer spacing for layered material. Moreover, from the energy point of view, AB-stacked GBN heterostructure is in the most stable state, while the other two kinds are in a metastable state. This does not, however, suggest that AA and AB′ stacked GBN heterostructure could not be prepared in real experiment. In fact, it has been reported by Kim et al. in an experimental work that AA-like stacked graphene/hBN heterostructure can be successfully synthesized using a dedicated

Table V.3: Equilibrium layer spacing in Å for AA, AB and AB′-stacked GBN heterostructure with and without vdW corrections. ref[a]:[Giovannetti 07], ref[b]:[Fan 11], ref[c]:[Haigh 12]

	AA		AB		AB'	
	None	vdW	None	vdW	None	vdW
Interlayer distance (Our work)	4.22	3.55	3.73	3.39	3.84	3.55
Interlayer distance [refs]	4.41[a]	3.62[a],3.50[b]	–	3.22[b],3.32[c]	–	3.40[b]

synthesis sequence[Kim 13]. Hence, in this work, we intend to compute the bending flexoelectric coefficient μ_{3311} of GBN heterostructures with the three types of stacking above mentioned.

V.4 Parameterization of the charge dipole model for Graphene/Boron Nitride heterostructure system

We first make a rough estimate of the parameters (R and χ) used in the charge dipole model using a self-made iterative algorithm program. Specifically, the bounds of the twelve parameters, inner and edged value for both R and χ each for three types of elements (carbon, nitrogen and boron), is initially specified, with R and χ belonging to [0,1] and [1,200], respectively. Considering the running time of optimization calculations, we first select some equidistant values, i.e, 0.1, 0.2, $0.3 \cdots$, 1 Å for R_α and 1, 2, 3, $\cdots$, 200 V for χ_α for parameters to be input into the program. With these selected parameters $\{R_\alpha\}_{\alpha=1,\cdots 12}$ and $\{\chi_\alpha\}_{\alpha=1,\cdots 12}$, multiple sets of effective charges may be obtained from charge dipole model through iterating over all possible parameter combinations. Each set of calculated charge values corresponds to a set of parameters. We evaluate how close the calculated charge value (Q_{QP}) is to that calculated by DFT (Q_{DFT}) by calculating the ratio of the difference between the charge value calculated by the charge dipole model and the DFT-computed charges divided by the DFT-computed charges, which can be formulated as $f(Q_{QP}) = |(Q_{QP} - Q_{DFT})/Q_{DFT}|$, with Q_{QP} being function of $\{R_\alpha\}_{\alpha=1,\cdots 12}$ and $\{\chi_\alpha\}_{\alpha=1,\cdots 12}$ for a configuration with known coordinates. We chose the set of parameters that yielded the minimum value of the objective function $f(Q_{QP})$ among all those we computed. More details about this algorithm can be found in our previous work[Yang 18].

These parameters, which are roughly estimated by using the procedure mentioned above, need to be refined in order to obtain higher precision parameters. In view of the difficulty of obtaining the derivatives of the objective function $f(Q_{QP})$ with respect to the R_α, χ_α, we exploited a numerical optimization al-

Table V.4: Values of the Gaussian charge density widths and atomic electronegativities for boron, nitride and carbon.

Atom	R(Å)		χ(V)	
	Inner	Edged	Inner	Edged
B	0.3017	0.4853	19.9221	47.7300
N	0.1466	0.3963	201.5337	91.8163
C	0.7712	0.9591	67.1012	67.4874

gorithm named BOBYQA (Bound Optimization BY Quadratic Approximation) developed by Michael J. D. Powell[Powell 09] to refine these parameters, since BOBYQA does not require to compute the derivative of the objective function with respect to its variables. The resultant refined values of R and χ for inner and edge boron, nitrogen and carbon atoms are listed in Table V.4. It can be seen that values of R are larger for edged atoms, which seems physical since atoms at the edges can be polarized more strongly than the inner atoms, due to the extra space available for the orbitals. These values are similar to the Gaussian charge distribution widths in sp^2-hybridized carbon nanomaterials[Mayer 07a] and MoS_2[Yang 18]. Concerning χ, it is well-known that the rank order of Pauling electronegativities is nitrogen (3.04) > carbon (2.55) > boron (2.04). Fortunately, the ordering of the electronegativity parameters obtained here (which are more like Mulliken electronegativities, though they do not seem to have the same order of magnitude) is exactly the same as that with Pauling's electronegativities.

A comparison is made between the distributions of intrinsic charges (in electron per atom), calculated by the charge dipole model and first principle calculations on AA-stacked GBN heterostructure flakes, as shown in Figure V.4(a). It can be seen that agreement on the average charge density of the intrinsic charge $\bar{\rho}$ is quite good, suggesting that the distribution of intrinsic charge in GBN heterostructure can be well captured by the QP model. Moreover, we can also see that the set of parameters obtained for the AA-stacked GBN flake can also be successfully applied to calculate the charge of the AB-stacked GBN flake, as shown in Figure V.4(b), illustrating that such a set of parameters possess good transferability, at least among GBN stackings.

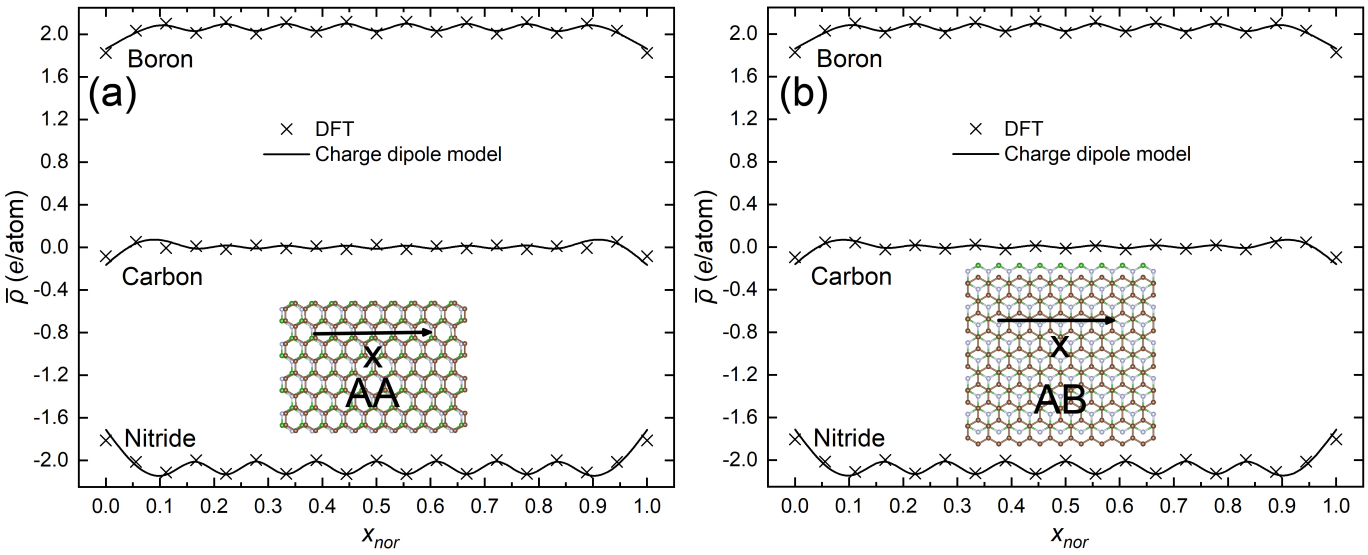

Figure V.4: y-averaged intrinsic charge density profile $\bar{\rho}$, in e/atom, for boron, nitride and carbon atoms in a (a) AA-stacked and (b) AB-stacked Graphene/Boron Nitride heterostructure vs the normalized x_{nor} coordinate along the flake ($x_{nor} = x/L$ where L is the length of the flake in the x direction).

V.5 Validation of the charge dipole model

In this section, the parameters obtained for the charge-dipole (QP) model will be validated by comparing the piezoelectric coefficients of AA-stacked GBN computed using the QP model with the same coefficients computed using VASP.

Since there are several possibilities for computing piezoelectric coefficients with VASP, we first conducted benchmark calculations of piezoelectric coefficient e_{222} for five selected 2D materials, using either Berry Phase approach[Vanderbilt 00] or Density Functional Perturbation Theory (DFPT)[Wu 05], as implemented in the VASP package.

For the former, an uniform strain, with its value ranging from -0.01 to 0.01 by steps of 0.005, is applied along armchair side of the rectangular cell (see inset of Figure V.5(b)) by changing the y-direction length of the lattice. A first set of coefficients, called clamped-ion coefficients, is then computed in order to concentrate on the purely electronic contribution and compare to the results of other authors[Duerloo 12]. Then, the atoms are relaxed, while preserving the shape and area of the supercell, to yield so-called relaxed-ion coefficients that thus include both the electronic and ionic contributions. When using the Berry phase method, the piezoelectric coefficient e_{222} can be defined as the ratio of change in polarization to a strain change, formulated as $e_{222} = \partial P_2/\partial \varepsilon_{22}$ and estimated as the slope of fitted straight lines in the graphs of P_2 as a function of ε_{22}, as can be seen on Figure V.5. Results are given in Table V.5.

Note that, since definitions and therefore values of thickness for 2D-materials vary between authors, it is customary to report total dipole per unit area for the 2D-material, since this quantity, contrarily to the usual polarization, is independent of the chosen thickness. In this subsection, polarization P_2 and coefficient e_{222} are therefore defined with respect to the area of the simulation box rather than to its volume, so that they are expressed in C/m instead of C/m^2 (see *e.g.* y axis legend in Fig. V.5).

For the DFPT method, there is only a single set of values in Table V.5, because in that method e_{222} is estimated using the change of stress caused by a change of external electric field: $e_{222} = -\partial\sigma_{22}/\partial E_2$.

The comparison of our results with reported data also given in Table V.5 clearly shows that using either DFPT or Berry phase method, the calculated results for piezoelectric coefficients for the five selected 2D materials are in good agreement with the data from the literature and that results of the Berry phase method for the relaxed structure are quite close to those of the DFPT method.

Surprisingly, though, the experimental value for MoS_2 (2.9×10^{-10} C/m) [Zhu 15] is closer to the clamped-ion piezoelectric coefficient (3.18×10^{-10} C/m) than to the two other coefficients.

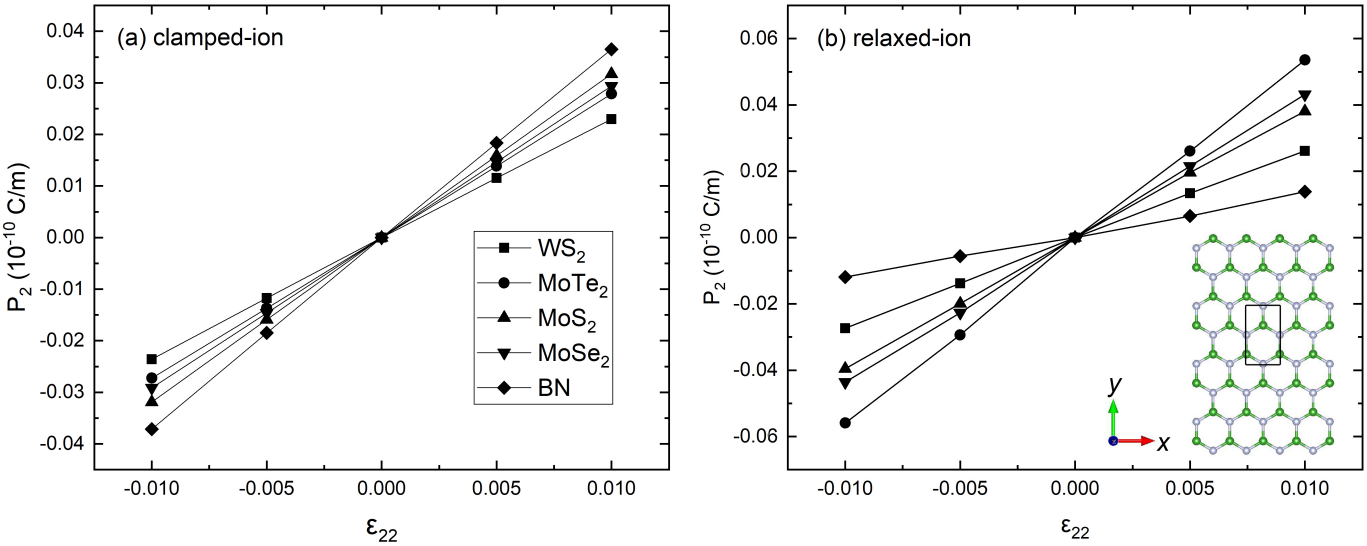

Figure V.5: (a) Clamped-ion and (b) relaxed-ion polarization change under applied uniaxial strain (ϵ_{22}) along the y direction for the selected 2D materials including h-BN, MoS_2, $MoTe_2$, WS_2 and $MoSe_2$. Piezoelectric coefficient is determined from the slope of the fitted straight line. The inset in (b) shows the geometry of a monolayer of boron nitride (h-BN) from top view, with the black rectangular frame representing a periodic cell used for computation of polarization

Secondly, we used the slope of the straight line fit of $P_2 = f(\epsilon_{22})$ to compute the relaxed-ion piezoelectric coefficient e_{222} for an AA-stacked GBN heterostructure, using the QP model with the parameters reported in Table V.4. As shown in Figure

Table V.5: Piezoelectric effective coefficient e_{222}/e_{yyy} for various 2D materials (in unit of 10^{-10} C/m since we do not divide by the thickness of the 2D-material), computed by DFT calculations using density functional perturbation theory or Berry phase method. First three lines give our results, last three lines give corresponding results from the literature.

Material	h-BN	2H-MoS_2	2H-$MoTe_2$	2H-WS_2	2H-$MoSe_2$
DFPT	1.39	3.68	4.70	2.44	3.83
clamped-ion (Berry phase)	3.68	3.18	2.76	2.33	2.93
relaxed-ion (Berry phase)	1.27	3.90	5.49	2.68	4.35
ref (DFPT)[Blonsky 15]	1.39	3.64	4.67	2.43	3.83
ref clamped-ion (Berry phase)[Duerloo 12]	3.71	3.06	2.98	2.20	2.80
ref relaxed-ion (Berry phase)[Duerloo 12]	1.38	3.64	5.43	2.47	3.92

V.6, the agreement is quite good with the results of the Berry phase method for the relaxed-ion configuration. This suggests that the polarization properties of 2D materials can be well captured by charge dipole model provided a set of good parameters ($\{R\}_{\alpha=1,\cdots N}$ plus $\{\chi\}_{\alpha=1,\cdots N}$) is used. However, we also note that for h-BN alone the QP model results (using the parameters for N and B found for the GBN heterostructure) compare less favorably with the DFT results, as shown in Figure V.7.

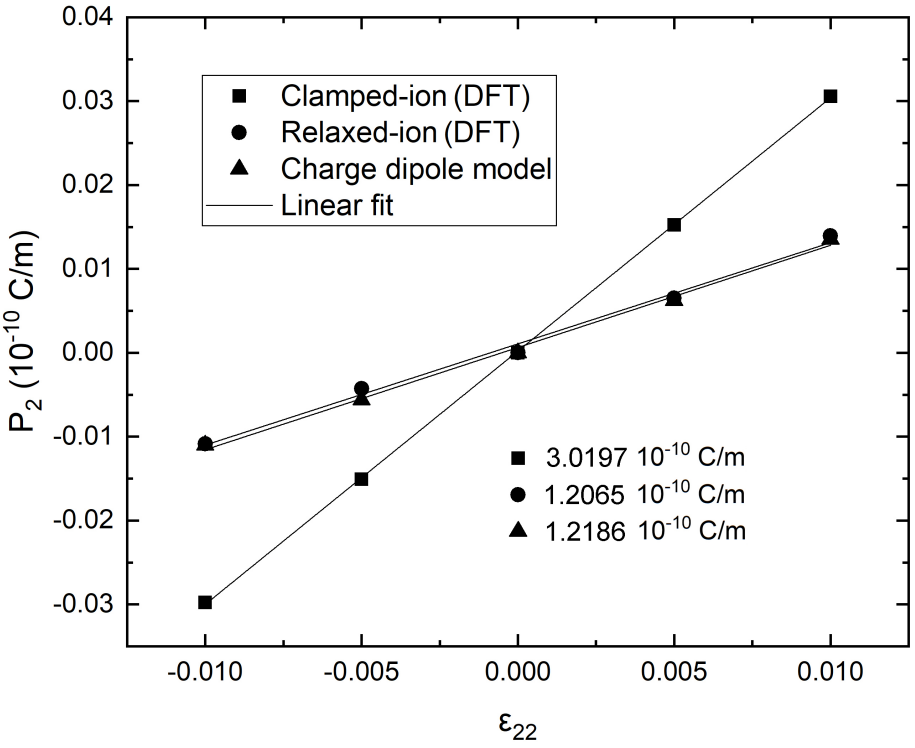

Figure V.6: Variations of P_2 as a function of applied uniaxial strain ϵ_{22} for graphene/h-BN heterostructure.

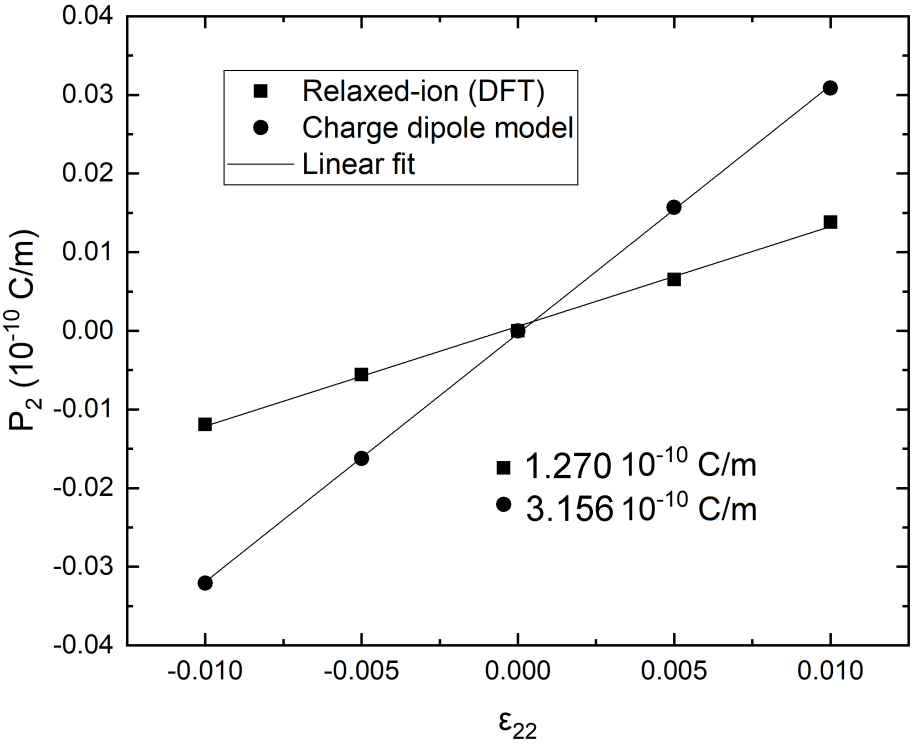

Figure V.7: Variations of P_2 as a function of applied uniaxial strain ϵ_{22} for h-BN monolayer.

V.6 Computation of bending flexoelectric coefficient for graphene, h-BN and their vertically stacked heterostructure

We now use the aforedescribed framework to calculate the bending flexoelectric coefficient μ_{3311} for graphene and h-BN monolayers considered independently. As shown in Figure V.8, we found 0.016 nC/m and 0.204 nC/m, respectively. Then, due to the significant disagreement between authors, associated with the thickness of 2D materials[Huang 06], we multiplied our value of μ_{3311} (in nC/m) by the thickness t of the corresponding monolayer (3.50 Å [Ishigami 07] for graphene and 0.906 Å [Yan 19] for h-BN) that we used to compute the volume of the system during the computation of the polarization, thus obtaining a result independant of t. Then, we converted the values of $\mu_{3311} \times t$ to electron charge unit (e) and got a value easier to compare with the data in other references, as shown in Table V.6. It can be seen that the result computed with Eq. V.3 for graphene are of the same order of magnitude as that computed using first principle method by S. Kalinin[Kalinin 08], suggesting that the theoretical method proposed by Kvashnin et al[Kvashnin 15] is capable of predicting or calculating the order of magnitude of the flexoelectric coefficient of curved graphene. Then, we performed again, the calculation of μ_{3311} for graphene alone, but this time using the QP method with the obtained parameters for carbon atom, shown in Table V.4. The computed result (-0.014 nC/m, see Figure V.9) is in good agreement with that obtained via Kvashnin's method, illustrating that these two methods are consistent.

In Table V.6, we can also see that our result of $\mu_{3311} \times t$ for h-BN, is of the same order of magnitude as the one computed by DFT [Kumar 21], which can be considered a fair agreement recalling that the R and χ parameters were not fitted for h-BN alone but for h-BN in GBN. Meanwhile, we can finally see that the values of μ_{3311} for both graphene and h-BN taken from the paper by Zhuang at al [Zhuang 19] differ by at least one order of magnitude with respect to the other values. As in the previous chapter, we tentatively attribute this problem to the use of a polarization defined without any charge term and the fact that charge conservation was not enforced in their calculations.

We now turn to the calculation of the bending flexoelectric coefficient for GBN. Unlike isolated graphene and h-BN, which are not ferroelectric, the GBN heterostructure is endowed with out-of-plane spontaneous polarization due to inter-

Table V.6: Comparison between μ_{3311} obtained in our work and from the literature, with μ_{3311} for BN and graphene computed with charge dipole (QP) model and Kvashnin et al.'s approach, respectively.

μ_{3311}	our result (nC/m)	our result (e)	DFT (e)	other QP (nC/m)
graphene	−0.016	−0.035	0.094 [Kalinin 08]	0.0014 [Zhuang 19]
h-BN	0.204	0.116	0.2 [Kumar 21]	0.00013 [Zhuang 19]

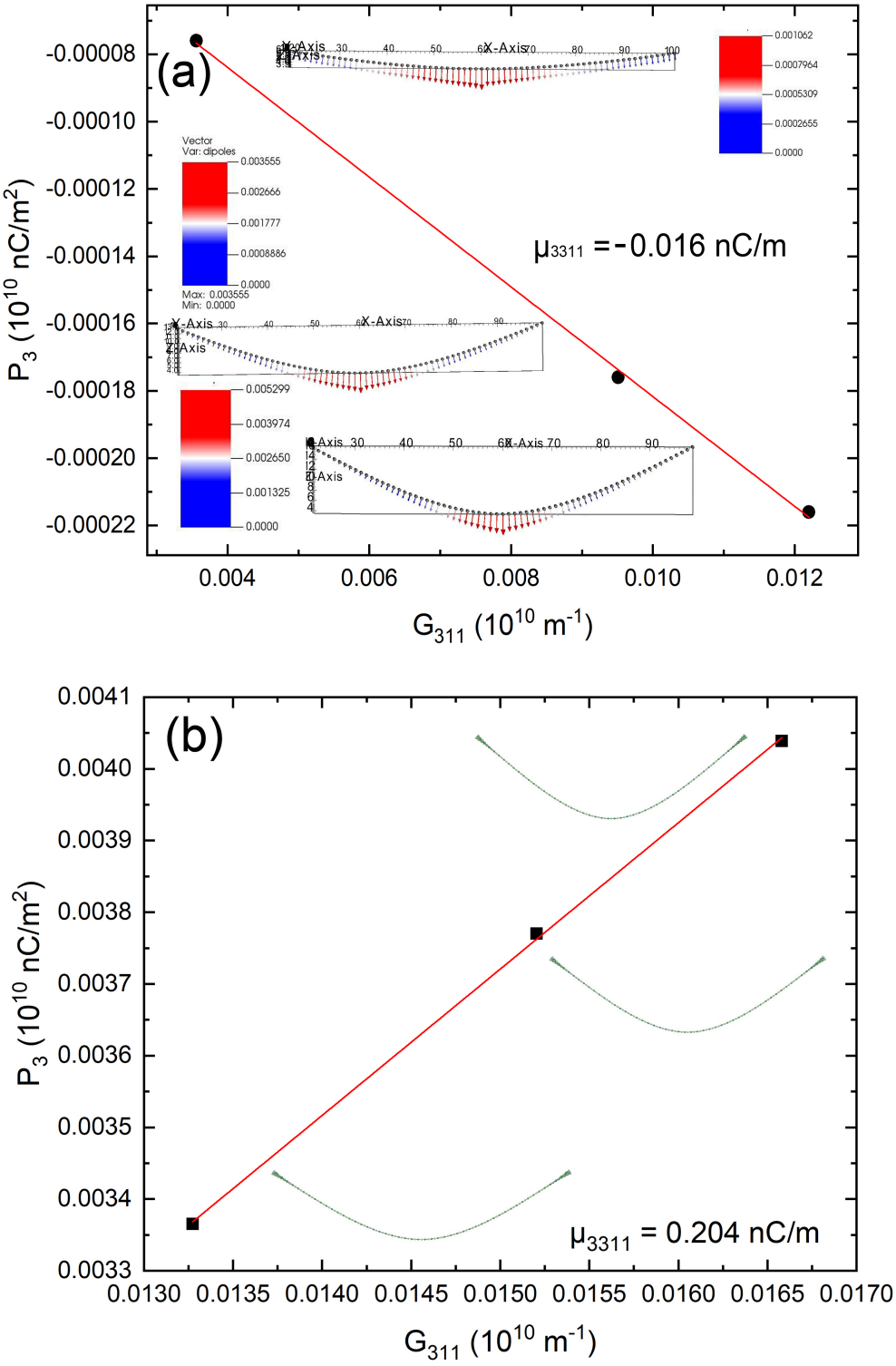

Figure V.8: Variation of P_3 with strain gradient G_{311} for graphene (dipoles and P_3 calculated via the method described in [Dumitrică 02] and [Kvashnin 15])(a) and h-BN (dipoles and P_3 calculated via the QP method) (b). The magnitude of the electric fields applied to (a) graphene for bending simulation is 0.0424, 0.0495, and 0.05656 V/Å and (b) h-BN is 0.03535, 0.0424 and 0.0495 V/Å. The angle between the electric fields and the the x-axis is set to 45°. Insets in (a) show the computed dipole moment vector for each atom, with the color of every arrow representing the magnitude of the corresponding dipole moment.

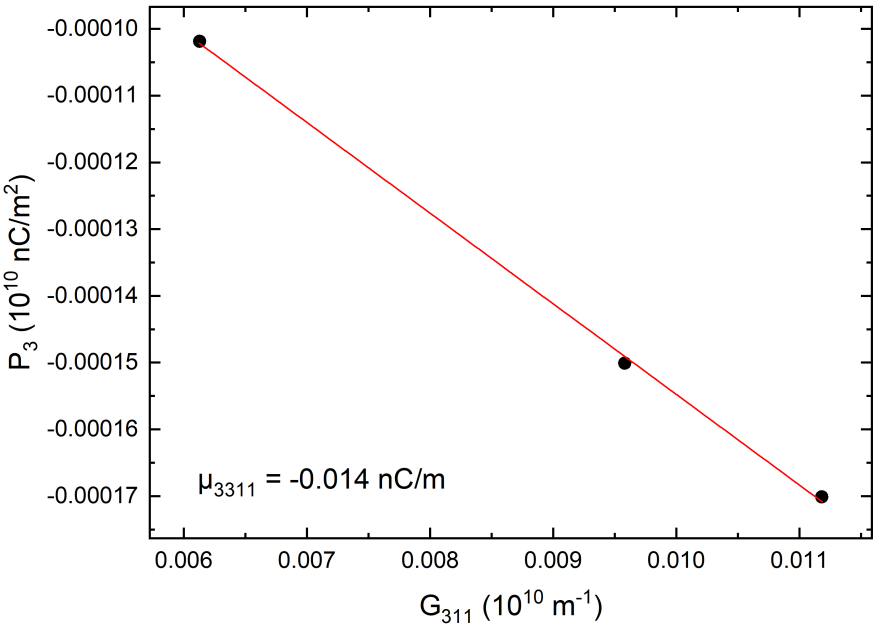

Figure V.9: Variation of polarization P_3 with strain gradient G_{311} for graphene.

layer charge transfer due to the differences in electronegativity between carbon, boron and nitrogen. It is therefore a ferroelectric material that could thus naturally possess a large flexoelectric coefficient and could therefore be used for nanogenerators and energy harvesters.

However, it is unexpected that the flexoelectric coefficient μ_{3311} computed with the charge dipole model and our values for the radii and electronegativities are as large as that for graphene and around two times smaller than that for h-BN alone, since we found 0.00596 nC/m (or 0.021 e since $t = 5.593$ Å) for AB stacking, 0.00338 nC/m (or 0.012 e since $t = 5.753$ Å) for AB′ stacking and 0.00702 nC/m (or 0.024 e since $t = 5.753$ Å) for AA stacking, as can be seen in Table V.7 and Figure V.10. This can be attributed to the fact that the out of plane polarization (P_3) produced by bending deformation for graphene and boron nitride will partially cancel each other due to the opposite signs in polarization (see y axis in Figure V.8 (a) and (b)). It should be noted that for multilayered materials, a key factor that determines the flexoelectric coefficient is not the inter-layer charge transfer, but the change in the amount of charge transfer with the curvature (strain gradient).

We also see in Table V.7 that the signs of the spontaneous polarizations for the undeformed GBN heterostructures, which correspond to the intercepts of the fitted straight lines, are obtained to be negative ($\approx -0.001 \times 10^{10}$ nC/m^2), suggesting that the polarization orientation is from the BN layer to the graphene layer.

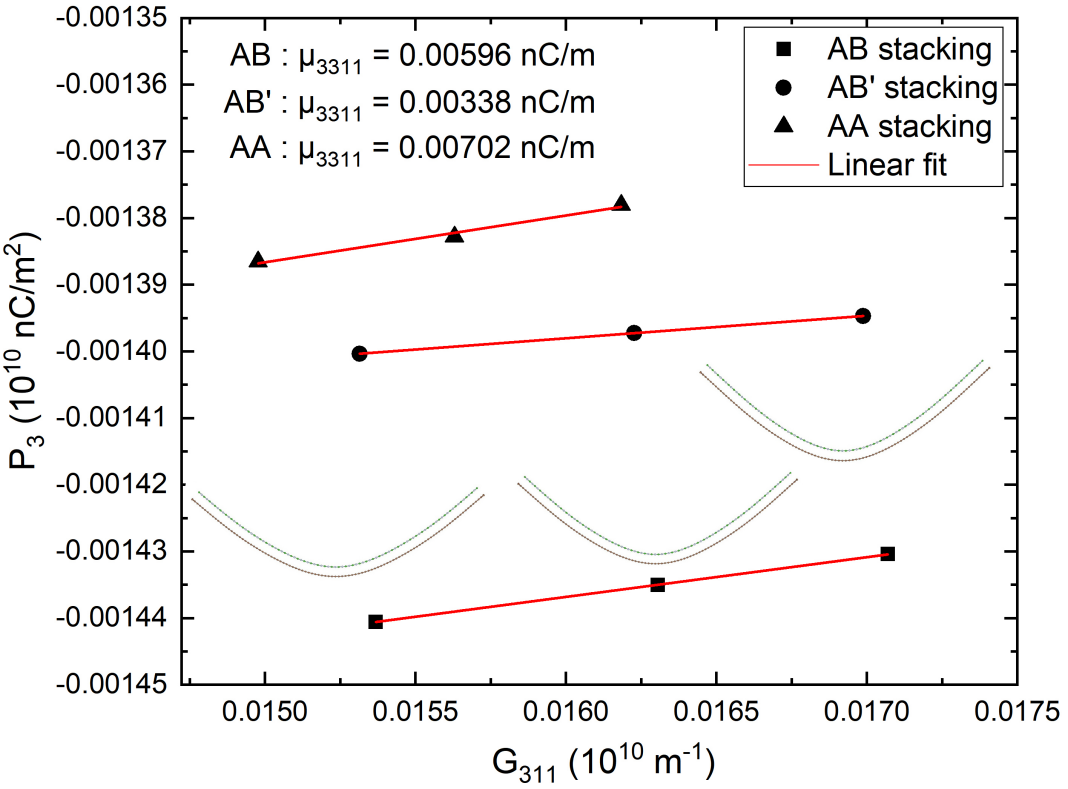

Figure V.10: Variation of polarization P_3 with strain gradient G_{311} for AA, AB, AB′ graphene/h-BN heterostructure.

Table V.7: Computed μ_{3311} and intercept of fitting equation for AA, AB and AB′-stacked heterostructure.

	μ_{3311} (nC/m)	$\mu_{3311} \times t(e)$	Intercept (10^{10} nC/m^2)
AB stacking	0.00596	0.021	-0.00153
AB′ stacking	0.00338	0.012	-0.00145
AA stacking	0.00702	0.024	-0.00149

To better understand that orientation, we calculated the z-axis total dipole moment (P_3^{tot}) for an AB-stacked GBN nanoribbon, put in a cubic box with a length of 13.00 nm, a width of 0.431 nm and a height of 3.00 nm (see Figure V.11), both with the charge dipole model and Berry phase method. The computed results for P_3^{tot} (-0.003 e/Å^2 with charge dipole model and -0.011 e/Å^2 using Berry phase method) are in fair agreement, which once again gives us confidence in our methodology. To gain a deeper understanding of the origin of the negative sign of spontaneous total dipole, hence spontaneous polarization, in both QP and Berry phase results, we plot on Figure V.12, the charge density difference between GBN and the isolated monolayers: $\Delta\rho = \rho_{GBN} - \rho_{BN} - \rho_G$, thus displaying the transfer of electron between atoms. The red regions show charge accumulation, while blue regions represent charge depletion. For AB′ stacking, it can be seen from Figure V.12(a) that red and blue areas are arranged alternately, in the bottom

graphene layer, causing the resulting z-direction dipole moments to cancel each other out, whereas in the top h-BN layer, the blue area largely clustered around the nitrogen atom indicates the transfer of charge from the valence electrons of nitrogen atoms to the carbon atom layer. Hence, we can assume that the direction of the polarization (total dipole moment per unit volume) points to the negative direction of the z-axis, in agreement with our negative sign for P_3^{tot}. We can also see that charges appear to be localized around the nitrogen atoms because of Coulomb repulsion between electron-rich nitrogen atoms and π electrons of carbon atoms. This argument can be rationalized with the result for charge density difference for AB-stacked GBN heterostructure, shown in Figure V.12(b), from which it can be seen that the inter-layer strip-like red regions seem to connect the carbon atom with cation boron, signifying that a strong charge transfer (Coulomb electrostatic attraction interplay) occurs between the electron-poor boron and the carbon atom directly below it. It is precisely because of this interlayer Coulomb attraction that the interlayer spacing of AB-stacked GBN heterostructure is smaller than that of the others. Such strong interlayer charge transfer between h-BN and graphene was also observed experimentally[Bjelkevig 10].

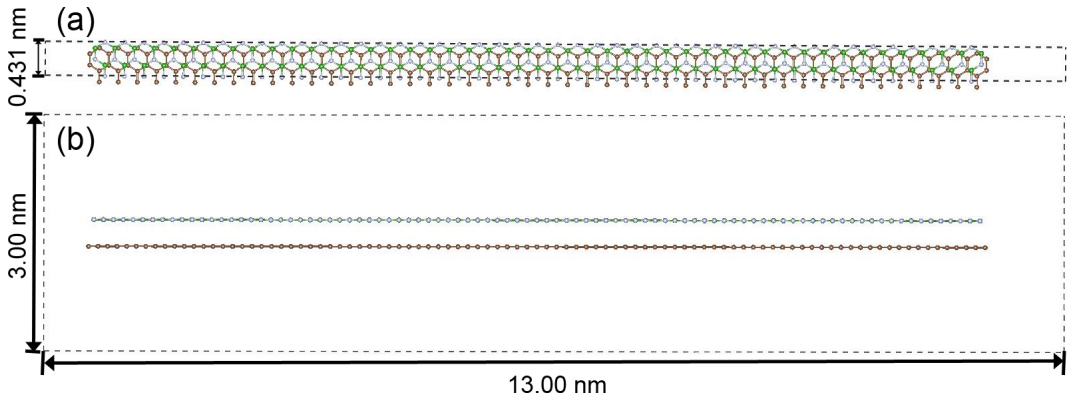

Figure V.11: Schematic diagram of AB-stacked graphene/hBN nanoribbon placed in a cubic box (a) top view, (b) side view.

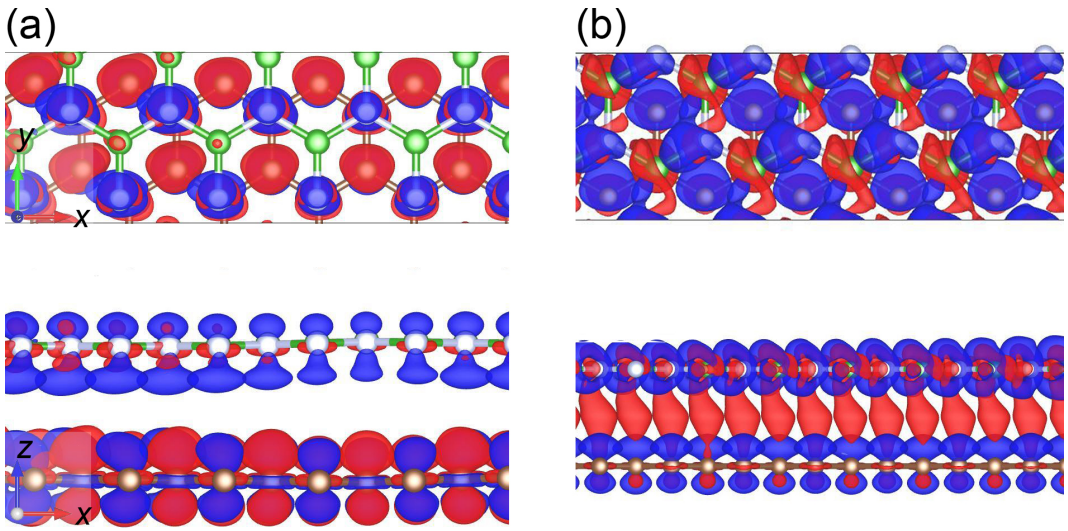

Figure V.12: Charge density difference plots for (a) AB′ and (b) AB-stacked heterostructures. The blue and red areas around the atoms represent apparent loss and gain of electrons, respectively.

V.7 Conclusion

Based on the simulation setup designed in Chapter 4 for bending simulation, we, with the use of LAMMPS package in combination with charge dipole model, computed bending flexoelectric coefficient μ_{3311} for AA, AB, AB′-stacked graphene/hBN heterostructure. These coefficients are as large as that for graphene and about twice smaller than that for h-BN which is due to the opposite out-of-plane directions of polarization of graphene and boron nitride. Hence, it is imperative to find other double-layer heterostructure for energy conversion use, with each layer of it having the same direction of polarization under bending deformation, such as, MoS_2/graphene heterostructure. These optimized heterostructures could then provide opportunities for the development of nanoelectronic devices, i.e., nanogenerators taking profit of the inhomogeneous mechanical deformation of GBN heterostructures.

Conclusions and perspectives

The goal of this thesis was to set up a methodology to compute the flexoelectric coefficient of various 2D materials and heterostructure of these materials within the QP model.

During chapter 2, we, within charge dipole model, calculated the force between two carbon atoms to check the equivalence (or not) of two different formulas for the forces within QP model (one that our group used in previous studies, e.g. [Wang 07a], [Wang 07b], [Wang 08b] and another one found in an article by Zhuang's group at Hanover [Javvaji 18]). The computed results indicate that for a simple electric equilibrium system containing two atoms, the calculation of the total forces is independent of whether the gradients of the charges and dipoles are taken into account or not. We then numerically confirmed the equivalence of the two formulas in a more general case. We finally proved analytically that both methods are equivalent in all cases using supermatrix formulation. At the end of the chapter, we, using charge dipole model with an improved definition of polarization with respect to the one used in [Javvaji 18], computed in-plane piezoelectric coefficient e_{111} for trapezium-shaped graphene and graphene with triangular defect and circular defect, respectively. Results made us believe that our computed result is physically more meaningful than that obtained by Javvaji et al.

In chapter 3, we tried to extend a previous work in the group (Gautier Lecoutre's PhD thesis), by incorporating terms involving effective charges into his analytical expression of the flexoelectric tensor as a function of permanent dipoles due to the change of hybridization during the curvature of a graphene sheet rolled into a CNT wall, to calculate the full flexoelectric tensor of ionic materials, such as MoS_2. Unfortunately, the orders of magnitude of computed results do not accord with those reported experimentally, due to problems of divergence in the new charge terms. We therefore stopped analytical development and proceeded with numerical studies.

In chapter 4, we designed three different setups that allowed us to calculate in-plane flexoelectric coefficients μ_{1111}, μ_{2222}, transverse flexoelectric coefficient μ_{3311} and out-of-plane flexoelectric coefficient μ_{3333}, for monolayer MoS_2, using Gaussian-regularized charge dipole model and charge conservation. The computed out-of-plane flexoelectric coefficient μ_{3333} and transverse flexoelectric coefficient μ_{3311} are compared with those obtained by experimental measurements and computed by DFT calculations, respectively. The calculated results for μ_{3333} or μ_{3311} are of the same order of magnitude as those reported experimentally and computationally, provided charge term is considered in the definition of polarization. In terms of sign, the computationally obtained flexoelectric coefficients μ_{3333} and μ_{3311} however, do not coincide with those shown in reference. We then discuss in details some possible origins of this discrepancy in sign between our calculated

flexoelectric coefficient μ_{3311} and other reported results, leading to two opposite effects for the sign of the polarization. Finally, we computed in-plane flexoelectric coefficient μ_{1111} and μ_{2222}, which are found to be quasi identical.

In the last part of the thesis, we, exploiting the bending simulation setup designed in chapter 4, computed the bending flexoelectric coefficient μ_{3311} for graphene/h-boron nitride heterostructure and h-boron nitride alone. The values of μ_{3311} for h-BN and graphene are of the same order of magnitude as those reported previously. The bending flexoelectric coefficient for graphene/h-BN heterostructure is by computation found to be twice smaller than that for h-BN and of same value as graphene, respectively, which is caused by opposite directions of the polarizations in the graphene and h-BN bent layers.

In summary, it can be seen from this PhD thesis that the charge dipole model (QP model) is indeed a very useful tool for computation of electrostatic properties of some 2D materials. In the near future, charge dipole model could be applied for computations of flexoelectric coefficients of other kinds of 2D materials, such as MXenes, particularly in their single - or few layer form. Moreover, charge dipole model could be further optimized in terms of enhancing accuracy of calculation of polarization by introducing the contribution of multipoles to the total energy, especially the quadrupole in the context of flexoelectricity since the quadrupolar part of the polarization can appear in the reverse flexoelectric effect $Q_{ij} = \mu_{ijkl}\nabla_k E_l$. It could also be interesting to study the distinction between surface (or edge) and bulk contributions to flexoelectricity or piezoelectricity by differentiating these contributions in simulations of multilayer structures.

The charge dipole model coded with FORTRAN can be ported into LAMMPS through interface. The merits of doing so is that there is no need to code new potential functions for those materials that have not been studied. In addition, the charge dipole model can also be used in conjunction with a potential functions library shared on the internet through interface.

Molecular simulation of nanobubbles could be another interesting project. In terms of reported literature, under anisotropic strain gradient, nanobubbles can generate quasi-constant pseudomagnetic field and manifest further opening of band gap. The applications of nanobubbles are interesting enough that its physical properties have been studied and reported by many researchers. Nanobubble structures initially originate from the entrapment of air molecules between the single layer graphene sheet. Very recently, it has been experimentally and theoretically reported that nanobubbles can induce a non-zero out-of-plane polarization due to a nonuniform strain (strain gradient). It has not, however, been studied computationally. We therefore intend to study the electromechanical coupling effects of mechanically strained nanobubbles on 2D materials or multilayered materials using the charge dipole model to calculate the resulting polarization, from which one can finally get the electrodynamic coupling coefficient. Such a simulation setup offers an alternative avenue for studying electromechanical coupling effects in 2D materials.

Finally, it is known that charge dipole model is an electrostatic model, which is of course not associated with time. In the future, it may nonetheless be possible for charge dipole model to be combined with lattice dynamics as a quasi-static approximation, to study dynamic flexoelectricity.

Figure V.13: Nanobubbles, adapted from [Bao 15]

Bibliography

[Abdollahi 14] A. Abdollahi, C. Peco, D. Millan, M. Arroyo & I. Arias. *Computational evaluation of the flexoelectric effect in dielectric solids.* J. Appl. Phys., vol. 116, no. 9, page 093502, 2014.

[Abdollahi 15a] A. Abdollahi & I. Arias. *Constructive and Destructive Interplay Between Piezoelectricity and Flexoelectricity in Flexural Sensors and Actuators.* J. Appl. Mech., vol. 82, no. 12, Sep 2015. 121003.

[Abdollahi 15b] A. Abdollahi, D. Millán, C. Peco, M. Arroyo & I. Arias. *Revisiting pyramid compression to quantify flexoelectricity: A three-dimensional simulation study.* Phys. Rev. B, vol. 91, no. 10, page 104103, Mar 2015.

[Abdollahi 15c] A. Abdollahi, C. Peco, D. Millán, M. Arroyo, G. Catalan & I. Arias. *Fracture toughening and toughness asymmetry induced by flexoelectricity.* Phys. Rev. B, vol. 92, no. 9, page 094101, Sep 2015.

[Abdollahi 19] A. Abdollahi, N. Domingo, I. Arias & G. Catalan. *Converse flexoelectricity yields large piezoresponse force microscopy signals in non-piezoelectric materials.* Nat. Commun., vol. 10, no. 1, pages 1–6, 2019.

[Anderson 99] E. Anderson, Z. Bai, C. Bischof, S. Blackford, J. D. J. Dongarra, J. D. Croz, A. Greenbaum, S. Hammarling, A. McKenney & D. Sorensen. Lapack users' guide. SIAM, Philadelphia, Pennsylvania, USA, third edition, 1999.

[Applequist 72] J. Applequist, J. R. Carl & K. K. Fung. *Atom dipole interaction model for molecular polarizability. Application to polyatomic molecules and determination of atom polarizabilities.* J. Am. Chem. Soc., vol. 94, no. 9, pages 2952–2960, 1972.

[Applequist 77] J. Applequist. *An atom dipole interaction model for molecular optical properties.* Acc. Chem. Res., vol. 10, no. 3, pages 79–85, 1977.

[Askar 70] A. Askar, P. Lee & A. Cakmak. *Lattice-dynamics approach to the theory of elastic dielectrics with polarization gradient.* Phys. Rev. B, vol. 1, no. 8, page 3525, 1970.

[Bao 15] Q. Bao, J. Chen, Y. Xiang, K. Zhang, S. Li, X. Jiang, Q.-H. Xu, K. P. Loh & T. Venkatesan. *Graphene nanobubbles: a new optical nonlinear material*. Adv. Opt. Mater., vol. 3, no. 6, pages 744–749, 2015.

[Baskaran 11a] S. Baskaran, X. He, Q. Chen & J. Y. Fu. *Experimental studies on the direct flexoelectric effect in α-phase polyvinylidene fluoride films*. Appl. Phys. Lett., vol. 98, no. 24, page 242901, 2011.

[Baskaran 11b] S. Baskaran, N. Ramachandran, X. He, S. Thiruvannamalai, H. J. Lee, H. Heo, Q. Chen & J. Y. Fu. *Giant flexoelectricity in polyvinylidene fluoride films*. Phys. Lett. A, vol. 375, no. 20, pages 2082–2084, 2011.

[Baskaran 12] S. Baskaran, X. He, Y. Wang & J. Y. Fu. *Strain gradient induced electric polarization in α-phase polyvinylidene fluoride films under bending conditions*. J. Appl. Phys., vol. 111, no. 1, page 014109, 2012.

[Bhaskar 16] U. K. Bhaskar, N. Banerjee, A. Abdollahi, Z. Wang, D. G. Schlom, G. Rijnders & G. Catalan. *A flexoelectric microelectromechanical system on silicon*. Nat. Nanotechnol., vol. 11, no. 3, pages 263–266, 2016.

[Birge 80] R. R. Birge. *Calculation of molecular polarizabilities using an anisotropic atom point dipole interaction model which includes the effect of electron repulsion*. J. Chem. Phys., vol. 72, no. 10, pages 5312–5319, 1980.

[Bitzek 06] E. Bitzek, P. Koskinen, F. Gähler, M. Moseler & P. Gumbsch. *Structural relaxation made simple*. Phys. Rev. Lett., vol. 97, no. 17, page 170201, 2006.

[Bjelkevig 10] C. Bjelkevig, Z. Mi, J. Xiao, P. Dowben, L. Wang, W.-N. Mei & J. A. Kelber. *Electronic structure of a graphene/hexagonal-BN heterostructure grown on Ru (0001) by chemical vapor deposition and atomic layer deposition: extrinsically doped graphene*. J. Phys. Condens, vol. 22, no. 30, page 302002, 2010.

[Blonsky 15] M. N. Blonsky, H. L. Zhuang, A. K. Singh & R. G. Hennig. *Ab initio prediction of piezoelectricity in two-dimensional materials*. ACS nano, vol. 9, no. 10, pages 9885–9891, 2015.

[Brennan 17] C. J. Brennan, R. Ghosh, K. Koul, S. K. Banerjee, N. Lu & E. T. Yu. *Out-of-plane electromechanical response of monolayer molybdenum disulfide measured by piezoresponse force microscopy*. Nano Lett., vol. 17, no. 9, pages 5464–5471, 2017.

[Brennan 20] C. J. Brennan, K. Koul, N. Lu & E. T. Yu. *Out-of-plane electromechanical coupling in transition metal dichalcogenides.* Appl. Phys. Lett., vol. 116, no. 5, page 053101, 2020.

[Bresteau 16] D. Bresteau, C. Drag & C. Blondel. *Isotope shift of the electron affinity of carbon measured by photodetachment microscopy.* Phys. Rev. A, vol. 93, no. 1, page 013414, 2016.

[Bursian 68] E. Bursian & Z. OI. *Changes in curvature of a ferroelectric film due to polarization.* Sov. Phys. Solid State, vol. 10, no. 5, page 1121, 1968.

[Bursian 74] E. Bursian & T. NN. *NONLOCAL PIEZO-EFFECT.* Fiz. Tverd. Tela (Leningrad), vol. 16, pages 1187–1190, 1974.

[Cao 15] Y. Cao, Q. Li, L.-Q. Chen & S. V. Kalinin. *Coupling of electrical and mechanical switching in nanoscale ferroelectrics.* Appl. Phys. Lett., vol. 107, no. 20, page 202905, 2015.

[Catalan 04] G. Catalan, L. Sinnamon & J. Gregg. *The effect of flexoelectricity on the dielectric properties of inhomogeneously strained ferroelectric thin films.* J. Phys. Condens. Matter., vol. 16, no. 13, page 2253, 2004.

[Chandratre 12] S. Chandratre & P. Sharma. *Coaxing graphene to be piezoelectric.* Appl. Phys. Lett., vol. 100, no. 2, page 023114, 2012.

[Chatzopoulos 16] A. Chatzopoulos, P. Beck, J. Roth & H.-R. Trebin. *Atomistic modeling of flexoelectricity in periclase.* Phys. Rev. B, vol. 93, no. 2, page 024105, Jan 2016.

[Chen 14] H. Chen, A. K. Soh & Y. Ni. *Phase field modeling of flexoelectric effects in ferroelectric epitaxial thin films.* Acta Mech., vol. 225, no. 4, pages 1323–1333, 2014.

[Chen 15] H. Chen, S. D. Zhang, A. K. Soh & W. Yin. *Phase field modeling of flexoelectricity in solid dielectrics.* J. Appl. Phys., vol. 118, no. 3, page 034106, 2015.

[Choi 17] W. Choi, N. Choudhary, G. H. Han, J. Park, D. Akinwande & Y. H. Lee. *Recent development of two-dimensional transition metal dichalcogenides and their applications.* Mater. Today, vol. 20, no. 3, pages 116–130, 2017.

[Choyal 22] V. Choyal & S. Kundalwal. *Electromechanical response of stacked h-BN layers: A computational study.* Diam Relat Mater., vol. 126, page 109126, 2022.

[Chu 12] B. Chu & D. Salem. *Flexoelectricity in several thermoplastic and thermosetting polymers.* Appl. Phys. Lett., vol. 101, no. 10, page 103905, 2012.

[Cross 06] L. E. Cross. *Flexoelectric effects: Charge separation in insulating solids subjected to elastic strain gradients.* J. Mater. Sci., vol. 41, no. 1, pages 53–63, 2006.

[Dai 21] Z. Dai, S. Guo, Y. Gong & Z. Wang. *Semiconductor flexoelectricity in graphite-doped $SrTiO_3$ ceramics.* Ceram. Int., vol. 47, no. 5, pages 6535–6539, 2021.

[Derzhanski 90] A. Derzhanski, A. Petrov, A. Todorov & K. Hristova. *Flexoelectricity of lipid bilayers.* Liq. Cryst., vol. 7, no. 3, pages 439–449, 1990.

[Dreyer 18] C. E. Dreyer, M. Stengel & D. Vanderbilt. *Current-density implementation for calculating flexoelectric coefficients.* Phys. Rev. B, vol. 98, no. 7, page 075153, Aug 2018.

[Duerloo 12] K.-A. N. Duerloo, M. T. Ong & E. J. Reed. *Intrinsic piezoelectricity in two-dimensional materials.* J. Phys. Chem. Lett., vol. 3, no. 19, pages 2871–2876, 2012.

[Dumitrică 02] T. Dumitrică, C. M. Landis & B. I. Yakobson. *Curvature induced polarization in carbon nanoshells.* Chem. Phys. Lett., vol. 360, no. 1-2, pages 182–188, 2002.

[El-Kelany 16] K. E. El-Kelany, P. Carbonnière, A. Erba, J.-M. Sotiropoulos & M. Rérat. *Piezoelectricity of functionalized graphene: a quantum-mechanical rationalization.* J. Phys. Chem. C, vol. 120, no. 14, pages 7795–7803, 2016.

[Falk 98] M. L. Falk & J. S. Langer. *Dynamics of viscoplastic deformation in amorphous solids.* Phys. Rev. E, vol. 57, no. 6, page 7192, 1998.

[Fan 11] Y. Fan, M. Zhao, Z. Wang, X. Zhang & H. Zhang. *Tunable electronic structures of graphene/boron nitride heterobilayers.* Appl. Phys. Lett., vol. 98, no. 8, page 083103, 2011.

[Fan 19] F. R. Fan & W. Wu. *Emerging devices based on two-dimensional monolayer materials for energy harvesting.* Research, vol. 2019, page 7367828, 2019.

[Fu 06] J. Y. Fu, W. Zhu, N. Li & L. E. Cross. *Experimental studies of the converse flexoelectric effect induced by inhomogeneous electric field in a barium strontium titanate composition.* J. Appl. Phys., vol. 100, no. 2, page 024112, 2006.

[Gharbi 11] M. Gharbi, Z. Sun, P. Sharma, K. White & S. El-Borgi. *Flexoelectric properties of ferroelectrics and the nanoindentation size-effect*. Int. J. Solids Struct., vol. 48, no. 2, pages 249–256, 2011.

[Giovannetti 07] G. Giovannetti, P. A. Khomyakov, G. Brocks, P. J. Kelly & J. Van Den Brink. *Substrate-induced band gap in graphene on hexagonal boron nitride: Ab initio density functional calculations*. Phys. Rev. B, vol. 76, no. 7, page 073103, 2007.

[Goerigk 17] L. Goerigk. *A comprehensive overview of the DFT-D3 London-dispersion correction*. Non-covalent interactions in quantum chemistry and physics, pages 195–219, 2017.

[Grimme 11] S. Grimme, S. Ehrlich & L. Goerigk. *Effect of the damping function in dispersion corrected density functional theory*. J. Comput. Chem., vol. 32, no. 7, pages 1456–1465, 2011.

[Guo 22] H. Guo, T. Yang, X. Xuan, Z. Zhang & W. Guo. *Flexoelectricity in hexagonal boron nitride monolayers*. Extreme Mech. Lett., vol. 52, page 101669, 2022.

[Haigh 12] S. J. Haigh, A. Gholinia, R. Jalil, S. Romani, L. Britnell, D. C. Elias, K. S. Novoselov, L. A. Ponomarenko, A. K. Geim & R. Gorbachev. *Cross-sectional imaging of individual layers and buried interfaces of graphene-based heterostructures and superlattices*. Nat. Mater., vol. 11, no. 9, pages 764–767, 2012.

[Han 16] J. K. Han, D. H. Jeon, S. Y. Cho, S. W. Kang, S. A. Yang, S. D. Bu, S. Myung, J. Lim, M. Choi, M. Lee*et al. Nanogenerators consisting of direct-grown piezoelectrics on multi-walled carbon nanotubes using flexoelectric effects*. Sci. Rep., vol. 6, page 295262, 2016.

[Han 19] S. A. Han, J. Lee, J. Lin, S.-W. Kim & J. H. Kim. *Piezo/triboelectric nanogenerators based on 2-dimensional layered structure materials*. Nano Energy, vol. 57, pages 680–691, 2019.

[Hana 06] P. Hana, M. Marvan, L. Burianova, S. Zhang, E. Furman & T. Shrout. *Study of the inverse flexoelectric phenomena in ceramic lead magnesium niobate-lead titanate*. Ferroelectrics, vol. 336, no. 1, pages 137–144, 2006.

[Hao 21] W. Hao, Z. Wu, X. Li & Y. Pu. *Edge effect on flexoelectronic properties of Janus MoSSe nanoribbons: A first-principles study*. J. Appl. Phys., vol. 129, no. 18, page 185101, 2021.

[Harris 65] P. Harris. *Mechanism for the shock polarization of dielectrics.* J. Appl. Phys., vol. 36, no. 3, pages 739–741, 1965.

[Hill 63] R. Hill. *Elastic properties of reinforced solids: some theoretical principles.* Journal of the Mechanics and Physics of Solids, vol. 11, no. 5, pages 357–372, 1963.

[Hirakata 21] H. Hirakata, Y. Fukuda & T. Shimada. *Flexoelectric properties of multilayer two-dimensional material MoS_2.* J. Phys. D: Appl. Phys., vol. 55, no. 12, page 125302, 2021.

[Hong 10] J. Hong, G. Catalan, J. Scott & E. Artacho. *The flexoelectricity of barium and strontium titanates from first principles.* J. Condens. Matter Phys., vol. 22, no. 11, page 112201, 2010.

[Hong 11] J. Hong & D. Vanderbilt. *First-principles theory of frozen-ion flexoelectricity.* Phys. Rev. B, vol. 84, no. 18, page 180101, Nov 2011.

[Hong 13] J. Hong & D. Vanderbilt. *First-principles theory and calculation of flexoelectricity.* Phys. Rev. B, vol. 88, no. 17, page 174107, 2013.

[Hu 15] S. Hu, H. Li & H. Tzou. *Distributed flexoelectric structural sensing: Theory and experiment.* J. Sound Vib., vol. 348, pages 126–136, 2015.

[Hu 18] T. Hu, Q. Deng & S. Shen. *Probing flexoelectricity via a split Hopkinson pressure bar experiment.* Appl. Phys. Lett., vol. 112, no. 24, page 242902, 2018.

[Huang 06] Y. Huang, J. Wu & K.-C. Hwang. *Thickness of graphene and single-wall carbon nanotubes.* Phys. Rev. B, vol. 74, no. 24, page 245413, 2006.

[Huang 11] W. Huang, K. Kim, S. Zhang, F.-G. Yuan & X. Jiang. *Scaling effect of flexoelectric $(Ba,Sr)TiO_3$ microcantilevers.* Phys. Status Solidi. RRL, vol. 5, no. 9, pages 350–352, 2011.

[Huang 16] W. Huang, F.-G. Yuan & X. Jiang. *5 - Flexoelectric effect, materials, and structures.* In F.-G. Yuan, editeur, Structural Health Monitoring (SHM) in Aerospace Structures, pages 119–148. Woodhead Publishing, 2016.

[Huang 17] S. Huang, T. Kim, D. Hou, D. Cann, J. L. Jones & X. Jiang. *Flexoelectric characterization of $BaTiO_3$-0.08$Bi(Zn_{1/2}Ti_{1/2})O_3$.* Appl. Phys. Lett., vol. 110, no. 22, page 222904, 2017.

[Huang 18] S. Huang, H.-M. Yau, H. Yu, L. Qi, F. So, J.-Y. Dai & X. Jiang. *Flexoelectricity in a metal/ferroelectric/semiconductor heterostructure*. AIP Adv., vol. 8, no. 6, page 065321, 2018.

[Ishigami 07] M. Ishigami, J. Chen, W. Cullen, M. Fuhrer & E. Williams. *Atomic structure of graphene on SiO_2*. Nano Lett., vol. 7, no. 6, pages 1643–1648, 2007.

[Iwata 18] T. Iwata & K. Shintani. *Reduction of the thermal conductivity of a graphene/hBN heterobilayer via interlayer sp^3 bonds*. Phys. Chem. Chem. Phys., vol. 20, no. 7, pages 5217–5226, 2018.

[Javvaji 17] B. Javvaji, B. M. Shenoy, D. R. Mahapatra, A. Ravikumar, G. Hegde & M. Rizwan. *Stable configurations of graphene on silicon*. Appl. Surf. Sci., vol. 414, pages 25–33, 2017.

[Javvaji 18] B. Javvaji, B. He & X. Zhuang. *The generation of piezoelectricity and flexoelectricity in graphene by breaking the materials symmetries*. Nanotechnology, vol. 29, no. 22, page 225702, 2018.

[Javvaji 19] B. Javvaji, B. He, X. Zhuang & H. S. Park. *High flexoelectric constants in Janus transition-metal dichalcogenides*. Phys. Rev. Mater., vol. 3, no. 12, page 125402, 2019.

[Javvaji 21] B. Javvaji, R. Zhang, X. Zhuang & H. S. Park. *Flexoelectric electricity generation by crumpling graphene*. J. Appl. Phys., vol. 129, no. 22, page 225107, 2021.

[Javvaji 22] B. Javvaji, X. Zhuang, T. Rabczuk & B. Mortazavi. *Machine-Learning-Based Exploration of Bending Flexoelectricity in Novel 2D Van der Waals Bilayers*. Adv. Energy Mater., vol. 12, no. 32, page 2201370, 2022.

[Jensen 02] L. Jensen, P.-O. Åstrand, A. Osted, J. Kongsted & K. V. Mikkelsen. *Polarizability of molecular clusters as calculated by a dipole interaction model*. J. Chem. Phys., vol. 116, no. 10, pages 4001–4010, 2002.

[Jones 24a] J. E. Jones. *On the determination of molecular fields.–I. From the variation of the viscosity of a gas with temperature*. Proceedings of the Royal Society of London. Series A, Containing Papers of a Mathematical and Physical Character, vol. 106, no. 738, pages 441–462, 1924.

[Jones 24b] J. E. Jones. *On the determination of molecular fields.–II. From the equation of state of a gas*. Proceedings of the Royal Society of London. Series A, Containing Papers of a Mathematical and Physical Character, vol. 106, no. 738, pages 463–477, 1924.

[Kalinin 08] S. V. Kalinin & V. Meunier. *Electronic flexoelectricity in low-dimensional systems*. Phys. Rev. B, vol. 77, no. 3, page 033403, Jan 2008.

[Kim 13] S. M. Kim, A. Hsu, P. Araujo, Y.-H. Lee, T. Palacios, M. Dresselhaus, J.-C. Idrobo, K. K. Kim & J. Kong. *Synthesis of patched or stacked graphene and hBN flakes: a route to hybrid structure discovery*. Nano Lett., vol. 13, no. 3, pages 933–941, 2013.

[Kim 19] M. Kim, S. H. Kim, M. U. Park, C. Lee, M. Kim, Y. Yi & K.-H. Yoo. *MoS_2 triboelectric nanogenerators based on depletion layers*. Nano Energy, vol. 65, page 104079, 2019.

[King-Smith 93] R. D. King-Smith & D. Vanderbilt. *Theory of polarization of crystalline solids*. Phys. Rev. B, vol. 47, no. 3, pages 1651–1654, Jan 1993.

[Kityk 00] A. V. Kityk, W. Schranz, P. Sondergeld, D. Havlik, E. K. H. Salje & J. F. Scott. *Low-frequency superelasticity and nonlinear elastic behavior of* $SrTiO_3$ *crystals*. Phys. Rev. B, vol. 61, no. 2, pages 946–956, Jan 2000.

[Kogan 64] S. M. Kogan. *Piezoelectric effect during inhomogeneous deformation and acoustic scattering of carriers in crystals*. Sov. Phys. Solid State, vol. 5, no. 10, pages 2069–2070, 1964.

[Kresse 96] G. Kresse & J. Furthmüller. *Efficient iterative schemes for ab initio total-energy calculations using a plane-wave basis set*. Phys. Rev. B, vol. 54, no. 16, page 11169, 1996.

[Krichen 16] S. Krichen & P. Sharma. *Flexoelectricity: A perspective on an unusual electromechanical coupling*. J. Appl. Mech., vol. 83, no. 3, 2016.

[Kumar 21] S. Kumar, D. Codony, I. Arias & P. Suryanarayana. *Flexoelectricity in atomic monolayers from first principles*. Nanoscale, vol. 13, no. 3, pages 1600–1607, 2021.

[Kundalwal 17] S. Kundalwal, S. Meguid & G. Weng. *Strain gradient polarization in graphene*. Carbon, vol. 117, pages 462–472, 2017.

[Kundalwal 20] S. Kundalwal, V. K. Choyal, N. Luhadiya & V. Choyal. *Effect of carbon doping on electromechanical response of boron nitride nanosheets*. Nanotechnology, vol. 31, no. 40, page 405710, 2020.

[Kundalwal 21] S. I. Kundalwal, V. K. Choyal & V. Choyal. *Flexoelectric effect in boron nitride–graphene heterostructures*. Acta Mech., vol. 232, no. 10, pages 3781–3800, 2021.

[Kvashnin 15] A. Kvashnin, P. Sorokin & B. Yakobson. *Flexoelectricity in Carbon Nanostructures: Nanotubes, Fullerenes, and Nanocones*. J. Phys. Chem. Lett., vol. 6, no. 14, pages 2740–2744, Jul 2015.

[Kwon 14] S. R. Kwon, W. Huang, L. Shu, F.-G. Yuan, J.-P. Maria & X. Jiang. *Flexoelectricity in barium strontium titanate thin film*. Appl. Phys. Lett., vol. 105, no. 14, page 142904, 2014.

[Kwon 16] S. R. Kwon, W. Huang, S. Zhang, F. G. Yuan & X. Jiang. *Study on a flexoelectric microphone using barium strontium titanate*. JMM, vol. 26, no. 4, page 045001, 2016.

[Langlet 04] R. Langlet, M. Arab, F. Picaud, M. Devel & C. Girardet. *Influence of molecular adsorption on the dielectric properties of a single wall nanotube: A model sensor*. J. Chem. Phys., vol. 121, no. 19, pages 9655–9665, 2004.

[Langlet 06] R. Langlet, M. Devel & P. Lambin. *Computation of the static polarizabilities of multi-wall carbon nanotubes and fullerites using a Gaussian regularized point dipole interaction model*. Carbon, vol. 44, no. 14, pages 2883–2895, 2006.

[Langlet 07] R. Langlet, A. Mayer, N. Geuquet, H. Amara, M. Vandescuren, L. Henrard, S. Maksimenko & P. Lambin. *Study of the polarizability of fullerenes with a monopole–dipole interaction model*. Diam. Relat. Mater., vol. 16, no. 12, pages 2145–2149, 2007.

[Langlet 08] R. Langlet, P. Lambin, A. Mayer, P. Kuzhir & S. Maksimenko. *Dipole polarizability of onion-like carbons and electromagnetic properties of their composites*. Nanotechnology, vol. 19, no. 11, page 115706, 2008.

[Laturia 18] A. Laturia, M. L. Van de Put & W. G. Vandenberghe. *Dielectric properties of hexagonal boron nitride and transition metal dichalcogenides: from monolayer to bulk*. NPJ 2D Mater. Appl., vol. 2, page 6, 2018.

[Lecoutre 18] G. Lecoutre. *Etude de la fléxoélectricité de nanosystèmes par le développement d'algorithmes mêlant approche atomistique et mécanique des milieux continus*. PhD thesis, Université Bourgogne Franche-Comté, 2018.

[Lee 15] Y. Lee, S. Park, H. Kim, G. H. Han, Y. H. Lee & J. Kim. *Characterization of the structural defects in CVD-grown monolayered MoS_2 using near-field photoluminescence imaging*. Nanoscale, vol. 7, no. 28, pages 11909–11914, 2015.

[Li 13] Y. Li, L. Shu, Y. Zhou, J. Guo, F. Xiang, L. He & H. Wang. *Enhanced flexoelectric effect in a non-ferroelectric composite.* Appl. Phys. Lett., vol. 103, no. 14, page 142909, 2013.

[Li 14] Y. Li, L. Shu, W. Huang, X. Jiang & H. Wang. *Giant flexoelectricity in $Ba_{0.6}Sr_{0.4}TiO_3/Ni_{0.8}Zn_{0.2}Fe_2O_4$ composite.* Appl. Phys. Lett., vol. 105, no. 16, page 162906, 2014.

[Li 15] X. Li & H. Zhu. *Two-dimensional MoS_2: Properties, preparation, and applications.* J. Mater., vol. 1, no. 1, pages 33–44, 2015.

[Li 20] X. Li, Y. Li & L. Wu. *Enhanced flexoelectricity in $Ba_{0.6}Sr_{0.4}TiO_3$/epoxy composite.* Mater. Lett., vol. 260, page 126953, 2020.

[Ma 01a] W. Ma & L. E. Cross. *Large flexoelectric polarization in ceramic lead magnesium niobate.* Appl. Phys. Lett., vol. 79, no. 26, pages 4420–4422, 2001.

[Ma 01b] W. Ma & L. E. Cross. *Observation of the flexoelectric effect in relaxor $Pb(Mg_{1/3}Nb_{2/3})O_3$ ceramics.* Appl. Phys. Lett., vol. 78, no. 19, pages 2920–2921, 2001.

[Ma 02] W. Ma & L. E. Cross. *Flexoelectric polarization of barium strontium titanate in the paraelectric state.* Appl. Phys. Lett., vol. 81, no. 18, pages 3440–3442, 2002.

[Ma 03] W. Ma & L. E. Cross. *Strain-gradient-induced electric polarization in lead zirconate titanate ceramics.* Appl. Phys. Lett., vol. 82, no. 19, pages 3293–3295, 2003.

[Ma 05] W. Ma & L. E. Cross. *Flexoelectric effect in ceramic lead zirconate titanate.* Appl. Phys. Lett., vol. 86, no. 7, page 072905, 2005.

[Ma 06] W. Ma & L. E. Cross. *Flexoelectricity of barium titanate.* Appl. Phys. Lett., vol. 88, no. 23, page 232902, 2006.

[Madziarz 21] M. Madziarz. *Transferability of Molecular Potentials for 2D Molybdenum Disulphide.* Materials, vol. 14, no. 3, 2021.

[Majdoub 08] M. S. Majdoub, P. Sharma & T. Çağin. *Dramatic enhancement in energy harvesting for a narrow range of dimensions in piezoelectric nanostructures.* Phys. Rev. B, vol. 78, no. 12, page 121407, Sep 2008.

[Maranganti 09] R. Maranganti & P. Sharma. *Atomistic determination of flexoelectric properties of crystalline dielectrics*. Phys. Rev. B, vol. 80, no. 5, page 054109, 2009.

[Mashkevich 57] V. Mashkevich & K. Tolpygo. *Electrical, optical and elastic properties of diamond type crystals*. Sov. Phys. JETP, vol. 5, no. 3, pages 435–439, 1957.

[Mayer 05a] A. Mayer. *Polarization of metallic carbon nanotubes from a model that includes both net charges and dipoles*. Phys. Rev. B, vol. 71, no. 23, page 235333, Jun 2005.

[Mayer 05b] A. Mayer. *A monopole-dipole model to compute the polarization of metallic carbon nanotubes*. Appl. Phys. Lett., vol. 86, no. 15, page 153110, 2005.

[Mayer 05c] A. Mayer & P. Lambin. *Calculation of the electrostatic forces that act on carbon nanotubes placed in the vicinity of metallic protrusions*. Nanotechnology, vol. 16, no. 11, page 2685, 2005.

[Mayer 06] A. Mayer, P. Lambin & R. Langlet. *Charge-dipole model to compute the polarization of fullerenes*. Appl. Phys. Lett., vol. 89, no. 6, page 063117, 2006.

[Mayer 07a] A. Mayer. *Formulation in terms of normalized propagators of a charge-dipole model enabling the calculation of the polarization properties of fullerenes and carbon nanotubes*. Phys. Rev. B, vol. 75, no. 4, page 045407, Jan 2007.

[Mayer 07b] A. Mayer, P. Lambin & P. O. Åstrand. *An electrostatic interaction model for frequency-dependent polarizability: Methodology and applications to hydrocarbons and fullerenes*. Nanotechnology, vol. 19, no. 2, page 025203, 2007.

[Mayer 08] A. Mayer & P.-O. Åstrand. *A Charge-Dipole Model for the Static Polarizability of Nanostructures Including Aliphatic, Olephinic, and Aromatic Systems*. J. Phys. Chem. A, vol. 112, no. 6, pages 1277–1285, 2008.

[Mayer 09a] A. Mayer & G. C. Schatz. *Enhanced polarizability of aromatic molecules placed in the vicinity of silver clusters*. J. Phys. Condens. Matter, vol. 21, no. 32, page 325301, 2009.

[Mayer 09b] A. Mayer, A. González, C. Aikens & G. Schatz. *A charge-dipole interaction model for the frequency-dependent polarizability of silver clusters*. Nanotechnology, vol. 20, no. 19, page 195204, 2009.

[Mbarki 14a] R. Mbarki, N. Baccam, K. Dayal & P. Sharma. *Piezoelectricity above the Curie temperature? Combining flexoelectricity and functional grading to enable high-temperature electromechanical coupling.* Appl. Phys. Lett., vol. 104, no. 12, page 122904, 2014.

[Mbarki 14b] R. Mbarki, J. Haskins, A. Kinaci & T. Cagin. *Temperature dependence of flexoelectricity in $BaTiO_3$ and $SrTiO_3$ perovskite nanostructures.* Phys. Lett. A, vol. 378, no. 30, pages 2181–2183, 2014.

[Merupo 17] V. I. Merupo, B. Guiffard, R. Seveno, M. Tabellout & A. Kassiba. *Flexoelectric response in soft polyurethane films and their use for large curvature sensing.* J. Appl. Phys., vol. 122, no. 14, page 144101, 2017.

[Meyer 69] R. B. Meyer. *Piezoelectric effects in liquid crystals.* Phys. Rev. Lett., vol. 22, no. 18, page 918, 1969.

[Miller 90] K. J. Miller. *Calculation of the molecular polarizability tensor.* J. Am. Chem. Soc., vol. 112, no. 23, pages 8543–8551, 1990.

[Mindlin 68] R. D. Mindlin. *Polarization gradient in elastic dielectrics.* Int. J. Solids Struct., vol. 4, no. 6, pages 637–642, 1968.

[Mizzi 22] C. A. Mizzi, B. Guo & L. D. Marks. *Experimental determination of flexoelectric coefficients in $SrTiO_3$, $KTaO_3$, TiO_2, and $YAlO_3$ single crystals.* Phys. Rev. Mater., vol. 6, no. 5, page 055005, May 2022.

[Narvaez 14] J. Narvaez & G. Catalan. *Origin of the enhanced flexoelectricity of relaxor ferroelectrics.* Appl. Phys. Lett., vol. 104, no. 16, page 162903, 2014.

[Narvaez 15] J. Narvaez, S. Saremi, J. Hong, M. Stengel & G. Catalan. *Large flexoelectric anisotropy in paraelectric barium titanate.* Phys. Rev. Lett., vol. 115, no. 3, page 037601, 2015.

[Neek-Amal 14] M. Neek-Amal & F. Peeters. *Graphene on boron-nitride: Moiré pattern in the van der Waals energy.* Appl. Phys. Lett., vol. 104, no. 4, page 041909, 2014.

[Olson 78] M. L. Olson & K. R. Sundberg. *An atom monopole–dipole interaction model with charge transfer for the treatment of polarizabilities of π-bonded molecules.* J. Chem. Phys., vol. 69, no. 12, pages 5400–5404, 1978.

[Ong 12] M. T. Ong & E. J. Reed. *Engineered piezoelectricity in graphene.* ACS nano, vol. 6, no. 2, pages 1387–1394, 2012.

[Pakdel 12] A. Pakdel, C. Zhi, Y. Bando & D. Golberg. *Low-dimensional boron nitride nanomaterials*. Mater. Today, vol. 15, no. 6, pages 256–265, 2012.

[Pandey 21a] T. Pandey, L. Covaci, M. V. Milošević & F. M. Peeters. *Flexoelectricity and transport properties of phosphorene nanoribbons under mechanical bending*. Phys. Rev. B, vol. 103, no. 23, page 235406, Jun 2021.

[Pandey 21b] T. Pandey, L. Covaci & F. M. Peeters. *Tuning flexoelectricity and electronic properties of zig-zag graphene nanoribbons by functionalization*. Carbon, vol. 171, pages 551–559, 2021.

[Perdew 96] J. P. Perdew, K. Burke & M. Ernzerhof. *Generalized gradient approximation made simple*. Phys. Rev. Lett., vol. 77, no. 18, page 3865, 1996.

[Petrov 86] A. Petrov & V. Sokolov. *Curvature-electric effect in black lipid membranes*. Eur. Biophys. J., vol. 13, no. 3, pages 139–155, 1986.

[Petrov 89] A. Petrov, R. Ramsey & P. Usherwood. *Curvature-electric effects in artificial and natural membranes studied using patch-clamp techniques*. Eur. Biophys. J., vol. 17, no. 1, pages 13–17, 1989.

[Petrov 93] A. G. Petrov, B. A. Miller, K. Hristova & P. N. Usherwood. *Flexoelectric effects in model and native membranes containing ion channels*. Eur. Biophys. J., vol. 22, no. 4, pages 289–300, 1993.

[Picaud 05] F. Picaud, R. Langlet, M. Arab, M. Devel, C. Girardet, S. Natarajan, S. Chopra & A. Rao. *Gas-induced variation in the dielectric properties of carbon nanotube bundles for selective sensing*. J. Appl. Phys., vol. 97, no. 11, page 114316, 2005.

[Plimpton 95] S. Plimpton. *Fast parallel algorithms for short-range molecular dynamics*. J. Comput. Phys., vol. 117, no. 1, pages 1–19, 1995.

[Ponomareva 12] I. Ponomareva, A. Tagantsev & L. Bellaiche. *Finite-temperature flexoelectricity in ferroelectric thin films from first principles*. Phys. Rev. B, vol. 85, no. 10, page 104101, 2012.

[Powell 09] M. J. Powell. *The BOBYQA algorithm for bound constrained optimization without derivatives*. Cambridge NA Report NA2009/06, University of Cambridge, Cambridge, vol. 26, 2009.

[Qi 10] Y. Qi, N. T. Jafferis, K. Lyons Jr, C. M. Lee, H. Ahmad & M. C. McAlpine. *Piezoelectric ribbons printed onto rubber for flexible energy conversion.* Nano Lett., vol. 10, no. 2, pages 524–528, 2010.

[Resta 10] R. Resta. *Towards a bulk theory of flexoelectricity.* Phys. Rev. Lett., vol. 105, no. 12, page 127601, 2010.

[Royo 19] M. Royo & M. Stengel. *First-principles theory of spatial dispersion: Dynamical quadrupoles and flexoelectricity.* Phys. Rev. X, vol. 9, no. 2, page 021050, 2019.

[Royo 22] M. Royo & M. Stengel. *Lattice-mediated bulk flexoelectricity from first principles.* Phys. Rev. B, vol. 105, no. 6, page 064101, 2022.

[Schiaffino 19] A. Schiaffino, C. E. Dreyer, D. Vanderbilt & M. Stengel. *Metric wave approach to flexoelectricity within density functional perturbation theory.* Phys. Rev. B, vol. 99, no. 8, page 085107, 2019.

[Scott 68] J. F. Scott. *Lattice perturbations in $CaWO_4$ and $CaMoO_4$.* J. Chem. Phys., vol. 48, no. 2, pages 874–876, 1968.

[Shandarov 12] S. Shandarov, N. Burimov, S. Shmakov, P. Zuev, A. Urban, V. Gorbachev, Y. F. Kargin & V. Shepelevich. *Contribution from the inverse flexoelectic effect to the photorefractive response in a bismuth titanium oxide.* BRSPEX, vol. 76, no. 12, pages 1297–1300, 2012.

[Shen 10] S. Shen & S. Hu. *A theory of flexoelectricity with surface effect for elastic dielectrics.* J. Mech. Phys. Solids, vol. 58, no. 5, pages 665–677, 2010.

[Shi 18] W. Shi, Y. Guo, Z. Zhang & W. Guo. *Flexoelectricity in monolayer transition metal dichalcogenides.* J. Phys. Chem. Lett., vol. 9, no. 23, pages 6841–6846, 2018.

[Shi 19] W. Shi, Y. Guo, Z. Zhang & W. Guo. *Strain gradient mediated magnetism and polarization in monolayer VSe_2.* J. Phys. Chem. C, vol. 123, no. 40, pages 24988–24993, 2019.

[Shu 13] L. Shu, X. Wei, L. Jin, Y. Li, H. Wang & X. Yao. *Enhanced direct flexoelectricity in paraelectric phase of $Ba(Ti_{0.87}Sn_{0.13})O_3$ ceramics.* Appl. Phys. Lett., vol. 102, no. 15, page 152904, 2013.

[Shu 14] L. Shu, W. Huang, S. Ryung Kwon, Z. Wang, F. Li, X. Wei, S. Zhang, M. Lanagan, X. Yao & X. Jiang. *Converse flexoelectric coefficient f_{1212} in bulk $Ba_{0.67}Sr_{0.33}TiO_3$*. Appl. Phys. Lett., vol. 104, no. 23, page 232902, 2014.

[Shu 17] L. Shu, T. Li, Z. Wang, F. Li, L. Fei, Z. Rao, M. Ye, S. Ke, W. Huang, Y. Wang*et al.* *Flexoelectric behavior in PIN-PMN-PT single crystals over a wide temperature range*. Appl. Phys. Lett., vol. 111, no. 16, page 162901, 2017.

[Singh 21] D. Singh, B. Roul, K. Nanda & S. Krupanidhi. *Light-Emitting Diodes and Photodetectors-Advances and Future Directions*, 2021.

[Song 21] Y. Song, M. Devel & Z. Wang. *An atomistic model for predicting charge distribution in hexagonal boron nitride*. Phys. E, vol. 127, page 114567, 2021.

[Springolo 21] M. Springolo, M. Royo & M. Stengel. *Direct and converse flexoelectricity in two-dimensional materials*. Phys. Rev. Lett., vol. 127, no. 21, page 216801, 2021.

[Stengel 13] M. Stengel. *Flexoelectricity from density-functional perturbation theory*. Phys. Rev. B, vol. 88, no. 17, page 174106, 2013.

[Stengel 14] M. Stengel. *Flexoelectricity via coordinate transformations*. In APS March Meeting Abstracts, volume 2014, pages G41–005, 2014.

[Stengel 15] M. Stengel. *From flexoelectricity to absolute deformation potentials: The case of $SrTiO_3$*. Phys. Rev. B, vol. 92, no. 20, page 205115, 2015.

[Stuart 00] S. J. Stuart, A. B. Tutein & J. A. Harrison. *A reactive potential for hydrocarbons with intermolecular interactions*. J. Chem. Phys., vol. 112, no. 14, pages 6472–6486, 2000.

[Sun 22] L. Sun, B. Javvaji, C. Zhang, X. Zhuang & W. Chen. *Effect of flexoelectricity on a bilayer molybdenum disulfide Schottky contact*. Nano Energy, vol. 102, page 107701, 2022.

[Sunyk 03] R. Sunyk & P. Steinmann. *On higher gradients in continuum-atomistic modelling*. Int. J. Solids Struct., vol. 40, no. 24, pages 6877–6896, 2003.

[Tagantsev 85] A. Tagantsev. *Theory of flexoelectric effect in crystals*. Zhurnal Eksperimental'noi i Teoreticheskoi Fiziki, vol. 88, no. 6, pages 2108–2122, 1985.

[Tagantsev 86] A. Tagantsev. *Piezoelectricity and flexoelectricity in crystalline dielectrics*. Phys. Rev. B, vol. 34, no. 8, pages 5883–5889, 1986.

[Tagantsev 91] A. K. Tagantsev. *Electric polarization in crystals and its response to thermal and elastic perturbations*. Phase Transit., vol. 35, no. 3, pages 119–203, 1991.

[Tagantsev 16] A. K. Tagantsev & P. V. Yudin. Flexoelectricity in solids: from theory to applications. World Scientific, 2016.

[Tersoff 88] J. Tersoff. *New empirical approach for the structure and energy of covalent systems*. Phys. Rev. B, vol. 37, no. 12, page 6991, 1988.

[Thole 81] B. T. Thole. *Molecular polarizabilities calculated with a modified dipole interaction*. Chem. Phys., vol. 59, no. 3, pages 341–350, 1981.

[Thompson 22] A. P. Thompson, H. M. Aktulga, R. Berger, D. S. Bolintineanu, W. M. Brown, P. S. Crozier, P. J. in 't Veld, A. Kohlmeyer, S. G. Moore, T. D. Nguyen, R. Shan, M. J. Stevens, J. Tranchida, C. Trott & S. J. Plimpton. *LAMMPS - a flexible simulation tool for particle-based materials modeling at the atomic, meso, and continuum scales*. Comp. Phys. Comm., vol. 271, page 108171, 2022.

[Tian 16] H. Tian, M. L. Chin, S. Najmaei, Q. Guo, F. Xia, H. Wang & M. Dubey. *Optoelectronic devices based on two-dimensional transition metal dichalcogenides*. Nano Res., vol. 9, no. 6, pages 1543–1560, 2016.

[Todorov 94] A. Todorov, A. Petrov & J. Fendler. *First observation of the converse flexoelectric effect in bilayer lipid membranes*. J. Phys. Chem., vol. 98, no. 12, pages 3076–3079, 1994.

[Tolpygo 63] K. Tolpygo. *Long wavelength oscillations of diamond-type crystals including long range forces*. Sov. Phys. Solid State, vol. 4, no. 7, pages 1297–1305, 1963.

[Torrens 99] F. Torrens, J. Sánchez-Marín & I. Nebot-Gil. *Polarization by the effect of a small torsional change in the benzothiazole (A)-benzobisthiazole (B) oligomer A-B13-A*. Molecules, vol. 4, no. 1, pages 28–51, 1999.

[Torrens 00] F. Torrens. *Molecular polarizability of Sc_n, C_n and endohedral $Sc_n@C_m$ clusters*. Microelectron. Eng., vol. 51, no. 3, pages 613–626, 2000.

[Torrens 01] F. Torrens. *Molecular polarizability of Sc and C (fullerene and graphite) clusters*. Molecules, vol. 6, no. 6, pages 496–509, 2001.

[Torrens 02a] F. Torrens. *Molecular polarizability of fullerenes and endohedral metallofullerenes*. J. Phys. Org. Chem., vol. 15, no. 11, pages 742–749, 2002.

[Torrens 02b] F. Torrens. *Molecular polarizability of semiconductor clusters and nanostructures*. Phys. E, vol. 13, no. 1, pages 67–71, 2002.

[Torrens 03] F. Torrens. *Effect of elliptical deformation on molecular polarizabilities of model carbon nanotubes from atomic increments*. J. Nanosci. Nanotechnol., vol. 3, no. 4, pages 313–318, 2003.

[Torrens 04] F. Torrens. *Effect of type, size and deformation on the polarizability of carbon nanotubes from atomic increments*. Nanotechnology, vol. 15, no. 4, page S259, 2004.

[Vanderbilt 00] D. Vanderbilt. *Berry-phase theory of proper piezoelectric response*. J Phys. Chem. Solids., vol. 61, no. 2, pages 147–151, 2000.

[Wang 07a] Z. Wang & M. Devel. *Electrostatic deflections of cantilevered metallic carbon nanotubes via charge-dipole model*. Phys. Rev. B, vol. 76, no. 19, page 195434, Nov 2007.

[Wang 07b] Z. Wang, M. Devel, R. Langlet & B. Dulmet. *Electrostatic deflections of cantilevered semiconducting single-walled carbon nanotubes*. Phys. Rev. B, vol. 75, no. 20, page 205414, May 2007.

[Wang 08a] Z. Wang. *Propriétés électro-mécaniques des nanotubes de carbone*. PhD thesis, Université de Franche-Comté, 2008.

[Wang 08b] Z. Wang, M. Zdrojek, T. Mélin & M. Devel. *Electric charge enhancements in carbon nanotubes: Theory and experiments*. Phys. Rev. B, vol. 78, no. 8, page 085425, Aug 2008.

[Wang 09a] Z. Wang. *Alignment of graphene nanoribbons by an electric field*. Carbon, vol. 47, no. 13, pages 3050–3053, 2009.

[Wang 09b] Z. Wang. *Effects of substrate and electric fields on charges in carbon nanotubes*. Phys. Rev. B, vol. 79, no. 15, page 155407, Apr 2009.

[Wang 09c] Z. Wang & L. Philippe. *Deformation of Doubly Clamped Single-Walled Carbon Nanotubes in an Electrostatic Field*. Phys. Rev. Lett., vol. 102, no. 21, page 215501, May 2009.

[Wang 10a] Z. Wang, L. Philippe & J. Elias. *Deflection of suspended graphene by a transverse electric field*. Phys. Rev. B, vol. 81, no. 15, page 155405, Apr 2010.

[Wang 10b] Z. Wang & R. W. Scharstein. *Electrostatics of graphene: Charge distribution and capacitance*. Chem. Phys. Lett., vol. 489, no. 4, pages 229–236, 2010.

[Wang 13] Z. Wang, X. X. Zhang, X. Wang, W. Yue, J. Li, J. Miao & W. Zhu. *Giant flexoelectric polarization in a micromachined ferroelectric diaphragm*. Adv. Funct. Mater., vol. 23, no. 1, pages 124–132, 2013.

[Wang 19] B. Wang, Y. Gu, S. Zhang & L.-Q. Chen. *Flexoelectricity in solids: Progress, challenges, and perspectives*. Prog. Mater. Sci., vol. 106, page 100570, 2019.

[Wen 17] M. Wen, S. N. Shirodkar, P. Plecháč, E. Kaxiras, R. S. Elliott & E. B. Tadmor. *A force-matching Stillinger-Weber potential for MoS_2: Parameterization and Fisher information theory based sensitivity analysis*. J. Appl. Phys., vol. 122, no. 24, page 244301, 2017.

[Wu 05] X. Wu, D. Vanderbilt & D. Hamann. *Systematic treatment of displacements, strains, and electric fields in density-functional perturbation theory*. Phys. Rev. B, vol. 72, no. 3, page 035105, 2005.

[Wu 21] M. Wu, Z. Jiang, X. Lou, F. Zhang, D. Song, S. Ning, M. Guo, S. J. Pennycook, J.-y. Dai & Z. Wen. *Flexoelectric Thin-Film Photodetectors*. Nano Lett., vol. 21, no. 7, pages 2946–2952, 2021.

[Xu 13] T. Xu, J. Wang, T. Shimada & T. Kitamura. *Direct approach for flexoelectricity from first-principles calculations: cases for $SrTiO_3$ and $BaTiO_3$*. J. Phys. Condens. Matter, vol. 25, no. 41, page 415901, 2013.

[Yan 13a] X. Yan, W. Huang, S. Kwon, S. Yang, X. Jiang & F. Yuan. *Design of a curvature sensor using a flexoelectric material*. In Sensors and Smart Structures Technologies for Civil, Mechanical, and Aerospace Systems 2013, volume 8692, pages 193–202. SPIE, 2013.

[Yan 13b] X. Yan, W. Huang, S. R. Kwon, S. Yang, X. Jiang & F.-G. Yuan. *A sensor for the direct measurement of curvature based on flexoelectricity*. Smart Mater. Struct., vol. 22, no. 8, page 085016, 2013.

[Yan 19] J. Yan, L. Tong, R. Luo & D. Gao. *Thickness of monolayer h-BN nanosheet and edge effect on free vibration behaviors*. IJMS, vol. 164, page 105163, 2019.

[Yang 18] Y. Yang, M. Devel & Z. Wang. *An atomistic model for the charge distribution in layered MoS_2*. J. Chem. Phys., vol. 149, no. 12, page 124102 (7), 2018.

[Yudin 13] P. Yudin & A. Tagantsev. *Fundamentals of flexoelectricity in solids*. Nanotechnology, vol. 24, no. 43, page 432001, 2013.

[Zhang 15a] S. Zhang, X. Liang, M. Xu, B. Feng & S. Shen. *Shear flexoelectric response along 3121 direction in polyvinylidene fluoride*. Appl. Phys. Lett., vol. 107, no. 14, page 142902, 2015.

[Zhang 15b] S. Zhang, M. Xu, X. Liang & S. Shen. *Shear flexoelectric coefficient μ_{1211} in polyvinylidene fluoride*. J. Appl. Phys., vol. 117, no. 20, page 204102, 2015.

[Zhang 16] S. Zhang, M. Xu, G. Ma, X. Liang & S. Shen. *Experimental method research on transverse flexoelectric response of poly (vinylidene fluoride)*. Jpn. J. Appl. Phys., vol. 55, no. 7, page 071601, 2016.

[Zhang 17a] S. Zhang, K. Liu, M. Xu, H. Shen, K. Chen, B. Feng & S. Shen. *Investigation of the 2312 flexoelectric coefficient component of polyvinylidene fluoride: Deduction, simulation, and mensuration*. Sci. Rep., vol. 7, page 3134, 2017.

[Zhang 17b] S. Zhang, K. Liu, M. Xu & S. Shen. *A curved resonant flexoelectric actuator*. Appl. Phys. Lett., vol. 111, no. 8, page 082904, 2017.

[Zhang 19] S. Zhang, K. Liu, X. Wen, T. Wu, M. Xu & S. Shen. *Converse flexoelectricity with relative permittivity gradient*. Appl. Phys. Lett., vol. 114, no. 5, page 052903, 2019.

[Zhang 22] J. Zhang, G. Li, B. Zhang & L. Xiang. *Flexoelectricity and electronic properties of monolayer GaSe under shear strain gradient*. Phys. Lett. A, vol. 436, page 128090, 2022.

[Zhong 94] W. Zhong, R. D. King-Smith & D. Vanderbilt. *Giant LO-TO splittings in perovskite ferroelectrics*. Phys. Rev. Lett., vol. 72, no. 22, pages 3618–3621, May 1994.

[Zhu 06] W. Zhu, J. Y. Fu, N. Li & L. Cross. *Piezoelectric composite based on the enhanced flexoelectric effects*. Appl. Phys. Lett., vol. 89, no. 19, page 192904, 2006.

[Zhu 10] Y. Zhu, S. Murali, W. Cai, X. Li, J. W. Suk, J. R. Potts & R. S. Ruoff. *Graphene and graphene oxide: synthesis, properties, and applications*. Adv. Mater., vol. 22, no. 35, pages 3906–3924, 2010.

[Zhu 15] H. Zhu, Y. Wang, J. Xiao, M. Liu, S. Xiong, Z. J. Wong, Z. Ye, Y. Ye, X. Yin & X. Zhang. *Observation of piezoelectricity in free-standing monolayer MoS_2*. Nat. Nanotechnol, vol. 10, no. 2, pages 151–155, 2015.

[Zhuang 19] X. Zhuang, B. He, B. Javvaji & H. S. Park. *Intrinsic bending flexoelectric constants in two-dimensional materials*. Phys. Rev. B, vol. 99, no. 5, page 054105, Feb 2019.

[Zubko 07] P. Zubko, G. Catalan, A. Buckley, P. Welche & J. Scott. *Strain-gradient-induced polarization in $SrTiO_3$ single crystals*. Phys. Rev. Lett., vol. 99, no. 16, page 167601, 2007.

[Zubko 13] P. Zubko, G. Catalan & A. K. Tagantsev. *Flexoelectric effect in solids*. Annu. Rev. Mater. Res., vol. 43, no. 1, pages 387–421, Jul 2013.

List of Figures

I.1 Effects of mechanical stimulus on centrosymmetric and non-centrosymmetric crystals. (a) and (b) homogeneous deformation polarizes only non-centrosymmetric materials. (c) and (d) inhomogeneous deformation breaks the symmetry of the material to generate non-zero polarization, in both cases. 3

I.2 Schematics of flexoelectric experimental setups for direct measurements of flexoelectric constants (a) Cantilever bending, (b) cylinder twisting, (c) four-point bending, (d) three-point bending, and (e) pyramid compression. Adapted from Figure 3.1 of Wang et al 2019. . 8

I.3 (a) Schematic of piezoresponse force microscopy measurement, adapted from Figure 1 of Abdollahi et al 2019. (b) electric field gradient generation method with a part-cylindrical bar and a trapezoid-section shaped structure, adapted from Figure 1 of Zhang et al 2019. (c) Diagram of sample assembly for converse flexoelectric measurement of the shear strain along x_1 direction generated by the electric field gradient along x_3 direction. Schematic deformation of the trapezoid sample in the lateral mode, adapted from Figure 1 of Shu et al 2014. (d) An optical measurement system based on the scanning Michelson laser beam interferometer. PD: photodiode; BS: beam splitter, adapted from Figure 3 of Fu et al 2006. 9

I.4 Beam curvature sensing: BST curvature sensor attached to beam, adapted from Figure 4 of Yan *et al.* 2013. (b) Relationship between charge output and beam curvature-experimental results of BST curvature sensor, adapted from Figure 7 of Yan *et al.* 2013. (c) Experimental set-up and (d) close-up of the actual curvature sensor attached on a beam, adapted from Figure 6 of *et al.* 2013 12

I.5 Fabrication process of buckled PZT ribbons. (A) PZT ribbons were patterned on an MgO substrate. Released PZT ribbons were transferred to a pre-stretched PDMS slab. Relaxation of PDMS caused the peel-off of certain areas of ribbons and formed the buckled structures. (B) SEM image of PZT ribbons transferred to PDMS with no prestrain. (C) Buckled PZT ribbons after transfer to PDMS with prestrain. Adapted from Figure 1 of Qi *et al.* 2011. 13

I.6 (a) Schematic diagram of a PVDF-based actuator. The symbol θ represents the angle of electrode attachment. To achieve a uniform electric field gradient and application safety, θ in this actuator is set as 120°, adapted from Figure 1 of Zhang *et al.* 2017. (b) Induced displacement as a function of voltage in that PVDF-based actuator, adapted from Figure 4 of Zhang *et al.* 2017. (c) Schematic view of the $SrTiO_3$-based actuator of Bhaskar *et al.*, adapted from Figure 1 of Bhaskar *et al.* 2016. (d) Comparison of the performance of flexoelectric $SrTiO_3$ with those of state-of-the-art piezoelectric bimorphs, adapted from Figure 4 of Bhaskar *et al.* 2016. 14

II.1 The three types of patterned graphene used by Javvaji et al. and us for our stretching simulations: (a) with a circular hole defect, (b) with a triangular hole defect, (c) trapezium shaped 35

II.2 A schematic representation of graphene under loading. Boundary and calculation regions are shown. Unit cell of the graphene lattice is highlighted. 36

II.3 Search algorithm for the static equilibrium of the system subjected to the action of an external load. The convergence criteria c of forces is set to 0.00004 eV/Å. 38

II.4 (a) Variation of polarization along x axis with strain, for trapezium-shaped graphene, graphene with a triangular defect and circular hole defect. The red straight line is the fitting result. The atoms covered with the red regions are fixed during the stretching simulations. (b) Fig. 2b from [Javvaji 18], shown for comparison. 40

II.5 Graphene divided into four pieces marked with A, B, C, D with p meaning dipole moment. 42

III.1 Representative volume element of MoS_2, with 3 atoms (1 Mo, and 2S on top of one another) 47

III.2 Illustration of the extended Cauchy-Born rule. F and G are respectively the first-order and second-order transformation gradients, in a mechanical continuum. 48

III.3 Computed distribution profiles for flexocoupling coefficient f_{2222} for (a) parallelogram-shaped and (b) rectangular RVE for MoS_2 monolayer, with three and six atoms included in (a) parallelogram-shaped and (b) rectangular RVE, respectively 57

IV.1 Schematic of bending simulation for MoS_2 nanoribbon subjected to an external electric field. The left and right parts of the MoS_2 sheet are submitted to an electric field in the bottom-right and top-right direction, respectively. The external electric field $\vec{E}$ is represented by the arrows. θ is the angle with the $+x$ direction. 68

IV.2 Induced charge on a MoS_2 nanoribbon subjected to external electric field. The positive charges move to the right side and the negative ones move to the left side. E represents external electric field, whose direction is denoted by the arrows. The atoms colored red and blue are positively and negatively charged, respectively. The atoms in the central gray zone are fixed. $\vec{\tau}_1$ and $\vec{\tau}_2$ stand for the induced bending moments acting on the MoS_2. 69

IV.3 (a) Schematic diagram of creation of strain gradient G_{333} inside monolayer MoS_2. h and t stand for the small upward shift for a layer of molybdenum atom and the geometric thickness of monolayer MoS_2, respectively. (b) Basic unit for periodic monolayer MoS_2, with length and width of basic unit being 6.570 nm and 6.322 nm, respectively. (c) Variation of polarization P_3 with strain gradient G_{333} for monolayer MoS_2. 72

IV.4 y-axis polarization P_2 vs uniaxial strain ε_{22} for an MoS_2 monolayer. The x axis corresponds to a zigzag edge while the y axis corresponds to an armchair edge. 73

IV.5 (a)Variation of P_3 with strain gradient G_{311}. The magnitude of the electric fields imposed to the MoS_2 monolayer for bending simulation are 0.0424 V/Å, 0.0566 V/Å, 0.0707 V/Å, respectively. (b)Transverse flexoelectric coefficient μ_{3311} vs number of atoms. An exponential function is used to describe the tendency to convergence. The lengths a and b of the sides of the MoS_2 flakes are marked next to each computed μ_{3311}. The first and second number for the size of MoS_2 flake corresponds to a and b, respectively. The unit of a and b is Å. δ denotes characteristic length of exponential function. The angle between the electric field and the positive direction of the x-axis is set to 45 degrees. 76

IV.6 Origin of flexoelectric effect in bending deformation. (a) Under bending deformation, the direction of induced dipole moment points to -z direction. For an undeformed MoS_2 flake, the total dipole moment along the direction normal to the surface of MoS_2 is zero. (b) Separation of the centers (in black) of positive (in red) and negative charges (in blue) due to bending deformation. 77

IV.7 (a) Charge distribution of a bent MoS_2 subjected to $E_x = E_z = 0.4$ V/Å. A and B are two representative regions for explanation of charges transfer from the upper layer to the lower layer, respectively. (b) Δq vs index. Δq is calculated as the charge of sulfur atoms in the lower layer minus the corresponding quantity for the upper layer. The upper and lower sulfur atoms are numbered by increasing value of z. Only the right portion of the bent MoS_2 is shown here. 78

IV.8 Illustration of the different definitions for strain gradient G_{311}. 79

IV.9 (a) Applied displacement field along x axis for each atom with Δd denoting the difference between the x coordinate of atoms in deformed MoS_2 and that in undeformed MoS_2. The two vertical lines are guides to the eye to see the displacements along x between the top and bottom sub-figures. (b) Displacement field $\Delta d = u_x(x)$, strain (ϵ_{xx}) and strain gradient ($\epsilon_{xx,x} = G_{111}$) vs the position along x axis for MoS_2. 81

IV.10 μ_{1111} and μ_{2222} as a function of width for MoS_2 nanoribbons with an infinite length and a finite width 81

IV.11 Variations of polarization P_1 and P_2 with strain gradient G_{111} and G_{222}, respectively. The rectangular frame surrounding the edge of molybdenum disulfide represents the enforcement of periodic boundary conditions in both directions. 82

V.1 Schematic of bending simulation for a 12.5621 nm by 2.0308 nm graphene/h-BN nanoribbon in which the upper layer is graphene and the lower layer is h-boron nitride. A $\searrow\nearrow$-like external electric field $\vec{E}$ is applied to the graphene/h-BN nanoribbon, keeping the middle row of atoms fixed. Periodic boundary conditions are imposed along the y axis. θ is the angle with the $+x$ direction. 88

V.2 Before bending, the π-orbitals of graphene are symmetric and oriented perpendicularly to the plane formed by the three C-C bonds. After bending, charges in π-orbitals are redistributed due to hybridization with σ orbitals. 89

V.3 Computationally obtained configurations for h-BN (a), graphene (b), AA-stacked (c), AB-stacked (d) and AB′ (e) graphene/h-BN heterostructure. Nearest and next-nearest neighbour distances for graphene and h-BN are respectively marked in (a) and (b). Boron atoms are in green and nitrogen atoms in white. The equilibrium inter-layer distances, computed within DFT-D3 plus PBE, for AA-stacked (c), AB-stacked (d) and AB′ (e) graphene/h-BN heterostructure are indicated in the corresponding subfigures 90

V.4 y-averaged intrinsic charge density profile $\bar{\rho}$, in e/atom, for boron, nitride and carbon atoms in a (a) AA-stacked and (b) AB-stacked Graphene/Boron Nitride heterostructure vs the normalized x_{nor} coordinate along the flake ($x_{nor} = x/L$ where L is the length of the flake in the x direction). 94

V.5 (a) Clamped-ion and (b) relaxed-ion polarization change under applied uniaxial strain (ϵ_{22}) along the y direction for the selected 2D materials including h-BN, MoS_2, $MoTe_2$, WS_2 and $MoSe_2$. Piezoelectric coefficient is determined from the slope of the fitted straight line. The inset in (b) shows the geometry of a monolayer of boron nitride (h-BN) from top view, with the black rectangular frame representing a periodic cell used for computation of polarization 95

V.6 Variations of P_2 as a function of applied uniaxial strain ϵ_{22} for graphene/h-BN heterostructure. 97

V.7 Variations of P_2 as a function of applied uniaxial strain ϵ_{22} for h-BN monolayer. 97

V.8 Variation of P_3 with strain gradient G_{311} for graphene (dipoles and P_3 calculated via the method described in [Dumitrică 02] and [Kvashnin 15])(a) and h-BN (dipoles and P_3 calculated via the QP method) (b). The magnitude of the electric fields applied to (a) graphene for bending simulation is 0.0424, 0.0495, and 0.05656 V/Å and (b) h-BN is 0.03535, 0.0424 and 0.0495 V/Å. The angle between the electric fields and the the x-axis is set to 45°. Insets in (a) show the computed dipole moment vector for each atom, with the color of every arrow representing the magnitude of the corresponding dipole moment. 99

V.9 Variation of polarization P_3 with strain gradient G_{311} for graphene. . . 100

V.10 Variation of polarization P_3 with strain gradient G_{311} for AA, AB, AB′ graphene/h-BN heterostructure. 101

V.11 Schematic diagram of AB-stacked graphene/hBN nanoribbon placed in a cubic box (a) top view, (b) side view. 102

V.12 Charge density difference plots for (a) AB′ and (b) AB-stacked heterostructures. The blue and red areas around the atoms represent apparent loss and gain of electrons, respectively. 103

V.13 Nanobubbles, adapted from [Bao 15] 107

List of Tables

I.1 Flexoelectric constants of various materials measured experimentally. The unit of measured flexoelectric coefficients shown is this table is in $\mu C/m$. 1, 2 and 3 represent different definitions of flexoelectric coefficients (1 for $P_l = \mu_{ijkl}\partial\varepsilon_{ij}/\partial x_k$, 2 for $P_i = \mu_{ijkl}\partial\varepsilon_{kl}/\partial x_j$ and 3 for $P_i = \mu_{ijkl}\partial\varepsilon_{jk}/\partial x_l$). 7

II.1 Data necessary to computing the forces in our two atoms case. 24

II.2 Computed forces (in eV/Å) considering the gradients of effective charges and dipoles, using equations II.16, II.17, II.18 and II.19 and without taking them into account (by removing the gradient terms in the previous equations) 25

II.3 Data necessary to computing the forces in our two atoms case, with different values for all parameters. 25

II.4 Computed forces (in eV/Å) considering the gradients of effective charges and dipoles, using equations II.16, II.17, II.18 and II.19 and without taking them into account (by removing the gradient terms in the previous equations), with different values for all parameters. . . 26

II.5 piezoelectric coefficients for trapezium-shaped graphene, graphene with triangular defect, and circular hole defect 41

III.1 Flexocoupling coefficients in volt for MoS_2 monolayer. I means infinity. 58

III.2 Comparison between transverse flexoelectric coefficient μ_{3311} obtained by charge dipole model and theoretical computation. 59

III.3 Flexoelectric coefficients in nC/m for MoS2 monolayer. I means infinity. 60

IV.1 SW potential parameters (part 1) 70

IV.2 SW potential parameters (part 2) 70

IV.3 Comparison between out-of-plane flexoelectric coefficients μ_{3333} obtained by charge-dipole model and experimental measurements. The two different contributions to the polarization coming from charges alone or dipoles alone are considered separately then together for the computation of μ_{3333} by the charge-dipole model. 74

IV.4 Comparison between transverse flexoelectric coefficient μ_{3311} obtained by charge dipole model and theoretical computation. 77

V.1 Parameters of LJ potential for the interactions between carbon and boron and between carbon and nitrogen 87

V.2 Nearest neighbor distance in Å of graphene and h-BN monolayer 90

V.3 Equilibrium layer spacing in Å for AA, AB and AB′-stacked GBN heterostructure with and without vdW corrections. ref[a]:[Giovannetti 07], ref[b]:[Fan 11], ref[c]:[Haigh 12] 92

V.4 Values of the Gaussian charge density widths and atomic electronegativities for boron, nitride and carbon. 93

V.5 Piezoelectric effective coefficient e_{222}/e_{yyy} for various 2D materials (in unit of 10^{-10} C/m since we do not divide by the thickness of the 2D-material), computed by DFT calculations using density functional perturbation theory or Berry phase method. First three lines give our results, last three lines give corresponding results from the literature. 96

V.6 Comparison between μ_{3311} obtained in our work and from the literature, with μ_{3311} for BN and graphene computed with charge dipole (QP) model and Kvashnin et al.'s approach, respectively. 98

V.7 Computed μ_{3311} and intercept of fitting equation for AA, AB and AB′-stacked heterostructure. 101

SPIM

Titre : Étude de la flexoélectricité d'hétérostructures de matériaux 2D, à l'aide d'un modèle atomistique

Mots clefs: flexoélectricité, matériaux 2D, modèle QP

Résumé : L'objectif principal de cette thèse est de mettre au point une méthode systématique pour calculer des coefficients flexoélectriques pour des matériaux bidimensionnels (2D) et des hétérostructures de ces matériaux, en utilisant la mécanique des milieux continus et/ou un modèle atomistique avec des charges et des dipôles effectifs correspondant à des distributions radiales gaussiennes de charge. Nous avons tout d'abord vérifié analytiquement l'équivalence de deux formules utilisées pour calculer les forces d'interaction électrostatique entre atomes dues à un champ électrique exterieur. Ensuite, nous avons cherché à étendre un travail précédent en incorporant des termes impliquant les charges effectives dans une expression analytique, pour calculer les coefficients flexoélectriques de cristaux ioniques, tels que MoS_2. Dans une deuxième partie plus numérique, nous avons pu trouver des configurations de simulation nous permettant de calculer les coefficients flexoélectriques dans le plan μ_{1111} et μ_{2222}, transversal μ_{3311} et hors-plan μ_{3333} pour une monocouche de MoS_2. Pour cela, nous avons utilisé une définition de la polarisation incluant à la fois les effets des charges et des dipôles effectifs, ainsi que le forçage de la conservation de la charge. Les résultats obtenus étant en bon accord avec les données disponibles dans la littérature, nous avons pu appliquer notre méthode au cas d'une structure bicouche graphène / h-BN et étudier l'influence des positions relatives des deux couches.

Title : Study of flexoelectricity in heterostructures of 2D materials, using an atomistic model

Keywords : Flexoelectricity, 2D materials, QP model

Abstract : The main objective of this thesis is to develop a systematic method for calculating flexoelectric coefficients for two-dimensional (2D) materials and heterostructures of these materials, using continuum mechanics and/or an atomistic model with effective charges and dipoles corresponding to Gaussian radial distributions of charges. We first checked analytically the equivalence of two formulas used to calculate the electrostatic interaction forces between atoms due to an external electric field. Next, we sought to extend a previous work by incorporating terms involving effective charges into an analytical expression for calculating the flexoelectric coefficients of ionic crystals, such as MoS_2. In a second, more numerical part, we were able to find simulation set-ups allowing us to calculate the in-plane μ_{1111} and μ_{2222}, transverse μ_{3311} and out-of-plane μ_{3333} flexoelectric coefficients for a monolayer of MoS_2. For this purpose, we have used a definition of polarization including the effects of both charge and effective dipole, as well as charge conservation enforcement. The results obtained being in good agreement with the data available in the literature, we were able to apply our method to the case of a graphene / h-BN bilayer structure and to study the influence of the relative positions of the 2 layers.

UBFC UNIVERSITÉ BOURGOGNE FRANCHE-COMTÉ

Université Bourgogne Franche-Comté
32, avenue de l'Observatoire
25000 Besançon